Search for heavy Higgs bosons A/H decaying to a top-quark pair in pp collisions at $\sqrt{s} = 8$ TeV with the ATLAS detector

DISSERTATION

zur Erlangung des akademischen Grades
doctor rerum naturalium
(Dr. rer. nat.)
im Fach Physik
Spezialisierung: Experimentalphysik

eingereicht an der
Mathematisch-Naturwissenschaftlichen Fakultät
der Humboldt Universität zu Berlin

von
M.Sc. Mădălina Stănescu-Bellu

Präsidentin der Humboldt-Universität zu Berlin
Prof. Dr.-Ing. Dr. Sabine Kunst

Dekan der Mathematisch-Naturwissenschaftlichen Fakultät
Prof. Dr. Elmar Kulke

Gutachter:	1. PD Dr. Klaus Mönig
	2. Prof. Dr. Thomas Lohse
	3. Prof. Dr. Johannes Haller
Tag der mündlichen Prüfung:	29.09.2020

Abstract

In this thesis a search is presented for heavy neutral pseudoscalar A and scalar H Higgs bosons, produced in gg fusion and decaying into a top-antitop quark pair $t\bar{t}$. The search is conducted on the full proton–proton collisions dataset recorded by the ATLAS detector at the Large Hadron Collider at a centre-of-mass energy of $\sqrt{s} = 8$ TeV and corresponding to an integrated luminosity of $\int L(t)\ \mathrm{d}t = 20.3\ \mathrm{fb}^{-1}$. The signal process and the main background from $gg \to t\bar{t}$ production via strong processes interfere heavily, distorting the signal shape from the pure Breit-Wigner resonance peak to a peak-dip structure. This analysis is the first one at the LHC that fully takes into account the interference between a signal and the background processes. The search relies on the statistical analysis of the $t\bar{t}$ invariant mass spectrum, which is reconstructed in signal candidate events with a high-transverse momentum electron or muon, large missing transverse energy from the undetected neutrino and at least four jets. No significant deviation from the expected SM background is observed in data. Exclusion limits are derived in the context of the type-II Two-Higgs-Doublet Model, for Higgs boson masses of 500 and 750 GeV and in the low $\tan\beta$ parameter region, where $\tan\beta$ is the ratio of the vacuum expectation values of the two Higgs doublet fields. These parameter regions have been largely unexplored by searches in any final state. The analysis is published in Ref. [1].

Zusammenfassung

In dieser Dissertation wird die Suche nach schweren neutralen pseudoskalaren A und skalaren H Higgs-Bosonen vorgestellt, die in gg-Fusionen erzeugt werden, und in ein Top-Antitop-Quark-Paar $t\bar{t}$ zerfallen. Gesucht wurde im vollständigen Datensatz von Proton–Proton-Kollisionen bei einer Schwerpunktsenergie von $\sqrt{s} = 8$ TeV, die vom ATLAS-Detektor am Large Hadron Collider aufgezeichnet wurde und einer integrierten Luminosität von $\int L(t)\ \mathrm{d}t = 20.3\ \mathrm{fb}^{-1}$ entspricht. Der Signalprozess und der Haupthintergrund aus der $gg \to t\bar{t}$-Produktion über starke Prozesse interferieren stark, was zu einer Verzerrung des reinen Breit-Wigner-Resonanzpeak in eine Peak-Dip-Struktur führt. Diese Analyse ist die erste am LHC, die die Interferenz zwischen Signal und Hintergrundprozessen vollständig berücksichtigt. Die Suche stützt sich auf die statistische Analyse des invarianten $t\bar{t}$-Massenspektrum, welches aus Ereignissen mit einem Elektron oder Myon mit hohem Transversalimpuls, einer hohen fehlenden Transversalenergie von dem nicht detektierten Neutrino und mindestens vier Jets rekonstruiert wird. In den Daten wird keine signifikante Abweichung vom erwarteten Standardmodell-Hintergrund beobachtet. Die Ausschließungsgrenzen wurden abgeleitet im Kontext des Typ II Two-Higgs-Doublet Model, für Higgs-Bosonen mit einer Masse von 500 und 750 GeV und mit niedrigerem $\tan\beta$-Parameter, bei der $\tan\beta$ das Verhältnis der Vakuumerwartungswerte der beiden Higgs-Dublett-Felder ist. Diese Parameterregionen sind weitgehend unerforscht in Untersuchungen von beliebigen Endzuständen. Die Analyse wurde veröffentlicht in [1].

"To my son Henrik-Aurel,
to mom and Stefan."

Acknowledgements

First of all I would like to express my admiration to all the ATLAS collaboration. An experimental particle physics analysis cannot be done nowadays unaided. It is the convoluted work of many people that contributes to the planning, building, operating, calibrating, developing detector software and interpreting physics results.

My most sincere gratitude goes foremost to my supervisor, PD. Dr. Klaus Mönig, who helped me directly in all my research topics during my PhD, with a lot of thorough and inestimable advice. His excellent theoretical interpretations were always a source of learning for me.

Besides my supervisor, I would like to especially thank Dr. Katharina Behr and Dr. Jike Wang, for their help in converging the last steps of the analysis by bringing in their limit setting tools. They helped as well by editing our publication and by being the publication's contact persons, while I had to pursue already another employment during the day. To Katharina my immense gratitude for her coaching me in many theoretical and experimental aspects, for sharing with me her experience from previous $t\bar{t}$ final state analyses and for proofreading thoroughly my thesis.

To Dr. Thorsten Kuhl my highest appreciation for his supervising our DESY group of top quark resonance analysis and for guiding us with his expertise in $t\bar{t}$ analysis and Monte Carlo generation. Thank you especially for your many pieces of advice during my months of blockage on interference simulation.

One special person I'd like to thank is Dr. Diogo Buarque Franzosi, who developed the theoretical model for the top loop structure with interference effects, that was used in this analysis as well. I appreciate your patience for my many questions.

I cordially thank Christoph Wasicki and Dr. Clemens Lange for building the software foundation for general top quark analyses at DESY. Many generations of PhD students like me had thus a good software starting point, so that they could focus on the software specifics of their individual analyses. To Dr. Elin Bergeås Kuutmann, who acted in the beginning of my PhD as second supervisor, and to Dr. Samuel Calvet, contact person of the $t\bar{t}$ analysis at ATLAS, thank you for your many pieces of advice on analysis details.

Last but not least, I thank my family for putting up with my continuous lack of time for them and for entertaining my perpetuum mobile son. Aurică, let's build that fire truck!

Contents

1. Introduction **1**

2. The Standard Model of Particle Physics **5**
2.1. History of Particle Physics . . . 5
2.2. Properties of Elementary Particles . . . 6
2.3. Forces . . . 9
2.3.1. Electromagnetic Force . . . 9
2.3.2. Weak Force . . . 9
2.3.3. Electroweak Force . . . 10
2.3.4. Strong Force . . . 11
2.4. Perturbation Theory . . . 11
2.5. Renormalisation . . . 12
2.6. Gauge Symmetries . . . 12
2.6.1. QED . . . 13
2.6.2. QCD . . . 13
2.6.3. Higgs Mechanism . . . 14
2.6.4. Electroweak Interaction Revisited . . . 16
2.6.5. Fermion-Scalar Interaction . . . 16
2.6.6. Higgs Boson Production and Decay . . . 17
2.7. Top Quark Properties . . . 18
2.8. Phenomena at Proton–Proton Collisions . . . 19
2.8.1. Parton Shower, Hadronisation and Jets . . . 19
2.8.2. Factorisation . . . 20
2.8.3. Proton–Proton Collisions and PDF . . . 20

3. The ATLAS detector at the LHC **21**
3.1. The Large Hadron Collider . . . 21
3.2. The ATLAS Detector . . . 24
3.2.1. Coordinate System . . . 24
3.2.2. Detector Challenges . . . 26
3.2.3. Inner Detector . . . 26
3.2.4. Calorimeters . . . 28
3.2.5. Muon Spectrometer . . . 30
3.2.6. Forward Detectors . . . 31
3.2.7. Trigger System . . . 31

4. Simulations in 2HDM **33**
4.1. The Two-Higgs-Doublet-Model . . . 33
4.1.1. Motivation for 2HDM and Supersymmetry . . . 33

4.1.2. Theoretical Aspects of 2HDM . . . 34
4.1.3. Production and Decay of A and H . . . 37
4.2. Top/Bottom Loop Structure in $gg \to A/H$ . . . 37
4.3. Setup in MadGraph5_aMC@NLO - NOVELTY . . . 43
4.3.1. Generation of Signal with Interference . . . 43
4.3.2. Comparison between Signal with Interference and Background . . . 44
4.4. Studies of Different Generation Configurations - NOVELTY . . . 44
4.4.1. Spin-Parity Correlations in Top Quark Decays . . . 44
4.4.2. Showering Configuration . . . 47

5. Data Analysis Setup **51**
5.1. Signal Signature . . . 51
5.1.1. Top Quark Pairs Reconstruction Challenges . . . 51
5.1.2. Chosen Signal Signature . . . 53
5.2. Data and Monte Carlo Samples . . . 53
5.2.1. Dataset . . . 54
5.2.2. Background Samples . . . 54
5.2.3. Signal Samples - NOVELTY . . . 55
5.3. Object Reconstruction and Event Selection . . . 60
5.3.1. Tracks, Vertices and Impact Parameters . . . 60
5.3.2. Pileup . . . 60
5.3.3. Electrons . . . 61
5.3.4. Muons . . . 62
5.3.5. Isolation of Leptons . . . 63
5.3.6. Jets . . . 63
5.3.7. b-jet Tagging . . . 66
5.3.8. Overlap Removal . . . 67
5.3.9. Missing Transverse Momentum . . . 68
5.3.10. Event Selection . . . 68
5.4. Mass Reconstruction . . . 70
5.4.1. Neutrino Reconstruction . . . 70
5.4.2. χ^2 Algorithm . . . 72
5.5. Background Estimation from Data . . . 72
5.5.1. W+jets Scale Factors Estimation . . . 75
5.5.2. Multijet Full Background Estimation . . . 76
5.6. Other Monte Carlo Corrections . . . 77
5.6.1. Efficiency Scale Factors . . . 77
5.7. Statistical and Systematic Uncertainties . . . 79
5.7.1. Luminosity Uncertainty . . . 79
5.7.2. Object Reconstruction Uncertainties . . . 80
5.7.3. PDF Uncertainty . . . 83
5.7.4. Background Modelling Uncertainties . . . 84
5.7.5. Signal Modelling Uncertainties - NOVELTY . . . 85

6. Data Analysis Results **89**
6.1. Comparison of Data and Background Expectations . . . 89
6.2. Upper Limits Setting - NOVELTY . . . 90
6.2.1. Motivation . . . 90
6.2.2. Terminology . . . 90
6.2.3. Hypothesis Testing in the Presence of Interference Effects . . . 95
6.2.4. Profile Likelihood Fit under the Background-only Hypothesis . . . 96
6.2.5. Upper Limits Interpretation in 2HDM . . . 97

7. Summary and Outlook **105**

A. Particle Detection Principles **107**
A.1. Interactions of Particles in Matter . . . 107
A.2. Silicon Detectors . . . 108
A.3. General Calorimetry . . . 109

B. Simulation Setup and Validation - NOVELTY **111**
B.1. Setup in MadGraph5_aMC@NLO: Code Excerpts . . . 111
B.2. Validation of the $S + I$ Generation . . . 112
B.3. Validation of the $S + I$ Showering . . . 112

C. Distributions of Systematic Shifts **119**
C.1. Systematics of Total Background . . . 119
C.2. Systematics of Signal with Interference - NOVELTY . . . 125

D. Additional Data Results **129**
D.1. Comparison of Data and Background Expectations . . . 129
D.1.1. b-tagging Category 1 . . . 129
D.1.2. b-tagging Category 2 . . . 134
D.1.3. b-tagging Category 3 . . . 138
D.2. Upper Limits Interpretation with the CLs Technique - NOVELTY . . . 142

Bibliography **145**

Chapter 1.

Introduction

In this thesis a search is described for neutral spin-0 Higgs bosons predicted in models extending the established Standard Model (SM) of Particle Physics, with high masses close to the TeV scale: the pseudoscalar A and the scalar H. They are produced via gluon fusion and decay into a pair of top and antitop quarks, $gg \to A/H \to t\bar{t}$. The search is conducted on the full pp collisions dataset recorded by ATLAS at $\sqrt{s} = 8$ TeV at an integrated luminosity of 20.3 fb^{-1}.

Novelties Presented in the Thesis

The analysis presented in this thesis is the first one at the LHC that takes into account the interference between a signal and the background processes, including the statistical treatment of the interference effect.

All processes with the same final and initial state exhibit interference, hence in this case the above mentioned signal interferes with the SM $gg \to t\bar{t}$ background continuum. These interference effects are significantly enhanced in the case of heavy Higgs bosons A/H due to an imaginary phase in the intermediate top-/bottom-quark production loop [2]. The effects strongly distort the Breit-Wigner resonance peak into a peak-dip structure. The effects are moreover predicted to be large at the LHC because the SM $pp \to t\bar{t}$ production is dominated by the gluon fusion process $gg \to t\bar{t}$ (see Section 3.1.1 in Ref. [3]).

In this thesis a modified statistical analysis technique in introduced, where the profile likelihood function is extended to include the interference of the signal and background amplitudes. The analysis is published in Ref. [1], together with its ATLAS internal documentation in Ref. [4].

Motivation for $t\bar{t}$ Final State and 2HDM Parameter Space

The top quark, produced at the LHC mostly in top-antitop quark ($t\bar{t}$) final state (Figure 2.1 in Ref. [5]), is a key factor in searches for new heavy particles beyond the SM (BSM). The reason is that the top quark is the heaviest particle in the SM, with the highest Yukawa coupling to the Higgs boson, of $\mathcal{O}(1)$, and mass almost identical to the electroweak symmetry breaking scale. Hence many new particles with masses above the $2m_t \approx 350$ GeV threshold are predicted to have large decay branching ratios (BR) to $t\bar{t}$.

The spin-0 states A/H targeted in this analysis are predicted by a class of models referred to as the Two Higgs Doublet Models (2HDM) [6], where the SM Higgs doublet field is extended with

a second Higgs doublet. 2HDMs are motivated by supersymmetry [7], axion models [8] or dark matter, where A/H could mix with scalar or pseudoscalar mediator particles that couple directly to dark matter [9, 10]. There are also 2HDMs that violate the CP charge-parity symmetry of nature [11, 12], where the violation might explain the matter-antimatter asymmetry in the early Universe [13].

The parameter $\tan\beta$, which is the ratio of the vacuum expectation values of the two Higgs doublet fields, is a central parameter, because it directly determines the couplings[1] of A and H, together with m_A and m_H. As one can see in Figure 1.1, the regions with low $\tan\beta$ and mass above 400 GeV have not been probed by analyses in any studied final state. Low values of $\tan\beta$ correspond to large couplings of A/H to the top quarks. This strongly motivates the search presented in this thesis.

The CP-conserving type-II 2HDM, a benchmark close to the Minimal Supersymmetric Standard Model [14], is employed in the signal modelling. The light scalar state h within the model is assumed to be the discovered SM Higgs boson [15, 16]. The assumption of SM couplings for h is referred to as the SM alignment limit and implies $\sin(\beta-\alpha)=1$, where α is the mixing angle between H and h.

Analysis Forerunner

This analysis is based on a comprehensive previous search in the same $t\bar{t}$ final state and on the same dataset [22]. The analysis investigated various benchmarks models as follows. The spin-1 colour-singlet Z', a Z-boson like particle, could arise either in models with top-colour assisted technicolour [23, 24] or as an s-channel mediator in simplified models of dark matter [25]. The warped extra-dimensions Randall-Sundrum models, with spin-1 colour-octet Kaluza-Klein gluons g_{KK} [26] and spin-2 Kaluza-Klein gravitons G_{KK} [27, 28], were searched as well. The interference of these resonances with the SM $t\bar{t}$ is either not present or leads to only slight changes of the $t\bar{t}$ invariant mass spectrum (see Sections 3.2 and 3.3 in Ref. [3]). A spin-0 resonance was investigated as well, albeit only in a generic model, in order to test the sensitivity of the search to spin-0 resonances without any interference effects.

Thesis Structure

The theoretical background of the Standard Model is described in Chapter 2, while the ATLAS experiment is described in Chapter 3. Chapter 4 goes beyond the SM and describes the 2HDM classes, among which type-II is employed in the signal modelling. The inclusion of the interference effects on the traditional signal modelling without interference, has been particularly challenging, since the background contribution must be subtracted from the aggregate of pure resonance signal (S), background (B) and interference (I). Considering that B has a cross-section a few order of magnitudes larger than the ones of S, the convergence of the $S+I$ generation is difficult to obtain.

[1] The couplings determine further the production cross-section, decay width and shape of the interference.

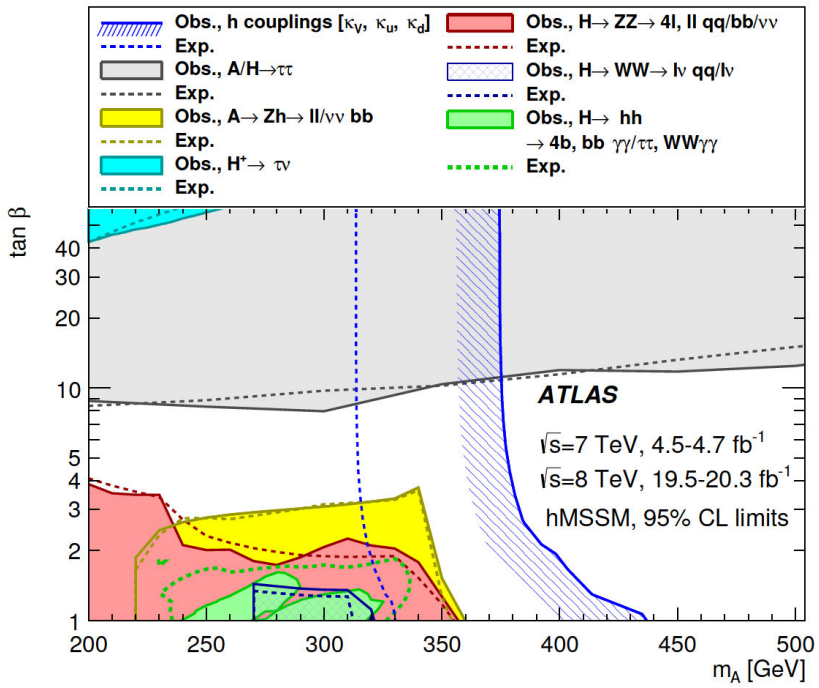

Figure 1.1.: Regions of the $(m_A, \tan\beta)$ plane excluded in the Simplified Minimal Supersymmetric Standard Model (hMSSM) [17, 18] by direct searches for neutral and charged heavy Higgs bosons, in different final states. An exclusion region derived from a measurement of the couplings of the 125 GeV Higgs boson is shown as well. The dashed lines indicate the expected exclusions and the full line and filled regions indicate the observed exclusions. (Figure 6 in Ref. [19])

The referred $\sqrt{s} = 7/8$ TeV results are superseded by the 2019 results at $\sqrt{s} = 13$ TeV [20], where $H \to hh$ covers the 500 GeV mass point at low $\tan\beta$. The earlier results are however referred, for a better comparison with the ones at $\sqrt{s} = 8$ TeV from this thesis.

The $A/H \to t\bar{t}$ results from the analysis presented in this thesis are not included though in the newest exclusions, because hMSSM has a small mass splitting between A and H, while A and H are assumed degenerate in mass in the present and the follow-up $\sqrt{s} = 8$ TeV [21] analyses. The non-degeneracy is planned to be investigated in a reiteration at $\sqrt{s} = 13$ TeV.

The signal region candidate events must be consistent with the decay channel $t\bar{t} \to bW^+ \, \bar{b}W^- \to bq\bar{q}' \, \bar{b}l\nu_l$. One W boson decays into a neutrino and an electron/muon and the other W into two quarks. This leads to a signature referred to as l+jets, with one high transverse momentum (p_{T}) charged lepton, large missing transverse momentum ($E_{\mathrm{T}}^{\mathrm{miss}}$) from the escaping neutrino and at least four jets. Chapter 5 describes the collision dataset, the simulated signal parameter points, the simulated or data-driven background contributions, the reconstruction and selection of physics objects and events, the reconstruction of the $t\bar{t}$ invariant mass ($m_{t\bar{t}}$) spectrum.

Chapter 5 follows closely the methodology from Ref. [22], with a few minor changes. Since in the current analysis only resonances with masses lower than 800 GeV are targeted, as motivated in Chapter 4, the top quark decay products are assumed well separated in the detector, due to the relatively low p_{T} of the top quark. Ref. [22] defines such a topology as "resolved". Higher resonance masses would collimate the decay products into a "boosted" topology, employed in Ref. [22] as well. However in this analysis all events are treated as resolved. Section 5.7 discusses the systematic uncertainties, with a few extra sources compared to Ref. [22], mostly related to the interference modelling.

In Chapter 6, based on the fact that in the model-independent search of Ref. [22] no significant excesses or deficits were observed, exclusion limits at 95% confidence level are derived for each signal parameter point in type-II 2HDM. The interference treatment is introduced as novelty in the exclusion technique, as mentioned above.

Chapter 2.

The Standard Model of Particle Physics

2.1. History of Particle Physics

Elementary particle physics, also called high energy physics or subnuclear physics, describes the nature and interactions of matter and of radiation constituents that have no sub-structure.

The first nature forces discovered were the gravitation and the electricity. After the atom (meaning "unable to cut") was long believed elementary, its negative electrons and positive protons constituents, bound by the electric force, were discovered by Rutherford in 1910 [29]. Neutrons were then discovered [30], as bound with protons in nuclei by a new nuclear strong force. In the 19^{th} century Maxwell unified the electric and the magnetic forces into electromagnetism [31]. The photon was introduced in 1900 by Planck and Einstein to explain the photoelectric effect [32–34]. Fermi proposed the neutrino ν in 1930 [35] to explain for the missing energy and angular momentum in the β decays $n \to p + e^- + \bar{\nu_e}$ and $p \to n + e^+ + \nu_e$, driven by a new nuclear weak force.

Cosmic-ray experiments allowed later the discovery of new subatomic particles such as the positron e^+, muon μ, pion π: very energetic but rare cosmic rays collide with the Earth's atmosphere nuclei, shower and are then reconstructed at the ground, for example with photographic plates. Ground accelerators allowed thereafter higher collision data rates (albeit at lower energy): beams of low mass particles were highly accelerated and collided head-on or to a fixed target, to break up and yield new particles, that were then analysed by surrounding detectors. In this way the quarks were discovered by the '70s. The gluon g that binds the quarks via the fundamental strong force was discovered at DESY [36, 37]. The proton (uud) and neutron (udd) became the $\pm 1/2$ symmetric instances of the strong isospin:

$$I_3 = \frac{(n_u - n_{\bar{u}}) - (n_d - n_{\bar{d}})}{2} \tag{2.1}$$

In the '80s the W and Z bosons, carriers of the weak force, were discovered at CERN [38–41]. Thus the basis of particle physics was complete, described most successfully by the Standard Model (SM) quantum field theory [42–46]. Section 2.2 and 2.3 in this chapter describe the properties and forces of elementary particles within the SM. Sections 2.4 and 2.5 explain how cross-sections depend on the interaction couplings α and how α vary with the collision scale. Section 2.6 re-explains the interactions in the gauge formalism, within the SM internal symmetry $U(1)_Y \times SU(2)_L \times SU(3)_C$ and concludes the properties of the Higgs boson. Section 2.7 describes the top quark properties and Section 2.8 the phenomena at pp collisions.[1][2]

[1] This chapter is documented from [47–50].

[2] In this thesis the natural units system $\epsilon_0 = c = \hbar = 1$ is employed.

	Quark	Mass [MeV]	Q	Lepton	Mass [MeV]	Q	Main decays
I	Up $u(\bar{u})$	2.2	$+\frac{2}{3}$	Electron neutrino $\nu_e(\bar{\nu}_e)$	< 2 eV*	0	Lighter ν
	Down $d(\bar{d})$	4.7	$-\frac{1}{3}$	Electron $e^-(e^+)$	0.511	∓ 1	–
II	Charm $c(\bar{c})$	1275	$+\frac{2}{3}$	Muon neutrino $\nu_\mu(\bar{\nu}_\mu)$	< 2 eV*	0	Lighter ν
	Strange $s(\bar{s})$	95	$-\frac{1}{3}$	Muon $\mu^-(\mu^+)$	105.66	∓ 1	$e^-\bar{\nu}_e\nu_\mu$
III	Top $t(\bar{t})$	173.3×10^3**	$+\frac{2}{3}$	Tau neutrino $\nu_\tau(\bar{\nu}_\tau)$	< 2 eV*	0	Lighter ν
	Bottom $b(\bar{b})$	4180	$-\frac{1}{3}$	Tau $\tau^-(\tau^+)$	1776.86	∓ 1	$\mu^-\bar{\nu}_\mu\nu_\tau$ (17%) $e^-\bar{\nu}_e\nu_\tau$ (17%) ν_τ+pions (65%)
Forces	EM, Weak, Strong			EM (only for charged leptons, not for ν), Weak			

Table 2.1.: The three generations (I, II, III) of elementary fermion flavors in SM. The first row in each generation is the up-type flavor (weak isospin $T_3 = 1/2$), the second row the down-type flavor ($T_3 = -1/2$). Included are their mass (for simplicity without errors), charge Q (in units of e^+), lifetime, main decays and corresponding forces. [51]

* Neutrinos in SM are massless; neutrino oscillations predict however mass. [52]

** The top quark mass is extracted from the kinematics of $t\bar{t}$ events, with a 173.3 GeV world average from the LHC and Tevatron results. [53]

2.2. Properties of Elementary Particles

Classification of Particles by Spin

The quantum number *spin* s parametrises the spin angular momentum S, an intrinsic angular momentum carried at rest as well. S_z can have only the eigenvalues $-s, -(s-1), \ldots, s-1, s$, where s can be: an odd multiple of $\frac{1}{2}$, in the case of *fermions*, obeying the Fermi-Dirac statistics, or integer, in the case of *bosons*, obeying the Bose-Einstein statistics.

SM has 12 elementary fermions: six quarks, six leptons, and their antiparticles (Table 2.1). They are further grouped in three generations, each generation containing weak isospin doublets (Section 2.3.3). Since members of higher generations are heavier and decay eventually to members of the first generation, matter is made up of u, d, e^-[3].

A particle is the local excitation of its respective field. The fermion fields interact via four fundamental forces (Table 2.2), called *gauge fields*, with *gauge bosons* as mediators, interactions that conserve charges and flavor quantum numbers[4]. Gravity is however not included in SM, because it is negligible at such low masses and because it is not possible to find a well-behaved gauge theory to describe gravity.

[3] Yet, matter as described by the SM occupies only 5% of the Universe. The unknown rest, 27% matter (*dark matter*) and 68% energy (*dark energy*), is investigated by SM extension theories called Beyond Standard Model.

[4] The weak force is the only force that does not conserve flavor.

[5] From $G_F/\sqrt{2} = g(m_W)^2/(8M_W^2)$ one gets the weak gauge running coupling g at the m_W scale, $g(m_W) = 0.66$. In analogy to the QED running coupling constant $\alpha(Q^2) = e(Q^2)^2/4\pi$, the weak coupling is $\alpha_W(m_W) = g(m_W)^2/4\pi = 1/29$.

Force	Coupling α **	Max range	Charge, symmetry	Gauge boson [GeV]	Mass	Q	Main decays
Weak	$\alpha_W = 1/29$[5]	$1/M_W = 10^{-3}$ fm	weak isospin T_3, SU(2)	$W^{\pm}$	80.379	± 1	$e^+\nu_e$ (11%) $\mu^+\nu_\mu$ (11%) $\tau^+\nu_\tau$ (11%) $u\bar{d}, c\bar{s}$ (67%)*
				Z	91.187	0	$\nu\nu$ (20%) l^+l^- (10%) q^+q^- (70%)
EM	$\alpha = 1/137$	∞	electric Q, U(1)	photon γ	0	0	–
Strong	$\alpha_S = 1$	1 fm	quark colour, SU(3)	8 gluons g	0	0	–

Table 2.2.: Fundamental interactions in SM, with their coupling strengths and maximum interaction range. Their cross-section is proportional to α^2 (since the interaction requires two vertices). Each force has a charge generator of symmetries (Section 2.6) and a gauge boson as carrier, with its mass (for simplicity without errors), charge and main decays. SM has also an elementary non-gauge boson, the scalar h (Section 2.6.3). [51]

* The W partial decay widths are proportional to 1 for leptons and $3|V_{ij}|^2$ for quarks, where 3 is the colour factor and V_{ij} the CKM matrix elements for u and c, with $V_{ud} \approx V_{cs} \approx 0.97$ as highest values.

** The interaction couplings are provided at the range from "Max range" column.

Virtual Particles

On short ranges the energy of an exchange particle is allowed to not be conserved and to be high, due to the uncertainty principle $\Delta E \Delta t \leq \hbar$. The particle is *virtual* and its mass off-shell, not satisfying $m^2 = E^2 - \mathbf{q}^2$. In virtual loops, $\mathbf{q^2}$ may even reach infinity. Interactions with high $Q^2 = |q^2|$ are needed to probe quarks in hadrons, given the de-Broglie wavelength $\lambda = 1/Q$.

Antiparticles

The antiparticle[6] is the result of charge conjugation $\mathcal{C}$, that preserves mass and lifetime, but reverses p^μ, spin and charges. A few particles in SM are their own antiparticle, thus neutral: γ, Z, h, π^0, etc. A particle going backward in time is equivalent to its antiparticle going forward in time.

Chirality, Helicity and Spin

Helicity is the projection of spin onto momentum, with eigenvalues $-s$, ... , $s-1, s$, thus $\pm 1/2$ for $s = 1/2$ and $-1, 0, 1$ for $s = 1$. Negative eigenvalues represent *left-handed* particle and positive represent *right-handed*. Regarding conservation, the spin is not necessarily conserved, but helicity is conserved. Regarding Lorentz invariance, for massive particles the helicity is frame dependent. In the extreme relativistic limit (or massless particles), used in this thesis, the left/right helicity projections $\psi_{L/R}$ can be expressed with the chirality operator γ^5, which is Lorentz invariant:

[6] In this thesis all accounts to a particle are binding to its antiparticles as well, unless otherwise mentioned.

Category	Spin	Parity	Bilinear forms	Particle examples
Scalar	0	even	$\bar{\psi}\psi$	h
Pseudoscalar	0	odd	$\bar{\psi}\gamma^5\psi$	π K
Vector	1	odd	$\bar{\psi}\gamma^\mu\psi$	W, Z, γ, g, ρ
Pseudo(Axial) Vector	1	even	$\bar{\psi}\gamma^5\gamma^\mu\psi$	
Tensor	2		$\bar{\psi}\sigma^{\mu\nu}\psi$	– (graviton in BSM)

Table 2.3.: Spin and parity categories [47] with corresponding Lagrangian bilinear terms and particles examples. Spin-0 fields have no direction, spin-1 have one direction, spin-2 stretch-squeeze space in two directions. The parity $\mathcal{P}$ flips the sign of one/three space coordinates as the $\mathcal{P}$-even $\mathcal{P}\psi = \psi$ or $\mathcal{P}$-odd $\mathcal{P}\psi = -\psi$, in practice together with the charge conjugation $\mathcal{C}$ operator as CP-even or CP-odd. Pseudoscalars require the γ^5 Dirac matrix as in Eq. 4.11.

$$\psi = \psi_L + \psi_R = \frac{1}{2}(1-\gamma^5)\psi + \frac{1}{2}(1+\gamma^5)\psi \tag{2.2}$$

The 1/2-spin fields are:

$$\psi = u(\mathbf{p})e^{-ipx}, \tag{2.3}$$

with u the four-component column Dirac spinor, that has four independent solutions: positive energy vs. negative (antiparticle) energy, and positive vs. negative helicity [54].

The bilinear Lagrangian terms $\bar{\psi}(...)\psi$ in Table 2.3 are relevant in the way they behave under Lorentz transformations, where $\bar{\psi} = \psi^\dagger\gamma^0$ is the Dirac row hermitian adjoint, $\psi^\dagger$ the conjugate transpose, γ^μ the 4×4 Dirac matrices and τ^i the three 2×2 Pauli matrices:

$$\gamma^0 = \begin{pmatrix} I & 0 \\ 0 & -I \end{pmatrix}, \quad \gamma^{1-3} = \gamma^0 \begin{pmatrix} 0 & \tau^{1-3} \\ \tau^{1-3} & 0 \end{pmatrix}, \quad \gamma^5 = i\gamma^0\gamma^1\gamma^2\gamma^3 = \begin{pmatrix} 0 & I \\ I & 0 \end{pmatrix} \tag{2.4}$$

The integer-spin fields are:

$$\begin{aligned} \phi &= Ne^{-ipx} \quad \text{for spin-0} \\ \psi &= \epsilon(\mathbf{p})^\mu e^{-ipx} \quad \text{for spin-1,} \end{aligned} \tag{2.5}$$

where N is a constant and ϵ^μ is a polarisation vector with only three components (the fourth, time, is zero): one longitudinal for helicity $s = 0$, missing for massless fields, and two transverse for helicity ±1. A massless field receives all polarisations when it becomes virtual.

Cross-Sections, Invariant Amplitudes and Decay Rates

The production cross-section σ is the likelihood of final states in a scattering, symbolically as effective interaction area measured in barns $1b = 10^{-28}m^2$. It is provided either as *differential* to an observable or integrated as *total* cross-section. $\sigma \sim |\mathcal{M}|^2$, with $\mathcal{M}$ the *invariant amplitude*, the intrinsic interaction probability, *matrix element* in the probability matrix mapping in–out states:

$$\mathcal{M} \sim \prod(I \times [V(\sqrt{\alpha})]^n \times O) \times P \sim \prod j \times P, \tag{2.6}$$

where I and O are the external in-out states (as in Eq. 2.3 and 2.5), V the interaction vertex factor of the order $\sqrt{\alpha}$, n the number of vertices, $P \sim 1/(q^2 - M^2)$ the internal virtual propagator from the force carriers. One I, the O that I flows into, and their vertex (with the antiparticle converted to its reversed particle) combine into a four-current $j^\mu = (\rho, \mathbf{j})$, where $\rho = Q|\psi|^2$ is the charge density and $\mathbf{j}$ the current density. If a process has contributions from multiple processes (channels), their $\mathcal{M}_i$ add up, with $\mathcal{M}_i^*$ the complex conjugate:

$$|\mathcal{M}_{total}|^2 = (\mathcal{M}_1 + \mathcal{M}_2 + \ ...)(\mathcal{M}_1^* + \mathcal{M}_2^* + \ ...) \tag{2.7}$$

A particle decays at the rate $\Gamma = -\frac{dN}{dt}/N = 1/\tau$ [GeV], with τ its lifetime. The probability to produce one short-lived particle of mass M, called *resonance*, is given by its relativistic Breit-Wigner distribution, where the distribution width equals the decay width Γ. Shorter lifetime means larger Γ, due to the uncertainty principle $\Delta E \Delta t \leq \hbar$:

$$f(\sqrt{s}) \sim \frac{1}{(s - M^2)^2 + M^2\Gamma^2} \tag{2.8}$$

Various channels of a process yield partial σ and Γ, with branching ratio $\text{BR} = \Gamma_{partial}/\Gamma_{total}$.

2.3. Forces

2.3.1. Electromagnetic Force

An electrically charged particle emits a photon γ, where the corresponding *em* four-potential is a vector boson $A^\mu = (\phi, \mathbf{A})$ as in Eq. 2.5, with ϕ the electric potential and $\mathbf{A}$ the magnetic potential. The interaction is called *quantum electrodynamics* (QED) and has the coupling strength $\alpha = e^2/4\pi$. Because the bare charge is *screened* with opposite charges from e^+e^- photon conversions, a closer probing with higher Q^2 increases the effective charge. α is thus a running coupling (Eq. 2.19), decreasing asymptotically at infinite range to 1/137, the electron charge *pole*.

To calculate an *em* current j_{em} from an initial state 1 to a final state 2, the antiparticle is converted to its particle, $\gamma \to e_1^+ e_2^- \ \equiv \ e_1^- \gamma \to e_2^-$, thus the current $e_1^- e_2^-$ has constant charge, denoted as *neutral current* (indicated as well by γ being neutral). j_{em} have the forms [47]:

$$\begin{aligned} j^\mu_{Dirac} &= e j^\mu_{em} = eQ\bar{\psi}_2\gamma^\mu\psi_1 \qquad \text{with spin-1/2 states from (2.3)} \\ j^\mu_{Klein-Gordon} &= ieQ(\phi_2^*\partial^\mu\phi_1 - \phi_1\partial^\mu\phi_2^*) \qquad \text{with spin-0 states from (2.5)} \end{aligned} \tag{2.9}$$

The j_{em} can be decomposed onto the left/right ψ projections from (2.2), acting hence on both the left and the right projections of both particles and antiparticles [47]:

$$j^\mu_{em} = Q(\bar{\psi}_{2R}\gamma^\mu\psi_{1R} + \bar{\psi}_{2L}\gamma^\mu\psi_{1L}) \tag{2.10}$$

2.3.2. Weak Force

The nuclear β-decays mentioned in Section 2.1 narrow down to the charged weak interaction, the only fundamental interaction that can change fermion flavor (see W decays in Table 2.2):

$$\begin{aligned} u\bar{d} &\to W^+ \to e^+\nu_e \\ \bar{u}d &\to W^- \to e^-\bar{\nu}_e \end{aligned} \tag{2.11}$$

and their *charge-raising* ($e^- \to \nu_e$) and *charge-lowering* ($\nu_e \to e^-$) currents [47]:

$$\begin{aligned} J_\mu^+ &= \bar{u}_\nu \gamma_\mu \frac{1}{2}(1-\gamma^5)u_e \quad \text{via } W^+ \\ J_\mu^- &= \bar{u}_e \gamma_\mu \frac{1}{2}(1-\gamma^5)u_\nu \quad \text{via } W^- \end{aligned} \tag{2.12}$$

It can be proved that the above vector-axial form $1-\gamma^5$ extracts in the Dirac Eq. 2.22 the left-handed fermions and the right-handed anti-fermions. Thus the weak interaction violates chirality. As a consequence, the ν_R and $\bar{\nu}_L$ do not exist at all, since they are rejected by the weak interaction and neutrinos interact only weakly [7].

The weak interaction violates parity $\mathcal{P}$ as well, for example a process $\pi^+ \to \mu^+\nu_L$ is allowed, but its parity conjugate $\pi^+ \to \mu^+\nu_R$ is forbidden. Charge conjugation $\mathcal{C}$ is violated by disallowing $\pi^- \to \mu^-\bar{\nu}_L$. The combined $\mathcal{CP}$ conjugate $\pi^- \to \mu^-\bar{\nu}_R$ is however allowed, except for the rare case of $\mathcal{CP}$ violation [11, 12], one of the hypothetical conditions for the early Universe creation [13].

Flavour conserving weak currents are mediated by $Z \to f\bar{f} \equiv f \to Zf$ (see Z decays in Table 2.2), issuing hence neutral weak currents [47]:

$$J_\mu^{NC} = \bar{u}_f \gamma_\mu \frac{1}{2}(c_V^f - c_A^f \gamma^5)u_f, \tag{2.13}$$

where f are fermions and c_V^f, c_A^f parameters that are normally different, indicating that the weak current is not pure vector-axial and hence it allows right-handed fermions. For neutrinos however, which can only be left-handed, $c_V = c_A = 1/2$.

2.3.3. Electroweak Force

The *em* and weak interactions are unified by Glashow, Salam and Weinberg into the GSW model [42–45]. The charged weak currents (2.12) can be rewritten in lepton generation doublets as listed in Table 2.1, such as $\chi_L = \binom{\nu}{e^-}_L$:

$$\begin{aligned} J_\mu^+ &= \bar{\chi}_L \gamma_\mu \tau_+ \chi_L \quad \text{with} \quad \tau_\pm = (\tau_1 \pm i\tau_2)/2 \\ J_\mu^- &= \bar{\chi}_L \gamma_\mu \tau_- \chi_L \end{aligned} \tag{2.14}$$

These currents must be the physical observables of a base triplet of weak currents:

$$J_\mu^i = \bar{\chi}_L \gamma_\mu T_i \chi_L \quad \text{with charge operator} \quad T_i = \frac{1}{2}\tau_i, \quad i = 1,2,3, \tag{2.15}$$

from which the third weak component, which proves to be neutral, of the form [47]:

$$J_\mu^3 = \frac{1}{2}\bar{\nu}_L \gamma_\mu \nu_L - \frac{1}{2}\bar{e}_L \gamma_\mu e_L, \tag{2.16}$$

[7] Provided that neutrinos are massless, otherwise a ν_L could Lorentz transform to a ν_R. However, neutrinos are still investigated whether they can be their own antiparticles, as Majorana massive fermions [55, 56].

provides the *weak isospin* charge T_3, which generates a symmetry $SU(2)_L$. The symbol L shows that only left-handed fermions are included (right-handed fermions have $T_3 = 0$). Each up-type fermion has $T_3 = 1/2$ and transitions via a $W^{\pm}$ (with $T_3 = \pm 1$) to its symmetric down-type of $T_3 = -1/2$, within the same generation [8]. Antiparticles have T_3 reversed.

In order to include the neutral *em* current, the currents base is extended with a neutral singlet J^Y_μ, that acts on both left and right singlet fermions:

$$J^Y_\mu = \bar{\psi}\gamma_\mu Y \psi \quad \text{such that} \quad j^{em}_\mu = j^3_\mu + \frac{1}{2} j^Y_\mu , \tag{2.17}$$

with the hypercharge operator Y generating the $U(1)_Y$ symmetry and following $Q = T_3 + \frac{1}{2}Y$.

2.3.4. Strong Force

The strong force binds quarks into *hadrons*, such as nucleons, and nucleons into nuclei, despite their *em* repulsion. It acts on the *colour* charge, red R, green G or blue B, via bi-coloured gluons, in a theory called *quantum chromodynamics* QCD: an R quark converts to a G quark by emitting a $\bar{R}G$ gluon. With coupling α_S quarks radiate gluons, gluons split into $q\bar{q}$ pairs or gluons emit other gluons, due to their self coupling.

The colour around a bare quark is enhanced by surrounding gluon loops (*anti-screening*), thus α_S increases highly with distance (Eq. 2.19) and keeps quarks and gluons together in *colour confinement* [57]. That is how the proton is confined as well to $\sim$1 fm, where $\alpha_S = 1$ [58]. At small Q^2, α_S becomes too large and perturbative QCD breaks down (Section 2.4). With a closer probing instead, the coupling decreases in *asymptotic freedom* to $\alpha_S = 0.1 - 0.2$, where quarks in hadrons don't interact any more (are free) and can be probed individually.

Free particles exist in nature only as colourless states, called **colour singlets**. Colour singlet hadrons must resemble "white", as $q_1q_2q_3$ / $\bar{q}_1\bar{q}_2\bar{q}_3$ (RGB / $\bar{R}\bar{G}\bar{B}$), called *baryons*, or $q\bar{q}$ ($R\bar{R}, G\bar{G}, B\bar{B}$), called *mesons*. Quarks and gluons are however **colour octets**, carrying net colour.

2.4. Perturbation Theory

A hard-scattering process can have additional corrections, that are either *real* emissions, as g, γ or $q\bar{q}$, or *virtual loops* around the vertex, around the propagator, or as polygon-type. When the coupling is small (asymptotic freedom in QCD), cross-sections can be expanded in powers of $\alpha_{(S)}$:

$$\sigma = C_0 \cdot \alpha^{B+0}_{(S)}(\mu^2_R) + C_1 \cdot \alpha^{B+1}_{(S)}(\mu^2_R) + C_2 \cdot \alpha^{B+2}_{(S)}(\mu^2_R) + \ ... \tag{2.18}$$

The first term is without corrections, called leading order (LO), first Born approximation or tree level (i.e. no loops). The first two terms provide the next-to-leading order (NLO) correction, the first three terms provide NNLO and so on, more and more suppressed.

[8] Quarks can transition with smaller probabilities from an up-type to a down-type of another generation, via the 3×3 CKM unitary mixing matrix, parametrised by three angles and one complex phase. The phase is a small source of CP-violation. [51].

2.5. Renormalisation

Integrating amplitudes around massless decay products can diverge when the decay products are soft or collinear with their parents, phenomena called *infrared* divergences[9]. The divergence can be regularised with cuts such as minimum energy, minimum angle or fictitious mass.

Ultraviolet divergences appear at unbound high energies, such as virtual loop corrections on internal propagators, on vertices or on external lines. The amplitude's infinity is removed via upper mass cuts M^2 on the loop's q^2. The M^2 term is absorbed in the amplitude's coupling factor, yielding a reference $\alpha_{(S)}$, in practice measured experimentally at an arbitrary *renormalisation scale* artefact $Q^2 = \mu_R^2$ [46]:

$$\alpha(Q^2) = \frac{\alpha(\mu_R^2)}{1 + \beta_0 \cdot \alpha(\mu_R^2) \cdot \ln\left(Q^2/\mu_R^2\right)}, \tag{2.19}$$

where $\beta_0 > 0$ for α_S and $\beta_0 < 0$ for α. The $\alpha_{(S)}$ are running couplings, depending on the physical scale Q^2 and on μ_R, with a much stronger dependence in QCD [59] than in QED [60]. A few couplings used in practice are $\alpha(m_Z) = 1/128$ and $\alpha_S(m_Z) = 0.118$, or values from Table 2.2.

2.6. Gauge Symmetries

Noether's theorem [61] postulates that for every invariance of a system under a symmetry action, there is a corresponding conserved physical quantity, called "charge", such as momentum conserved under translation in space-time. The idea that quantities are conserved not only globally, but locally as well, issues the gauge symmetries theory. The evolution of a particle is best described by the Lagrangian $\mathcal{L}$:

$$L(\phi, \partial_\mu\phi, x_\mu) = T - V \qquad \text{with} \quad L = \int \mathcal{L}\ \mathrm{d}^3x, \tag{2.20}$$

where x_μ is the point in space-time, $\phi(x_\mu)$ the value of the particle's field, T and V the kinetic and potential energy. Substituting $\mathcal{L}$ into the minimum action Euler-Lagrange equation issues the relativistic wave equation. The simplest Lagrangian forms [47] are for free particles (meaning without external potential) with mass, such as the Klein-Gordon Lagrangian for spin-0:

$$\begin{aligned} \mathcal{L}_{Klein-Gordon} =& \frac{1}{2}(\partial_\mu\phi)^2 - \frac{1}{2}m^2\phi^2 \\ \text{with equation} \quad & \partial_\mu\partial^\mu\phi + m^2\phi = 0 \end{aligned} \tag{2.21}$$

and the Dirac Lagrangian for spin-1/2 is:

$$\begin{aligned} \mathcal{L}_{Dirac} =& \bar{\psi}(i\gamma_\mu\partial^\mu - m)\psi \\ \text{with equation} \quad & (i\gamma^\mu\partial_\mu - m)\psi = 0 \end{aligned} \tag{2.22}$$

The two Lagrangian have the field terms squared, which represent the kinetic energy, respectively the mass of the in-out particles. The next sub-sections explain how the gauge vector bosons arise via local gauge invariance and how their masses are generated via the Higgs mechanism.

[9] The phenomena is called "infrared" in analogy to the infrared radiation, which has low frequency, hence low energy.

2.6.1. QED

Consider an abelian phase transformation $U(\alpha) = e^{i\alpha}$ applied to a Dirac field, with α an arbitrary constant. An invariance $\delta\mathcal{L} = 0$ of the Lagrangian (2.22) under an infinitesimal transformation $U(\alpha) = 1 + i\alpha$ is equivalent to the charge-current conservation:

$$\partial_\mu j^\mu = 0 \tag{2.23}$$

Noether's theorem is verified and a $U(1)_{em}$ global *gauge* (old name for phase) symmetry group is set. Generalising to local gauge $\alpha(x)$, $\partial_\mu\psi$ receives an extra term $\partial_\mu\alpha(x)$ that can be compensated by introducing the photon gauge field A_μ with the constructs [47]:

$$\begin{aligned} &\partial_\mu \to D_\mu = \partial_\mu + ieQA_\mu \quad \text{where} \quad A_\mu \to A_\mu - \frac{1}{eQ}\partial_\mu\alpha \\ &\text{such that} \quad D_\mu\psi \to e^{i\alpha(x)}D_\mu\psi \end{aligned} \tag{2.24}$$

Hence $\mathcal{L}$ receives a fermion-photon interaction term $-j^\mu_{Dirac}A_\mu$ (Eq. 2.9). To add a squared term as the photon's kinetic energy, gauge invariant under (2.24), the photon's field strength tensor $F_{\mu\nu} = \partial_\mu A_\nu - \partial_\nu A_\mu$ is used, which brings (2.22) to the final QED Lagrangian [48]:

$$\begin{aligned} \mathcal{L}_{QED} &= \mathcal{L}_{Dirac} + \mathcal{L}_{interaction} + \mathcal{L}_{\gamma-kinetic} \\ &= \bar{\psi}(i\gamma_\mu\partial^\mu - m)\psi - eQ\bar{\psi}\gamma^\mu A_\mu\psi - \frac{1}{4}F_{\mu\nu}F^{\mu\nu} \end{aligned} \tag{2.25}$$

A mass term of the photon would break again the gauge invariance, thus the photon is massless.

2.6.2. QCD

In QCD the $U(1)_{em}$ group is extended as $SU(3)_C$ for the three colour Dirac spinors q_1, q_2, q_3:

$$q(x) \to e^{i\alpha_a(x)T_a}q(x) \quad \text{with} \quad a = 1 \ldots 8 \tag{2.26}$$

The group has eight generators $T_a = \lambda_a/2$, with λ_a the 3×3 Gell-Mann matrices [62]. To reach local gauge invariance, the same steps from QED are followed, which introduce eight G^a_μ gluon gauge fields and a strong coupling g [47]:

$$\partial_\mu \to D_\mu = \partial_\mu + igT_aG^a_\mu \quad \text{where} \quad G^a_\mu \to G_\mu - \frac{1}{g}\partial_\mu\alpha_a - f_{abc}\alpha_b G^c_\mu \tag{2.27}$$

$$\text{and strength tensor} \quad G^a_{\mu\nu} = \partial_\mu G^a_\nu - \partial_\nu G^a_\mu - gf_{abc}G^b_\mu G^c_\nu \tag{2.28}$$

The Lagrangian (2.22) receives the quark-gluon interaction term and the gluon kinetic energy term, leaving $m_g = 0$. The final QCD Lagrangian becomes [48]:

$$\begin{aligned} \mathcal{L}_{QCD} &= \mathcal{L}_{Dirac} + \mathcal{L}_{interaction} + \mathcal{L}_{g-kinetic} \\ &= \bar{q}(i\gamma_\mu\partial^\mu - m)q - g(\bar{q}\gamma^\mu T_a q)G^a_\mu - \frac{1}{4}G^a_{\mu\nu}G^{\mu\nu}_a \end{aligned} \tag{2.29}$$

The gluon field and its strength tensor are more complex than in QED, with an extra term coming from the non-zero $[T_a, T_b] = if_{abc}T_c$ (QCD is non-Abelian), with f_{abc} real structure constants. Thus the gluon kinetic term in (2.29) introduces two new terms, gG_μ^3 and $g^2G_\mu^4$, signifying three and four gluon self-interaction vertices, as the gluons carry colour charge as well.[10]

2.6.3. Higgs Mechanism

This subsection describes how the mechanism proposed by Brout, Englert and Higgs (BEH), generates the masses of the gauge vector bosons (VB) via spontaneous symmetry breaking [63, 64], extending the GSW electroweak model of Section 2.3.3. BEH made the assumption that there is an extra scalar field, for which the simplest $\mathcal{L}$ is invariant under the reflection $\phi \to -\phi$ for a real scalar ϕ, as:

$$\mathcal{L} = T - V = (\partial_\mu \phi)^2 - (\mu^2\phi^2 + \lambda\phi^4) \quad \text{with} \quad \lambda > 0, \tag{2.30}$$

The case $\mu^2 > 0$ is the known Klein-Gordon Lagrangian for a scalar with mass μ (Eq. 2.21) and with an extra four-scalar self-interaction $-\lambda\phi^4$, where V has a stable minimum $V_{\phi=0} = 0$. Our case study is however $\mu^2 < 0$, thus without mass. The potential minima are at $V_{\phi=\pm v} = 0$, where $v = \sqrt{-\mu^2/\lambda}$ is called **vacuum expectation value VEV**, since $\phi \neq 0$ at the ground state $V = 0$. Perturbative calculations of $\mathcal{L}$ around $\phi = 0$ are not possible, as the point is unstable, thus they are calculated around one random particular vacuum, such as $\phi(x) = v + \eta(x)$ [63, 64]:

$$\mathcal{L} = \frac{1}{2}(\partial_\mu \eta)^2 - \mu^2\eta^2 - \lambda v\eta^3) - \frac{1}{2}\lambda\eta^4 \tag{2.31}$$

$\mathcal{L}$ has now a kinetic and a *mass term* for the real scalar η, and 3-4 η self-interactions. The *spontaneous* positioning around a VEV *breaks* the reflection *symmetry* of $\mathcal{L}$ (due to the term in η^3). We generalise further to a local gauge $SU(2)$ symmetry with doublets of complex fields:

$$\phi = \begin{pmatrix} \phi^+ \\ \phi^0 \end{pmatrix} = \begin{pmatrix} \phi_1 + i\phi_2 \\ \phi_3 + i\phi_4 \end{pmatrix} / \sqrt{2}, \tag{2.32}$$

where ϕ^+ denotes that the scalar doublet has positive weak hypercharge $Y = 1$. $\mathcal{L}$ keeps its (2.30) form, where $(\ )^2 = |\ |^2 \equiv (\ )^\dagger(\ )$, and the minima is now at a sphere $v^2 = \phi_1^2 + \phi_2^2 + \phi_3^2 + \phi_4^2$. For $\mathcal{L}$ to be invariant under $\phi(x) \to e^{i\alpha(x)_a\tau_a/2}\phi(x)$, with $a = 1, 2, 3$ and $T_a = \tau_a/2$ the weak isospin, three massless vector gauge fields W_μ^a are introduced, similarly to the eight ones in QCD [63, 64]:

$$\partial_\mu \to D_\mu = \partial_\mu + ig\frac{\tau_a}{2}W_\mu^a \quad \text{where} \quad W_\mu^a \to W_\mu^a - \frac{1}{g}\partial_\mu\alpha^a - g\epsilon^{abc}\alpha^b W_\mu^c \tag{2.33}$$

$$\text{and strength tensor} \quad W_{\mu\nu}^a = \partial_\mu W_\nu^a - \partial_\nu W_\mu^a - g\epsilon^{abc}W_\mu^b W_\nu^c, \tag{2.34}$$

where ϵ is the Levi-Civita symbol for vector cross product and g the gauge weak coupling. The last term in (2.34), similarly to QCD's (2.28), is due to τ_a not commuting to one another, yielding thus a non abelian group. This adds to the W kinetic term (2.36) 3-4 self-interaction vertices. We

[10] In QED the photons do not self-interact, as they do not carry electric charge.

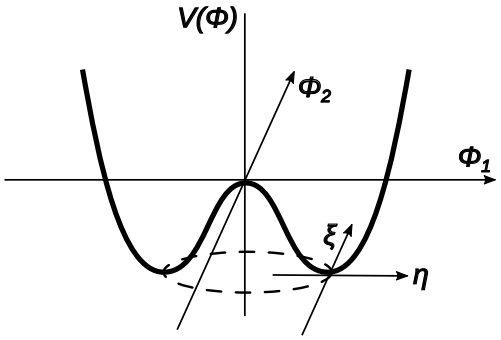

Figure 2.1.: The potential $V(\phi) = -(\mu^2\phi^2 + \lambda\phi^4)$ of a complex scalar field $\phi = (\phi_1 + i\phi_2)/\sqrt{2}$, with $\mu^2 < 0$, $\lambda > 0$ and a circle of radius v at the minima of V. Perturbation expansions $v + \eta + i\xi$ suggest no inertia along ξ, thus a massless Goldstone boson. [47]

break now again the symmetry spontaneously by perturbation around a vacuum point, by choice $\phi_1 = \phi_2 = \phi_4 = 0$ and $\phi_3 = v$ [63, 64], as in Figure 2.1:

$$\phi(x) = \frac{1}{\sqrt{2}} \begin{pmatrix} \theta_1 + i\theta_2 \\ v + h + i\theta_3 \end{pmatrix} \equiv \frac{1}{\sqrt{2}} \begin{pmatrix} 0 \\ v + h \end{pmatrix} \tag{2.35}$$

$\mathcal{L}$ has now a real neutral scalar *Higgs* field $h(x)$ with its mass and kinetic term, three scalar fields θ_i with kinetic terms but no masses (Goldstone bosons) and three massive vector gauge fields W^a_μ. The θ_i fields can be shifted to the ϕ's exponential, and thus completely eliminated with a proper choice of gauge $\alpha(x)_a$.

Similarly to QED is introduced another vector boson gauge field B_μ of abelian group $U(1)$, thus not self-interacting. The final Lagrangian for the VB kinetic terms and their self-interactions becomes [48]:

$$\mathcal{L}^{VB-kin-self-int}_{GSW} = -\frac{1}{4} W^a_{\mu\nu} W^{\mu\nu}_a - \frac{1}{4} B_{\mu\nu} B^{\mu\nu} \tag{2.36}$$

The final Lagrangian for the Higgs and VB masses and couplings becomes [48]:

$$\begin{aligned} \mathcal{L}^{h-VB-mass-int}_{GSW} =& |(\partial_\mu + igT_a W^a_\mu + ig'\frac{1}{2} Y B_\mu)\phi|^2 - V(\phi) \\ \sim& \frac{1}{2}(\partial_\mu h)^2 - \lambda v^2 h^2 && h \text{ kinetic and mass term, } m_h = \sqrt{2\lambda v^2} \\ & -(\lambda v h^3 + \lambda h^4) && h \text{ cubic/quartic self-couplings} \\ & +\frac{1}{2} m_V^2 V^2 && \text{VB mass term} \\ & +\frac{m_V^2}{v} VVh + \frac{m_V^2}{v^2} VVhh && h\text{-VB trilinear/quadrilinear couplings} \end{aligned} \tag{2.37}$$

As one can see, λ is the Higgs self-coupling parameter, a parameter whose exact value is however not predicted in SM and has been instead measured experimentally. The Higgs field VEV v and the scale of electroweak symmetry breaking v_{EW} are defined [48] with the Fermi weak coupling G_F[11]:

[11] The Fermi weak coupling was measured in muon decays to $G_F = 1.16 \times 10^{-5} GeV^{-2}$ [65].

$$\begin{aligned} v &= \frac{1}{\sqrt{\sqrt{2}G_F}} = 246\text{GeV} \\ v_{\text{EW}} &= \frac{1}{\sqrt{2}}v = 174\text{GeV} \end{aligned} \tag{2.38}$$

2.6.4. Electroweak Interaction Revisited

To deduct the fermion–VB interaction, the gauge invariance of the fermions Dirac Lagrangian is imposed, analogue to Sections 2.6.1 and 2.6.2: $SU(2)_L$ symmetry on χ_L doublets, that couple with coupling g[5] to three W_μ^i; $U(1)_Y$ symmetry on ψ singlets (both $\psi_{L,R}$ components), that couple with coupling g' to B_μ:

$$\mathcal{L}_{GSW}^{EW} = -g(J^i)^\mu W_\mu^i - \frac{g'}{2}(J^Y)^\mu B_\mu, \tag{2.39}$$

with the base weak currents from (2.15) and (2.17). These gauge fields however do not correspond to physical states, the physically observed gauge fields are their mixing, with masses generated by the BEH mechanism [63, 64]:

$$\begin{aligned} W_\mu^\pm &= (W_\mu^1 \mp iW_\mu^2)/\sqrt{2} && \text{for the charged } W^\pm && m = \frac{1}{2}vg \\ A_\mu &= B_\mu \cos\theta_W + W_\mu^3 \sin\theta_W && \text{for the neutral } \gamma && m = 0 \\ Z_\mu &= -B_\mu \sin\theta_W + W_\mu^3 \cos\theta_W && \text{for the neutral } Z && m = \frac{1}{2}v\sqrt{g^2+g'^2}, \end{aligned} \tag{2.40}$$

where the EW couplings can be reduced to e and to the weak mixing Weinberg angle θ_W[12] via:

$$g\sin\theta_W = g'\cos\theta_W = e \qquad \text{with} \quad \frac{M_W}{M_Z} = \cos\theta_W \tag{2.41}$$

The form (2.39) is applied in practice as effective interactions of $W^\pm/Z$, using the current forms (2.12) and (2.13) [47]:

$$\begin{aligned} \mathcal{L}_{W^\pm}^{int} &= -\frac{g}{\sqrt{2}}J^{\pm\mu}W_\mu^\pm = \bar{\psi}_f\left[-\frac{g}{\sqrt{2}}\gamma^\mu\frac{1}{2}(1-\gamma^5)\right]\psi_i W^\pm \\ \mathcal{L}_{Z^0}^{int} &= -\frac{g}{\cos\theta_W}J_\mu^{NC}Z^\mu = \bar{\psi}_f\left[-\frac{g}{\cos\theta_W}\gamma^\mu\left[\frac{1}{2}(1-\gamma^5)T^3 - \sin^2\theta_W Q\right]\right]\psi_i Z \end{aligned} \tag{2.42}$$

2.6.5. Fermion-Scalar Interaction

The Lagrangian (2.39) cannot have a fermion mass term $m\bar{f}f = m(\bar{f}_R f_L + \bar{f}_L f_R)$, since f_L and f_R belong to different symmetry groups, with different gauge transformations, thus the term would break gauge invariance explicitly. The fermion mass may however originate via spontaneous symmetry breaking, by introducing a fermion-scalar Lagrangian:

$$\mathcal{L}_{f-\phi} = -\frac{\sqrt{2}m_f}{v}(\chi_L\phi f_R + \bar{f}_R\bar{\phi}\chi_L), \tag{2.43}$$

[12] The weak mixing angle θ_W is measured experimentally to $\sin^2\theta_W = 0.231$ [66]

with ϕ the scalar field defined in (2.32) and m_f a parameter specific for each fermion field f. The fermion applies here only to down-type flavours, where f_R is its right-handed singlet. The left-handed component of f is included together with the left-handed component of the equivalent up-type flavour in the χ_L doublet. Applying the perturbation from (2.35), $\mathcal{L}_{f-\phi}$ becomes [48]:

$$\mathcal{L}_{f-\phi} = -m_f \bar{f} f - \frac{m_f}{v} \bar{f} f h = \mathcal{L}_{m_f} + \mathcal{L}_{Yukawa} \tag{2.44}$$

m_f represents thus the mass acquired by the fermion. The exact values of the fermion masses are however not predicted in SM and have been measured experimentally. $\mathcal{L}_{Yukawa}$ represents the fermion's interaction with the Higgs boson, with the *Yukawa* coupling m_f/v. Heavier fermions couple stronger with the scalar field.

Masses of up-type fermions are generated similarly to the down-type ones, replacing in (2.32) the scalar doublet ϕ with a construction based on its conjugate ϕ^* with $Y = -1$ and in (2.35) the perturbation with $\frac{1}{\sqrt{2}} \begin{pmatrix} v+h \\ 0 \end{pmatrix}$. [47]

Conclusions

Together with the lepton-quark kinetic term $i\bar{\psi}\gamma^\mu \partial_\mu \psi$, the GSW model is now complete. The symmetry group of the SM is given by the EW one (which includes the QED as well), combined orthogonally with the QCD one: $U(1)_Y \times SU(2)_L \times SU(3)_C$.

2.6.6. Higgs Boson Production and Decay

Figure 2.2 depicts the production and decay modes of the SM Higgs boson h at the LHC pp collisions, up to a mass of 2 TeV. Besides mass threshold requirements, they are consequences of h coupling preferentially to heavier particles: W, Z, t, b. The following paragraphs address production and decay around the 125.09 GeV mass of the SM h discovered at ATLAS and CMS [15, 16].

Production: The light valence quarks do not contribute directly to Higgs boson production, because their Yukawa couplings are very small (even though Section 2.8.3 shows that they are the partons with the highest momentum fraction x).

The production is highly dominated by gluon fusion $gg \to h$ (in the figure $pp \to h$), which is accomplished with an intermediate heavy quark triangular loop of either top, or rarely bottom, as the Higgs boson does not couple to massless particles such as gluons. Next production modes are VB fusion (in the figure $pp \to qqh$), accomplished as $qq\prime \to qq\prime\, W^*W^*/Z^*Z^* \to qq\prime\, h$, and associated VB production (in the figure $pp \to Wh$ and $pp \to Zh$), accomplished as $q\bar{q} \to W^*/Z^* \to W/Z\ h$.

Decay: The highest BR have, in order, the channels $b\bar{b}$, WW, gg, $\tau\tau$, while the decay to $t\bar{t}$ is suppressed because $m_h < 2m_t$. However, in the gg fusion production channel, the best detection channels with a high signal to background significance are $h \to ZZ^* \to 4l$, $h \to WW^* \to ll\nu\nu$ (with one intermediate VB off-shell, in order to allow h to be on-shell) and $h \to \gamma\gamma$ (a rare but one of the most sensitive decay channels, due to its high purity), channels in which the Higgs boson was discovered as well.

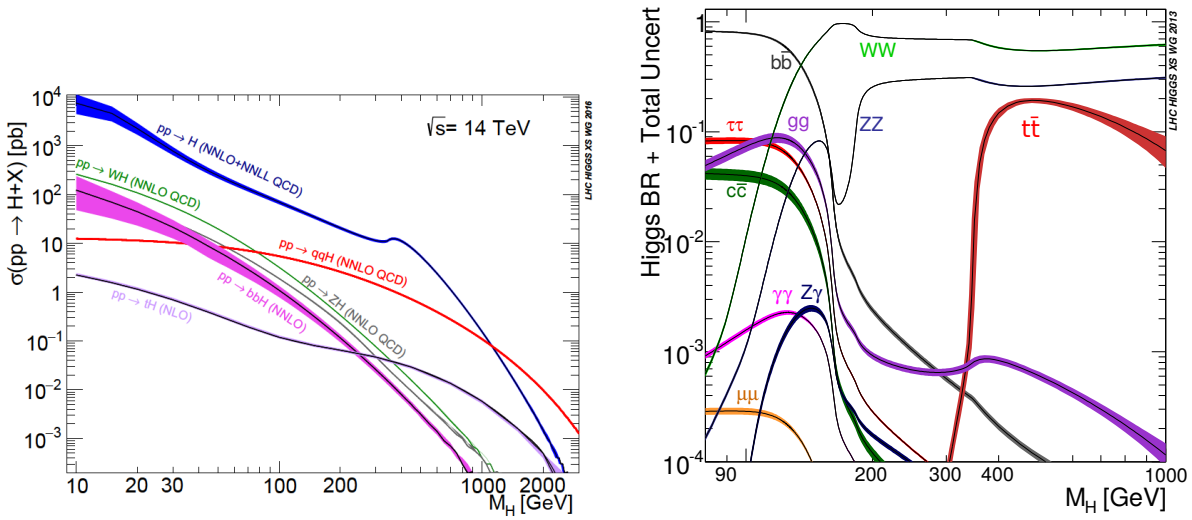

(a) Production σ at $\sqrt{s}$=14 TeV **(b)** Branching Ratio

Figure 2.2.: Production σ and BR of the SM Higgs boson h, on a mass range up to 2 TeV. Up to high masses, the dominant production is gg fusion. At its discovered 125.09 GeV mass, the highest BR is to $b\bar{b}$, while at higher masses dominate WW/ZZ and $t\bar{t}$. The bands represent the combined theoretical uncertainties summed in quadrature. [67]

2.7. Top Quark Properties

The top quark properties[13] and phenomenology are a consequence of its large mass. The top quark mass has been determined from the LHC and Tevatron data directly by reconstructing its decay products and by fitting Monte Carlo mass templates, or indirectly, using the relationship between $\sigma_{t\bar{t}}$ and m_t. The world average value is $m_t = 173.34 \pm 0.76$ GeV [53].

The top quark is hence the most massive particle in the SM, with its mass close to the electroweak symmetry breaking scale v_{EW} defined in (2.38). It has the highest Yukawa coupling, of $m_t/v = \mathcal{O}(1)$.

Top Quark Production

At hadron colliders the top quark is produced copiously in SM $t\bar{t}$ pairs (Figure 4.4), via strong interactions. The following cross-sections apply for the LHC pp collisions at $\sqrt{s} = 8$ TeV, where the top quark was measured to have $m_t = 172.5$ GeV. The cross-sections systematic uncertainties treatment is left for Section 5.7.4.

The top quark pairs are produced with $\sigma_{t\bar{t}} = 252.9$ pb at NNLO+NNLL accuracy [68–74]. The higher the center-of-mass energy $\sqrt{s}$, the more the partons with low-x (Section 2.8) are accessible, such as the gluons (Section 2.8.3). Hence at the $\sqrt{s} = 8$ TeV pp collisions from the LHC, gg fusion dominates $t\bar{t}$ production with 80%.

The top quarks are produced weakly as well, as SM single top quarks, with the following cross-sections at NNLO accuracy: s-channel $q\bar{q}\prime \to W \to t\bar{b}$ with $\sigma_{t+\bar{t}} = 5.5$ pb; t-channel $qb \to q\prime t$ with $\sigma_{t+\bar{t}} = 84.6$ pb, where a bottom quark transforms to a top quark by exchanging a W boson with

[13] The top quark properties in this section are taken from [51].

other quarks; $bg \to Wt$ associated production, where $\sigma_{t+\bar{t}} = 22.1$ pb [75–77]. At LHC, single top quark production does not only have much lower cross-section than the $t\bar{t}$ production, but its decay signature has $t\bar{t}$ as large background as well.

Top Quark Decay

As its lifetime is very short ($\tau_t \approx 5 \times 10^{-25}$ s, $\Gamma_t \approx 1.35$ GeV), the top quark decays before it could hadronise[14], being the only quark that does not form hadrons. As it is heavier than the W boson, it decays "reverse" weakly, to an on-shell W and b. Its weak cross-sections are proportional to $|V_{ti}|^2$, the squared transition probabilities from the CKM matrix where i are the down-type quarks: $V_{td} \approx 0.008$, $V_{ts} \approx 0.04$, $V_{tb} \approx 1$, hence t interacts almost exclusively with the b quark.

The W boson decays either leptonically, into a charged lepton[15] and its lepton neutrino, or hadronically, into two quarks that evolve into hadron jets. The final states of the $t\bar{t} \to W^+bW^-\bar{b}$ decay are classified as:

$$\begin{aligned} &\text{fully hadronic} && t\bar{t} \to (q\bar{q}b)\ (q\bar{q}\bar{b}) && (\approx 4/9) \\ &\text{dileptonic} && t\bar{t} \to (l^+\nu_l b)\ (l^-\bar{\nu}_l\bar{b}) && (\approx 1/9) \\ &\text{semileptonic or } l\text{+jets} && t\bar{t} \to (q\bar{q}b)(l^-\bar{\nu}_l\bar{b}) + (l^+\nu_l b)(q\bar{q}\bar{b}) && (\approx 4/9), \end{aligned} \tag{2.45}$$

where the l and q fermion flavours are assumed to not be necessarily the same.

2.8. Phenomena at Proton–Proton Collisions

2.8.1. Parton Shower, Hadronisation and Jets

In a $q\bar{q}$ pair, the colour field lines are often modelled as thin tubes of self-interacting gluons. The more the energetic quarks are separated, the higher their strong potential becomes, until it is more efficient to break the tube in two via an extra $q\bar{q}$ pair. This phenomenon, together with gluon radiation and gluon splitting, develops a *parton shower*.

When losing momentum, partons will eventually *hadronise (fragment)* [78, 79] due to colour confinement, into hadrons. The fragments are mostly pions, as pions are the lightest hadrons. Hence quarks and gluons, also called *parton level* in Monte Carlo simulations, are never observed free. Their colourless products (*particle level*) are instead observed in these collimated spray of hadrons, called *hadron jets*. Jets have approximately the same four-momentum as their initial parton.

Around a quark with momentum magnitude p_q, hadrons fragment in narrow cone jets with relative transverse momentum $\langle k_t \rangle \approx 300$ MeV and angle [47]:

[14] Hadrons such as nucleons have the size $\mathcal{O}(10^{-15})$, hence are formed in at least $t = d/c = \mathcal{O}(10^{-23})$ s, a time interval larger than the top quark's lifetime.

[15] Lepton universality e, μ or τ is assumed here, albeit in data analysis τ has reconstruction particularities that can be seen in Section 5.1.

$$\langle\theta\rangle \approx \frac{\langle k_t\rangle}{p_q} \approx \frac{300\ \text{MeV}}{Q/2} \tag{2.46}$$

However, the quark radiating gluons enhances the $\langle k_t\rangle$, making the jet "fatter" and the dependency logarithmic [47]:

$$\langle\theta\rangle \approx \frac{1}{\ln Q^2} \tag{2.47}$$

2.8.2. Factorisation

Deeply inelastic scatterings take place at short-time scales, $\Delta t \sim 1/Q$, due to Heisenberg's uncertainty. The quark-gluon dynamics within a hadron of mass m and $p \sim Q$ happen however at longer time scales, $\Delta t \sim 1/m$, or $\Delta t \sim Q/m^2$ if including the Lorentz boost [80]. As α_S can be perturbatively described only at short distances and times, an arbitrary artefact is introduced, *factorisation scale* μ_F, that decides where one time scale ends and the other begins. μ_F is set as parameter for the parton distribution function.

Both μ_R and μ_F scales are usually set to Q, or to a typical value such as m_Z. Cross-sections have overall only remnant dependency on them, which decreases the more N^nLO corrections are included.

2.8.3. Proton–Proton Collisions and PDF

The proton consists of three *valence quarks*, *uud*, that determine the proton's quantum numbers. The valence quarks' momenta are however not equal to the proton's momentum, as they are redistributed via *gluon* exchange. Such gluons split as well into low momentum $q\bar{q}$ pairs, called *sea quarks*. All these quarks and gluons are named **partons**.

A proton p moves with $p_\text{T} = 0$ and $p_\text{z} \neq 0$, while its parton i moves with $p_\text{T} = 0$ and xp_z, where the fraction x has the probability $f_{i/p}(x, Q^2)$, such that all x integrate to 1. The probabilities f are called **parton distribution functions** (PDF) and depend on Q^2 in that a quark could originate from a higher momentum fraction quark, that radiated a gluon with $\alpha_S(Q^2)$. This dependency is handled analytically [81], while its dependency on x is fitted from experimental data. Experimental results [82, 83] show that the valence quarks dominate at high x, gluons and sea-quarks dominate at low x and gluons carry overall half of the proton's momentum.

pp collisions at low Q^2 are elastic. With higher Q^2 they become inelastic, where excited protons issue hadrons. At even higher Q^2 such as at $\sqrt{s} = 8$ TeV in this thesis, they become **deeply inelastic**, where protons break up and their partons recombine. The amplitudes $\mathcal{M}$ are given by partonic production cross-sections $\hat{\sigma}_{ab\to X}$, where particle X is produced via hard scattering of partons ab [48]:

$$\sigma_{pp\to X} = \int dx_1 dx_2 \left[f_{a/p}(x_1, \mu_F^2) \cdot f_{b/p}(x_2, \mu_F^2) \right] \hat{\sigma}_{ab\to X} \tag{2.48}$$

Chapter 3.

The ATLAS detector at the LHC

This chapter is an overview of the experimental setup to study top quark pair resonances in proton-proton (pp) collisions. Section 3.1 describes the LHC accelerator and the conditions of the beams and collisions. Section 3.2 describes ATLAS, a multipurpose detector at the LHC, that will analyse the many particles produced in the collisions.

3.1. The Large Hadron Collider

The LHC is the newest accelerator of the CERN accelerator complex (Figure 3.1) near Geneva. It is a superconducting machine that accelerates and collides two counter-rotating beams with each other: primarily protons (*hadrons*), but also lead ions, during four weeks per year, or, rarely, protons with lead ions. These particles have been chosen because they are stable, charged (the electromagnetic acceleration acts on charged particles) and, because of their high mass, they lose little synchrotron radiation.

The LHC features are shown in Table 3.1. LHC has a variety of magnets, the biggest being the dipoles, that keep the beam circular, and the quadrupoles, that focus the beam. Protons are accelerated in cavities via electromagnetic resonance only when the radio frequency field is correctly oriented. This issues a bunch structure for the beam.

LHC reuses the tunnel from the previous Large Electron Positron Collider (LEP) and has seven detectors operating on it (see their history in Table 3.2):

- ALICE - A Large Ion Collider Experiment [87] analyses $PbPb$ collisions, to study for example quark-gluon plasma. This is a state where quarks and gluons are no longer bound to hadrons, state that probably existed right after the Big Bang.
- ATLAS, CMS - A Toroidal LHC ApparatuS [88] and the Compact Muon Solenoid [89]. General purpose detectors that analyse pp collisions, for precision measurements of the discovered Standard Model Higgs boson, for searches for supersymmetry, extra dimensions, signs of dark matter and other new physics beyond the Standard Model.
- LHCb - The LHC beauty Experiment [90] searches for the cause of the asymmetry between matter and antimatter in the early Universe, by studying rare decays of the B-hadrons, that violate the fundamental charge-parity symmetry of nature.
- LHCf - The LHC forward Experiment [91], a small experiment near ATLAS, measures particles produced closely to the beam, in order to calibrate models of high energy cosmic rays.

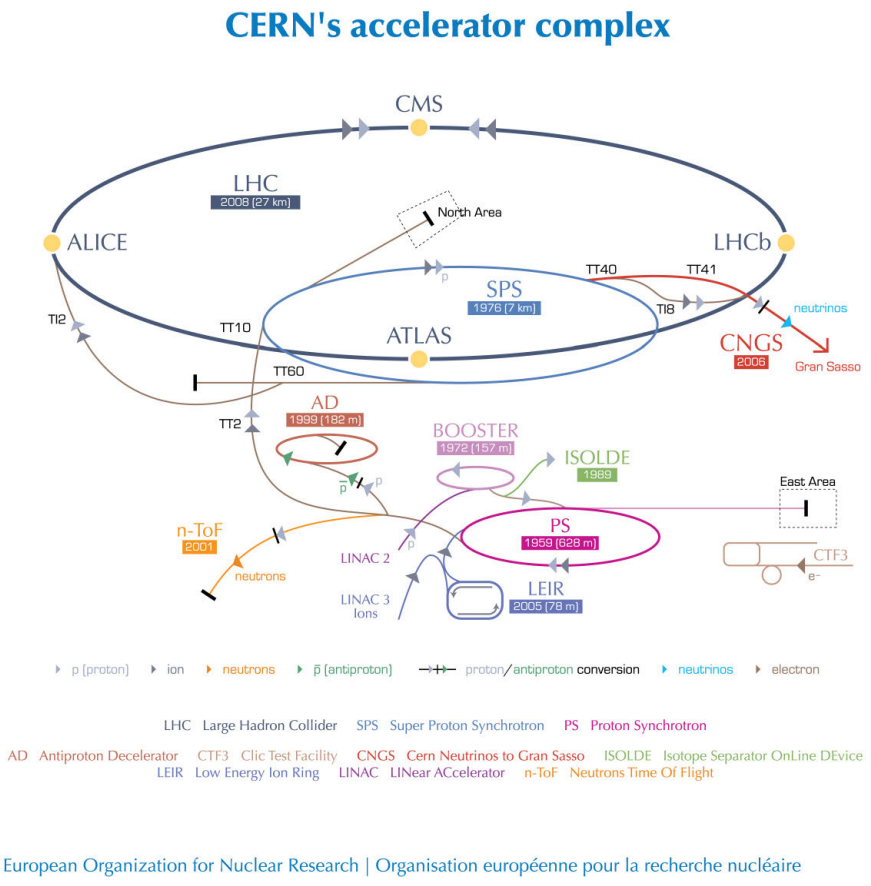

Figure 3.1.: The CERN accelerator complex. Protons (hydrogen atoms stripped from electrons) are accelerated in the Linac2 (to 50 MeV), then in the PS Booster (to 1.4 GeV) and SPS (450 GeV). They are then injected in bunches of beams into the LHC, ramped up to stable energy (7 TeV nominal value), then circulated and collided for hours in the beam-crossing points of ATLAS, CMS and LHCb. Lead ions (ionised vapours of heated lead) are accelerated in sequence in the LEIR, PS, SPS and LHC to 2.76 TeV per Pb^{82+} pair, then collided in the ALICE detector. [84]

Parameter	Value	Remarks
Circumference	26.7 km	
Underground depth	45–170 m	For shielding against radiation.
Dipole temperature	1.9 K	Ensures the dipole superconductivity.
$\sqrt{s}$ per pp	14 TeV	Center-of-mass energy.
$\sqrt{s_{NN}}$	2.76 TeV	Per Pb^{82+} pair.
Total no. of magnets	9593	
Peak p beam L	10^{34} cm^{-2}s^{-1}	
Peak Pb^{82+} beam L	10^{27} cm^{-2}s^{-1}	
Peak magnetic dipole field	8.33 T	
Bunch spacing per p beam	25 ns	50 ns in Run 1, 25 ns since Run 2.
Initial no. of p per bunch	1.15×10^{11}	Losses mainly from collisions. At IP, the density is limited by the beam-beam interaction.
No. of bunches per p beam	2808	
Revolution frequency f_{rev}	11.245 kHz	
Lorentz γ factor for p beams	7461	
Crossing angle	285 µrad	At ATLAS and CMS.

Table 3.1.: The design or nominal features of the LHC [85, 86].

- MOEDAL - The MOnopole and Exotics Detector At the LHC [92], a small experiment near LHCb, searches for magnetic monopoles (theoretical highly ionising particles).
- TOTEM - The TOTal Elastic and diffractive cross-section Measurement Experiment [93], located near CMS, measures the total pp cross-section and studies elastic and diffractive scatterings.

The instantaneous LHC luminosity can be defined for Gaussian distributed beams as [85]:

$$L = \frac{N_{\text{part/bunch}}^2 N_{\text{bunch/beam}} f_{\text{rev}} \gamma}{4\pi\epsilon_n \beta^*} F, \tag{3.1}$$

where $N_{\text{part/bunch}}$ is the number of particles per bunch, $N_{\text{bunch/beam}}$ the number of bunches per beam, f_{rev} the revolution frequency, γ the relativistic $1/\sqrt{1-(v/c)^2}$, ϵ_n the normalised transverse beam emittance, F the luminosity reduction due to the crossing angle at the IP, β^* the acceleration β function at the interaction point (IP), with β a measure of the beam width and β and β^* minimum at the IP. L determines the event rate as $N = L\sigma$, where σ is the process cross-section, thus a high L are important in searches for low cross-section processes. The integrated luminosity $\int L(t)\ \mathrm{d}t$ (see in Table 3.2) indicates the total amount of collision data, specified as delivered by the LHC, recorded by the detectors or, in lower amount, "good" (Section 5.2.1) for physics analysis.

Possible future colliders to follow the LHC are currently being discussed. The High-Luminosity LHC is designed to increase the nominal luminosity of the LHC by a factor of 10 and is confirmed to become operational at the end of 2027 [100]. Other proposed colliders, that are not yet confirmed, are the Future Circular Collider, a 100 km circular tunnel near Geneva, colliding protons up to $\sqrt{s} = 100$ TeV, and the International Linear Collider or the Compact Linear Collider, colliding electrons with positrons up to $\sqrt{s} = 3$ TeV [101, 102].

Mar 1984	CERN proposes the LHC inside the LEP tunnel.
Jul 1989	The first beam circulates the LEP.
Oct 1993	The proposed US Superconducting Super Collider is cancelled and leaves LHC the only future high energy hadron collider.
1994 – 1998	LHC, then ATLAS, CMS, ALICE and LHCb are approved.
Nov 2000	LEP is decommissioned to allow construction of the LHC.
Jun 2003	The ATLAS detector cavern is inaugurated as LHC's first cavern.
Sep 2008	The first proton beam circulates the LHC.
1 week later	An electrical fault damages 100 magnets and halts the operation.
Nov 2009	Beams recirculated, beating Tevatron's beam world record of ~ 1 TeV [94].
2010	Run 1: $\sqrt{s} = 7$ TeV, $L = 2 \times 10^{32}$ cm^{-2}s^{-1}, $\int L(t)\ \mathrm{d}t = 45$ pb^{-1}.
2011	Run 1: $\sqrt{s} = 7$ TeV, $L = 3.6 \times 10^{33}$ cm^{-2}s^{-1}, $\int L(t)\ \mathrm{d}t = 5.2$ fb^{-1}.
2012	Run 1: $\sqrt{s} = 8$ TeV, $L = 7.7 \times 10^{33}$ cm^{-2}s^{-1}, $\int L(t)\ \mathrm{d}t = 20.8$ fb^{-1}.
Jul 2012	ATLAS and CMS discover a new particle of $m = 125$ GeV, consistent with the SM Higgs boson, for which F. Englert and P. Higgs receive the Nobel prize.
2013 – 2014	Long Shutdown 1 for machine upgrades [95].
2015 – 2018	Run 2 at $\sqrt{s} = 13$ TeV and peak $L = 2 \times 10^{34}$ cm^{-2}s^{-1}.
2019 – 2020	Long Shutdown 2 for machine upgrades.
2021 – 2023	Run 3 at $\sqrt{s} = 14$ TeV.

Table 3.2.: The main timeline of the LHC, with $\sqrt{s}$, peak L and $\int L(t)\ \mathrm{d}t$ of pp collisions recorded by ATLAS [96–99].

3.2. The ATLAS Detector

ATLAS, A Toroidal LHC ApparatuS, is a general-purpose detector, with an approximate cylinder shape around the beam pipe and with forward-backward symmetry to the IP. It has an onion layering, with the following components starting from the innermost (Figure 3.2): an inner tracker, a thin solenoid central magnet, electromagnetic and hadronic calorimeters, toroidal outer magnets, and a muon spectrometer. The data collected for physics analysis is considered good only when all sub-detectors are functional. How particles interact with ATLAS is summarised in Figure 3.3 and the principles behind it detailed in Appendix A. The ATLAS coordinate system and the ATLAS sub-detectors are described in the following sections.

3.2.1. Coordinate System

The coordinate system at ATLAS (Figure 3.4) is right-handed, with the origin at the IP (the actual primary vertices PV being along the IP, in the beam-spot): the x-axis points to the center of the LHC, the y-axis upwards, the positive z-axis (the beam pipe) to the side-A of the detector and the negative to side-C. The spherical coordinates (r, ϕ, θ) are used, with ϕ the azimuthal angle to the x-axis in the transverse $x - y$ plane and θ the polar angle to the z-axis in the $R - z$ plane. Since in hadron collisions the p_z of the incoming parton is unknown (Section 2.8.3), but their transverse component is zero, transverse kinematics are used : p_T, E_T, E_T^{miss}, for momentum, energy and missing energy. The rapidity $y = 1/2 \ln[(E + p_z)/(E - p_z)]$ for objects with mass is an important kinematic, since Δy is Lorentz invariant under z-axis boosts. In the massless approximation or

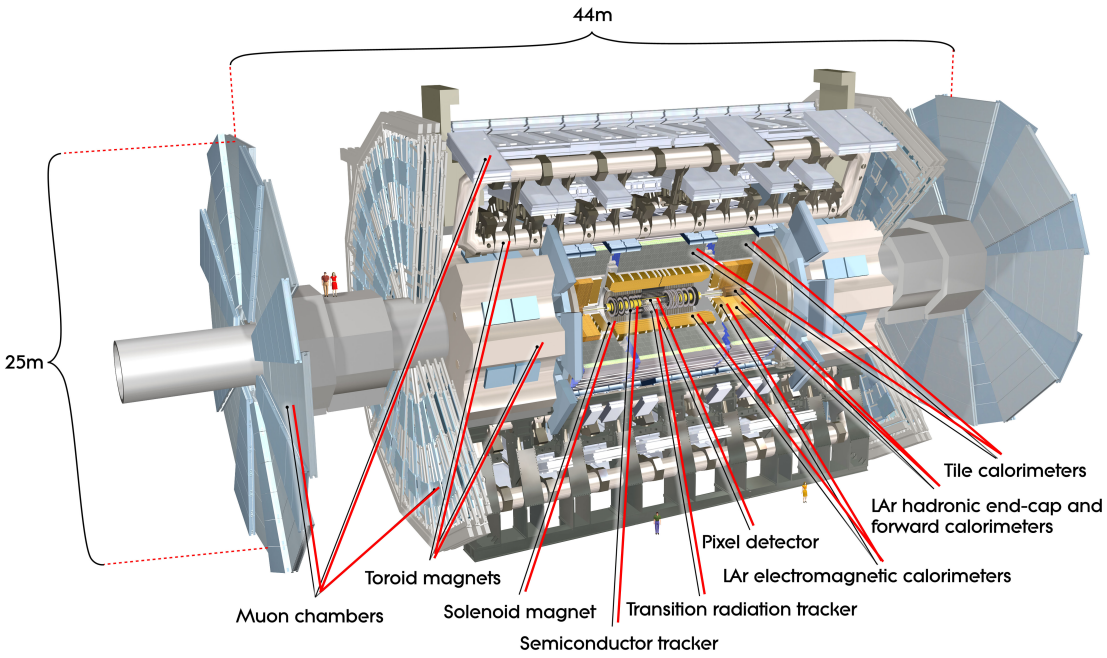

Figure 3.2.: Overview of the ATLAS detector at the LHC [88].

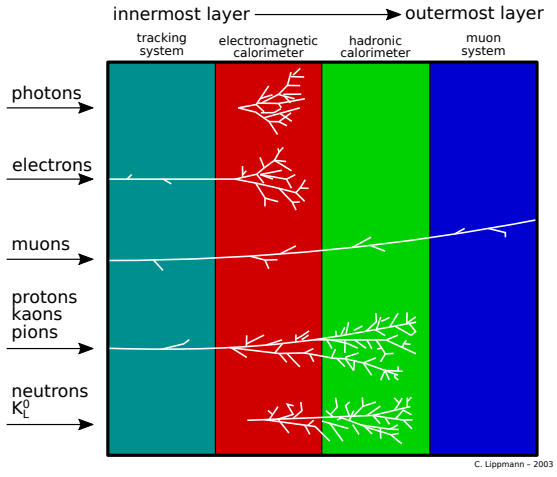

Figure 3.3.: In a general detector such as ATLAS, each particle has its own signature: charged particles are deflected and leave an ionisation trail in the inner tracker (muons in the muon system as well), photons and electrons are stopped via showering in the electromagnetic calorimeter, hadrons shower in the electromagnetic and hadronic calorimeters; neutrinos do not interact. [103]

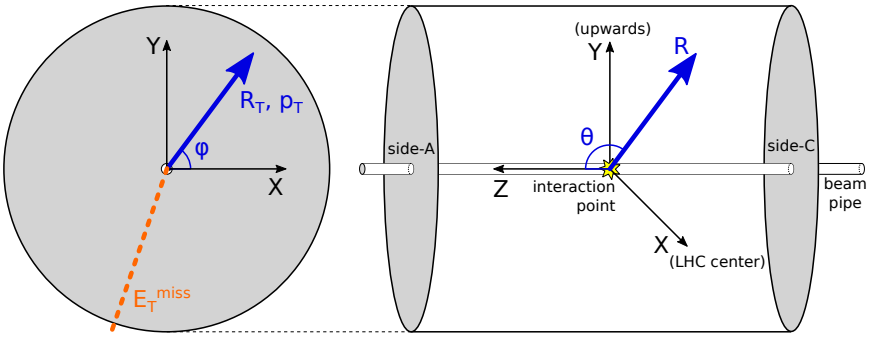

Figure 3.4.: The ATLAS coordinate system.

close to the speed of light, y becomes the pseudorapidity $\eta = -\ln[\tan(\theta/2)]$. η has the advantage to depend only on θ, and not on energy. Close to the beam in the forward-backward region, $|\eta|$ is high. The angular separation is measured with $\Delta R = \sqrt{(\Delta\eta)^2 + (\Delta\phi)^2}$, again Lorentz invariant. [88]

3.2.2. Detector Challenges

Due to the high rate and luminosity of collisions, the detector has to withstand high particle flow rates, which makes it more difficult to reconstruct the physics objects and creates radiation damage as well. QCD background dominates in cross-section the rare processes searched. Thus ATLAS requires fast and radiation-hard electronics, large $|\eta\ |$ and full ϕ coverage, good identification for muons and isolated high-p_{T} photons and electrons, good charged particles momentum resolution and good electromagnetic calorimeter resolution. The resolutions required are based on the SM Higgs boson search.

3.2.3. Inner Detector

The ATLAS inner detector, ID, or tracker (Figure 3.5), is the component closest to the beryllium beam pipe and IP. It detects charged particles or photons converted to e^+e^-, at $|\eta| < 2.5$ and $p_{\mathrm{T}} > 0.5$ GeV (or $p_{\mathrm{T}} > 0.1$ GeV for minimum-bias events [104]). The ID has a length of 7 m and a diameter of 2.3 m, around the 7.2 cm thick beam pipe. The ID is immersed in a 2 T axial magnetic field, parallel to the beam, from the surrounding superconducting solenoid coil. The charged particles are thus bent in the $x-y$ plane via the Lorentz force, with positive and negative particles in opposite directions, and their charge and momentum measured as $p_{\mathrm{T}} = m_0\gamma\beta c = RzeB$.

Appendix A.2 explains how signals are formed in silicon detectors and how they are affected by radiation damage. The ID reads synchronised to the bunch interval: "1" if the signal is above an electric threshold for the whole bunch interval (*time-over-threshold*), "0" otherwise. Nearby signals cluster in *hits* and two hits on each side of a detector module create a *space-point*. A reconstructed fitted line of such hits is a *track* and their crossings *vertices* (Section 5.3.1). Higher p_{T} tracks have a higher bending radius R, which is more imprecisely reconstructed. Low p_{T} tracks move helically along the magnetic field and are affected by scattering. The overall designed resolution is $\sigma_{p_{\mathrm{T}}}/p_{\mathrm{T}} = 0.05\%\ p_{\mathrm{T}} \oplus 1\%$, where $\oplus$ is summation in quadrature. The p_{T} resolution is moreover worse at high $|\eta|$, due to fewer existing hits and to multiple scattering from increased material. [106]

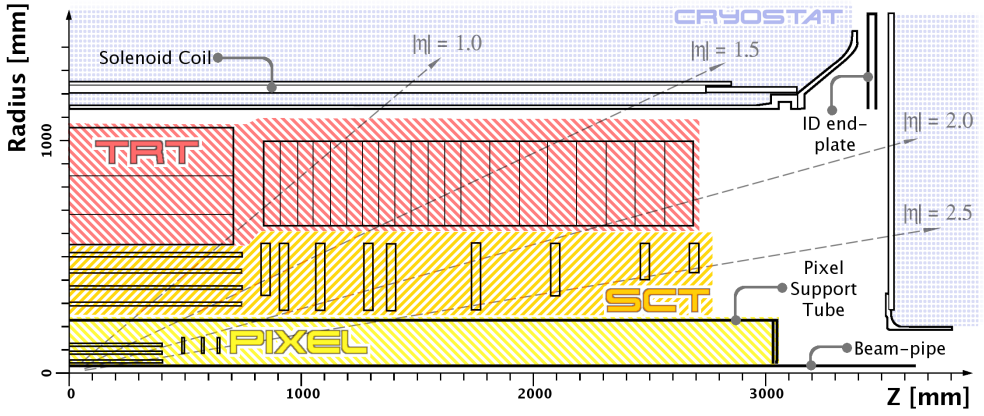

Figure 3.5.: $R-z$ view of one quarter of the ATLAS ID, with the IP at z=0. For a higher coverage, its sub-detectors have concentric cylinders around the beam pipe (*barrel*) and transverse disks in each forward region (*end-caps*): the pixel detector has 3 barrel layers (*B*-layer, layer 1 and layer 2) and 3 disks per end-cap; the SCT has 4 barrel layers and 9 disks per end-cap; the TRT has 73 barrel layers of straws, split in 3 rings, and 160 planes of straws per end-cap, split in wheels. [105]

The ID must sit closely to the IP, in order to detect the tracks soon after they emerge from the primary vertex PV, hence the ID is the ATLAS subsystem most affected by radiation. For this reason an additional innermost pixel barrel layer, called Insertable B-Layer, has been installed in the shutdown at the end of Run 1, to improve the tracking efficiency [107].

Pixel Detector

The silicon pixel tracker has the highest granularity, since tracks are here the densest: $\sim$80 million pixels (one readout channel per pixel) distributed in 1744 sensor modules. Usually a track has three pixel hits. A pixel has the nominal size in $R-\phi \times z$ of 50×400 µm^2. The resolution is 10 µm in the $R-\phi$ plane and 115 µm in the $z(R)$ direction, for the barrel (end-caps).

The pixel system provides additional particle identification via the ionisation loss function of momentum, especially to separate $\pi/K/p$. However, it cannot separate μ/π, as they are close in mass. Against radiation damage, the highly irradiated B layer can be replaced easily every few years, as opposed to layers 1, 2 and the disks, which should stand minimum ten years. [106]

SemiConductor Tracker (SCT)

The silicon strips tracker has $\sim$6.3 million strips (one readout per strip) distributed in 4088 sensor modules. A barrel module is rectangular and an end-cap module is trapezoidal, both having two 285 µm thick sensor sides, rotated at 40 mrad, to add an extra dimension. Usually a track has eight SCT hits (four space-points). The resolution is 17 µm in the $R-\phi$ plane and 580 µm in the $z(R)$ direction, for the barrel (end-caps). [106]

Transition Radiation Tracker (TRT)

The TRT is situated at higher radii and $|\eta| < 2$. It is made of 4 mm diameter drift straws filled with Xe–CO_2–O_2 gas. An electric field multiplies and drifts the ionisation electrons to the readouts at the end of an end-cap straw or at both ends of a barrel straw. The position of the straw and the drift time (maximum 48 ns) provide the signal coordinates. The end-cap straws are 37 cm long, radially oriented at constant ϕ and spaced at $z = 8(15)$ mm in the inner (outer) wheels. The barrel straws are 144 cm long, distributed axially and spaced at 7 mm. Thus a total of 351,000 readout channels. The TRT has a good accuracy only in $R - \phi$ and of only 130 µm per straw. The TRT compensates however with its typically 36 large number of hits. [106]

The straws are blended within materials of other dielectric constant materials, such that an ultra-relativistic charged particle emits X-ray transition radiation (TR) when crossing from a material to another. Since TR leaves a much higher signal than a *mip* and an electron's TR leaves as well a higher signal than a hadron's TR, different signal thresholds are set in the TRT: 250 eV to track any particle, 6 keV to detect TR. The latter threshold discriminates electrons from hadrons (especially pions) complementing hence the EM calorimeter in electron identification. The TR is used to estimate the particle's energy as well, since the TR increases with it. [108]

3.2.4. Calorimeters

The incoming single particles or jets (Section 2.8.1) are completely absorbed in a calorimeter, in order to measure their energy and position, via principles explained in Appendix A.3. The ATLAS calorimeters (Figure 3.6) surround the inner detector over full ϕ and $|\eta| < 4.9$, reducing losses at their transition regions via small overlaps. They have a finer granularity at $|\eta| < 2.5$, range common with the inner detector and dedicated to precision measurements. As opposed to homogeneous calorimeters, where the entire material is both absorber and sensor, ATLAS calorimeters are sampling, with metallic absorbers alternating with sensor materials. The total particle energy is estimated from the measured signals via *calibration*. ATLAS uses as active material mostly liquid argon (LAr), which has an ionisation energy of only 24 eV and has linear and stable response. LAr becomes however liquid at 85 K, thus cryostats are needed for cooling it down. The ATLAS calorimeter components are described in the following sections [88].

Electromagnetic Calorimeters

The LAr EM calorimeter has a 6.4 m long barrel surrounding the central solenoid at $|\eta| < 1.475$ and 1.4 m $< R <$ 2 m (at least 22 X_0 in depth), and two 63 cm thick end-caps (EMEC) at $1.375 < |\eta| < 3.2$ and 0.33 m $< R <$ 2.1 m (at least 24 X_0 in length). The EM calorimeter displays a barrel/end-cap inactive transition region at $1.37 < |\eta| < 1.52$ and a 4 mm barrel gap at $z = 0$. The barrel is divided in depth in three layers, with varying $\Delta\eta \times \Delta\phi$ granularity. The middle layer has the higher granularity, 0.025×0.025 at $|\eta| < 2.5$, since high energetic electrons and photons are central in η and their showers peak longitudinally in that area. The center of the first layer is segmented in 0.003×0.1, in order to measure the impact points, discriminate multiple showers, or

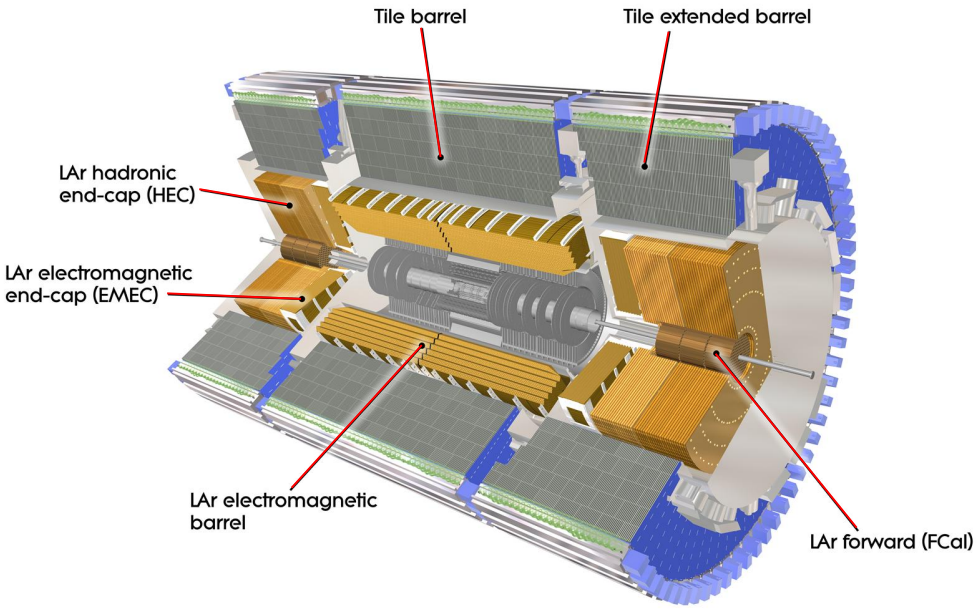

Figure 3.6.: Overview of the ATLAS calorimeters. [88]

discriminate γ versus $\pi^0 \to \gamma\gamma$. The rest of the calorimeter has granularity of up to 0.1×0.1, which is designed for the trigger. A start LAr layer called presampler, at $|\eta| < 1.8$, estimates the energy lost before the calorimeter. The calorimeter consists of accordion-shaped lead absorber plates, interleaved with LAr readout gaps. The required energy resolution is $10\%\sqrt{E} \oplus 0.7\%$. [88, 109]

Hadronic Calorimeters

The **tile calorimeter** has steel plates as absorber and scintillating tiles as sensor. Radiation ionises the scintillator molecules, that emit photons while returning to the ground state. These photons are then amplified by photomultiplier tubes (PMT) and measured. The calorimeter spans over 2.2 m $< R <$ 4.2 m (7.4 λ_I) in three barrels: a 5.8 m long one at $|\eta| < 1.0$, surrounding the LAr EM calorimeter, and two 2.6 m long side extended barrels at at $0.8 < |\eta| < 1.7$, surrounding the EM and HAD end-caps. They are split in $\Delta\phi \approx 0.1$ wedge modules with tiles radial and transverse to the beam pipe. The $\Delta\eta \times \Delta\phi$ granularity is mostly 0.1×0.1. [88, 110]

The **LAr hadronic end-cap calorimeter (HEC)** sits in extension to the EMEC at $1.5 < |\eta| < 3.2$, having the same inner and outer radius. It has 1.8 m length per end-cap and 2 wheels, each wheel split as well azimuthally in wedges. A wedge has copper plates as absorber, alternating with LAr drift gaps as active material. The $\Delta\eta \times \Delta\phi$ granularity is 0.1×0.1 at the lower $|\eta\ |$ and 0.2×0.2 at the upper $|\eta\ |$. [88, 110]

The required energy resolution of the hadronic calorimeters is $50\%\sqrt{E} \oplus 3\%$.

Forward Calorimeter (FCal)

The LAr Forward Calorimeter (FCal) surrounds the beam pipe at the highest $|\eta\ |$, $3.1 < |\eta| < 4.9$, extending the EMEC and HEC. To decrease the back-scattering of radiation to the ID (*albedo*),

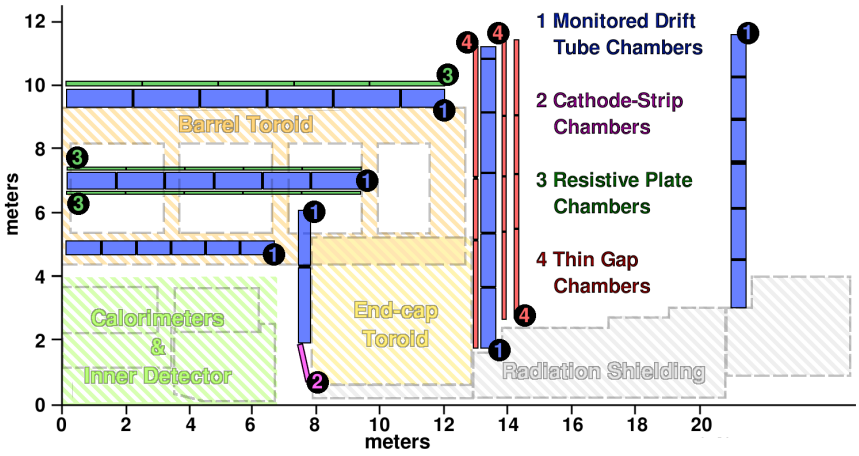

Figure 3.7.: $R-z$ view of one quarter of the ATLAS muon system. The blue areas represent the barrel (longitudinal and concentric) or end-cap (transverse) tracking chambers. The barrel and end-cap toroids are magnets. [105]

it's z is shifted 1.2 m away from the EMEC, to $z = 4.7$ m. FCal is optimised to the limited space and highest irradiation by having very dense absorbers and very thin LAr gaps, that allow a fast readout and prevent ion accumulations. The various metal absorber rods are surrounded by LAr readout gaps and copper tubes, parallel to the beam line. Each FCal end-cap spans over 10 λ_{I} in 3 longitudinal modules: FCal 1 closer to the IP, with copper rods optimised for EM calorimetry; FCal 2 and FCal 3 with the much denser tungsten rods optimised to limit the hadronic shower; a last brass layer prevents radiation to pass to the muon spectrometer. The required FCal energy resolution is $100\%\sqrt{E} \oplus 10\%$. [88, 109]

3.2.5. Muon Spectrometer

As explained in Appendix A.1, muons are *mip*, with a long lifetime and little energy deposits in the calorimeters. Therefore an additional ATLAS tracker dedicated to muons, called muon spectrometer MS, sits at the detector periphery. Muons are hence the only particles detected in both the inner and the muon detector.

In the MS, muons are bent by barrel and end-cap toroid magnets, in order to measure their p_{T} and coordinates in each tracking chambers (Figure 3.7): barrel chambers ($|\eta| < 1.4$), end-cap chambers ($1.6 < |\eta| < 2.7$) and transition chambers ($1.4 < |\eta| < 1.6$). ATLAS detects muons efficiently and precisely up to 1 TeV, with $\sigma_{pT}/p_{\mathrm{T}} = 10\%$ at $p_{\mathrm{T}} = 1$ TeV. [108]

Tracking Chambers

The Monitored Drift Tubes (MDT) and the Cathode Strip Chambers (CSC) provide **precision measurements**. MDT are filled with Ar-CO_2 gas and with a central tungsten-rhenium wire and span on most of the $|\eta|$ range. The CSC are multiwire chambers, cover the higher $|\eta|$ range and must cope with the high rate of low p_{T} muons.

The lower precision **trigger measurements** are employed in the Resistive Plate Chambers (RPC, parallel electrode plates with gas in between) in the barrel, and the Thin Gap Chambers (TGC,

multi-wire proportional chambers) in the end-caps. They set a p_T threshold and measure together with the sandwiched MDT two perpendicular coordinates.

The chamber alignment is very important for performance and is monitored via 12000 optical sensors up to 30 µm precision. [111]

Toroidal Magnets

The superconducting air-core toroids are interleaved with the chambers: one barrel toroid around the chambers and calorimeters, two end-caps in line with the central solenoid. A toroid has eight $R-z$ plane coils, with a $\pi/8$ angle between an end-cap and a barrel coil, to provide as much magnetic coverage as possible. The magnetic field circulates inside the coil and the air-core reduces the multiple scattering. [112]

3.2.6. Forward Detectors

In the ATLAS forward regions are three small detectors. LUCID (LUminosity measurement using Cerenkov Integrating Detector) lies at ± 17 m and is the online relative luminosity monitor of ATLAS, measuring inelastic pp scattering. The ZDC (Zero-Degree Calorimeter) lies at ± 140 m, where the common beam pipe splits in two beam pipes. It measures how central are the heavy-ion collisions, by detecting neutral particles at $|\eta| > 8.3$. At ± 240 m lies ALFA (Absolute Luminosity For ATLAS), which measures the absolute luminosity via elastic pp scattering.

3.2.7. Trigger System

In the Trigger and Data Acquisition System (TDAQ) [108, 113], the data is read at the nominal 40 MHz collision rate, then passed through a chain of three online trigger levels: L1, L2 and the Event Filter, which lower sequentially its rate. The data is filtered in real time, rejecting the low energetic but high cross-section QCD background.

L1 is hardware-based and uses the muon trigger chambers (L1Muon) and the lower granularity calorimeter (L1Calo) information. Its Central Trigger Processor selects then muons, EM clusters, jets, hadronic τ decays and E_T^{miss} regions, all with specific isolation, multiplicity and E_T threshold (or p_T threshold for muons). Such areas are stored in η and ϕ as Regions of Interest (RoI) and seeded to L2, at 75 kHz.

L2 is software-based, running on PC farms, and analysing only the received RoI within the event ($\approx 2\%$ of the total event). It improves the event selection, adding calorimeter full granularity information and inner detector tracks. L2 algorithms are offline-like, yet optimised for time performance (such as taking highest E_T calorimeter cells instead of full slide-window algorithm). L2 lowers the data rate to 3 kHz.

The **Event Filter** is as well software-based, reconstructing and selecting events now with full detector readout and with offline analysis techniques, such as pattern and calibration tools. Events are then stored for offline analysis at 200 Hz and 300 MB/s at the CERN Tier-0 permanent storage.

The L2 and Event Filter are merged to form the High-Level Trigger (HLT) in Run 2.

Chapter 4.

Simulations in 2HDM

4.1. The Two-Higgs-Doublet-Model

4.1.1. Motivation for 2HDM and Supersymmetry

Beyond Standard Model (BSM) scalar[1] resonances that couple strongly to top quark pairs are introduced by the Two-Higgs-Doublet-Model (2HDM) classes. These are generic models with two Higgs $SU(2)$ doublet fields, one extra doublet than in the SM. 2HDMs are motivated by theories such as supersymmetry (SUSY), originally introduced in Ref. [7], axion models [8], CP violation or dark matter, where A/H could mix with scalar or pseudoscalar mediator particles that couple directly to dark matter [9, 10]. The doublet extension is the simplest solution that maintains the relative strength of the neutral to charged weak currents $\rho = m_W/(m_Z \cos\theta_W)$ (Eq. 2.41) to unity as constrained in the SM and observed experimentally as well.

The main argument for SUSY are the ultraviolet divergent corrections to the Higgs boson mass, given by h, W, Z or t loops. Cutting at a scale Λ yields, in the first term approximation [114]:

$$\Delta m_h^2 = m_h^2 - (m_h^0)^2 = \frac{3\Lambda^2}{8\pi^2 v^2}[m_h^2 + 2m_W^2 + m_Z^2 - 4m_t^2] \tag{4.1}$$

The Λ scale could be the Grand Unification scale 10^{16} GeV, where the coupling strengths of the three fundamental forces described in the SM meet and the forces reach the same strengths, or the Planck scale 10^{19} GeV, where gravity finally reaches strong quantum effects. To keep $m_h \sim 100$ GeV at very high Λ, the term in square brackets should be ~ 0, fine-tuned at the smallest decimals.

As fine-tuning up to 16–19 decimals is highly unnatural ("the naturalness fine-tuning problem") SUSY proposes instead that each SM particle P has a supersymmetric partner $\tilde{P} = P - ino$ with opposite coupling to the Higgs boson, such that the divergence cancels out and leaves, in the approximation of the second term [14]:

$$\Delta m_H^2 \sim (m_P^2 - m_{\tilde{P}}^2) \log\left(\frac{\Lambda}{m_{\tilde{P}}}\right), \tag{4.2}$$

where the logarithm would dampen a divergence even at very high Λ, if $m_{\tilde{P}} \leq \mathcal{O}(1\text{ TeV})$.

SUSY transforms a boson into an *s-boson* of spin 1/2 and a fermion into an integer spin *s-fermion*, both partners belonging to the same chiral superfield. The lightest supersymmetric particles are

[1] Throughout the thesis, "scalar" will refer to "pseudoscalar" as well, unless otherwise explicitly mentioned.

candidates for dark matter as well, as they are stable, neutral, not too heavy and are weakly interacting [115, 116].

The Minimal Supersymmetric Model [14] is a SUSY model example, that considers a minimum number of new SUSY particles and requires two doublet scalar fields. This requirement can be motivated with at least two arguments. Firstly, in the SM there are fermionic triangular loop anomalies which affect the renormalisation, but that are cancelled out by summing all fermions charges. In MSSM, with only one Higgs doublet there would be one additional fermion, the Higgsino, superpartner of the Higgs field, that would prevent the cancellation. Two Higgs doublets would generate more fermions that maintain the cancellation [117]. Secondly, the SUSY potential cannot generate with only one doublet the masses of opposite chirality fermions [118]. Hence the two doublets are introduced.

4.1.2. Theoretical Aspects of 2HDM

The SM doublet of complex scalar fields from Eq. 2.32 is extended in 2HDM to two doublets $\Phi_a = \begin{pmatrix} \phi_a^+ \\ \phi_a^0 \end{pmatrix}$ a=1,2, each with $Y = 1$ and real VEV v_a[2]. The generic potential form in 2HDM is:

$$\begin{aligned} V = {} & m_{11}^2 \Phi_1^\dagger \Phi_1 + m_{22}^2 \Phi_2^\dagger \Phi_2 - m_{12}^2 (\Phi_1^\dagger \Phi_2 + \text{h.c.}) \\ & + \frac{\lambda_1}{2} (\Phi_1^\dagger \Phi_1)^2 + \frac{\lambda_2}{2} (\Phi_2^\dagger \Phi_2)^2 + \lambda_3 \Phi_1^\dagger \Phi_1 \Phi_2^\dagger \Phi_2 + \lambda_4 \Phi_1^\dagger \Phi_2 \Phi_2^\dagger \Phi_1 \\ & + \left\{ \frac{\lambda_5}{2} (\Phi_1^\dagger \Phi_2)^2 + [\lambda_6 (\Phi 1^\dagger \Phi_1) + \lambda_7 (\Phi_2^\dagger \Phi_2)](\Phi_1^\dagger \Phi_2) + \text{h.c.} \right\}, \end{aligned} \tag{4.3}$$

with h.c as Hermitian conjugate. When the parameters m_{ij} and λ are complex, the model is a source of CP violation (see $\mathcal{C}$ and $\mathcal{P}$ conjugation in Section 2.3.2), case for which 2HDM was originally proposed [120]. This thesis however assumes CP-conservation, hence all parameters are real. The fluctuation around V_{min} is done similarly to Eq. 2.35, with eight real fields:

$$\Phi_a = \begin{pmatrix} \phi_a^+ \\ (v_a + \rho_a + i\eta_a)/\sqrt{2} \end{pmatrix}, \quad a = 1, 2, \tag{4.4}$$

where for each scalar doublet Φ_a, v_a is its VEV, ϕ_a^+ the original charged complex field, ρ_a and η_a real fluctuation fields. These fields generate the same physical vector gauge fields as in SM (Eq. 2.40), but five Higgs scalar physical fields instead of the one in SM: two neutral CP-even (light h and heavy H) generated by ρ_a, one neutral heavy CP-odd A generated by η_a and two charged heavy CP-even $H^\pm$ generated by ϕ_a^+. The CP-even H and h are mixed with a rotation angle α such that $m_h < m_H$:

$$\begin{aligned} h &= \rho_1 \sin\alpha - \rho_2 \cos\alpha \\ H &= -\rho_1 \cos\alpha - \rho_2 \sin\alpha \end{aligned} \tag{4.5}$$

[2] The equations and formulas in Section 4.1.2 are taken from [6] and [119].

The most important parameter is however β, a rotation angle that mixes the massless non-physical states (also called Goldstone) into the massive physical states, for the charged, respectively pseudoscalar fields:

$$\tan\beta = \frac{v_2}{v_1} = \frac{v\sin\beta}{v\cos\beta}, \tag{4.6}$$

where $v_1^2 + v_2^2 = v^2$ and v=246 GeV the SM VEV. The A and $H^\pm$ masses are, respectively:

$$\begin{aligned} m_A^2 &= [m_{12}^2/(v_1 v_2) - 2\lambda_5](v_1^2 + v_2^2) \\ m_{H^\pm}^2 &= [m_{12}^2/(v_1 v_2) - \lambda_4 - \lambda_5](v_1^2 + v_2^2) \end{aligned} \tag{4.7}$$

In the neutral CP-even sector there is the following relation to the SM Higgs boson:

$$h_{\mathrm{SM}} = h\sin(\beta-\alpha) - H\cos(\beta-\alpha) \tag{4.8}$$

A further 2HDM classification is given by allowing or not allowing **flavour-changing neutral currents** (FCNC). A neutral current $s \leftrightarrow d$ for example, that exchanges a neutral scalar Φ, would allow $K_L - K_S$ mixing via Φ. The scalar would need a $\mathcal{O}(100)$ TeV mass in order to compensate the 10^{-15} GeV kaons mass difference [121]. To suppress this problematic FCNC and to impose strict mass bounds on the additional Higgs bosons, the Yukawa couplings $y_{ij}^{1,2}$:

$$\mathcal{L}_{Yukawa} = y_{ij}^1 \bar{f}_i f_j \Phi_1 + y_{ij}^2 \bar{f}_i f_j \Phi_2 \tag{4.9}$$

must be diagonal, which is easier done if each fermion flavour couples only to one Φ (fermions are by choice right-handed, since Eq. 2.43 shows it is enough to impose the restriction to only one chirality). The easiest way is through the $\mathcal{Z}$ discreet symmetry: $\Phi \to -\Phi$ in the Yukawa regime for the decoupled field and $\Phi \to \Phi$ for the coupled field, symmetries that yield four 2HDM types. In **type I** 2HDM the up-type u_R and down-type d_R quarks couple to the same field (by convention Φ_2, via $\Phi_1 \to -\Phi_1$ symmetry). In **type-II** 2HDM u_R couples to Φ_2 and d_R couples to Φ_1 ($\Phi_1 \to -\Phi_1$ and $d_R \to -d_R$). The leptons l_R couple to the same field as d_R. In **type-III ("Lepton-specific")** and **type-IV ("Flipped")** the quarks couplings are the same as in type I and II, but the leptons couple to Φ_1, respectively Φ_2. [6]

To preserve the $\mathcal{Z}$ symmetry, $\lambda_6 = \lambda_7 = 0$ as well.

The 2HDM classes have hence seven real free parameters at tree level: m_h, m_H, m_A, $m_{H+} = m_{H-}$, α, β and m_{12}^2. The term in Eq. 4.3 containing the parameter m_{12}^2 renders the symmetry $\mathcal{Z}$ not exact, because of the non-zero value of m_{12}^2. It breaks $\mathcal{Z}$ however only softly, because the term is only quadratic in the field and not quartic. The Higgs to fermion coupling coefficients relative to the SM ones are listed in Table 4.1. The Higgs to W/Z coupling coefficients are [6]:

$$c_A^{W/Z} = 0 \qquad c_H^{W/Z} = \cos(\beta-\alpha) \qquad c_h^{W/Z} = \sin(\beta-\alpha) \tag{4.10}$$

MSSM versus 2HDM

Type-II 2HDM is compatible to MSSM, hence one reason to investigate the type-II 2HDM. There are however a few differences between the two models. MSSM has only two free parameters at tree level,

	Type-I	Type-II
c_h^u	$\sin(\beta-\alpha)+\cos(\beta-\alpha)/\tan\beta$	$\sin(\beta-\alpha)+\cos(\beta-\alpha)/\tan\beta$
$c_h^{d,l}$	$\sin(\beta-\alpha)+\cos(\beta-\alpha)/\tan\beta$	$\sin(\beta-\alpha)-\cos(\beta-\alpha)\cdot\tan\beta$
c_H^u	$\cos(\beta-\alpha)-\sin(\beta-\alpha)/\tan\beta$	$\cos(\beta-\alpha)-\sin(\beta-\alpha)/\tan\beta$
$c_H^{d,l}$	$\cos(\beta-\alpha)-\sin(\beta-\alpha)/\tan\beta$	$\cos(\beta-\alpha)+\sin(\beta-\alpha)\cdot\tan\beta$
c_A^u	$1/\tan\beta$	$1/\tan\beta$
$c_A^{d,l}$	$-1/\tan\beta$	$\tan\beta$

Table 4.1.: Yukawa coupling coefficients of the neutral bosons h, H and A to up-type quarks (u), down-type quarks (d) and charged leptons (l), in the 2HDM types I and II. These coefficients scale the SM Yukawa couplings as in Eq. 4.11. The fact that the fermions couple to the same or to different scalar doublets sets that the u coefficients are the same in type I as in type-II, and l coefficients are the same as d coefficients. [119]

by convention $\tan\beta$ and m_A, it imposes the h upper bound $m_h \leq \min(m_A, m_Z)\cdot|\cos(2\beta)| \leq m_Z$ and the hierarchies $m_H > \max(m_A, m_Z)$ and $m_{H^\pm} > m_W$. [14]

Alignment to SM

Any extended Higgs sector must include a scalar compatible in mass and couplings to the discovered 125 GeV SM Higgs boson. In 2HDM this is implemented for h, which, according to Eq. 4.8, becomes SM *aligned* via $m_h = 125$ GeV and the limit $\sin(\beta-\alpha)\to 1$.

In the "decoupling" alignment approach [122] $m_h = \mathcal{O}(v)$, while $m_A, m_H, m_H^\pm$ are very heavy, $\gg v$, which enforces $\cos(\beta-\alpha) = \mathcal{O}(v^2/m_A^2)\to 0$.

In the "natural" alignment approach [123] one sets directly $m_h = 125$ GeV and $\sin(\beta-\alpha)\sim 1$. However, in type-II, the alignment could become *delayed* if $\tan\beta$ is high enough such that $|\cos(\beta-\alpha)|\tan\beta \sim \mathcal{O}(1)$, as the couplings of h to the down-type quarks would deviate from the SM value of 1 (see Table 4.1).

2HDM Benchmark Employed

In this analysis the A and H scalars are investigated in the FCNC suppressed type-II 2HDM model. The angles are chosen such that $\tan\beta > 0$ and $\sin(\beta-\alpha)\geq 0$. The parameter λ_5 is chosen zero, which together with Eq. 4.7 sets the parameter $m_{12}^2 = m_A^2\tan\beta/(1+\tan^2\beta)$. Masses are degenerate $m_A = m_H = m_{H^\pm}$ and the natural alignment $\sin(\beta-\alpha) = 1.0$ is employed, which causes both H and A to be boson-phobic and decay only to fermions. The low $\tan\beta < 10$ region is investigated, in order to enhance the decay to top quark pairs and to suppress the decay to bottom quark pairs. The region $\tan\beta \leq 0.3$ is avoided, because the Yukawa couplings to the top quark form Table 4.1 would become non-perturbative. [119]

In this thesis the 2HDM parameters are provided as recommendations by the ATLAS BSM Higgs Group, which themselves follow the LHC Higgs Cross-Section WG recommendations [67, 124]. The cross-sections are calculated for $\sqrt{s} = 8$ TeV at NNLO accuracy in QCD with SusHi [125, 126] and 2HDM Calculator [127].

4.1.3. Production and Decay of A and H

Figure 4.1 and Figure 4.2 show the production cross-sections, respectively decay BR of A and H in type-II 2HDM at low $\tan\beta$. In comparison to the SM modes in Figure 2.2 at high masses, the processes hierarchy is maintained, with the difference that the VB modes are suppressed, including the decay to $\gamma\gamma$ via a W loop, since A/H do not couple to VB. The decay to gg has too high background at the LHC, thus ignored here.

The dominant production mechanism is gluon fusion, followed by associated A/H production with $b\bar{b}$[3]. The cross-section decreases with the scalar's mass point. At higher $\tan\beta$ however, $b\bar{b}A/b\bar{b}H$ are not negligible any more.

The dominant decay channels are in order $t\bar{t}$, $b\bar{b}$ and $\tau\bar{\tau}$, with ratios $c_t^2 m_t^2/c_b^2 m_b^2$ between the first two and $3m_b^2/m_\tau^2$ between the last two (Eq. 4.17). Since the top quark is the heaviest fermion, A/H predominantly decay to $t\bar{t}$ above the threshold $2m_t$=345 GeV, except for the higher $\tan\beta$ region in type-II, where $b\bar{b}$ starts to dominate.

Figure 4.3 depicts the percentage decay widths of A and H relative to their masses. A higher $\tan\beta$ suppresses the coupling to t, narrowing $\Gamma_{t\bar{t}}$ (and Γ_{total} in the low $\tan\beta$ region). Requiring $\Gamma < 20\%$, in order to see definite signal peaks in the data, corresponds to $\tan\beta > 0.5$.

4.2. Top/Bottom Loop Structure in $gg \to A/H$

In type-II 2HDM, the highest production and decay rate of A/H in the low $\tan\beta$ regime have thus $gg \to A/H \to t\bar{t}$. As in the SM (Section 2.6.6), the gluons fuse via virtual loops of heavy quarks, namely top and more rarely bottom. At the $\sqrt{s} = 8$ TeV pp collisions from the LHC, gg fusion dominates $t\bar{t}$ production with 80% [51] and represents the highest background to the aforementioned signal.

Figure 4.4 depicts the background and signal $t\bar{t}$ final state diagrams. All processes with the same final and initial state exhibit interference, hence in this case the SM $gg \to t\bar{t}$ and the $gg \to A/H \to t\bar{t}$. The intermediate loop in the gg fusion presents an imaginary phase in the amplitude (Eq. 4.12) which significantly enhances the interference effect, making it non-negligible. The Breit-Wigner shape of the pure resonance signal is distorted to a peak-dip structure around the resonance mass.

The colour state (Section 2.3.4) is a decisive interference factor as well. The gg SM s-channel (Figure 4.4b) is colour-octet, since the intermediate gluon is colour-octet. The gg SM t-channel (Figure 4.4c) is colour-octet or colour-singlet, while the signal process (Figure 4.4d) is colour-singlet, since A/H is colour-singlet. Hence the signal is interfering with the SM gg colour-singlet t-channel. The SM s-channel and the SM colour-octet t-channel interfere as well, though contributing only to the background. The interference between A and H is negligible and ignored.

[3] Calculated in both four-flavour scheme (4FS), where b is not considered parton, or , conversely, 5FS.

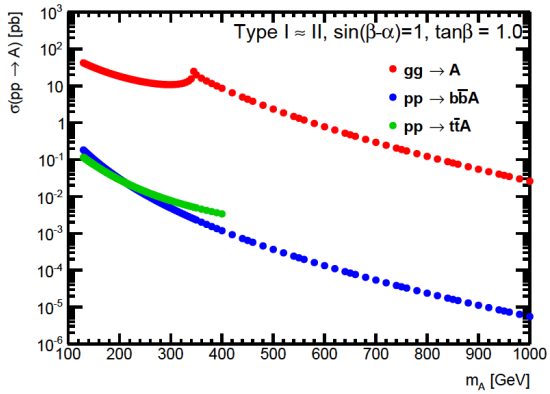

(a) A, $\tan\beta = 1.0$

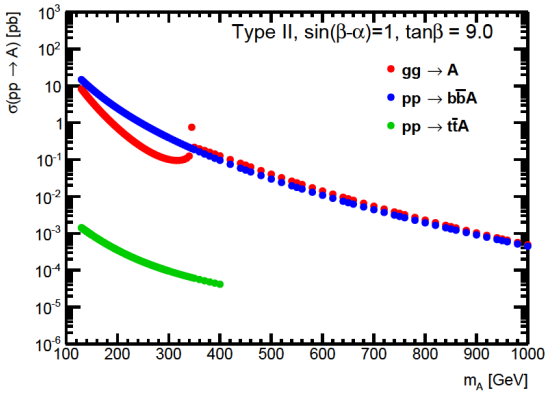

(b) A, $\tan\beta = 9.0$

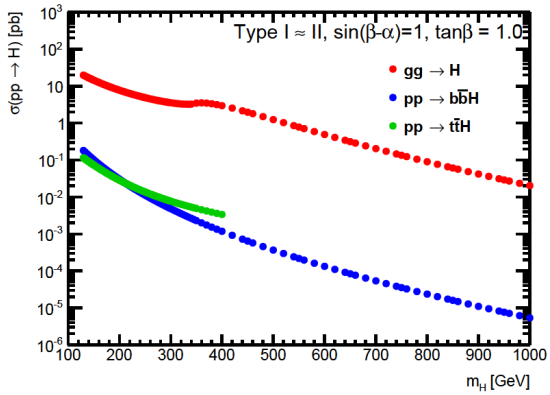

(c) H, $\tan\beta = 1.0$

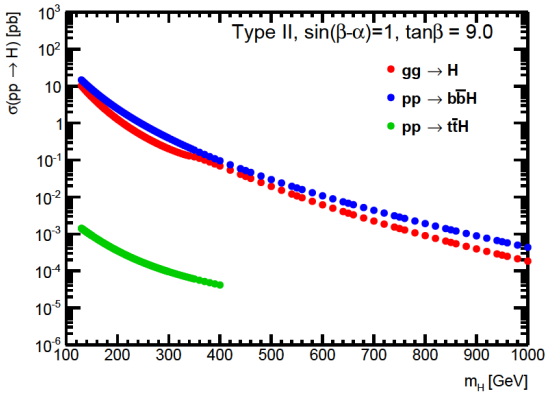

(d) H, $\tan\beta = 9.0$

Figure 4.1.: Production cross-sections of A (first row) and H (second row), in the investigated type-II 2HDM, with $\sin(\beta - \alpha) = 1.0$. For masses above 400 GeV and low $\tan\beta$ the gluon fusion mode dominates.

Comparisons with type-I are provided for the record:
(Left) For $\tan\beta = 1$ type-I and type-II have comparable cross-sections because in Table 4.1 the type-I and type-II couplings are identical at $\tan\beta = 1$.
(Right) For $\tan\beta = 9$ the $b\bar{b}A/b\bar{b}H$ production modes start to dominate (while for type-I there is no change from the left column).

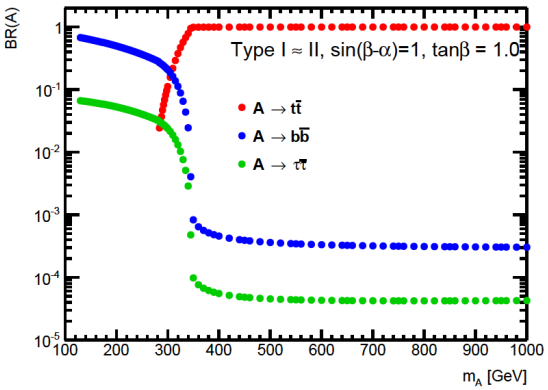

(a) A, $\tan\beta = 1.0$

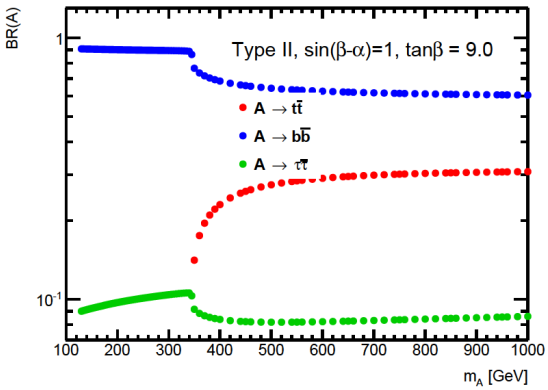

(b) A, $\tan\beta = 9.0$

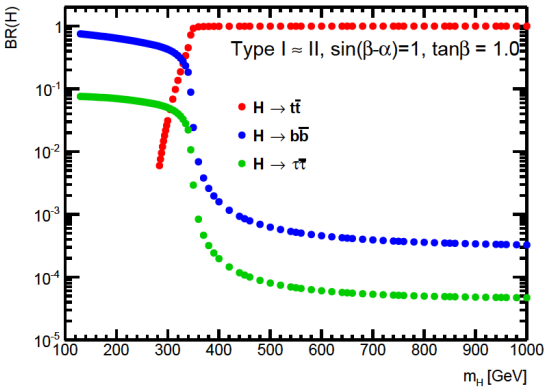

(c) H, $\tan\beta = 1.0$

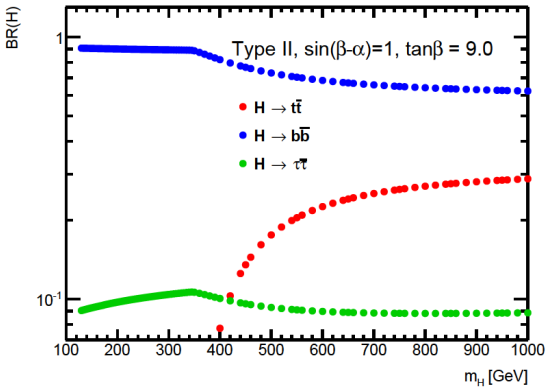

(d) H, $\tan\beta = 9.0$

Figure 4.2.: Branching ratios of A (first row) and H (second row), in the investigated type-II 2HDM, with $\sin(\beta - \alpha) = 1.0$. For masses above 400 GeV and low $\tan\beta$ the $t\bar{t}$ decay mode dominates.

Comparisons with type-I are provided for the record:
(Left) For $\tan\beta = 1$ type-I and type-II have comparable BR because in Table 4.1 the type-I and type-II couplings are identical at $\tan\beta = 1$.
(Right) For $\tan\beta = 9$ the $b\bar{b}$ decay mode starts to dominate (while for type-I there is no change from the left column).

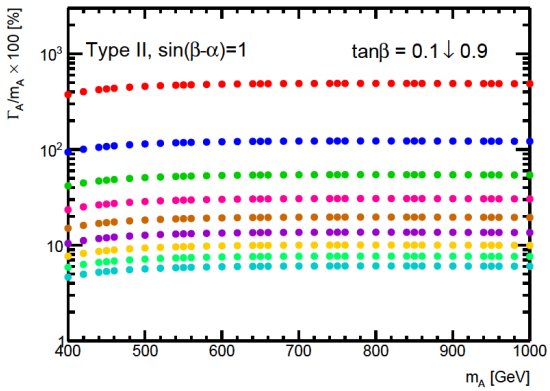

(a) A, $\tan\beta = 0.1 - 0.9$ in steps of 0.1

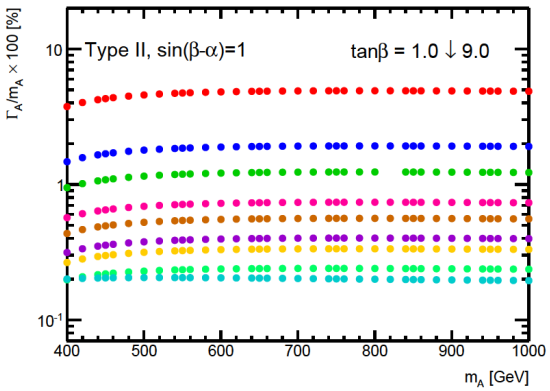

(b) A, $\tan\beta = 1 - 9$ in steps of 1

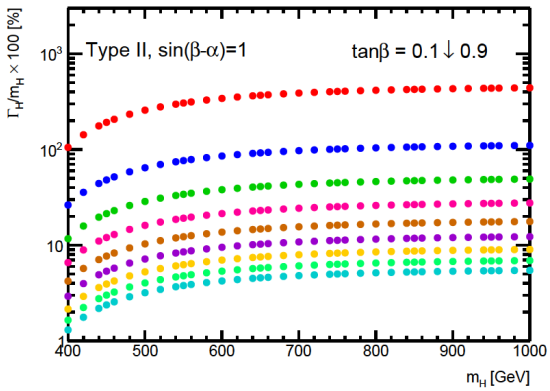

(c) H, $\tan\beta = 0.1 - 0.9$ in steps of 0.1

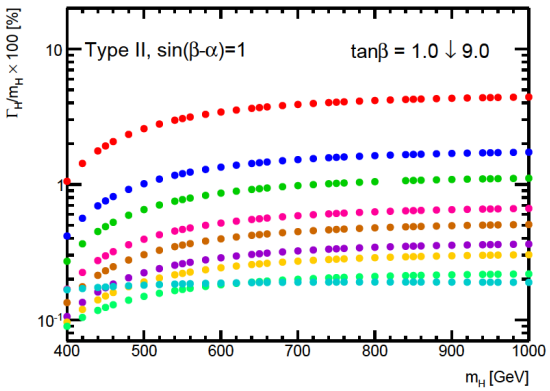

(d) H, $\tan\beta = 1 - 9$ in steps of 1

Figure 4.3.: Percentage decay widths of A (first row) and H (second row) relative to their mass, in type-II 2HDM with $\sin(\beta - \alpha) = 1.0$, for $\tan\beta = 1$ (left) and $\tan\beta = 9$ (right). The width decreases with $\tan\beta$.

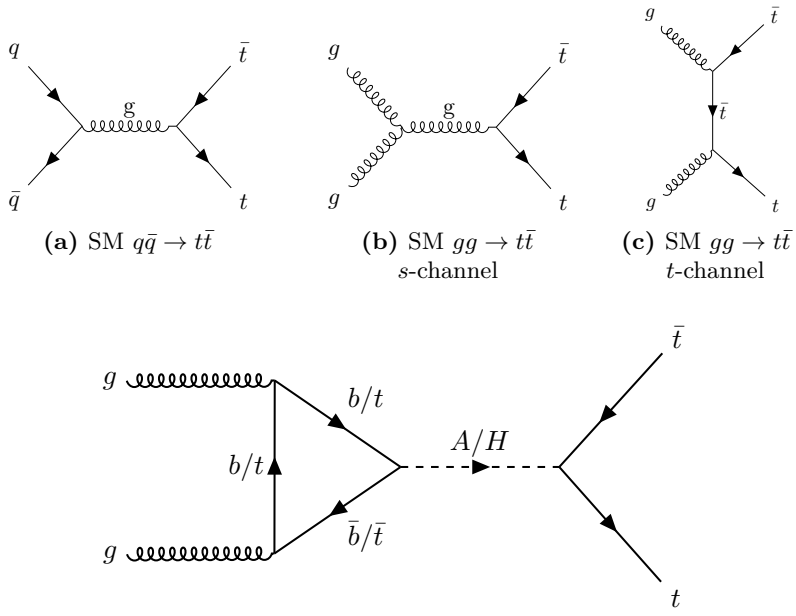

(a) SM $q\bar{q} \to t\bar{t}$ **(b)** SM $gg \to t\bar{t}$ s-channel **(c)** SM $gg \to t\bar{t}$ t-channel

(d) $gg \to A/H \to t\bar{t}$

Figure 4.4.: Leading order $t\bar{t}$ final state diagrams: (a) background SM-QCD $q\bar{q}$ annihilation, (b) and (c) background SM-QCD gg fusion, where the t-channel has an additional contribution with the gluons crossed as well, (d) signal gg fusion with intermediate A/H.
(b) and (c) heavily interfere with (d), while (a) is small and not relevant for this analysis.

The $Z\prime \to t\bar{t}$ resonance investigated in [22] is produced via $q\bar{q}$ annihilation[4], hence with direct coupling to the top quark and without intermediate loop, which renders the interference to the SM $t\bar{t}$ negligible.

The following is a description of the *Higgs Effective Couplings Form Factor Model* [129] of couplings and amplitudes applied in this analysis, in order to compute scalars with loop-induced gg fusion. The reason this model is employed is that the MadGraph5 event generator (Section 4.3) can only model interference between tree-level processes. Hence the loop in the signal production needs to be replaced by an equivalent vertex. The model is based on phenomenology from [2, 130] and is further applied in computations in [131, 132].

As in Section 2.6.5, the tree-level scalar couplings to quarks are proportional to the quark mass:

$$\begin{aligned} Af\bar{f} &: \quad \gamma^5 \, \frac{c_f m_f}{v} \\ Hf\bar{f} &: \quad -i \, \frac{c_f m_f}{v} \end{aligned} \tag{4.11}$$

, where $c_f = y_f^m / m_f = y_f \, v/\sqrt{2} m_f$ is the coupling coefficient from Table 4.1, while y_f^m and y_f are the input Yukawa couplings in the event generator. The γ^5 factor is an indicator for pseudoscalar, as in Table 2.3.

The loop-level couplings of four-momentum p scalars to the four-momentum $p_{1,2}$ gluons are:

[4] Yang's theorem [128] prohibits gluon fusion to produce a resonance of total angular momentum 1.

$$
\begin{aligned}
A(p)g^{a,\mu}(p_1)g^{b,\nu}(p_2) \;:\; & \frac{i\,g_s^2}{8\pi^2 v}\left[c_t\frac{f(\tau_t)}{\tau_t}+c_b\frac{f(\tau_b)}{\tau_b}\right]\epsilon^{\mu\nu\rho\sigma}p_{1,\rho}p_{2,\sigma}\,\delta^{ab} \\
H(p)g^{a,\mu}(p_1)g^{b,\nu}(p_2) \;:\; & \frac{i\,g_s^2}{12\pi^2 v}\Big[c_t A_S(t)+c_b A_S(b)\Big](p_1^\mu p_2^\nu - p_1\,\cdot\,p_2 g^{\mu\nu})\delta^{ab},
\end{aligned}
\tag{4.12}
$$

where a, b are the gluon colour indices, g_s the weak gauge coupling, ϵ the Levi-Civita tensor, $\tau_i = p^2/4m_i^2 \equiv s/4m_i^2$ and $\beta \equiv (1-4m_i^2/s)^{1/2}$ is the velocity of the top quarks in the center-of-momentum frame. The square brackets include top/bottom loops with the form factors:

$$
\begin{aligned}
A_S(\tau_f) &= \frac{3}{2\tau^2}\left(\tau+(\tau-1)f(\tau)\right) \\
f(\tau) &= \begin{cases} \arcsin^2(\sqrt{\tau}), & \tau \le 1 \\ -\frac{1}{4}\left[\log\left(\frac{1+\sqrt{1-\tau^{-1}}}{1-\sqrt{1-\tau^{-1}}}\right)-i\pi\right]^2, & \tau > 1 \end{cases}
\end{aligned}
\tag{4.13}
$$

The threshold condition implies $\tau_t > 1$, which yields imaginary coupling components to t.

In the following, the pure signals $gg \to A/H \to t\bar{t}$ are labelled as S (A or H), the SM-QCD background continuum $gg \to t\bar{t}$ as B, and their interference as I (A and H do not interfere with each other). Given Eq. 2.7, the cross-section of the inclusive $gg \to t\bar{t}$ ($S+B+I$) can be broken down as a linear sum. For the scalar H it has the form [2]:

$$
\begin{aligned}
\frac{d\sigma}{dz} =& \frac{\alpha_s^2 G_F^2 c_t^2 m_t^2 s^2}{1536\pi^3}\beta^3\left|\frac{\sum_f c_f A_S(\tau_f)}{s-m_H^2+im_H\Gamma_H(s)}\right|^2 && H \\
&-\frac{\alpha_s^2 G_F c_t m_t^2 s}{384\pi\sqrt{2}}\beta^3\left(\frac{1}{p_1\,\cdot\,p_3}+\frac{1}{p_2\,\cdot\,p_3}\right)\mathrm{Re}\left[\frac{\sum_f c_f A_S(\tau_f)}{s-m_H^2+im_H\Gamma_H(s)}\right] && I \\
&+\frac{d\sigma_{QCD}}{dz} && B
\end{aligned}
\tag{4.14}
$$

, where $p_{3,4}$ are the four-momentum of the outgoing top quarks, Γ_H the total H width, and z the cosine angle between a gluon and the top quark. Similarly for the pseudoscalar A [2]:

$$
\begin{aligned}
\frac{d\sigma}{dz} =& \frac{3\alpha_s^2 G_F^2 c_t^2 m_t^2 s^2}{2048\pi^3}\beta\left|\frac{\sum_f c_f f(\tau_f)/\tau_f}{s-m_A^2+im_A\Gamma_A(s)}\right|^2 && A \\
&-\frac{\alpha_s^2 G_F c_t m_t^2 s}{256\pi\sqrt{2}}\beta\left(\frac{1}{p_1\,\cdot\,p_3}+\frac{1}{p_2\,\cdot\,p_3}\right)\mathrm{Re}\left[\frac{\sum_f c_f f(\tau_f)/\tau_f}{s-m_A^2+im_A\Gamma_A(s)}\right] && I \\
&+\frac{d\sigma_{QCD}}{dz} && B
\end{aligned}
\tag{4.15}
$$

Within the loop there is a sum over the top and bottom contributions. The cross-section of the continuum QCD production is [2]:

$$
\frac{d\sigma_{QCD}}{dz} = \frac{\pi\alpha_s^2}{12s}\beta\left(\frac{s^2}{p_1\,\cdot\,p_3 p_2\,\cdot\,p_3}-9\right)\left[\frac{(p_1\,\cdot\,p_3)^2}{s^2}+\frac{(p_2\,\cdot\,p_3)^2}{s^2}+\frac{m_t^2}{s}-\frac{m_t^4}{4p_1\,\cdot\,p_3 p_2\,\cdot\,p_3}\right]
\tag{4.16}
$$

The partial decay width of the Higgs boson into fermion pairs, at leading order, is as in SM [14]:

$$\begin{aligned}\Gamma(H \to f\bar{f}) &= \frac{G_F N_c}{4\pi\sqrt{2}} m_H c_f^2 m_f^2 \beta^3 \\ \Gamma(A \to f\bar{f}) &= \frac{G_F N_c}{4\pi\sqrt{2}} m_A c_f^2 m_f^2 \beta,\end{aligned} \tag{4.17}$$

where N_c is the colour factor (3 for quarks, 1 for leptons) and c_f the coupling coefficient, 1 in SM. Hence A is wider than H, as one can see in the pure signal processes in Figure 5.2 and 5.3. Different Γ and different form factors in Eq. 4.14 and 4.15 entail that A and H interfere differently to B ($A+I$ and $H+I$ in the same figures).

The figures show as well that the $S+I$ shape is highly dependent on the $(m_{A/H}, \tan\beta)$ parameter points. The dip is located around the mass point, migrating hence with it, while the peak is located around the SM $t\bar{t}$ peak. The cross-section of S and the magnitude of their peak decrease with $\tan\beta$ or with the mass point. Similarly decrease the magnitudes of the $S+I$ peak and dip. The resonance decay width decreases with $\tan\beta$, which can be seen at $S+I$ as a narrowing of the dip, while the peak is a broader remnant of B.

4.3. Setup in MadGraph5_aMC@NLO - NOVELTY

The signal samples in this thesis are modelled with the MadGraph5_aMC@NLO event generator, version 2.0.1 [133, 134] and with the model described in Section 4.2. Albeit the generator can, as its name states, compute at NLO, the top loop and the interference can be computed only at LO, hence all signal samples are produced at LO.

The setup techniques are a product of discussions with the MadGraph5 authors [135] and are exemplified in Appendix B.1. What is chosen in the analysis are the m_A, m_H and $\tan\beta$ parameter points. These points determine the couplings to t and b, which are calculated based on their Yukawa coefficients from Table 4.1 as $m_{t,b} \cdot c_{t,b}$. They determine as well via Eq. 4.17 the total decay width of the scalars, values provided by the ATLAS BSM Higgs Group. Since there is only one input Yukawa couplings set, A and H must be generated separately. The renormalisation and factorisation dynamic scales are set to $\sqrt{\sum_{\text{decay products}}(p_{\text{T}}^2 + m^2)}$. A k-factor scales the MadGraph5 cross-sections to the computed one at NNLO accuracy, as related in Section 5.2.3.

Narrow Width Approximation

MadGraph5_aMC@NLO computes the cross-section of $\Gamma \ll M$ resonances using the narrow-width approximation NWA [136]. The massive resonance is produced on-shell at its pole mass, the cross-section scaled with the BR and the invariant mass smeared to the Breit-Wigner shape. NWA deviates hence from the off-shell results with an $\mathcal{O}(\Gamma/M)$ error. The error affects the interference as well due to the LO approach and would clear away when the interference is calculated at NLO.

4.3.1. Generation of Signal with Interference

Given that pure S cannot be separated from B, one needs to describe the inclusive $S+B+I$ in order to test the S hypothesis. The $S+I$ event rate relative to B decreases however highly with the scalar

mass point (Figure 4.6). Thus an $S+B+I$ production would require for each signal parameter point very large statistics, $\mathcal{O}(\gg 100\ M)$ events, such that $S+I$ overcomes the fluctuations of B. Moreover, a B production in MadGraph5 is not needed, because Powheg+Pythia6 provided already the most reliable SM $t\bar{t}$ sample at higher NNLO+NNLL corrections, tuned to agree well with data and applied in Ref. [22] as well.

Therefore, a method called **"diagram removal scheme"** or ***S + I* "direct"**, has been devised to extract $S+I$ from $S+B+I$ in MadGraph5, a **NOVELTY** brought by this thesis. Given Eq. 4.14 and 4.15, MadGraph5 code is modified to remove the B amplitude from the total amplitude of $S+B+I$, on an event-by-event basis. $S+B+I$ is to be generated as usual, but now it results to $S+I$ instead, with both positive and negative event weights, that form the characteristic peak-dip shape in the $m_{t\bar{t}}$ distribution. The sample size needed decreases considerably to 1 M events, an amount however still a few order of magnitudes higher than that of a pure S, in order to allow the generator to converge in this very challenging process. $\mathcal{O}(100\ K)$ events are extracted to be passed to the full detector simulation.

Yet, $S+I$ does not represent physical states, it is only a technical trick. The "direct" aproach is validated by subtracting reconstructed histograms between one very large $S+B+I$ sample of $\mathcal{O}(\gg 100\ M)$ events and one B, approach called **"diagram subtraction scheme"** or **"indirect"**. Figure 4.5 shows that both generations converged with correct $\mathrm{BR}_{t\bar{t}}$ and that their $m_{t\bar{t}}$ reconstructed at generator level agree well, with a small difference taken as systematic uncertainty in Section 5.7.5. More comparisons are in Appendix B.2.

The "direct" approach is used to generate the actual $S+I$ effect, which is overlaid in the data analysis to the Powheg+Pythia6 background.

4.3.2. Comparison between Signal with Interference and Background

Figure 4.6 depicts at LO and parton (generator) level the $S+I$ distributions in "direct" approach, stacked to a SM $pp \to t\bar{t}$ MadGraph5 sample. $\tan\beta$ is such chosen to determine $\Gamma^{A/H}_{\mathrm{total}}$ to $\sim$ 1%, 5% and 10% of the mass point. Resonance masses cannot go below 400 GeV, because of the $2m_{t\bar{t}}$ threshold and because NWA badly models the region right above the threshold. For resonance masses above 800 GeV the cross-sections are too low, however in the $m_{t\bar{t}}$ slices of the dip, the ratio between the $S+I$ event rate and the B one does not deteriorate much with the mass point.

4.4. Studies of Different Generation Configurations - NOVELTY

4.4.1. Spin-Parity Correlations in Top Quark Decays

The decay products of t and $\bar{t}$ manifest important spin correlation effects, that arise because the top quark decays before spin decorrelation occurs through strong interaction effects [51]. They have been seen at ATLAS at the expected level in the dilepton final state [137] but are also expected in fully hadronic and semileptonic decays. Since these correlations can impact the detector acceptance and resolution, it is important that they be correctly described in the Monte Carlo simulations.

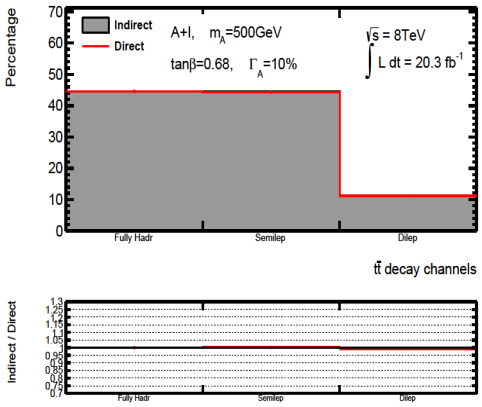

(a) $A + I$, $t\bar{t}$ decay BR

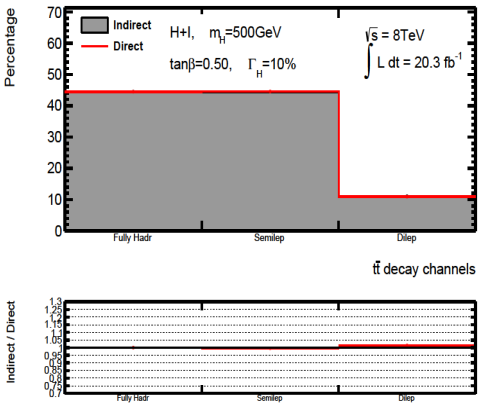

(b) $H + I$, $t\bar{t}$ decay BR

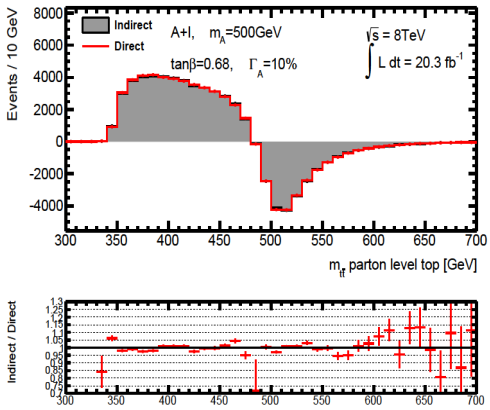

(c) $A + I$, $m_{t\bar{t}}$

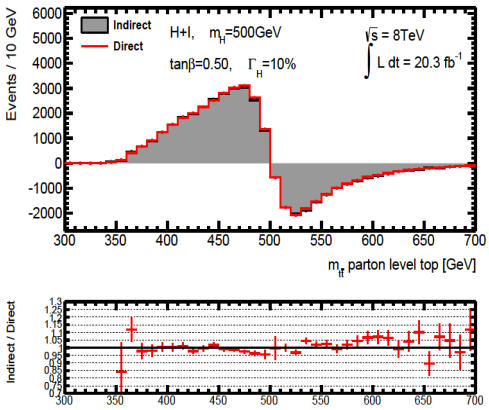

(d) $H + I$, $m_{t\bar{t}}$

Figure 4.5.: Comparison between "indirect" and "direct" approach to generate $S + I$ for A (left) and H(right), at scalar mass points 500 GeV and total decay widths of 10% from the mass point. The two approaches show good agreement and the $t\bar{t}$ BR shows correct values.

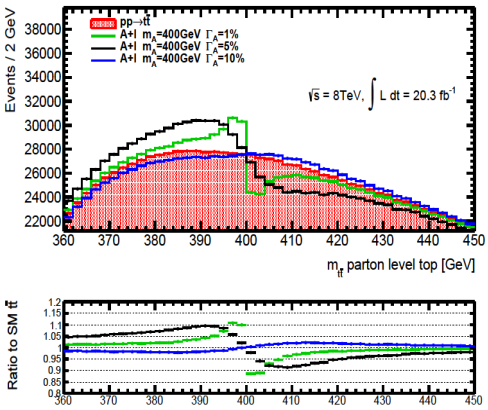

(a) $m_A = 400$ GeV

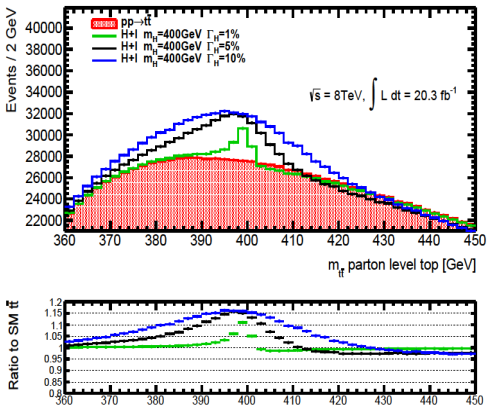

(b) $m_H = 400$ GeV

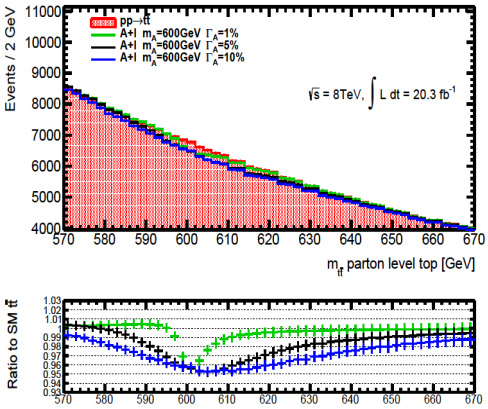

(c) $m_A = 600$ GeV

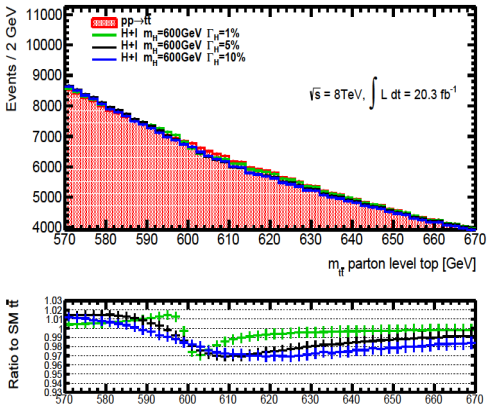

(d) $m_H = 600$ GeV

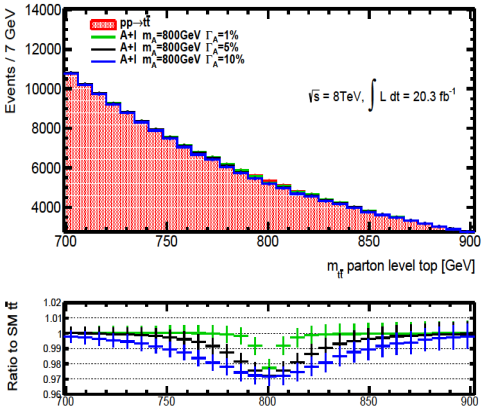

(e) $m_H = 800$ GeV

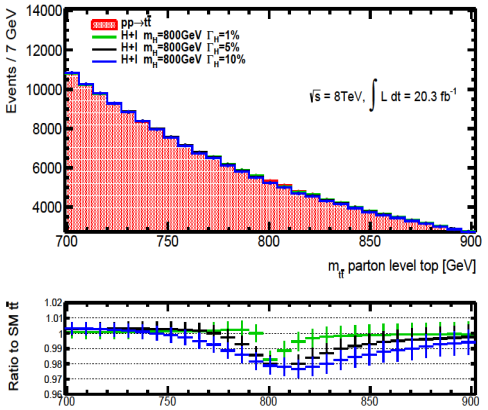

(f) $m_A = 800$ GeV

Figure 4.6.: $m_{t\bar{t}}$ distribution of $gg \to A/H \to t\bar{t}$ and interference to SM $pp \to t\bar{t}$, stacked to the SM distribution, for scalar mass points of 400, 600 and 800 GeV and decay width 1%, 5% and 10% from the mass point.

The correlations reflect the spin-parity of intermediate resonances, hence $S + I$ must be validated against them. The official SM $t\bar{t}$ sample is known to contain the correct correlations.

Validation of the Resonance Spin

The Collins-Soper angle θ^* [138] is sensitive to the spin of the intermediate resonance X in $pp \to X \to t\bar{t}$. It is the angle between the protons momenta axis in the $t\bar{t}$ rest frame (bisecting axis if not collinear) and t momentum. Similarly is calculated for the $\bar{t}$. The angle is equivalent to the one between $t(\bar{t})$ and the beam axis, if ISR is missing.

It can be proved that the SM amplitude $|\mathcal{M}(pp \to t\bar{t})|^2$ depends on $\cos^2\theta^*$, while $|\mathcal{M}(pp \to X \to t\bar{t})|^2$ for a scalar X does not depend on θ^* [3]. Figure 4.7b confirms that the angle is flat for both A and H, hence spin-0 resonances are indeed generated.

Validation of the Resonance Parity

It has been shown in Ref. [139–141] that the polarisation of the top quark is fully correlated with the direction of its down-type fermion decay products f_d (e, μ or c/s jets). Moreover, the angle $\phi*$ between f_d^+ and f_d^- in the $t\bar{t}$ decay should discriminate between a pseudoscalar and a scalar [142][5]. To calculate ϕ^*, perform a boost on all objects to the $t\bar{t}$ rest frame, then boost f_d^+ and f_d^- to the rest frame of the new top quarks, as in Ref. [3]. Figure 4.7c validates the parity of A and H.

Figure 4.8 illustrates the ϕ^* distribution after showering a $S + I$ sample in Pythia6. When the top quarks are not decayed in MadGraph5, Pythia6 decays them without preserving their spin correlations, flattening ϕ^*. Hence the top quarks must be decayed in MadGraph5.

4.4.2. Showering Configuration

Since the SM $t\bar{t}$ amplitude is removed in the "direct" generation of $S + I$, the chosen configuration for parton showering and hadronisation of $S + I$ must approximate the Powheg+Pythia6 $t\bar{t}$ sample normalised at NNLO+NNLL. It is not possible to generate processes at such high correction orders, hence a few other shower configurations (Table 4.2) are tested for best approximation. Adding extra jets would improve the result, though it would require a parton-jet matching and merging algorithm. This is complicated considering the varying jet count in top decays.

Figure 4.9 and Appendix B.3 illustrate truth jets level comparison between the shower configurations. The object selection and reconstruction is similar to the analysis on data (Section 5.3): $\Delta R = 0.4$ jets, leptons and missing energy $E_{\mathrm{T}}^{\mathrm{miss}}$, all with $p_{\mathrm{T}} > 25$ GeV and $|\eta| < 2.5$. Jets are matched within $\Delta R(j, q) < 0.2$ to the truth quarks originating from W and t. Electrons are subtracted from their matched lepton jets.

[5] In spin correlation studies ϕ^* is reconstructed in data between e/μ, as leptons have strong signatures. Hadron jets cannot be easily tagged as up/down type. However, employing that down-type non b-jets usually have a smaller p_T than the up-type, improves the spin discrimination. [142]

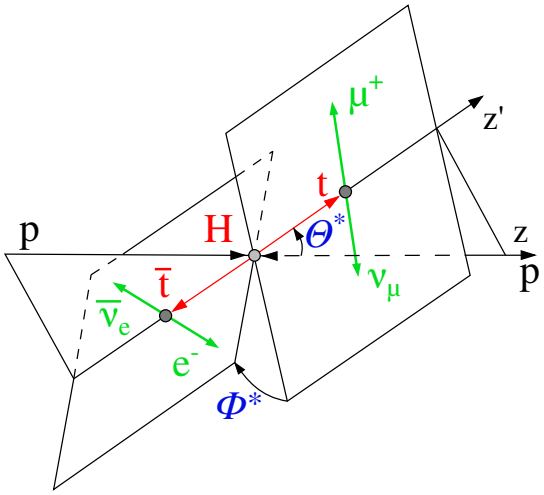

(a) Angles correlating spin and parity in $t\bar{t}$

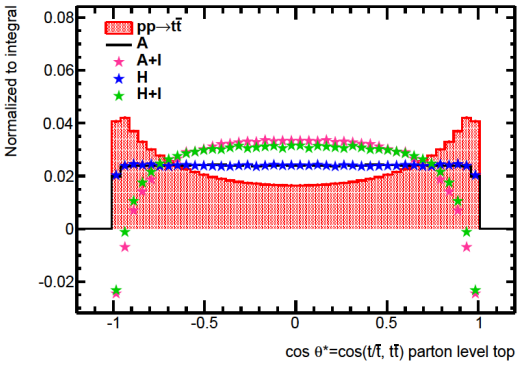

(b) θ^*

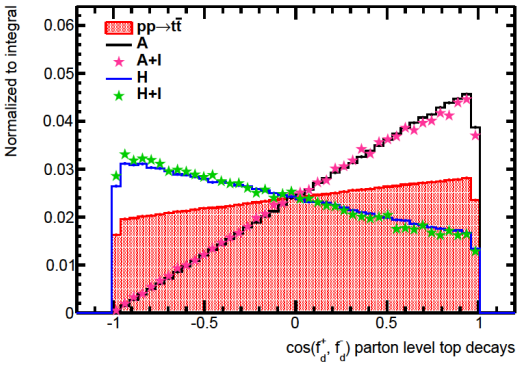

(c) $\phi^*(f_d^+, f_d^-)$

Figure 4.7.: Distributions of spin-relevant angles (a), compared between S, $S+I$ and the SM $t\bar{t}$. (b) The Collins-Soper angle θ^* is as in theory flat for scalars and inverse parabolic for SM, yielding $S+I$ parabolic. (c) The ϕ^* angle discriminates, as expected, between scalar and pseudoscalar, but is identical between S and $S+I$ (the lower values in the -1 and 1 bins are a numerical margin effect).
All distributions are in good agreement with Figures 14, 15 and 18 from [3].

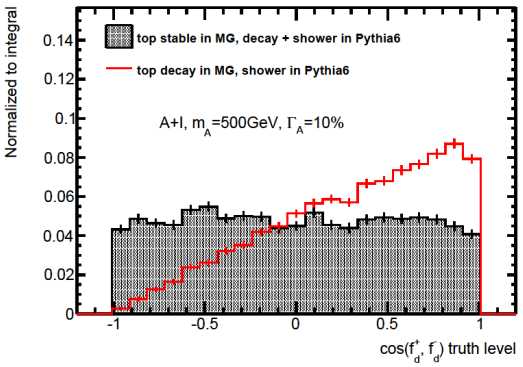

Figure 4.8.: The angle between down-type fermions in $t\bar{t}$ decay is flattened by PYTHIA6 if the top quarks are not decayed in MADGRAPH5.

	Event and shower generator	Cross-section accuracy	Remarks
red	POWHEG-BOX [143–146] + PYTHIA6 [147] Perugia 2011c [148]	NNLO+NNLL [68–74]	centrally produced, tuned to data, applied in [22]
green	MADGRAPH5 v.1 + PYTHIA6 Perugia 2011c	LO, [0–3] extra jets	centrally produced, MLM jet matching and merging [149], t stable in MG
black	MADGRAPH5 v.2 + PYTHIA6 Perugia 2011c	LO	own production, t decayed in MADGRAPH5
blue	MADGRAPH5 v.2 + PYTHIA8 [150]	LO	own production, t decayed in MADGRAPH5

Table 4.2.: SM $pp \to t\bar{t}$ distributions investigated for showering configurations, all with semileptonic+dileptonic $t\bar{t}$ decay and PDF set CT10 [151]. The colour code for Figure 4.9 is provided.

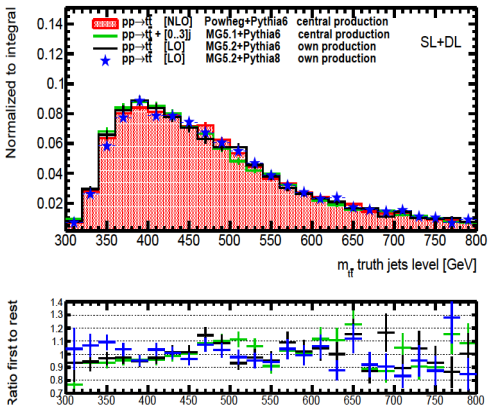

(a) $m_{t\bar{t}}$

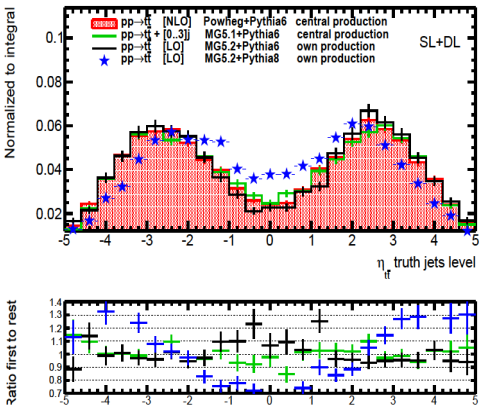

(b) $\eta_{\mathrm{T},t\bar{t}}$

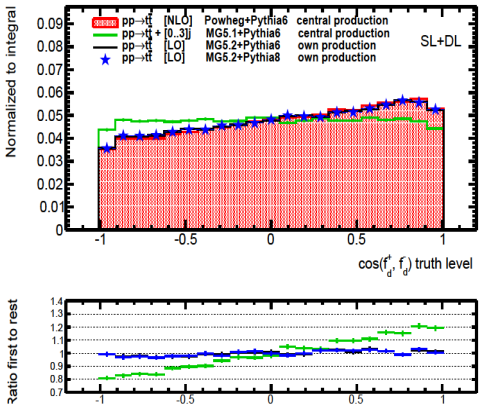

(c) $\cos\left(f_d^+, f_d^-\right)$

Figure 4.9.: Comparison between various $pp \to t\bar{t}$ showering configurations in the semileptonic+dileptonic $t\bar{t}$ decay channels, in order to validate a configuration for the showering of $S + I$.

The MadGraph5 + Pythia8 (blue) configuration is highly mis-matched. The own MadGraph5 + Pythia6 (black) production is in very good agreement with Powheg+Pythia6 (red) even without extra jets, both maintaining spin correlations as well (Figure 4.9c). In conclusion, $S + I$ should be generated in MadGraph5 at LO, with top quarks decayed, without extra jets, and consequently showered and hadronised in Pythia6 with Perugia 2011c tune.

Chapter 5.

Data Analysis Setup

This chapter describes how the data, signal and background samples are passed through the physics analysis chain. The reconstruction challenges of various $t\bar{t}$ decay channels and the chosen signal signature are described in Section 5.1. The employed dataset and simulated samples are listed in Sections 5.2 and 5.5. They are processed by the same *online trigger* and *offline* algorithms, from which the latter are described in the following sections. Physics objects in the form of tracks, electrons, muons, jets and missing transverse momentum are reconstructed and selected in Section 5.3. Section 5.4 describes how the final physical observable, the invariant mass $m_{t\bar{t}}$ of the candidate top quark pairs, is reconstructed. Section 5.6 lists various corrections applied to the Monte Carlo (MC) prediction, in order to bring it in agreement with the data. The effects of experimental and modelling systematic uncertainties on the reconstructed $m_{t\bar{t}}$ are described in Section 5.7.

The samples and analysis procedures follow with minor variations the ones of Ref. [22], which are described in more detail in the ATLAS internal Ref. [152–154]. The physics objects are reconstructed with algorithms and correction scale factors provided by the official ATLAS software, or, where explicitly mentioned, developed in this analysis according to official recommendations. The selection algorithms are developed in this analysis.

5.1. Signal Signature

This section describes the reconstruction challenges the $t\bar{t}$ event face, in order to motivate the choice for the $t\bar{t}$ semileptonic decay channel, which is presented at the end of the section.

5.1.1. Top Quark Pairs Reconstruction Challenges

High Background from QCD Jets

A $t\bar{t}$ event has hadronic jets fragmented from the quark decay products of the top quarks. The event has extra jets as well, in the form of initial state radiation ISR or final state radiation FSR[1].

At LHC, for each SM $t\bar{t}$ event there is however a very large background of $\mathcal{O}(10^9)$ events with hadronic multijets (QCD) alone (Figure 2.1 in Ref. [5]). Against this high background the $t\bar{t}$ events can be nonetheless discriminated with kinematic cuts: the colliding partons carry no p_{T} (if disregarding the ISR), hence p_{T} and η can be safely used as cuts against the QCD background[2];

[1] Quarks and gluons radiation is called ISR if it is emitted by the incoming particles before the interaction, or FSR if emitted by the decay products.

[2] Kinematic cuts on the z axis are not practical, due to the parton distribution functions on p_z.

the high mass of the top quark yields decay products with high p_{T}, hence low $|\eta|$ as well, while the QCD background jets are soft, hence low in p_{T} and high in $|\eta|$; the heavy intermediate A/H signal will Lorentz boost in p_{T} the top quarks even more, highly collimating their decay products.

The physics objects will therefore require in Section 5.3 high E_{T} or p_{T} and low $|\eta|$, for which reason the central ATLAS region was designed for precision measurements as well.

Prompt, non-Prompt and Fake Leptons

In this analysis, **prompt** leptons are defined as real (in contrast to fake) leptons originating as direct decay products of the top quark through a leptonically decaying W boson. The other real leptons are called **non-prompt** and originate from semileptonic decays within jets of heavy flavoured $b/c-$hadrons or light-flavoured hadrons, such as kaons and charged pions (which decay mostly to muons). All these hadrons have as well much longer mean lifetimes ($10^{-8} - 10^{-12}$ s) in comparison to W/t (10^{-25} s), hence their semileptonic decay products originate later in the decay chain. Non-prompt electrons originate from photon conversions as well.

Instrumental **fake electrons** are represented by hadronic jets with low mass (hence with the risk to be associated to the low $m_e \sim 0$) that mimic the electrons requirements to shower significantly in the EM calorimeter and to match a track, hence mis-identified as electrons. Common sources of fake electrons are $\pi^0 \to \gamma\gamma$, since π^0 have low mass, γ convert to e^+e^- that yield tracks, tracks are often miscounted or the track going into the opposite ϕ hemisphere is skipped, and γ/e have EM calorimeter signature. Very energetic hadronic jets punching through to the muon spectrometer lead to **fake muons**.

Fake leptons and non-prompt mis-identified as prompt leptons deteriorate the lepton reconstruction purity[3].

Choice of Semileptonic $t\bar{t}$ Decay Channel

The properties and decay channels of the top quarks have been already detailed in Section 2.7.

The **fully hadronic** channel has the advantage of lacking the neutrino, hence the four-momenta of the six jets from the top quark decay products can be fully determined. The bad hadronic energy resolution can be especially improved via the W and t mass constraints. The channel is however most affected by the QCD background and is difficult to trigger as well, because of a lack of prompt leptons. Even though to measure $m_{t\bar{t}}$ the final states are just added up, the jet combinatorics poses an impediment at identifying intermediate particles or at measuring spin information [3, 155].

The **dileptonic** channel has the advantage of low QCD background and of two-lepton triggers. It has however only four visible final states, two b-jets and two leptons. The two invisible neutrinos can be reconstructed from the one total missing energy $E_{\mathrm{T}}^{\mathrm{miss}}$ with W and t mass constraints,

[3] The detection **purity** for a physics object is the proportion of the true objects from the total number of reconstructed and selected objects. It is inversely proportional to the efficiency.

albeit with eight solutions. Despite low BR, when well reconstructed, the channel is useful in spin correlation studies [156, 157].

The **semileptonic** channel is the **GOLDEN CHANNEL**, a good compromise to the other two decay channels and hence is chosen in this analysis. The single-lepton serves as trigger that reduces the QCD background. The single neutrino can be recovered from $E_{\mathrm{T}}^{\mathrm{miss}}$ via W mass constraints issuing only 2 solutions, as detailed in Section 5.4.1.

Leptonic Decay to τ

The W boson decays leptonically with equal probability to e, μ and τ, as shown in Table 2.2, however in data analyses it is easier to search only for e and μ, since τ is difficult to reconstruct. As shown in Table 2.1, τ decays 65% to hadronic jets, 17% to e and 17% to μ. In the $t\bar{t}$ semileptonic channel of this analysis, the hadronic τ decay is ignored, since it cannot be discriminated against the QCD background, while the leptonic τ decay is included in the e+jets and μ+jets $t\bar{t}$ search channels.

5.1.2. Chosen Signal Signature

The final chosen $t\bar{t}$ decay mode is hence the semileptonic one, as depicted in Figure 5.1. It includes the leptonic τ decays as well, which yields overall BRs of 17% from the e channel and 17% from the μ channel. One W boson decays to a charged lepton (e or μ) and neutrino, while the other W decays in the opposite ϕ hemisphere to two quarks that hadronise into jets. The signal signature is hence l+jets, classified into e+jets or μ+jets: a charged lepton with high p_{T}, a large $E_{\mathrm{T}}^{\mathrm{miss}}$ from the undetected neutrino and jets.

Considering that in this analysis $m_{A/H} < 750$ GeV, the top quarks are low enough in p_{T} such that their decay products are well separated in ΔR. Such a topology was referred in [22] as *resolved*. The topology where the decay products would have such high p_{T} that they would overlap into merged objects is referred in [22] as *boosted*, it is however at very small-scale in this thesis and therefore all events are treated as belonging to the *resolved* topology.

5.2. Data and Monte Carlo Samples

The analysis is performed on the same dataset and background samples employed in Ref. [22], where the background sources have been chosen on the basis that they could look like $t\bar{t}$, passing the same l+jets signal region event selection.

The **background** processes with prompt leptons are **Monte Carlo modelled** and are already provided, as listed in Section 5.2.2. Dedicated **signal** processes are modelled in this analysis as listed in Section 5.2.3. The multijets **background** with non-prompt leptons are **data-driven** in this analysis as described in Section 5.5.

MC simulated signal and background processes are passed through generators that shower, hadronise and decay. The events are then passed through the full ATLAS detector simulation [158] that

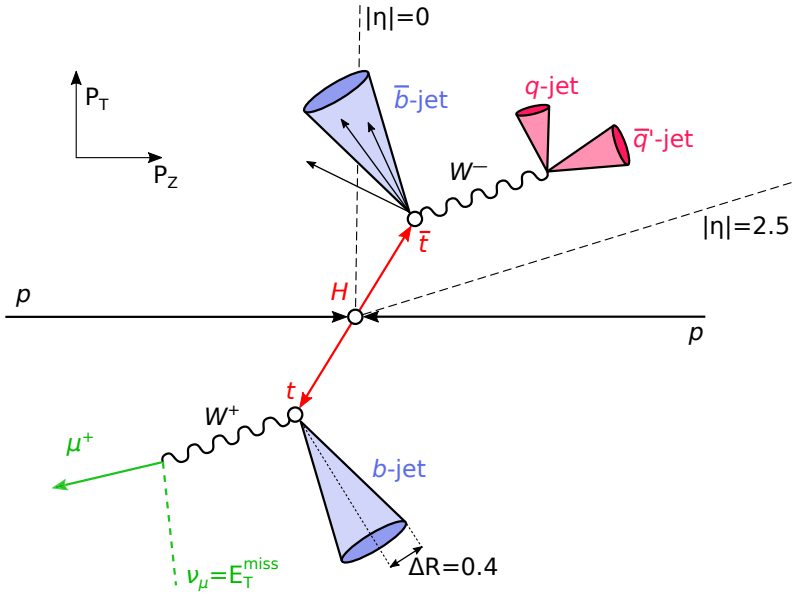

Figure 5.1.: A $t\bar{t}$ decay event in $R-z$ view, following the signature employed in this thesis. Each top quark decays into a W boson and a b-quark that hadronises into a b-jet. One W decays leptonically into a e/μ and a neutrino (the missing transverse momentum). The other W decays hadronically in the opposite ϕ hemisphere into two quarks, predominantly u, d, c, s, that issue hence light jets. Jets are reconstructed at $\Delta R = 0.4$, as described in Section 5.3.6 and are marked with tracks and particles within.

models the interaction of the stable particles with the detector material, based on the GEANT4 toolkit [159]. As the full detector simulation is the most time-consuming step of the event generation, another faster ATLAS detector simulation is available, where the electromagnetic and hadronic calorimeter showers are only parametrized [160]. The faster version is preferred for the many signal parameter points samples.

5.2.1. Dataset

The full pp collisions dataset recorded by ATLAS in 2012 at $\sqrt{s} = 8$ TeV is employed. Data-taking is quantified in approximately one minute long *lumiblocks*, which are the shortest intervals with stable beam conditions. A Good Runs List (GRL) provides the lumiblocks that have all ATLAS sub-detectors in operation, issuing a total integrated luminosity $\int L(t)\ \mathrm{d}t = 20.3\ \mathrm{fb}^{-1}$.

5.2.2. Background Samples

Irreducible SM $t\bar{t}$

The dominant background after event selection is SM $t\bar{t}$. It represents an *irreducible* background to the BSM signal $A/H \to t\bar{t}$. This means it has the exact same signature as the signal and the signal cannot be discriminated via kinematic cuts or event selection, only by the deviation of the reconstructed $m_{t\bar{t}}$ in data from the one in the SM continuum, performed later in Section 6.2.

The sample is normalised to the $\sigma = 252.9$ pb calculated in TOP++ v2.0 [161] at next-to-next-to-leading order (NNLO) accuracy in α_S and next-to-next-to-leading-logarithmic (NNLL) soft gluon

Process	Event and shower generator	Cross-section accuracy	PDF
Top			
$t\bar{t}$	POWHEG-BOX [143–146]+PYTHIA6 [147]	NNLO+NNLL [68–74]	CT10 [151]
$t\bar{t}+V$	MADGRAPH5_aMC@NLO+PYTHIA6	NLO [164]	CTEQ6L1 [165]
single top	POWHEG-BOX [144–146]+PYTHIA6	NNLO [75–77]	CT10
***VB*+jets**			
W+jets	ALPGEN [166]+PYTHIA6	Data-driven scale factors	CTEQ6L1
Z+jets	ALPGEN+PYTHIA6	NNLO [167]	CTEQ6L1
Diboson			
$WW/ZZ/WZ$	SHERPA [168–171]	NLO [172]	CT10
Multijet			
jj	Fully data-driven		

Table 5.1.: List of background samples, Monte Carlo simulated or data-driven, with their generator specifics and PDF sets used. The tools used to calculate the cross-section are given as reference near the cross-section accuracy in QCD. All occurrences of PYTHIA6 shower generator employ the Perugia 2011c tune [148].

corrections. Higher order electroweak corrections [162] were applied as well, all in order to match the modelling better to data. A few smaller samples at higher invariant $m_{t\bar{t}}$ are included as well, in order to enhance statistics in the higher mass tail. More details about the top quark production and its decay channels in Section 2.7.

Reducible

The other background sources can be rejected with the signal region event selection and are called hence *reducible*. A small fraction of events still passes the selection, therefore these background sources must be included in the analysis as well.

W boson radiated from hard quarks, produced in association with extra jets and decaying leptonically, is the highest such background. W is generated with up to five extra inclusive-flavoured partons, as ***W*+jets**. Samples with additional heavy flavours $W+c+$ jets, $W+c\bar{c}+$ jets and $W+b\bar{b}+$ jets and a few smaller samples with higher parton p_{T} are included as well.

Single top quark $Wt/s/t$ productions, as described in Section 2.7, are considered as well, where the overlap between Wt and $t\bar{t}$ was taken care of with the diagram removal scheme [163]. **Other minor background sources** of prompt leptons include Z boson produced in association with jets (Z+jets, including extra heavy flavour contributions $Z+c\bar{c}+$ jets and $Z+b\bar{b}+$ jets), heavy dibosons and heavy boson in association with $t\bar{t}$ ($t\bar{t}+V$).

Table 5.1 lists all background sources, with their generator specifics and cross-section calculation tools given as reference. Their event yields after full event selection are listed in Table 6.1.

5.2.3. Signal Samples - NOVELTY

As concluded in Chapter 4, the signal processes are modelled in MADGRAPH5_aMC@NLO v.2.0.1 at LO for $\sqrt{s}=8$ TeV, with type-II 2HDM couplings and with the CT10 [151] PDF set. The

inclusive signal+background+interference $S + B + I$ process $gg \to t\bar{t}$ is simulated with B removed internally within MadGraph5.

The generated events are thereafter showered and hadronised in Pythia6 using the Perugia 2011c tune. Events are then passed through the fast ATLAS detector simulation, with a minimum one lepton filter[4].

The signal process of interest is $gg \to A/H \to t\bar{t}$ interfering with the SM $gg \to t\bar{t}$, also called $S+I$. The pure resonance samples S are however generated as well, as they are needed in the search and exclusion procedures in Section 6.2.

Tables 5.2 to 5.5 list the mass and $\tan\beta$[5] parameter points chosen for the signal, in alignment limit of the light CP-even and spin-0 h boson to SM, via $\sin(\beta-\alpha)=1$. Two mass points are chosen, 500 GeV and 750 GeV. Masses below 500 GeV would get too close to the $2m_t$ threshold, region badly modelled, while for masses above 750 GeV the cross-sections become too low.

Figures 5.2 and 5.3 depict the S and $S+I$ distributions, which one can see are of the same order of magnitude. The figures are interpreted at the end of Section 4.2, section that describes the theoretical model that computes the scalars with loop-induced gg fusion.

Cross-sections

The cross-sections adopted for S and $S+I$ are the ones provided by MadGraph5 in the semileptonic+dileptonic $t\bar{t}$ decay channels and listed in Tables 5.2 to 5.5. The integrated cross-sections of $S+I$ are in general however not a strong indicator, due to the fact that the peak and the dip cancel each other, even though the cancellations are never entirely.

k-factors

Correction k-factors for the S samples are derived as cross-section ratios between the theoretical ones for type-II 2HDM at NNLO precision in QCD [125–127], and the ones provided by MadGraph5 when decaying S inclusively to all $t\bar{t}$ decay modes, at LO.

The question on which k-factor to apply to $S+I$ is not straightforward to answer and it has, to date, no official recommendation. As $S+I$ is a linear combination between S and I, in this analysis the k-factors from S are adopted for $S+I$ and more precise k-factor calculations are left for follow-up studies. The k-factor of B alone would not be a good choice for $S+I$, as only the colour singlet component of B is interfering.

[4] The filter assumes lepton universality, requiring minimum one e, μ or τ. The dileptonic $t\bar{t}$ decay mode is hence included in addition to the main semileptonic mode, in order to increase statistics in case one of the two leptons is not reconstructed.

[5] The non-round $\tan\beta$ values were historically needed in a few studies that required $\tan\beta$ to yield $\Gamma = \sim 10\% \cdot m$.

$\tan\beta$	Γ_A [GeV]	σ_A [pb]	σ_{A+I} [pb]	k-factor
0.40	142.95	2.591	0.344	3.11
0.50	91.48	1.867	0.522	2.76
0.68	49.46	1.108	0.477	2.52
1.40	11.68	0.156	0.090	4.23
2.00	5.75	0.138	0.080	2.35
5.00	1.14	0.018	0.003	2.42
9.00	1.02	0.002	-0.007	2.49

Table 5.2.: $\tan\beta$ parameter points for the samples of pure signal A and signal with interference $A+I$, at $m_A = 500$ GeV. The cross-sections are provided by MadGraph5 in the semileptonic+dileptonic $t\bar{t}$ decay channels and are to be scaled with the given k-factor, as described in the text.

$\tan\beta$	Γ_A [GeV]	σ_A [pb]	σ_{A+I} [pb]	k-factor
0.40	230.23	0.381	0.346	1.69
0.50	147.35	0.246	0.359	1.67
0.70	75.18	0.123	0.254	1.71
1.40	18.82	0.029	0.077	1.82
2.00	9.26	0.014	0.038	1.86

Table 5.3.: $\tan\beta$ parameter points for the samples of pure signal A and signal with interference $A+I$, at $m_A = 750$ GeV. The cross-sections are provided by MadGraph5 in the semileptonic+dileptonic $t\bar{t}$ decay channels and are to be scaled with the given k-factor, as described in the text.

$\tan\beta$	Γ_H [GeV]	σ_H [pb]	σ_{H+I} [pb]	k-factor
0.40	80.55	1.336	0.414	3.21
0.50	51.55	0.929	0.328	2.95
0.70	26.30	0.512	0.206	2.73
1.40	6.59	0.075	0.035	4.63
2.00	3.25	0.066	0.032	2.54
5.00	0.90	0.008	0.004	2.37
9.00	0.74	0.0009	0.0016	2.02

Table 5.4.: $\tan\beta$ parameter points for the samples of pure signal H and signal with interference $H+I$, at $m_H = 500$ GeV. The cross-sections are provided by MadGraph5 in the semileptonic+dileptonic $t\bar{t}$ decay channels and are to be scaled with the given k-factor, as described in the text.

$\tan\beta$	Γ_H [GeV]	σ_H [pb]	σ_{H+I} [pb]	k-factor
0.40	189.64	0.205	0.175	2.27
0.50	121.37	0.140	0.156	2.12
0.64	74.08	0.089	0.117	2.04
1.40	15.50	0.019	0.031	1.98
2.00	7.63	0.009	0.016	1.98

Table 5.5.: $\tan\beta$ parameter points for the samples of pure signal H and signal with interference $H+I$, at $m_H = 750$ GeV. The cross-sections are provided by MadGraph5 in the semileptonic+dileptonic $t\bar{t}$ decay channels and are to be scaled with the given k-factor, as described in the text.

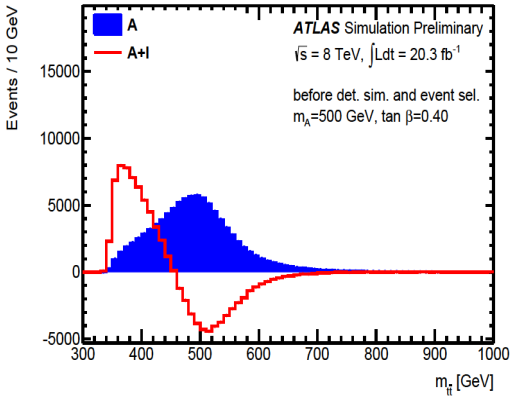

(a) $m_A = 500$ GeV, $\tan\beta = 0.40$

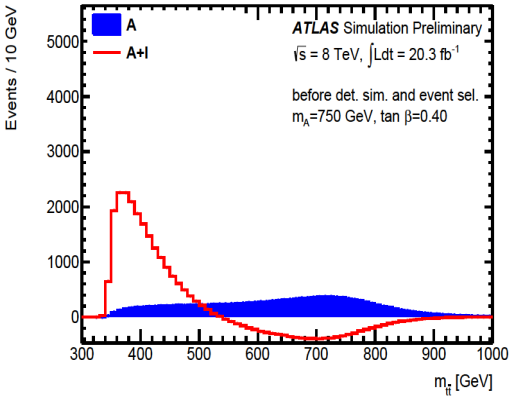

(b) $m_A = 750$ GeV, $\tan\beta = 0.40$

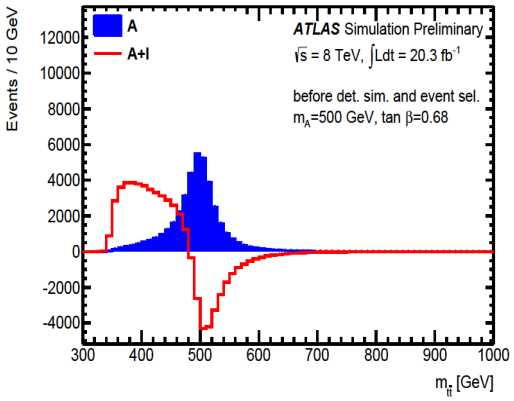

(c) $m_A = 500$ GeV, $\tan\beta = 0.68$

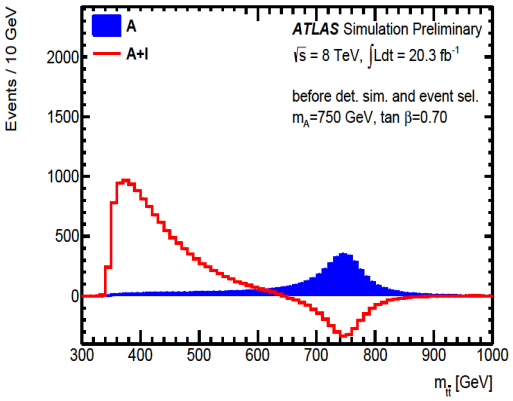

(d) $m_A = 750$ GeV, $\tan\beta = 0.70$

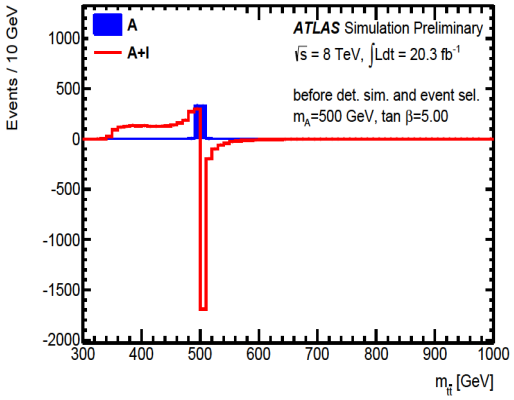

(e) $m_A = 500$ GeV, $\tan\beta = 5.00$

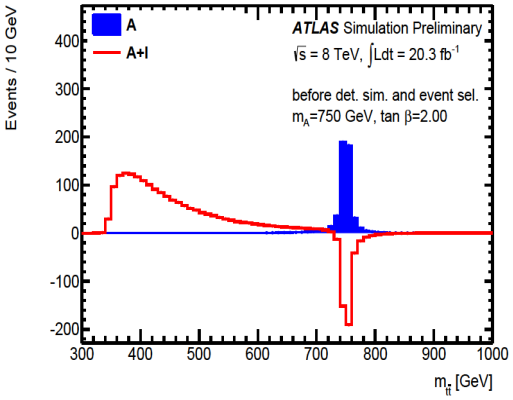

(f) $m_A = 750$ GeV, $\tan\beta = 2.00$

Figure 5.2.: Distribution of the $t\bar{t}$ invariant mass at parton level and LO, from the pseudoscalar resonance process $gg \to A \to t\bar{t}$ and from its interference to SM-QCD $gg \to t\bar{t}$. Events from all $t\bar{t}$ decay channels are included, without selection. Distributions are normalised to the cross-section and to the integrated luminosity of 20.3 fb^{-1}. *Left column*: $m_A = 500$ GeV for $\tan\beta$ values of (a) 0.4 (c) 0.68 (e) 5.0. *Right column*: $m_A = 750$ GeV for $\tan\beta$ values of (b) 0.4 (d) 0.7 (f) 2.0. The parameter $\sin(\beta - \alpha)$ is set to unity in all cases.

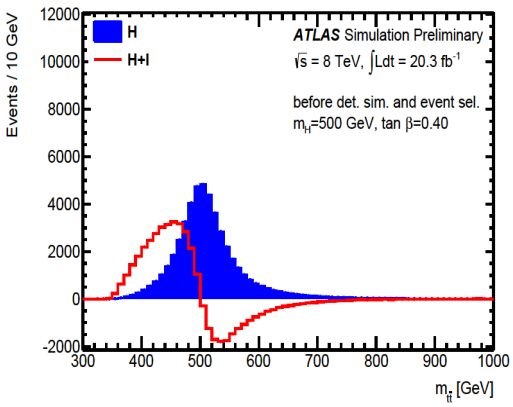

(a) $m_H = 500$ GeV, $\tan\beta = 0.40$

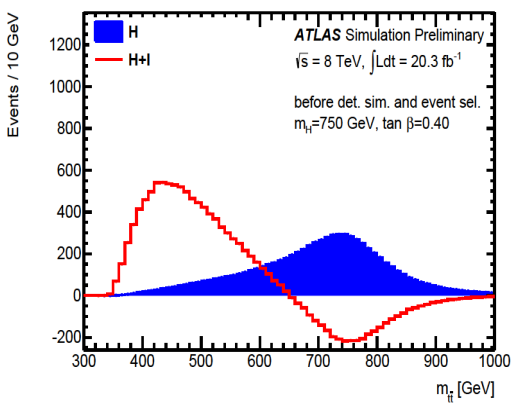

(b) $m_H = 750$ GeV, $\tan\beta = 0.40$

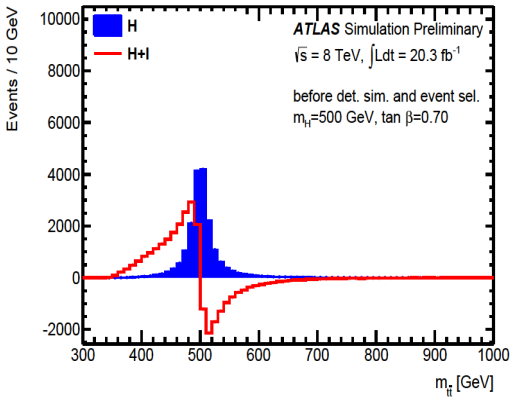

(c) $m_H = 500$ GeV, $\tan\beta = 0.70$

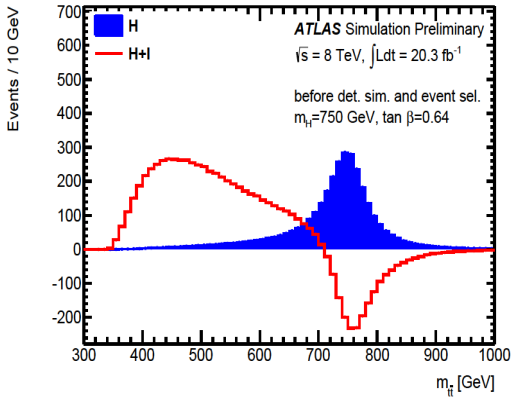

(d) $m_H = 750$ GeV, $\tan\beta = 0.64$

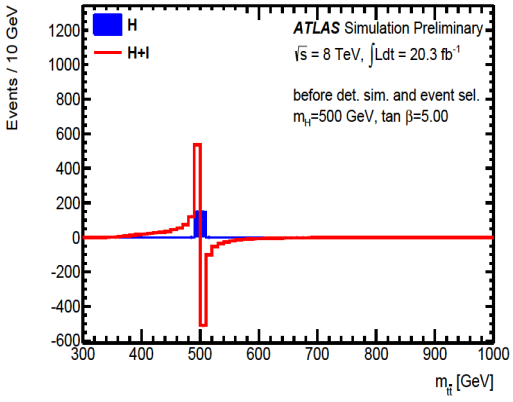

(e) $m_H = 500$ GeV, $\tan\beta = 5.00$

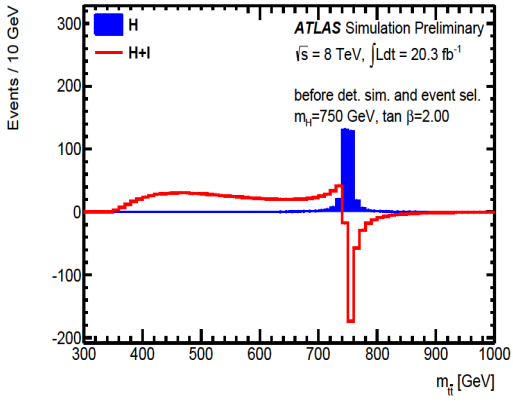

(f) $m_H = 750$ GeV, $\tan\beta = 2.00$

Figure 5.3.: Distribution of the $t\bar{t}$ invariant mass at parton level and LO, from the scalar resonance process $gg \to H \to t\bar{t}$ and from its interference to SM-QCD $gg \to t\bar{t}$. Events from all $t\bar{t}$ decay channels are included, without selection. Distributions are normalised to the cross-section and to the integrated luminosity of 20.3 fb^{-1}. *Left column*: $m_H = 500$ GeV for $\tan\beta$ values of (a) 0.4 (c) 0.7 (e) 5.0. *Right column*: $m_H = 750$ GeV for $\tan\beta$ values of (b) 0.4 (d) 0.64 (f) 2.0. The parameter $\sin(\beta - \alpha)$ is set to unity in all cases.

5.3. Object Reconstruction and Event Selection

This section describes the reconstruction and selection of physics objects and, eventually, of $t\bar{t}$ events, criteria that apply identically (up to a few minor differences explicitly mentioned) to all signal, background and data samples. For the signal and background specifically, these criteria issue the so called **nominal** event yield, denoted as such in contrast to the criteria that includes systematic errors as well, described in Section 5.7. The object and event selection must provide high background suppression, maintaining still a high enough signal efficiency[6].

5.3.1. Tracks, Vertices and Impact Parameters

The most computing intensive part of the event reconstruction represents the multistage combination and fitting of *hits* from different inner detector layers into *tracks*. Ambiguity resolution is specifically important here, in order to reduce fake tracks and the large combinatorial candidates at high luminosity.

The tracks are extrapolated towards the beamline, to identify the vertices in an iterative χ^2 fit. The vertex with the maximum $\sum p_{\mathrm{T}}^2$ of associated tracks is chosen as *primary vertex* (PV). The *impact parameters* are defined as follows: the transverse impact parameter d_0 is the closest approach distance from the PV to the track, in the transverse plane; the z coordinate at this closest approach point is named z_0. Due to the track and vertex reconstruction resolution and to the bending of the track, the d_0 distribution is distributed around 0, symmetrically for the tracks originating from the PV. As particles decay usually very fast, most tracks will originate from the PV, with a small $|d_0|$ and $|z_0|$, where a small $|z_0|$ is also a condition for the track to be located within the beam spot. In some cases the significances d_0/σ_{d_0} and z_0/σ_{z_0} are considered instead of d_0 and z_0, in order to give more weight to the tracks that are more precisely measured, where σ represents the uncertainty of the track fit and of the vertex position.

Long-lived particles will decay in a vertex distanced from the PV, called *secondary vertex* SV. Tracks originating from the SV are hence displaced from the PV and give higher d_0 and z_0.

This analysis uses the standard tracking [173, 174] and vertexing [175] algorithms.

5.3.2. Pileup

The number μ of inelastic[7] pp collisions in one bunch crossing increases with the luminosity:

$$\mu = \frac{L \cdot \sigma_{\mathrm{inelastic}}}{N_{\mathrm{bunch/beam}} \cdot f_{\mathrm{rev}}}, \tag{5.1}$$

where L is the instantaneous luminosity, $\sigma_{\mathrm{inelastic}}$ the pp inelastic cross-section, $N_{\mathrm{bunch/beam}}$ the number of bunches per beam and $f_{\mathrm{rev}} = 11.245$ kHz the revolution frequency at the LHC [176].

[6] The **detection efficiency** for a physics object is the ratio of the number of objects after reconstruction and selection, to the true number before the any reconstruction or selection.

[7] Inelastic collisions do not conserve the total kinetic energy, as opposed to elastic collisions, that conserve it.

This number consists of only one hard-scattering process of interest, as there is very low chance to have more of them, and of many other lower energy processes called **pileup**. All the collisions in one bunch crossing represent in physics analysis one **event**.

In-time pileup is generated by collisions within the same bunch crossing. **Out-of-time pileup** is generated by collisions from nearby bunch crossings, that leave electronic signals in the current bunch crossing since the detector's response time is higher than a bunch interval. $\boldsymbol{N_{\mathrm{PV}}}$ represents the number of primary vertices within the event, among which one PV is the main hard-scatter one, and indicates the in-time pileup. When both in-time and out-of-time pileup are present, N_{PV} is not a good pileup indicator any more and $\boldsymbol{\mu}$ is used instead. The two observables N_{PV} and μ are counter-intuitively not linear to each other, because the multiple interactions are often located close-by and reconstructed as a single vertex.

Average μ values function of lumiblocks and bunch crossing IDs are provided by the experiment as input to reweight each simulated sample, in order to bring it in agreement with the data pileup profile. Averaging L over the full analysed dataset yields $\langle\mu\rangle$, with the following values at ATLAS: $\langle\mu\rangle = 9.1$ in 2011 and $\langle\mu\rangle = 20.7$ in 2012 (corresponding to the dataset used in this analysis), with $\mu = 10$–35 for the latter. [99, 177]

5.3.3. Electrons

Electron Reconstruction

Electron candidates are reconstructed by identifying their energy deposits in the central EM calorimeter, called *clusters*, and by matching them to their inner detector (ID) tracks.

The *sliding-window* offline algorithm reconstructs the EM clusters. In units of $\Delta\eta \times \Delta\phi = 0.025 \times 0.025$, windows of a fixed 3×5 size are iterated over the EM calorimeter, in 1×1 steps. The window with the maximum local $E_{\mathrm{T}} > 2.5$ GeV is set as pre-cluster seed. The seed must find an associated track extrapolated from the inner detector, within $|\Delta\eta| < 0.05$ to the seed's barycenter and best matched in ΔR. The seed is then extended with the nearby cells to a 3×7 (5×5) cluster in the barrel (end-caps). The cluster's energy is then adjusted with the energy deposited in front of the EM calorimeter, estimated by the presampler and with the estimated leakage, lateral to the cluster or longitudinal towards the hadronic calorimeter. The fixed cluster size has the advantage of precise cluster energy calibration, but the disadvantage to be more sensitive to noise. [178]

The electron is hence a combined cluster-track object, central within $|\eta_{\mathrm{cluster}}| < 2.47$ (slightly less than 2.5, in order to exclude transition regions). The area $1.37 < |\eta_{\mathrm{cluster}}| < 1.52$ from the barrel/end-cap inactive transition region is excluded as well. The electron energy is given by the cluster, while the momentum and direction (η, ϕ) are given by the ID track, hence $E_{\mathrm{T}} = E_{\mathrm{cluster}} / \cosh \eta_{\mathrm{track}}$.

Electron Calibration and Resolution

The electron energy reconstructed value is corrected in the offline algorithm to the true electron energy with a *calibration scale*, derived from test beams[8]. The scale is further corrected against leakage and losses in the inactive calorimeter regions via MC simulations. An *in-situ* η-intercalibration ensures a uniform energy response in η via $Z \to ee$ events in data, similarly to the jet in-situ intercalibration from Section 5.3.6. Measurements in $W \to e\nu$ events in data, that constrain $E/p \sim 1$, improve as well the calibration scale. [179]

The *energy resolution* is defined in Eq. A.3. At high energies it is represented mostly by the constant term c, which is derived from fitting $J/\phi \to ee$ and $Z \to ee$ MC events to data and measuring the width of the Breit-Wigner peak. The resolution is 1% in the barrel calorimeter and 3% in the endcaps. [179]

Due to their small mass, electrons can lose a substantial amount of energy in the form of *bremsstrahlung*, in their interactions with the ID, affecting hence their reconstructed tracks as well. ID algorithms correct the tracks of electron candidates (after distinguishing them from pion or muon tracks) by refitting them against bremsstrahlung before their match to the electron cluster.

Electron Selection

There are three increasingly strict quality criteria sets that discriminate signal electrons against fake or non-prompt ones: *loose, medium* (medium events selection set being included in the loose selection set) and *tight* (tight set being included in the medium set). They refer to shower shape, leakage to the hadronic calorimeter, cluster-track quality match, hits count, rejecting electrons from photon conversions and so on. The tight criteria provides the highest background rejection, though it reduces as well the efficiency[6]. [178]

Electron candidates require $E_{\mathrm{T}} > 25$ GeV, *tight* identification criteria and their tracks to be matched to the PV via $|z_0| < 2$ mm.

5.3.4. Muons

Muon tracks are reconstructed at first independently in the inner detector ID and in the muon spectrometer MS. The ID muon tracks are reconstructed as in Section 5.3.1. The MS tracks start with local hit patterns in each muon chamber, that are then combined in an MS track. The hits from both ID and MS are then globally re-fit, to form a *combined muon* track. The momentum resolution ranges from 1% at low p_{T}, to 4% at $p_{\mathrm{T}} = 100$ GeV. [180].

Muons require $p_{\mathrm{T}} > 25$ GeV and to lie centrally within $|\eta| < 2.5$. Muon candidates are matched to the PV via the the longitudinal impact parameter condition $|z_0| < 2$ mm. To additionally reject muons decaying from long-lived particles, the significance of the transverse impact parameter must satisfy $|d_0/\sigma_{d_0}| < 3$.

[8] In test beams particles of known (true) energies are targeted towards a component of the detector. The ratio between the energy measured with the sub-detector and the true energy is taken as calibration scale.

5.3.5. Isolation of Leptons

Non-prompt and fake leptons are surrounded by their sibling decay products and by preceding showers, while prompt leptons are isolated, neighboured at the distance only by the b-jet. An isolation criterion [181] studied in Ref. [22] eliminates non-prompt and fake leptons:

$$\sum_{\text{excluding}-\text{lepton}-\text{track}}^{\text{tracks}} p_{\mathrm{T}}^{\text{track}} < 0.05 \cdot p_{\mathrm{T}}^{\text{lepton}}, \tag{5.2}$$

summing all p_{T} of the tracks located in a variable-size cone $\Delta R = 10\ \text{GeV}/p_{\mathrm{T}}^{\text{lepton}}$ [9]. The variable size of the cone reflects the increasing collimation of the top-quark decay products $\Delta R(\text{lepton}, W) \sim 1/p_{\mathrm{T}}^{\text{top}}$. Tracks must satisfy $p_{\mathrm{T}}^{\text{track}} > 1$ GeV, in order to avoid spiralling tracks.

5.3.6. Jets

As described in Section 2.8.1, jets are collimated sprays of hadrons that represent the experimental signatures of quarks and gluons from ISR, FSR or from decay products. When interacting with the detector, jets produce particle showers that deposit energy in both the EM and hadronic calorimeters, though with a higher fraction in the hadronic one. Jets produce tracks as well and are reconstructed either from the calorimeter constituents, or from the tracks.

Calorimeter Jets Constituents

Jet calorimeter constituents are reconstructed as *topological clusters* [182] of variable number of cells. The clustering starts from seed-cells that have the highest signal-to-noise threshold, a method that is effective in suppressing both the electronic and the pileup noise. The *noise* component is previously reconstructed from non-collision events such as beam-gas interactions or cosmic rays showers. The clusters are then extended sequentially with the neighbouring cells, decreasing iterative the signal-to-noise threshold in order to include the shower tails.

Calorimeter Jets Reconstruction

The pseudojet clusters are then passed through an iterative inclusive[10] *jet finding algorithm* to reconstruct the jet candidates. Jet algorithms must satisfy a few requirements. *Infrared safety* ensures that adding or removing very soft particles does not change the jet properties (flavor, four-momenta, angles etc.). *Collinear safety* ensures that splitting particles into collinear components does not affect the result. The algorithm should provide the same jets in any reference frame as well (*invariance under boost*). Overall, the jets should be approximately equivalent to their original partons.

A general jet finding algorithm [183] defines the following distances:

[9] E_{T} for electrons and p_{T} for muons

[10] An inclusive jet algorithm does not need to find all jets exhaustively and can ignore very soft jets.

$$d_{ij} = min(k_{ti}^{2p}, k_{tj}^{2p}) \frac{\Delta R_{ij}^2}{R^2}$$
$$d_{iB} = k_{ti}^{2p}, \tag{5.3}$$

where d_{ij} is the distance between cluster i and j, d_{iB} the distance between cluster i and the beam, k_{tj} the p_{T} of cluster i and R a reference parameter that sets the approximate jet-cone radius, in this thesis $R = 0.4$. The smallest of the distances is iteratively searched: if it is a d_{ij}, then the clusters i and j are merged; if it is a d_{iB}, then i is considered a jet and is removed from the clusters list.

The parameter p regulates the energy in relation to the size: $p > 0$ defines the k_t algorithms family, $p = 0$ the Cambridge/Aachen family and $p < 0$ defines the $Anti - k_t$ algorithms family. This analysis employs an $Anti - k_t$ algorithm with $p = -1$, provided and optimised for speed by the FastJet package [184]. An $Anti - k_t$ algorithm has the advantage that soft constituents tend to cluster to the hard ones instead of clustering among themselves. Hence jet boundaries are resilient to soft radiation and hard jets will have perfectly conical shapes of radius R, though clipped if the jets are overlapping (see Figure 1 in Ref [183]).

Jet Calibration and Energy Scale

The reconstructed jet energy is corrected to the true parton-level one in a process called *calibration*. The calorimeter cells are first calibrated using a local cluster weighting (LCW) scheme. The method classifies the topological clusters as either hadronic or electromagnetic, based on the shower shape and energy density . Hence hadronic and EM deposits can be weighted with different energy scales, since EM objects yield a relatively higher response due to the non-compensation of the calorimeter (see in Appendix A.3). The calibration scheme undergoes then four steps [185, 186]:

- **Pileup subtraction:** The number of reconstructed jets is increasing with pileup (Section 5.3.2), where pileup jets typically have low p_{T}. The following correction subtracts the pileup contribution from the jets. If the corrected jet p_{T} reaches below threshold, the jet is rejected [187]:

$$p_{\mathrm{T},jet}^{corr} = p_{\mathrm{T},jet}^{reco} - \rho \cdot A_{jet} - r_1 \cdot (N_{\mathrm{PV}} - 1) - r_2 \cdot \langle \mu \rangle \tag{5.4}$$

  The first term captures the event-by-event pileup fluctuations with $\rho = \mathrm{median}(p_{\mathrm{T,jet}}^i / A_{\mathrm{jet}}^i)$, the median p_{T} density of the event. Each jet i is a component of the k_t algorithm, however here without the p_{T} cut, in order to include the soft pileup. A_{jet}^i is the jet area prone to pileup, where the $\rho \cdot A$ term removes most of the in-time pileup. The last two terms are the *residual* or *offset* N_{PV} and μ terms: low energy pileup that overlapped with other signals and was hence disregarded by the topological clustering. The residual factors are derived from MC dijet events by fitting the ratios of $p_{\mathrm{T}}^{\mathrm{reco}} - p_{\mathrm{T}}^{\mathrm{true}}$ to N_{PV} and to $\langle \mu \rangle$, as function of $p_{\mathrm{T}}^{\mathrm{true}}$.

- **Origin correction:** The jet direction is corrected to point to the PV instead of to the IP.

- **Jet energy scale and η calibration:** The LCW weighted energy is brought to the energy of the truth jet via a jet energy scale JES, the result being referred to as LCW+JES. *Truth*

jets are built with the same jet finding algorithm defined above, but from stable simulated particles in MC multijets simulations. Since pileup should be already corrected in the previous calibration step, these MC samples do not include multiple pp interactions. A reconstructed jet is matched to a truth jet if they are within $\Delta R < 0.3$. The JES calibration is a Gaussian fitted function $\mathcal{F}$ inverse to the *jet energy response* $\mathcal{R}$:

$$\mathcal{R}_{\text{jet}} = \frac{E_{\text{jet}}^{\text{reco}}}{E_{\text{jet}}^{\text{truth}}} = \frac{1}{\mathcal{F}(E_{\text{jet}}^{\text{reco}}, \eta)}, \tag{5.5}$$

where $E_{\text{jet}}^{\text{reco}}$ is the original uncalibrated energy. $\mathcal{R}$ depends on the jet direction η due to the varying calorimeter technology and dead material in front of the calorimeters, with better response in the central ATLAS regions.

In the regions with worse detector instrumentation, the measured jet η is biased as well. The jet η is further corrected with the average of $\Delta\eta = \eta_{truth} - \eta_{origin}$, in each $(E, \eta)-$bin.

- **Residual in situ η-intercalibration:** The jets measured in data are further corrected with an *in situ* η correction, in order to ensure an energy response uniform in η. In events with two high p_{T} jets, the p_{T} of the jet centrally located at $|\eta| < 0.8$, is considered better calibrated and used as *reference* to calibrate the more forward jet, called *probe*. Their p_{T} asymmetry $\mathcal{A}$ is converted into a correction factor c, considering that in theory the two jets should have equal p_{T}:

$$c = \frac{p_{\text{T}}^{\text{ref}}}{p_{\text{T}}^{\text{probe}}} = \frac{2-\mathcal{A}}{2+\mathcal{A}} \quad \text{, where} \quad \mathcal{A} = \frac{p_{\text{T}}^{\text{probe}} - p_{\text{T}}^{\text{ref}}}{p_{\text{T}}^{\text{avg}}} \quad \text{and} \quad p_{\text{T}}^{\text{avg}} = \frac{p_{\text{T}}^{\text{probe}} + p_{\text{T}}^{\text{ref}}}{2} \tag{5.6}$$

The statistics of the reference jets can be expanded outside $|\eta| < 0.8$, by considering jets in multiple η regions such that $|\eta_{\text{reference}}| < |\eta_{\text{probe}}|$, in bins of η and $p_{\text{T}}^{\text{avg}}$ [186].

Jet Energy Resolution

The jet energy resolution JER has been measured on the bisector (vector sum of the momenta) of the two leading jets in data dijets events, assuming momentum conservation between the two jets. Figures [6-9] in [188] show a JER of 5-17%, decreasing with the jet p_{T}. The JER is however not applied as a smearing on the nominal jet measurements. Instead, the differences between the JER obtained in data and the one obtained in MC are applied as systematic uncertainty, as described in Section 5.7.2.

Corrections from non-Prompt Decay to Muons

The energy of jets with semileptonic decays to muons, mostly from $b/c-$ hadrons, but from light flavor hadrons as well, is underestimated because the muon leaves only a small contribution in the calorimeter.

To correct the jet energy, the muons within $\Delta R = 0.4$ to the jet axis are added to the jet, in four-momentum. The small muon energy loss in the calorimeter is subtracted however, in order to

avoid double counting. The correction is applied after the jet and muons are calibrated, but before the event selection.

The neutrinos accompanying the decays remain undetected and cannot be corrected for, because the correction factors would depend on the jet flavor [22].

Jet Selection. Jet Vertex Fraction

The jets are required to have $p_{\mathrm{T}} > 25$ GeV and $|\eta| < 2.5$. A loose quality identification criteria rejects in addition fake jets such as from calorimeter spikes and jets from non-collision background [186].

An additional requirement rejects the residual in-time pileup jets. As pileup is in general poorly modelled, a few jets still remain after the pileup subtraction, due to local pileup fluctuations. The hard-scatter PV is selected as the PV with the highest $\sum_{\mathrm{tracks}} p_{\mathrm{T}}^2$. For each jet a jet vertex fraction JVF is then calculated as the ratio between the p_{T} sum of the tracks within the jet and associated to the hard-scatter PV, and the p_{T} sum of all tracks within the jet. To suppress pileup, the requirement is $|JVF| > 0.5$[11], yet only for jets with $|\eta| < 2.4$, in order to have good tracking information, and $p_{\mathrm{T}} < 50$ GeV, as pileup jets are soft [187].

5.3.7. *b*-jet Tagging

b-tagging algorithms [189] discriminate jets that originate from b-quarks, against jets that originate from c-quarks or from light-flavor quarks u, d, s, g (LF). b-tagging discriminates the $t\bar{t}$ signal against background that does not usually contain b-jets, such as W+jets. The tag is not useful against QCD background, which is often enriched in b/c flavors.

The distinguishing features of B-hadrons, illustrated in Figure 5.4, are their **long lifetime** 1.5×10^{-12} s (respectively long decay length of 0.45 mm), large semileptonic BR to soft leptons and high decay tracks multiplicity[12]. Due to its long flight path, the B-hadron's decay vertex will be displaced from the PV, as a **secondary vertex** (SV), inside the b-jet that originates from the PV. The outgoing SV tracks have hence a higher $|d_0/\sigma_{d_0}|$ than the PV originating tracks.

The **sign of the track d_0** is a discriminating factor as well, where by convention $d_0 > 0$ if the track crosses or extrapolates to the jet axis in front of the PV, and negative otherwise. Tracks originating from the SV are enhanced in $d_0 > 0$, while PV tracks have d_0 distributed symmetrically around zero, due to the ID resolution.

The **high B-hadron mass** cut improves the b-tagging purity[3] against other long-lived LF hadrons, such as $K_S^0 = (d\bar{s} - s\bar{d})/\sqrt{2}$ and $\Lambda = uds$.

The above features are combined in a MC trained neural network algorithm called MV1, that issues for each jet a probability density as tag weight, respectively for each of the three flavor categories. The performance is described by the **b-jet efficiency**[6] ϵ_b, by the **c-jet efficiency** ϵ_c,

[11] Even though p_{T} are non-negative quantities, JVF is by convention -1 for calorimeter jets without associated tracks. In order to avoid rejecting such jets, the JVF cut is applied on its absolute value.

[12] The charged particle multiplicity in the final state of a decay is called *prong: 1-prong, 2-prong, multi-prong.*

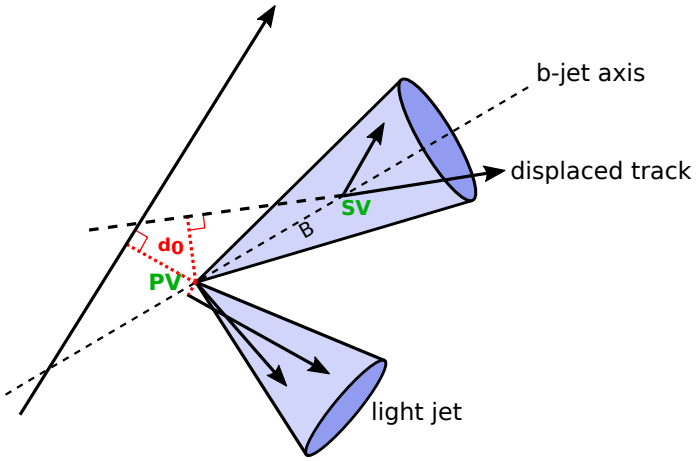

Figure 5.4.: Distinguishing features of a b-jet: a B-hadron originates from the PV and decays after a long distance in a displaced vertex SV. The SV originating tracks have the transverse impact parameter $|d_0|$ higher than PV originating tracks. SV tracks cross the jet axis after the PV, symbolised with $d_0 > 0$. Due to the ID resolution, d_0 of PV tracks are not exactly zero.

that represents the probability to mistakenly tag a c-jet as b-jet, or by the **mistag rate**, that represents the probability to tag a light-flavoured jet as b-jet. The efficiencies depend on the jet p_{T} and jet η.

Working Points and Selection

Cuts applied on the tag weights define working points, where stronger cuts lower the b-jet efficiency while increasing the b-jet purity[3]. MV1 allows working points of 60%, 70% and 80% on the b-jet efficiency, from which this analysis applies the 70% one, where the cut on the MV1 weight is higher than 0.7892. [189]

b-jets must satisfy in addition the same selection criteria as the regular jets.

5.3.8. Overlap Removal

The leptons and jets defined above are all built out of calorimeter clusters and/or associated tracks, that have a high possibility to overlap in the detector. After the previous object reconstruction and selection procedures, a technique investigated in Ref. [22] identifies the real source of the object and subtracts the other overlapping objects.

Firstly, muons are removed from the event if they are within $\Delta R < 0.04 + 10\ \mathrm{GeV}/p_{\mathrm{T}}^{\mu}$ to any jet, as these muons are most likely non-prompt.

Secondly, if the cluster of an electron is within $\Delta R < 0.4$ from a jet, both the electron and the jet are preliminary marked for removal. The electron four-momentum is subtracted from the jet four-momentum. If the electron track was included in the jet's JVF calculation, the electron track is removed from the JVF as well. The jet is passed again, now with its recalculated quantities, through the standard selection $p_{\mathrm{T}} > 25$ GeV, $|\eta| < 2.5$ and $|JVF| > 0.5$, adding now $|E| > 0$. If the jet fails the selection criteria, the jet is removed from the event. Moreover, if the jet was the

only b-jet candidate on the leptonic side of the event, the whole event is discarded. If the jet passes however the selection criteria, and in addition the electron track and jet are within $\Delta R < 0.2$, the electron is removed and its four-momentum and track are added back to the jet.

Thirdly, any electron whose track is within $\Delta R < 0.2$ to a jet, is removed as well from the event.

5.3.9. Missing Transverse Momentum

As related in Section 5.1, the total p_{T} in the decay chain of the event must be zero and conserved. Many factors however contribute to a momentum imbalance, called missing transverse momentum and with total magnitude $E_{\mathrm{T}}^{\mathrm{miss}}$. The $E_{\mathrm{T}}^{\mathrm{miss}}$ source of interest in this analysis represents the neutrino, which is not detected by ATLAS because at the energy levels investigated, the neutrinos do not interact with the detector material (see interaction of neutrinos in Appendix A.1).

Objects outside the detector acceptance, poorly reconstructed objects and non-collision background contribute in this analysis to the *fake* $E_{\mathrm{T}}^{\mathrm{miss}}$. The overall object and event selection minimise the *fake* $E_{\mathrm{T}}^{\mathrm{miss}}$, together with the criterion $E_{\mathrm{T}}^{\mathrm{miss}} > 20$ GeV.

The (x, y) components of $E_{\mathrm{T}}^{\mathrm{miss}}$ are computed as negative vector sum of the E_{T} of selected electrons and jets and of the p_{T} of selected muons [190]:

$$\begin{aligned} E_{x(y)}^{\text{miss, calo}} &= -\sum_{c=1}^{\text{calo cells}} E_c \sin\theta_c \cos(\sin)\phi_c \\ E_{x(y)}^{\text{miss, }\mu} &= -\sum_{\text{muons}} p_{x(y)}^{\mu} \\ E_{\mathrm{T}}^{\mathrm{miss}} &= \sqrt{(E_x^{\text{miss, calo}})^2 + (E_y^{\text{miss, calo}})^2 + (E_x^{\text{miss, }\mu})^2 + (E_y^{\text{miss, }\mu})^2} \end{aligned} \tag{5.7}$$

A few extra sources are included as well: non-isolated muons, MS muon tracks extrapolated towards the ID, soft jets, the residual energy deposit of muons in calorimeters and the calorimeter cells not belonging to any reconstructed object, scaled with the LCW+JES within the topological clustering [190].

5.3.10. Event Selection

The event selection proceeds as a series of cutflow steps, as described in the following.

Common Selection

Events that are incomplete, that have liquid argon noise burst or have corrupted tile calorimeter data, are rejected. Only events where the **online** single-electron or single-muon triggers fired, are analysed. For each lepton channel two triggers of various p_{T} thresholds and various medium quality criteria for electrons and tight for muons are OR-ed, in order to improve the lepton efficiency[6]. The triggers contain isolation criteria as well but the offline criteria from Eq. 5.2 is stronger. [191, 192].

The next steps represent the **offline** selection criteria. Each event must have exactly one electron or one muon, that pass the object selection criteria described in the previous sections, and that

matches geometrically the respective triggered object. The criterion $E_{\mathrm{T}}^{\mathrm{miss}} + m_{\mathrm{T}}^{W} > 60$ GeV suppresses even more the multijets background, where $m_{\mathrm{T}}^{W} = \sqrt{2 \cdot p_{\mathrm{T}}^{l} \cdot E_{\mathrm{T}}^{\mathrm{miss}} \cdot (1 - \cos\phi_{l\nu})}$ is the transverse W mass in the lepton decay, calculated from the charged lepton p_{T} and the angle ϕ between the lepton transverse momentum vector and $E_{\mathrm{T}}^{\mathrm{miss}}$ direction.

The criteria so far are common for both the resolved and boosted topologies selection, as defined in Section 5.1, and would diverge from this point onward. Unlike Ref. [22], all events are treated in this analysis as belonging to the *resolved* topology.

Resolved-Topology Selection

The events require at least four jets, among which at least one must be b-tagged. The χ^2 reconstruction fit value, that assesses the event kinematic compatibility to an l+jets $t\bar{t}$ event, as defined in Section 5.4, must fulfil $\log_{10}\chi^2 < 0.9$.

After the top quark candidates are matched to the b-jets by the χ^2 reconstruction algorithm, the events are divided into three orthogonal ***b*-tagging categories**:

- **Category 1**: Both the hadronic and leptonic top quark candidates have b-jets associated.
- **Category 2**: Only the hadronic top quark candidate has a b-jet associated.
- **Category 3**: Only the leptonic top quark candidate has a b-jet associated.

There are three categories for each e+jets and μ+jets channels, generating overall six categories. Merging the three b-categories yields the *inclusive b-category*.

Selection Efficiency

The selection efficiency represents the number of events that pass the selection after iterative steps within the **selection cutflow**, relative to the initial event yield before any selection. It is exemplified here for the pure resonance A sample (respectively $A + I$) of $m_A = 500$ GeV and $\tan\beta = 0.68$, in the e+jets channel:

1. The single-lepton trigger causes the highest efficiency drop, to 26% (22%). The samples have been already generated with a filter of minimum one e, μ or τ at parton level (hence semileptonic and dileptonic $t\bar{t}$ channels), but the single-lepton trigger rejects the dileptonic $t\bar{t}$ events, the hadronic τ decays and applies quality criteria.
2. The offline criterion of exactly one e/μ does not affect much more the efficiency, dropping it to 18% (16%).
3. The $E_{\mathrm{T}}^{\mathrm{miss}}$ and m_{T}^{W} cuts drop the efficiency to 16% (12%).
4. The first resolved topology cut, on jet multiplicity, drops the efficiency to 9% (4%).
5. The χ^2 cut, the last cut before the b-tagging categorising, drops the efficiency to 4.5% (3%).

The last step from above is depicted in Figure 5.5, scaled with the $t\bar{t}$ decay BR to the semileptonic and dileptonic channels and as a function of the resonance mass and $\tan\beta$. The efficiency distributions are flat in $\tan\beta$, which is beneficial for the analysis.

In the Figures 5.5a and 5.5b of the pure resonant signal, the scalar H has a slightly better efficiency than the pseudoscalar A, since its top quarks are more central in the detector (see the more central η in Figure B.3). The μ+jets channel is moreover slightly less efficient than the e+jets channel. This inefficiency is due to the single μ trigger being 20% inefficient relative to the offline selection, in comparison to the single e trigger, which has a difference of less than 5%. The cause lies at a lack of coverage of the μ trigger in the detector areas with support structures [193].

Figures 5.5c and 5.5d reveal the efficiencies for $S + I$ lower than for S, due to the sharp peak-dip fall in the $m_{t\bar{t}}$ distribution, that is smeared away by the finite detector resolution. For the signal parameter point $m_A = 500$ GeV and $\tan\beta = 5.0$, the weights are balanced before selection in a cross-section overall positive but close to 0 (see Table 5.2). After the selection the balance becomes negative, hence the atypical negative efficiency. The efficiency for H is higher than for A, similarly to the pure resonance case, except for the bin $m_A = 500$ GeV with $\tan\beta = 9.0$, where the order is reversed because the cross-section is negative. The comparison between the e and μ channels is not conclusive any more.

5.4. Mass Reconstruction

This section describes the reconstruction of the invariant $m_{t\bar{t}}$, that will then be used in Chapter 6 to search for deviations caused by signal in the data spectrum. There are a few notable factors that reduce $m_{t\bar{t}}$, alter their distributions and affect hence the search: the $m_{t\bar{t}}$ distribution is smeared by the finite detector resolution, defined as the average of $(m_{t\bar{t}}^{\text{reco}} - m_{t\bar{t}}^{\text{truth}})/m_{t\bar{t}}^{\text{truth}}$; the highly boosted top quarks tend to radiate strongly; the high resonance masses are more likely to be produced in an off-shell tail of lower-x PDF.

5.4.1. Neutrino Reconstruction

In order to reconstruct the neutrino, it is assumed that the majority of $E_{\text{T}}^{\text{miss}}$ originates from the neutrino p_{T} and that the reconstructed charged lepton stems from the $W \to l\nu$ decay. The p_{z}^{ν} is calculated with recommendations from Ref. [22], with an on-shell m_W constraint imposed on the system, which yields a quadratic equation in p_{z}^{ν} (described in detail in Section 4.2.1 and Appendix A.4 of Ref [194]).

If the equation has only one real solution, that solution is taken as p_{z}^{ν}. If the equation has two real solutions, the one with the smallest χ^2 kinematic fit value is selected.

If the equation has no real solution, it is assumed that the cause is the incorrectly measured $E_{\text{T}}^{\text{miss}}$. $E_{\text{T}}^{\text{miss}}$ is rescaled and rotated, or E_x^{miss} and E_y^{miss} are varied iterative, maintaining approximately the same $E_{\text{T}}^{\text{miss}}$ magnitude, until a real solution is found.

Previous studies on the non-interfering Z' resonance decaying to $t\bar{t}$ show that the escaping neutrino degrades the $m_{t\bar{t}}$ resolution with 20-30% [22].

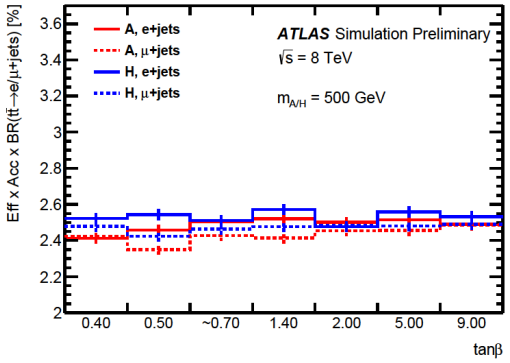

(a) pure signal resonance, $m_{A/H} = 500$ GeV

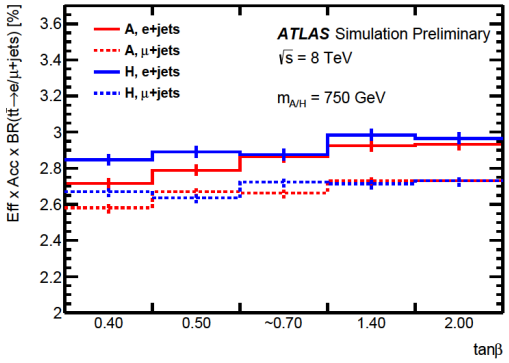

(b) pure signal resonance, $m_{A/H} = 750$ GeV

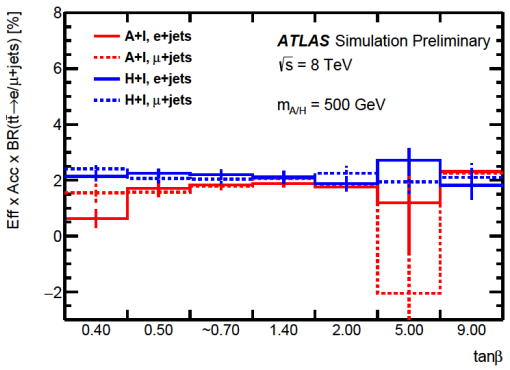

(c) signal with interference, $m_{A/H} = 500$ GeV

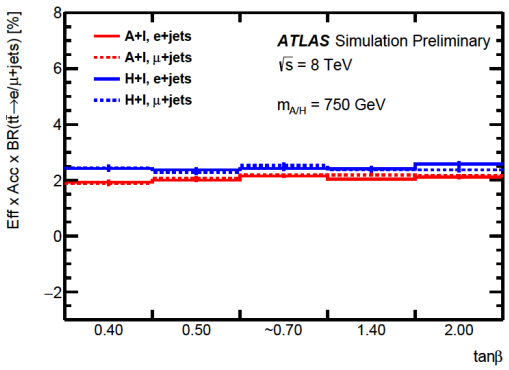

(d) signal with interference, $m_{A/H} = 750$ GeV

Figure 5.5.: The selection efficiencies scaled with the signal generation BR, for the signal samples without interference (first row) and with interference (second row), at masses of (a) 500 GeV and (b) 750 GeV.

5.4.2. χ^2 Algorithm

In order to build the hadronic and leptonic top quarks from jets and leptons, the latter are combined in various associations. A χ^2 algorithm developed for Ref. [22], based on various mass and momenta constraints and assuming that the b-tagged jets originate from the top quarks, indicates the goodness of the permutation. The permutation with the lowest χ^2 is selected.

$$\chi^2 = \left[\frac{m_{jj} - m_W}{\sigma_W}\right]^2 + \left[\frac{m_{jjb} - m_{jj} - m_{th-W}}{\sigma_{th-W}}\right]^2 + \left[\frac{m_{j\ell\nu} - m_{t\ell}}{\sigma_{t\ell}}\right]^2 + \left[\frac{(p_{\mathrm{T},jjb} - p_{\mathrm{T},j\ell\nu}) - (p_{\mathrm{T},th} - p_{\mathrm{T},t\ell})}{\sigma_{\mathrm{diff}p\mathrm{T}}}\right]^2 \tag{5.8}$$

The first term corresponds to the hadronically decaying W boson. The second term corresponds to the hadronically decaying top quark; the hadronic W mass was subtracted to decouple m_{jj} from m_{jjb}. The third term corresponds to the leptonic top quark. The fourth term corresponds to the p_{T} balance in the top quark decays.

The parameters were derived in Ref. [22] from Z' MC events on a resonance mass range $m_{Z'} = 0.5 - 2$ TeV, where the correct permutations were provided as truth information: $m_W = 82.4$ GeV, $m_{th-W} = 89.0$ GeV, $m_{t\ell} = 166.0$ GeV, $\sigma_W = 9.6$ GeV, $\sigma_{th-W} = 15.7$ GeV, $\sigma_{t\ell} = 17.5$ GeV, $p_{\mathrm{T},th} - p_{\mathrm{T},t\ell} = 0.43$ GeV and $\sigma_{\mathrm{diff}p\mathrm{T}} = 46.1$ GeV.

The invariant $m_{t\bar{t}}$ distribution reconstructed with the χ^2 algorithm is illustrated in Figures 5.6 and 5.7 for $S + I$. In comparison to the the parton level distributions in Figures 5.2 and 5.3, the sharp peak-dip fall is smeared away by the finite detector resolution. The fall is hence even more smeared away at narrower resonances (larger values of $\tan\beta$) than at broader resonances. The number of events (yields) is highly decreased as well by the detector acceptance and event selection, in both the dip and the peak regions.

5.5. Background Estimation from Data

The shapes, normalisation and uncertainties of the W+jets and multijet background are estimated from control regions in data. **Control regions** are acquired by reverting or eliminating all or part of the signal selection criteria and are hence orthogonal to the signal.

Section 5.5.1 describes how scale factors are derived from data in order to correct the total cross-section and the flavour fractions in the W+jets ALPGEN simulation. The scale factors are provided by Ref. [22], where it was proved as well that the SFs lower the experimental systematic uncertainties (PDF, jet energy scale, b-tagging etc.) on the W+jets samples, in comparison to using simulation alone.

Section 5.5.2 describes how the multijets background is entirely estimated from data in this analysis, similarly to Ref. [22], for which the respective control regions have been validated in the publication's ATLAS internal document [153].

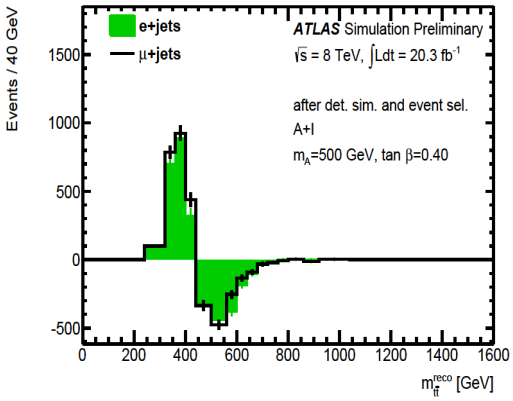

(a) $m_A = 500$ GeV, $\tan\beta = 0.40$

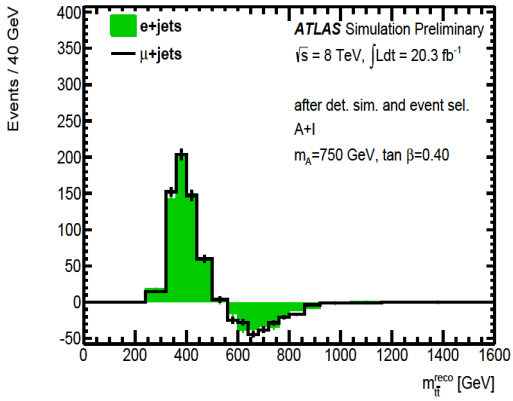

(b) $m_A = 750$ GeV, $\tan\beta = 0.40$

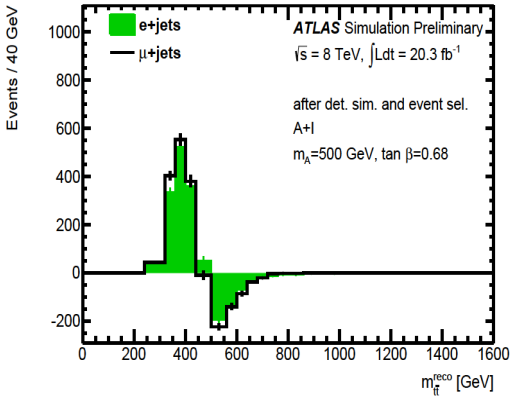

(c) $m_A = 500$ GeV, $\tan\beta = 0.68$

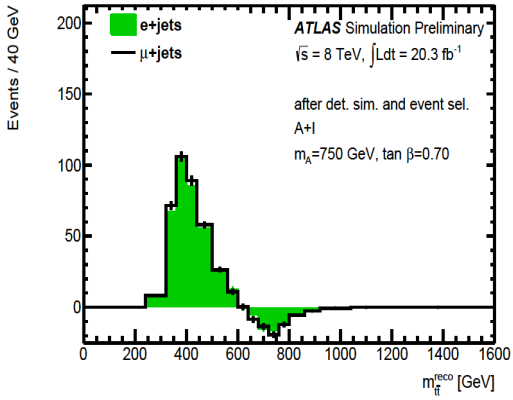

(d) $m_A = 750$ GeV, $\tan\beta = 0.70$

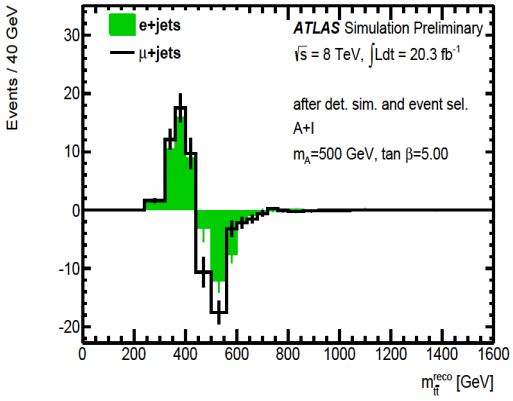

(e) $m_A = 500$ GeV, $\tan\beta = 5.00$

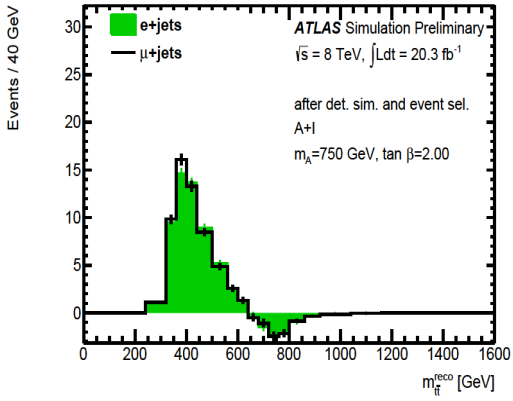

(f) $m_A = 750$ GeV, $\tan\beta = 2.00$

Figure 5.6.: Distribution of the $t\bar{t}$ invariant mass reconstructed with the χ^2 algorithm, from the pseudoscalar resonance process $gg \to A \to t\bar{t}$ and from its interference to SM-QCD $gg \to t\bar{t}$. Events fulfil the e+jets (blue) and μ+jets (red) selections. Distributions are normalised to the cross-section and to the integrated luminosity of 20.3 fb^{-1}. *Left column*: $m_A = 500$ GeV for $\tan\beta$ values of (a) 0.4 (c) 0.68 (e) 5.0. *Right column*: $m_A = 750$ GeV for $\tan\beta$ values of (b) 0.4 (d) 0.7 (f) 2.0. The parameter $\sin(\beta - \alpha)$ is set to unity in all cases.

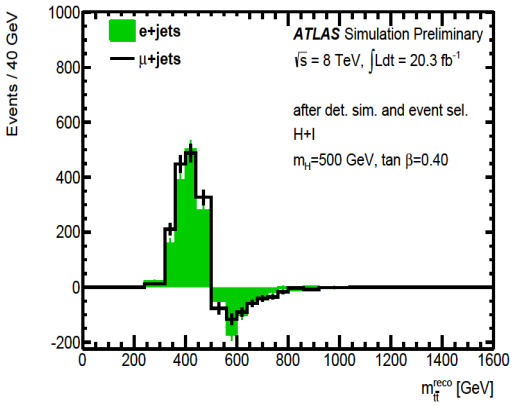

(a) $m_H = 500$ GeV, $\tan\beta = 0.40$

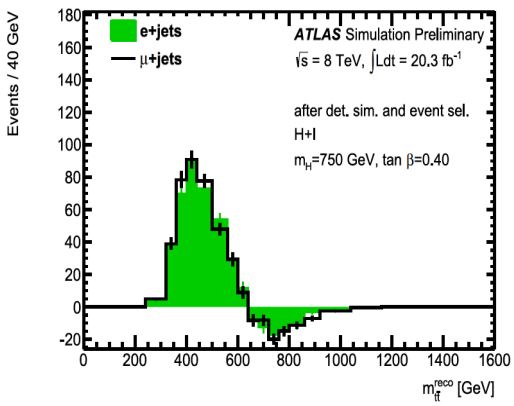

(b) $m_H = 750$ GeV, $\tan\beta = 0.40$

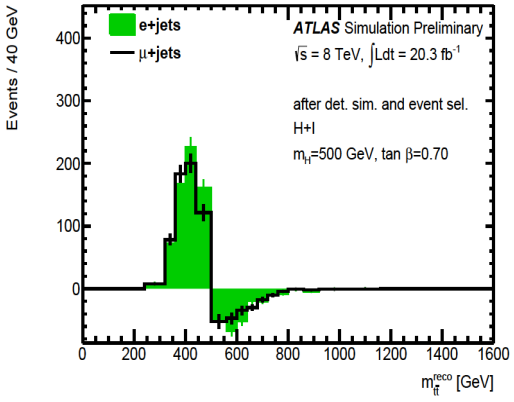

(c) $m_H = 500$ GeV, $\tan\beta = 0.70$

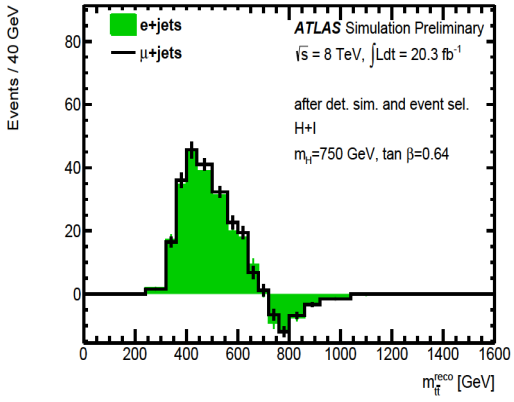

(d) $m_H = 750$ GeV, $\tan\beta = 0.64$

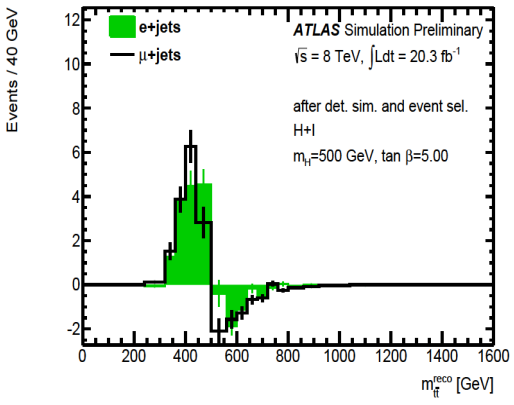

(e) $m_H = 500$ GeV, $\tan\beta = 5.00$

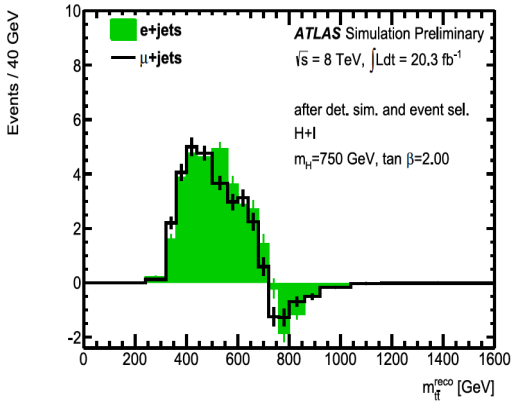

(f) $m_H = 750$ GeV, $\tan\beta = 2.00$

Figure 5.7.: Distribution of the $t\bar{t}$ invariant mass reconstructed with the χ^2 algorithm, from the scalar resonance process $gg \to H \to t\bar{t}$ and from its interference to SM-QCD $gg \to t\bar{t}$. Events fulfil the e+jets (blue) and μ+jets (red) selections. Distributions are normalised to the cross-section and to the integrated luminosity of 20.3 fb^{-1}. *Left column*: $m_H = 500$ GeV for $\tan\beta$ values of (a) 0.4 (c) 0.7 (e) 5.0. *Right column*: $m_H = 750$ GeV for $\tan\beta$ values of (b) 0.4 (d) 0.64 (f) 2.0. The parameter $\sin(\beta - \alpha)$ is set to unity in all cases.

5.5.1. W+jets Scale Factors Estimation

Overall Normalisation Scale Factors

The W^++ jets have at the LHC pp collisions a higher prevalence than W^-+ jets, due to the fact that the proton has more valence u quarks than valence d quarks. This asymmetry and the difference between data and MC in respect to this asymmetry, are exploited as a scale factor C_A that normalises the total W+jets cross-section.

In data it is easier to extract the W+jets asymmetry by looking instead at the asymmetry between the inclusive positively charged leptons D_+ and the negative ones D_-, since such asymmetry in data originates predominantly from the W+jets events[13]. The smaller contributions from the other charge-asymmetric events (single top, WZ, $t\bar{t}+W$) are MC simulated and subtracted from the data.

In the MC modelling of W+jets, $N^{\mathrm{MC}}_{W^{+(-)}}$ represent the number of respective $W^{+(-)}$+ jets events, yet their ratio $r_{\mathrm{MC}} = \frac{N^{\mathrm{MC}}_{W^+}}{N^{\mathrm{MC}}_{W^-}}$ was proved to be a better estimated value and is hence used instead.

The event selection from Section 5.3 is applied to both the corrected data and to the simulated W+jets events, excluding however the b-tagging requirements (i.e. it is a *pretag* control region). The scale factor C_A is derived as follows [195, 196]:

$$\begin{aligned} N^{\mathrm{data}}_{W^+} + N^{\mathrm{data}}_{W^-} &= \left(\frac{r_{\mathrm{MC}}+1}{r_{\mathrm{MC}}-1}\right)(D_+ - D_-) \\ C_A &= \frac{N^{\mathrm{data}}_{W^+} + N^{\mathrm{data}}_{W^-}}{N^{\mathrm{MC}}_{W^+} + N^{\mathrm{MC}}_{W^-}}, \end{aligned} \tag{5.9}$$

to a value of $C_A = 1.026 \pm 0.011$ in the e+jets channel and $C_A = 0.978 \pm 0.010$ in the μ+jets channel, given their statistical uncertainties as well [22].

Flavour Fractions Scale Factors

The flavour fractions $b\bar{b}$, $c\bar{c}$, c and light-jets within the inclusive W+jets receive as well scale factors (SF) derived from data [195, 196]. Instead of looking at the charge asymmetries, one has to investigate now the total yields of W^++jets and W^-+jets, in both data and MC. Data must be hence corrected from all non W+jets background contributions, by subtracting the MC predicted $t\bar{t}$, single top, Z+jets, VV, $t\bar{t}+V$ and the data derived multijets (as described in Section 5.5.2).

The W+jets MC samples have for simplicity a lower jet multiplicity, of two jets. The event selection from Section 5.3 is applied to both corrected data and MC, excluding however the minimum four jets and b-tagging requirements. There are exactly two jets required, while the b-tagging requirement variations create two control regions (CR): one without any b-tagging requirements (*pretag* CR), one requiring minimum one b-jet (*tag* CR).

[13] $t\bar{t}$ yields equal number of positive versus negative leptons. However, $t\bar{t}$ events at LHC present more central $\bar{t}$ and more forward t [195]

The correction factors $K_{b\bar{b}} = K_{c\bar{c}}$[14], K_c and K_{light} for the respective fractions f are determined from the below equation system [22]:

$$\begin{aligned} D_{+(-)} &= C_A \cdot \left(K_{b\bar{b},c\bar{c}} \cdot (N^{b\bar{b}}_{\text{MC},W^{+(-)}} + N^{c\bar{c}}_{\text{MC},W^{+(-)}}) + K_c \cdot N^{c}_{\text{MC},W^{+(-)}} + K_{\text{light}} \cdot N^{\text{light}}_{\text{MC},W^{+(-)}} \right) \\ 1.0 &= K_{b\bar{b},c\bar{c}} \cdot (f_{b\bar{b}} + f_{c\bar{c}}) + K_c \cdot f_c + K_{\text{light}} \cdot f_{\text{light}} \end{aligned} \tag{5.10}$$

The three equations are applied for each of the two control regions, hence in total six equations, from which the pretag normalisation SF C_A deducted in the previous section is considered unchanged. The tag factor C_A and all six K factors are recalculated from one another in an iterative procedure. The K factors found for the two-jet region with the b-tagging requirement are extrapolated to higher jet multiplicity regions, by maintaining the same ratios between them.

The SFs final values are applied as event weights to the W+jets events, with the following nominal values and statistical uncertainties, respectively in the e+jets (μ+jets) channels [22]:

$$\begin{aligned} K_{b\bar{b},c\bar{c}} &= 1.36 \ \pm 0.07 \qquad (1.51 \pm \ 0.08) \\ K_c &= 0.71 \ \pm 0.03 \qquad (0.66 \pm \ 0.03) \\ K_{\text{light}} &= 0.934 \pm 0.005 \qquad (0.873 \pm 0.004) \end{aligned} \tag{5.11}$$

5.5.2. Multijet Full Background Estimation

The QCD multijets are the major source of non-prompt and fake leptons. In the signal region defined in this thesis, multijets simulations suffer from large systematic and especially statistical uncertainty, since most of their phase space is located outside the respective region. Therefore the multijets shape, normalisation and systematic uncertainties must be fully derived from data.

This analysis employs the *matrix method* data derivation technique defined in Ref. [197,198]. Events in data are selected via two lepton identification criteria. The *tight* one refers to the standard nominal criteria employed in this analysis in the signal region. The *loose* one was developed in Ref. [22] specially for the multijets derivation. It discards any lepton isolation requirements and replaces the electrons tight criterion with the respective medium one, albeit still rejecting electrons from photon conversion.

The total number of loose leptons in data is a sum of prompt, non-prompt and fake leptons, the latter two encompassing the leptons from QCD jets:

$$N_{\text{Loose}} = N_{\text{prompt}} + N_{\text{QCD}} = N_{\text{prompt}} + (N_{\text{non-prompt}} + N_{\text{fake}}) \tag{5.12}$$

The total number of tight leptons in data is a fraction of the loose ones:

$$N_{\text{Tight}} = \epsilon \cdot N_{\text{prompt}} + f \cdot N_{\text{QCD}}, \tag{5.13}$$

[14] The ratio of the $W + b\bar{b}$ + jets to $W + c\bar{c}$ + jets contributions in MC is considered well estimated and at a fixed value, similarly to r_{MC} from the overall normalisation.

where the efficiencies ϵ and f, also called *real* and *fake* efficiencies, are calculated separately for the electron and muon channels as follows.

The *real efficiency* ϵ defines the number of loose leptons passing the tight criteria as well, in a pool of prompt leptons (decaying from W/Z). It is measured on $Z \to ee$ and $Z \to \mu\mu$ events in data using the tag-and-probe technique (as defined in Section 5.6.1, including the m_Z, lepton charge and ϕ cuts). Firstly, the tag lepton is selected with the tight criterion, in order to have certainty that the event is a prompt $Z \to ll$ decay. Secondly, the probe lepton is selected with the loose criterion. Thirdly, the selected probe leptons that pass the tight criterion as well, issue the efficiency.

The *fake efficiency* f defines the number of loose leptons passing the tight criteria as well, in a pool of non-prompt or fake leptons. It is measured in data in a control region enriched in QCD-multijets, constructed as follows: $E_{\mathrm{T}}^{\mathrm{miss}} < 20$ GeV, $E_{\mathrm{T}}^{\mathrm{miss}} + m_{\mathrm{T}}^{W} < 60$ GeV, $|d_0/\sigma_{d_0}| > 3$ for muons, no $|d_0/\sigma_{d_0}|$ cut for electrons and no χ^2 cut [22]. The contamination with prompt muons from W/Z decay was beforehand subtracted via MC simulations.

After measuring f and ϵ and counting N_L and N_T, Eq. 5.12 and 5.13 are solved for N_{prompt} and N_{QCD}. The final QCD estimation that passes the signal region selection is delivered as $f \cdot N_{\mathrm{QCD}}$.

5.6. Other Monte Carlo Corrections

The signal predictions and background contributions are to be combined and compared to the data in the search procedure of Chapter 6. The predictions should be hence brought to a good agreement with the data, regarding the overall normalisation, object reconstruction and object selection.

The MC predictions are already normalised to their theoretical or data-driven cross-sections, which decides their relative contribution. Their normalisation is scaled additionally to $\int L(t)\ \mathrm{d}t = 20.3\ \mathrm{fb}^{-1}$, the **total integrated luminosity** of the 2012 pp collision dataset. A series of additional MC corrections are listed below.

5.6.1. Efficiency Scale Factors

The efficiency[6] in reconstruction and selection of objects in MC simulations is different than the one in data. To correct the MC one, their ratio is computed as Scale Factors (SF) and used as event reweighting factor on the MC samples.

Tag-and-Probe Technique

The technique most often used to derive efficiencies from data is the tag-and-probe. As an illustration is taken the muon isolation efficiency derivation. $Z \to \mu\mu$ events are searched in data by requiring two muons of opposite charge and in opposite ϕ hemispheres, with an invariant total mass cut around m_Z. If one muon passes the isolation cut, that muon is pinned down as *tag* and the assumption can be made that the other muon, called *probe*, is isolated in "truth". The fraction of probe muons that pass the isolation criteria serves as isolation efficiency and reference for the SF.

Electron and Muons SF

For electrons and muons, the overall efficiency is a factorisation of the efficiencies of the trigger, isolation and quality criteria (loose vs. tight). For electrons an additional efficiency of matching clusters to tracks is included. For electrons, efficiencies are computed in $(\eta_{cluster}, E_{\mathrm{T}})$ bins in both data and MC using $Z \to ee$ events, in case of energies higher than 30 GeV, respectively $J/\psi \to ee$ events for lower energies. Similarly are investigated the efficiencies for muons, in (η, p_{T}) bins.

For electron energies higher than 30 GeV, the efficiencies are 95% in the calorimeter barrel and 90% in the endcaps, decreasing for lower energies. The scale factors are $0.95 - 1.05$ [179]. The overall muon efficiencies are larger than 95%, with the MC ones agreeing better with data, with the exception of a larger inconsistency at $\eta = +1.5$, where a few faulty pixels in the b-layer should have been disabled. The muon p_{T} in MC samples is smeared as well in order to correct its resolution, using data tag-and-probe resolution results. [180, 193]

Jets SF

The jet reconstruction efficiency is computed as well with a tag-and-probe technique in dijet events with jets built out of Inner Detector tracks[15]. The track jet highest in p_{T} is selected as tag jet. The probe jet is selected as the one balancing in opposite ϕ the tag jet. The fraction of probe jets that match a calorimeter jet defines the efficiency. Comparing to data, simulations have a small inefficiency at $p_{\mathrm{T}}^{\mathrm{jet}} < 30$ GeV, which is corrected by randomly discarding jets in that region, until the correct efficiency is reached. [199]

b-tagging SF

The b-jet MC efficiencies and mistag rates are calibrated to the data ones, each with individual scale factors, at the 70% b-tagging working point.

The efficiency ϵ_b combines measurements of two techniques. One searches for jets with a muon within and yields SF$= 0.90 - 0.95$ [200]. Another one searches with tag-and-probe for the two b-jets in dilepton $t\bar{t}$ events. Such events are "clean" of other jets, allowing pure b-jet probes, with SF~ 1. [201]

The efficiency ϵ_c is measured in jets containing $D^{*+} = c\bar{d}$ mesons (D^{*-} is implied as well) that decay to $D^0(\to K^-\pi^+)\pi^+$. A fit on $m(K\pi\pi) - m(K\pi)$ in data and MC discriminates against D^{*+} originating from B-hadrons. The ϵ_c efficiency ranges between 35-45%, with a SF~ 0.9. [202]

The efficiency of the mistag rate ϵ_l in data is difficult to measure directly, because data is inclusive in flavour jets and cannot be freed of heavy-flavour (HF) jets. An approximation is based on the fact that d_0 of light-flavour (LF) tracks is symmetric around 0 and that both LF and HF tracks look similarly at $d_0 < 0$. Hence an efficiency on $d_0 < 0$ is measured instead in the inclusive flavour data, a method called *negative tag*. The mistag rate ranges between 0.5-2.5%, with a SF~ 1. [202]

[15] **Track jets** are built by running the anti-k_t jet algorithm with tracks as input

5.7. Statistical and Systematic Uncertainties

After the signal and background events are reconstructed and selected, a series of uncertainties are assigned to their nominal event yields and physical quantities. A well modelled background must eventually agree in the invariant $m_{t\bar{t}}$ to the data, within the uncertainties, when no signal is discovered. In the other kinematic observables the background must always[16] agree to the data, within their own uncertainties.

Statistical uncertainties represent stochastic fluctuations caused by the fact that a sample is finite and scale inversely with the sample size. Successive measurements of the same physical observable yield different results, within the statistical uncertainty.

Systematic uncertainties however, are caused by instrumentation or modelling errors, occur repeatedly at successive measurements and do not scale with the sample size.

For a measured observable P the **total uncertainties** are defined as following:

$$\begin{aligned} P &= P_0 \pm \sigma_{stat} \pm \sigma_{syst} \\ \sigma_{stat} &= \sigma/\sqrt{N} \\ \sigma_{syst} &= \sigma\sqrt{\sum(\delta e/e)^2}, \end{aligned} \tag{5.14}$$

where P_0 is the nominal value, σ the standard deviation, N the sample size, σ_{stat} the statistical uncertainty also called *standard error of the mean* and σ_{syst} the systematic uncertainty as sum in quadrature of all individual systematic errors of effects e.

The **systematic uncertainties** are evaluated by using other models. The ones considered in Ref. [22] are followed here as well, with the exception of a different W+jets shape uncertainty, that was recommended later in the respective analysis for having a reduced effect at high $m_{t\bar{t}}$. Dedicated modelling uncertainties for the signal samples are derived as well.

The systematic errors impact the normalisation or shape of $m_{t\bar{t}}$ and either increase the nominal value, as **up variation**, or decrease it, as **down variation**. Experimental uncertainties refer to luminosity (Section 5.7.1) and object reconstruction (Section 5.7.2) and apply to all simulated samples. PDF modelling uncertainties apply to the $t\bar{t}$, W+jets and signal samples (Section 5.7.3), while other MC uncertainties are specific to each background (Sections 5.7.4) and signal sample (Section 5.7.5). The impacts are initially given in percent of the nominal values of the respective physical observables (selection efficiency, calibration, flavor fractions, normalisation, etc.) and are then converted in respect to $m_{t\bar{t}}$ in Table 5.6. The distributions of $m_{t\bar{t}}$ systematic shifts are provided to the profile likelihood fit in Section 6.2 and can be seen in Appendix C.

5.7.1. Luminosity Uncertainty

The uncertainty on the integrated luminosity is derived with beam-separation scans performed by the Beam Conditions Monitor (BCM) and LUCID ATLAS sub-detectors. The relative positions of

[16] With the exception of the angles describes in Section 4.4.

the colliding beams are slightly varied, in order to observe the interaction rate change [203]. The variation is applied as a 2.8% normalisation constant factor to all MC samples, excluding W+jets and multijets, that are already estimated or corrected from data.

5.7.2. Object Reconstruction Uncertainties

Electrons and Muons

The **electron efficiency scale factors** uncertainties originate mainly (2%) from the isolation efficiency difference between the busy $t\bar{t}$ and clean Z tag-and-probe environments and from the electron-jet overlap removal. The variation is evaluated by applying the tag-and-probe method on inclusive Z+jets samples, with the electron close or not to the jet. Smaller contributions arise from the loose vs. tight quality of the tag-electron, from the sliding window size, matching of cluster to track and pileup.

The **electron energy scale** variation is within 1-2% at $|\eta_{cluster}| < 2.47$. It is caused by the energy scale and material of the presampler located in front of the calorimeter and is determined in MC by adding more material. The variation on the **electron energy resolution** is due to the constant resolution term c and is within 1%. [178]

The **muon efficiency scale factors** uncertainties stem from the statistical errors of the tag-and-probe selection, the choice of cone size to match the trigger muon object to the probe, the uncertainty on calorimeter muon energy losses at high muon p_{T}, pileup. The isolation SF is affected similarly to the electron case.

The **muon momentum correction** uncertainty has a larger component and is evaluated by varying the dimuon mass window in the $Z \to \mu\mu$ tag-and-probe method. [180]

Jet Energy Scale

JES represents the **largest source of experimental uncertainties** and is related to the calibration of hadronic jets. Its various components are described below, according to Ref. [186].

The JES variations measured in-situ[17] are treated specifically with an *eigenvector variation method*, a method developed in order to reduce the number of variations. The covariance matrices[18] of all sources of uncertainty are added up and six eigenvectors and eigenvalues are computed. The four largest eigenvalues are listed in Table 5.6, where the square root of the respective eigenvalues gives the variations size.

The non in-situ JES measurements are extracted individually.

- **Calibration non-closure:** After the jets are calibrated with the inverse of the calorimeter response described in Eq. 5.5, the jet response should become 1. It deviates however from 1

[17] **In-situ** measurements and validations are performed within one sample, as opposed to, for example, validations of MC samples from data or from other MC samples.

[18] The **variance** of a variable X is defined as $\mathrm{Var}(X) = E[(X-\mu)^2]$, where the expectation E a is probability-weighted average and $\mu = E[X]$ is the mean. Generalising to multiple variables X_i yields the **covariance matrix** $V_{ij} = E[\,(X_i - E[X_i]) \cdot ([X_j - E[X_j]) \,]$.

especially at $p_{\mathrm{T}} < 30$ GeV, with up to 2%, in a phenomenon called *non-closure*. It occurs because jets E and p_{T} are corrected with the same factor, which requires that the reconstructed jet mass is close to the true jet mass. The requirement does not hold at low p_{T} jets and the response deviation from unity is taken as systematic uncertainty.

- **Calorimeter response**: The uncertainty on the calorimeter response in the best instrumented region (central $|\eta|$) is derived with in-situ energy measurements in single hadron test beams[8]. The variations are caused by response non-linearities at high p_{T}, longitudinal leakage at high p_{T}, low p_{T} particles that do not pass the clustering noise threshold or do not reach the calorimeter, the choice on EM versus hadronic scale, the response to neutral hadrons.

- **Detector simulation**: The non-collision **noise** level is an important factor contributing to the cluster count and cluster shapes in the topological clustering described in Section 5.3.6. The simulated noise can however differ from the real noise from data, since the data noise chances in time, while the simulated one is fixed. To estimate the uncertainty, the jet reconstruction is performed in simulations with noise thresholds adapted to the cell noise in data, while maintaining the same simulated energy and noise. The difference in jet response to the default noise threshold is taken as JES variation.

  The simulated **detector material** could deviate as well from reality. To estimate its impact, the ID material is increased with 5% and 0.1 X_0 are added between the presampler and EM calorimeter, in the barrel-endcap transition and in the cryostats.

- **MC modelling**: The MC modelling of fragmentation and underlying events[19] affects the JES as well. The comparison of the jet energy response in Pythia and Alpgen+Herwig+Jimmy simulations, employing the same Pythia Perugia2010 tune, estimates the JES variation.

- ***η* intercalibration**: The intercalibration correction factor computed in-situ in Eq. 5.6 differs between data and MC at low p_{T} and large $|\eta|$ due to the modelling uncertainty and at high p_{T} due to low MC statistics. The difference is taken as JES variation.

- **Pileup**: After the pileup is subtracted via Eq. 5.4, the jet p_{T} still has a residual dependency on N_{PV} or $\langle\mu\rangle$. The dependency is estimated in simulated samples of $Z + 1$ jet, with $Z \to ll$. The two leptons are considered well reconstructed and measured and the p_{T} difference between the jet and the leptons is fit to N_{PV}, respectively $\langle\mu\rangle$, with their deviations from 0 extracted as the *pileup* N_{PV} *and* $\langle\mu\rangle$ *variation*.

  As the jet p_{T} increases, the root of the jet is more prone to pileup. The dependency of the r_1 and r_2 coefficients of the offset residual terms to $p_{\mathrm{T}}^{\mathrm{true}}$ is similarly deducted in simulations and taken as the *pileup* p_{T} *variation*.

  The fit of ρ to $\langle\mu\rangle$ in the $Z + 1$ jet events is extracted to describe the underlying events topology of the main hard-scattering interaction, called *pileup* ρ *topology variation*. [187]

- ***b*-JES**: The JES uncertainty on heavy-flavour jets plays an important role in precision measurements of the top quark, impacting as well the b-tagging calibration, and has to be hence taken as a separate component.

[19] An **underlying event** in a hadron collision is any event not originating from the primary hard scattering: ISR, FSR, beam-beam remnants, pileup, multiple parton interactions, non-collision noise.

The uncertainty on the calorimeter b-jets response is measured for single hadrons from dijet and $b\bar{b}$ samples in-situ and in test beams[8]. Other sources of uncertainties arise from modelling of the b-quark fragmentation, evaluated by comparing the jet response at various MC generators and showering tunes, and from the detector material, evaluated by simulating more dead material.

The calorimeter jet response is then validated by comparing the jet p_{T} with the total p_{T} of the tracks associated to the jet, both in data and in MC, as well as both in inclusive flavor jets and b-tagged jets. [204]

- **Flavor Composition and Response**:

  The flavor of the parton initiating the jet plays a role in the jet hadronisation and shower shape, which finally impacts the jet response as well. Since the impact of JES from the heavy flavours was treated in the previous section, this section treats the difference in response between gluon initiated jets and light quarks (LQ) initiated jets.

  It can be proved that the uncertainty on the calorimeter response $\mathcal{R}$ of an inclusive-flavor jets sample can be approximated as [205]:

$$\frac{\Delta\mathcal{R}}{\mathcal{R}} = \Delta f_g \times \left(\frac{\mathcal{R}_q - \mathcal{R}_g}{\mathcal{R}}\right), \tag{5.15}$$

  being thus dependent on the variations $\Delta f_q + \Delta f_g = 0$ on the $g - \mathrm{LQ}$ flavor fractions (considering here that the other flavors have fixed fractions) and on the response difference between the two flavor jets. The latter is evaluated on MC dijet events by varying the calibration scheme between EM+JES, LCW+JES and a more complex "global" scheme GS that corrects the jet based on its shower properties, described in Ref. [186]. LQ-jets yield up to 5-6% higher response that g-jets.

  The $g - \mathrm{LQ}$ flavor composition is estimated from the jet properties that influence the shower shape. Gluons have low-x PDF, hence they are likely low in p_{T}. Thus their fragmentation particles tend to be multiple, soft and separated in ΔR (the magnetic field bends as well the low-p_{T} tracks more), leading to broad jets. LQ-jets have on the other hand the opposite characteristics.

  Templates were built from MC dijet events employing the jet width and number of associated tracks as $g - \mathrm{LQ}$ discriminators, in bins of jet p_{T}, η and ΔR distance between jets. The jet flavor was identified by matching in ΔR the jet to the origin parton. The templates were then reweighted to data, in order to account for data-MC differences such as the jet width. The templates were validated in γ-jet high p_{T} events, where the jet was expected to be LQ.

  The flavor composition variation is obtained by re-deriving the templates with other MC generators, since the modelling affects the jet width and track count, and by varying the fraction of heavy-flavour jets.

Jet Energy Resolution

Another large source of jet uncertainty is the 10% JER difference between data and MC. In order to estimate the uncertainty on $m_{t\bar{t}}$, reconstructed jets from MC or data are Gaussian smeared with

their JER difference as following: in the phase-space where the MC predicted JER is smaller than in data, the MC jets are smeared; in the other phase-spaces the data jets are smeared. $m_{t\bar{t}}$ is then recalculated and since a JER variation can only increase (worsen) the resolution by lowering $m_{t\bar{t}}$ with a "down" variation, the "up" one is artificially symmetrically calculated. [188]

b-jet Tagging

The uncertainties on the ***b*-tagging efficiency scale factor** are evaluated by re-deriving the scale factors after varying with $\pm 1\sigma$ each source of object reconstruction uncertainties. To derive the SF, the tag-and-probe dilepton $t\bar{t}$ method is employed, as it is more precise than the other methods. The highest contribution to the SF variation have the JES and the $t\bar{t}$ modelling variations, albeit all sources are fed into a ten eigenvectors variation method, similarly to the JES [201]. From the ten eigenvalues, most have trivial effect, except for the four listed in Table 5.6.

The uncertainty on the ***c*-tagging efficiency scale factor** originates from the fit on the D^{*+} mass and from the b-tagging of the B-hadrons that are background sources for these mesons. The uncertainty is evaluated by varying the fit constraints for the former and by including b-tagging SF for the latter. The uncertainty on the **mistag rate scale factor** originates from simulation statistics, dependence on the data taking period, heavy flavor fractions, track multiplicities. Their total efficiencies are however of very small impact on the $t\bar{t}$ mass and hence are not broken down into eigenvalues either. [202]

Missing Transverse Momentum

The real missing transverse momentum has been validated in simulated $W \to l\mu$ events, where $E_{\mathrm{T,True}}^{\mathrm{miss}}$ originates entirely from the escaping neutrino. The variation was extracted by fitting $(E_{\mathrm{T}}^{\mathrm{miss}} - E_{\mathrm{T,True}}^{\mathrm{miss}})/E_{\mathrm{T,True}}^{\mathrm{miss}}$ in various momentum bins and was evaluated to maximum 5% at $E_{\mathrm{T}}^{\mathrm{miss}} < 40$ GeV and to maximum 3% at $E_{\mathrm{T}}^{\mathrm{miss}} > 40$ GeV, though with a better uncertainty for electrons, of 1%, due to the underestimation of the muon calorimeter term. [190]

5.7.3. PDF Uncertainty

The variation on the choice of the PDF set is applied to the $t\bar{t}$, W+jets and signal samples. The global fit on the PDF is affected by theoretical uncertainties such as on the values of α_S, m_c and m_b or on the truncation in perturbation expansions. The variation is evaluated in this analysis as an envelope of the CT10 [151], MSTW2008NLO [83] and NNPDF2.3 [206] PDF sets uncertainties, provided at 68% confidence level, in accordance to the PDF4LHC recommendations [207]. The PDF has one of the highest systematic impacts, especially for the signal with interference, as shown in Table 5.6.

5.7.4. Background Modelling Uncertainties

Top Quark Pairs

The variation on the SM $t\bar{t}$ modelling is the highest source of **background modelling uncertainty**. This is because SM $t\bar{t}$ has the highest nominal background yield already.

Another reason is that the variations are estimated by crude generator comparison, which likely overestimates the uncertainties. The comparisons are however a generally accepted phenomenon at the moment, due to lacking other better alternatives. The uncertainties are nevertheless heavily constraint in Section 6.2.4.

The dominant component is on the reconstructed invariant $m_{t\bar{t}}$ **normalisation**, pre-calculated in Ref. [22]. A few other components affect the **shape** of the $m_{t\bar{t}}$ distribution and are derived in this analysis via dedicated $t\bar{t}$ MC samples. The modelling of the **parton shower and ISR/FSR** have the highest impact on the shape.

- **Normalisation uncertainty:** The uncertainty has been specially derived in Ref. [22] similarly to the nominal cross-section, in Top++ v2.0 [161] at NNLO accuracy in α_S and NNLL soft gluon corrections [68–74]. The uncertainties include the ones on the renormalisation and factorisation scales, on the α_S and PDF set choice and a variation of ± 1 GeV on m_t, all added in quadrature. The respective uncertainties on the PDF and α_S are extracted at 68% confidence level for each of the three sets, according to the PDF4LHC recommendations [207]: CT10 [151], MSTW2008NLO [83] and NNPDF2.3 [206]. The result is applied in this analysis as a constant 6.5% normalisation factor for the $t\bar{t}$ sample.
- **Parton Shower:** The uncertainty on the modelling of parton shower, decay and fragmentation is investigated by comparing the $m_{t\bar{t}}$ distribution predicted with the nominal Powheg-Box event generator, interfaced with two different shower generators, Pythia 6 versus Herwig.
- **ISR and FSR:** The uncertainty on the QCD ISR and FSR rate is determined by varying the Pythia parameter that regulates the levels of ISR and FSR, in samples generated with AcerMC and interfaced with Pythia 6.
- **MC generator:** The effect of the choice of NLO generator is investigated by comparing the $m_{t\bar{t}}$ distribution predicted with the nominal Powheg-Box generator, to the one predicted with MC@NLO [208, 209]. To exclude here the uncertainty on the parton shower, both generators are interfaced with Herwig [210, 211].
- **Top quark mass:** The $m_{t\bar{t}}$ distribution is predicted with the nominal Powheg-Box + Pythia generator, once with the nominal $m_t = 172.5$ GeV, once with $m_t = 170.0$ GeV and once with $m_t = 175$ GeV. The differences between them are scaled by 0.4, in order to account for the variation corresponding to ± 1.0 GeV.
- **Electroweak corrections:** The uncertainty on the electroweak corrections is extracted by varying with $\pm 10\%$ the deviation of the EW correction factors from unity. The EW scale uncertainty has a negligible effect, since the EW scale is already small.

W+jets

The **change in $m_{t\bar{t}}$ shape** at the W+jets samples is investigated by changing the minimum p_{T} cut on the partons of the hard process, from the nominal 15 GeV to 25 GeV, in the ALPGEN generation [166]. The shape change is applied by reweighting the events in bins of the leading[20] jet p_{T}, with factors provided in Ref. [22]. The $m_{t\bar{t}}$ spectrum is normalised to the same nominal cross-section and data-derived scale factors.

The **SFs on heavy flavor fractions and normalisation** do not have a special uncertainty source. Their impact is evaluated by re-deriving the SFs after applying each object reconstruction uncertainty defined for this analysis, with the procedure from Section 5.5.1. The respective detector uncertainties are proved in Ref. [22] to be reduced when applying the SFs.

Multijets

The uncertainty has been specially derived in Ref. [22] by defining control regions alternative to the nominal ones defined in the multijets data derivation from Section 5.5.2. The respective control region criteria are eliminated or reverted in various combinations. In addition, the largest object reconstruction uncertainties (JES and b-tagging efficiency), $t\bar{t}$ MC modelling uncertainties and statistical uncertainties of the efficiencies f and ϵ, are additionally included in the multijets variations.

The resulting variations are applied in this thesis as a constant 20.1% normalisation factor on the multijets e+jets channel and 22.6% on the multijets μ+jets channel.

Other Electroweak Backgrounds

The systematic uncertainties on the cross-sections of the other electroweak backgrounds are set in this analysis to constant normalisation scales of the $t\bar{t}$ mass spectra. The cross-section uncertainty on the single top quark background is 7.7% [75–77]. The cross-section uncertainty on the Z+jets background is 48% [212], caused by uncertainty at higher jet multiplicities. The cross-section uncertainty on the diboson background is 34% [22] and originates from the PDF, scale and jet multiplicity uncertainties. The one on $t\bar{t}+V$ is 13% [22].

5.7.5. Signal Modelling Uncertainties - NOVELTY

The complex interference pattern requires evaluation of special $S+I$ systematics, a **NOVELTY** brought by this thesis. The uncertainties on the modelling of pure signal resonance S and signal with interference $S+I$ include two special derivations, depicted in Figure 5.8. They are both evaluated at parton level from a reference sample of the pseudoscalar resonance A at $m_A = 500$ GeV and $\tan\beta = 0.68$ (which approximates $\Gamma_A = 10\%$).

[20] The leading jet is the jet highest in p_{T}.

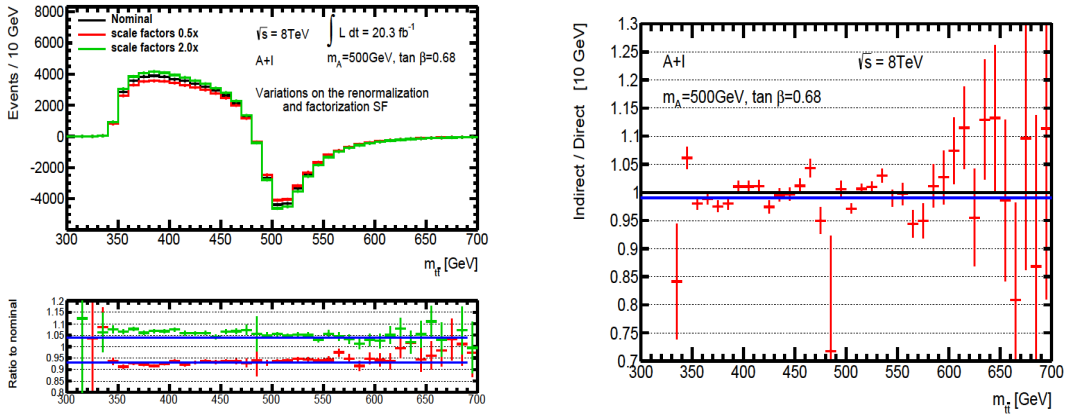

(a) Renormalisation and factorisation SF

(b) "Indirect" versus "direct" $S + I$ generation

Figure 5.8.: (a) Variation on the renormalisation and factorisation scale factors. The two linear fits yield 1.073 and 0.961, hence their maximum 7.5% is chosen as total variation and adopted for both S and $S + I$.
(b) Variation on the discrepancy between the "indirect" and "direct" $S + I$ generation approaches. The linear fit yields 0.9966, hence a constant 0.4% normalisation factor is chosen as total variation.
Both studies are for A at $m_A = 500$ GeV and $\tan\beta = 0.68$.

The uncertainty on the choice of the renormalisation and factorisation scale factors is estimated by varying each scale by factors of 0.5 and 2.0. The impact on $S + I$ is found to be high, 7.5% and the value is adopted for all S and $S + I$ samples.

An additional uncertainty of 0.4% is derived from the inconsistency between the $m_{t\bar{t}}$ distributions obtained with the "indirect" and "direct" generation approaches described in Section 4.3.1.

The systematic variations on the k-factors may have an impact, but at the moment there are no such theoretical prescriptions available. A possible difference between the full and fast detector simulations is not included, as it is predicted to be small in comparison to all other uncertainties[21].

[21] The ATLAS fast simulation has been proven to have very good detector approximations, especially in non-boosted topologies as used in this thesis.

Syst. effect	tot.bgr	$t\bar{t}$	sing.top	W+jets	QCD	Z+jets	Dibosons	$t\bar{t}+V$	A	$A+I$
b-tag EV 6	0.1	0.1	0.0	0.1	0.0	0.0	0.0	0.1	0.1	0.2
b-tag EV 7	0.2	0.2	0.4	0.2	0.0	0.2	0.0	0.2	0.1	0.3
b-tag EV 8	0.8	0.8	1.2	0.5	0.0	0.6	0.2	0.7	0.6	0.7
b-tag EV 9	1.2	1.2	1.7	0.9	0.0	1.1	0.4	1.1	1.1	0.7
c-tag	0.2	0.2	0.1	4.6	0.0	3.9	6.0	0.0	0.2	0.8
Electron scales	0.5	0.5	0.5	0.6	0.0	0.5	0.5	0.5	0.5	0.6
$E_{\mathrm{T}}^{\mathrm{miss}}$ scales	0.1	0.1	0.1	0.4	0.0	1.2	0.7	0.1	0.4	0.8
JES EV 1	**3.4**	3.0	5.0	7.0	0.0	8.1	6.7	1.6	2.5	5.0
JES EV 2	**1.2**	1.1	1.8	2.6	0.0	2.6	1.9	1.0	1.0	1.5
JES EV 3	**0.4**	0.3	0.5	0.6	0.0	0.5	0.7	0.4	0.4	0.3
JES EV 4	**0.2**	0.2	0.2	0.4	0.0	0.2	0.8	0.3	0.3	0.5
JES *b*	**0.5**	0.5	0.7	0.5	0.0	0.6	0.6	0.1	0.4	2.0
JES η intercal. model.	**0.5**	0.4	0.7	1.2	0.0	1.6	0.9	0.2	0.3	1.1
JES η intercal. stat.	**0.8**	0.7	1.2	1.9	0.0	2.0	1.4	0.4	0.6	1.2
JES flavor composition	**3.5**	3.1	4.9	8.5	0.0	9.6	7.7	1.6	2.6	5.2
JES flavor response	**1.9**	1.7	2.8	4.5	0.0	5.6	4.1	0.8	1.3	3.4
JES pileup μ offset	**0.3**	0.2	0.4	0.6	0.0	0.6	1.0	0.2	0.2	0.4
JES pileup N_{PV} offset	**2.1**	1.9	3.0	3.9	0.0	4.0	3.5	1.0	1.8	2.4
JES pileup p_{T}	**0.1**	0.1	0.2	0.2	0.0	0.2	0.1	0.3	0.2	0.9
JES pileup ρ topology	**2.5**	2.2	3.5	5.2	0.0	5.8	4.7	1.2	1.9	2.7
Jet energy resolution	**1.3**	1.6	0.6	6.5	0.0	12.1	4.6	1.6	1.6	1.7
Luminosity	2.6	2.8	2.8	0.0	0.0	2.8	2.8	2.8	2.8	2.8
Mistag	0.3	0.0	0.0	3.5	0.0	3.7	2.6	0.0	0.0	0.1
Muon scales	1.1	1.2	1.2	1.2	0.0	0.6	1.1	1.1	1.2	1.6
PDF	2.5	2.5	0.0	5.3	0.0	0.0	0.0	0.0	2.1	12.3
$t\bar{t}$ EW correction	0.2	0.2	0.0	0.0	0.0	0.0	0.0	0.0	0.0	0.0
$t\bar{t}$ ISR/FSR	**3.6**	4.3	0.0	0.0	0.0	0.0	0.0	0.0	0.0	0.0
$t\bar{t}$ MC generator	2.1	2.5	0.0	0.0	0.0	0.0	0.0	0.0	0.0	0.0
$t\bar{t}$ parton shower	**4.7**	5.3	0.0	0.0	0.0	0.0	0.0	0.0	0.0	0.0
$t\bar{t}$ top quark mass	0.8	1.0	0.0	0.0	0.0	0.0	0.0	0.0	0.0	0.0
$t\bar{t}$ cross-section	**5.6**	6.5	0.0	0.0	0.0	0.0	0.0	0.0	0.0	0.0
QCD data-driven e	0.5	0.0	0.0	0.0	16.7	0.0	0.0	0.0	0.0	0.0
QCD data-driven μ	0.1	0.0	0.0	0.0	3.7	0.0	0.0	0.0	0.0	0.0
Dibosons cross-section	0.1	0.0	0.0	0.0	0.0	0.0	34.0	0.0	0.0	0.0
Single top cross-section	0.3	0.0	7.7	0.0	0.0	0.0	0.0	0.0	0.0	0.0
W+jets shape	1.7	0.0	0.0	26.0	0.0	0.0	0.0	0.0	0.0	0.0
Z+jets cross-section	0.5	0.0	0.0	0.0	0.0	48	0.0	0.0	0.0	0.0
$t\bar{t}+V$ cross-section	0.0	0.0	0.0	0.0	0.0	0.0	0.0	13.5	0.0	0.0
Dir/Indir	0.0	0.0	0.0	0.0	0.0	0.0	0.0	0.0	0.0	**0.4**
Ren/Fact scale	0.0	0.0	0.0	0.0	0.0	0.0	0.0	0.0	**7.5**	**7.5**
Statistic	0.5	0.3	1.5	1.5	2.3	2.5	3.0	0.8	2.4	11.2
$\sqrt{\text{Quadratic sum}}$	11.4	11.8	12.4	31.4	17.3	52.4	37.4	14.3	9.8	20.7

Table 5.6.: Impact of systematic effects and statistic uncertainty on the yields of the background, pure resonance signal A and signal with interference $A+I$ with $m_A = 500$ GeV and $\tan\beta = 0.68$. The impacts are given in percent of the nominal yield by taking the maximum between the up and down shifts. The very small variations are not listed. The total uncertainty is obtained by summing all uncertainties in quadrature. In bold are given the highest background uncertainty sources (JES, unfolded in sub-components, and $t\bar{t}$) and the signal uncertainty sources.

Chapter 6.

Data Analysis Results

6.1. Comparison of Data and Background Expectations

The full event selection for the resolved topology presented in Section 5.3 yields 226,003 data events and 219,000 expected total background events, as shown in Table 6.1. The yields listed represent the three b-tagging categories summed up as a single inclusive b-tag multiplicity category and split into the e+jets and μ+jets channels. Their associated total uncertainties are listed as well, corresponding to the last row in Table 5.6. The data and background are found in the total event yield in good agreement.

Sample	e+jets	μ+jets	Sum
SM $t\bar{t}$	95,000 ± 11,000	93,000 ± 11,000	188,000 ± 22,000
Single top quark	3,900 ± 500	3,800 ± 500	7,700 ± 1,000
$t\bar{t}V$	290 ± 40	280 ± 40	560 ± 80
W+jets	6,600 ± 2,100	7,200 ± 2,300	13,800 ± 4,300
Z+jets	1,400 ± 620	650 ± 250	2,100 ± 900
Diboson	320 ± 120	310 ± 120	630 ± 240
Multijet e	5,300 ± 1,100	-	5,300 ± 1,100
Multijet μ	-	1,060 ± 230	1,060 ± 230
Total background	112,000 ± 13,000	106,000 ± 12,000	219,000 ± 25,000
Data	115,785	110,218	226,003

Table 6.1.: Data and expected background yields after the full event selection and before the profile likelihood fit of the background to data. The total uncertainties on the nominal background yields are included as well, containing both systematic and statistical uncertainties, summed in quadrature.

Figure 6.1 and Figure 6.2 demonstrate visually that the data agrees with the background prediction, within the total systematic and statistical uncertainties (hashed area), in the reconstructed $t\bar{t}$ invariant mass spectrum. All background sources mentioned in the above table are overlaid and the distributions are inspected separately in all six channels (three b-tagging categories for each lepton channel). The $A + I$ and $H + I$ distributions at mass points of 500 GeV are shown as well, for the parameter points $\tan\beta = 0.68$ and 0.50 respectively, which are equivalent to $\Gamma = 10\%$. For a better view the signal distribution is scaled by a factor of five.

While the invariant $m_{t\bar{t}}$ is a variable sensitive to the signal, the other kinematic distributions[16] are expected to be insensitive and are used instead to check that the background modelling is reliable. Comparisons between data and background for these other kinematic distributions are displayed in Appendix D.1 and present a good agreement.

A search for local excesses and deficits in the data $m_{t\bar{t}}$ spectrum, in comparison to the expected background, was performed in Ref. [22] with BumpHunter [213]. Poisson[1] fluctuations of the expected background (B) were compared with the observed data (D), employing bin-by-bin the signal significance formula $S/\sqrt{B} = (D-B)/\sqrt{B}$, or more complex formulas in bins combinations. The search was performed in all channels, individually and combined, assuming that if a channel exhibits a bump (dip) at a specific $t\bar{t}$ invariant mass region, the same bump (dip) should exhibit in the other channels as well at the same mass region. The search considered no signal shape, hence it was a model-independent search for local excesses or deficits of various widths.

No significant deviation of the data from the SM hypothesis was found, hence in Ref. [22] for each resonant signal benchmark (without interference) upper exclusion limits were derived for their respective cross sections.

6.2. Upper Limits Setting - NOVELTY

6.2.1. Motivation

The previous limits from Ref. [22], obtained with a simple "bump hunt", cannot be re-interpreted to the case with complicated interference effects and with different signal shapes, present in this analysis. Hence a dedicated limit setting procedure that includes the interference effect is developed here, a **NOVELTY** brought by this thesis.

A binned profile likelihood fit of the data to the expected distributions under the signal+background and background-only hypotheses is performed. In this fit, the background and signal reconstructed invariant $m_{t\bar{t}}$ distributions are allowed to float within the shapes of their respective uncertainties. This is particularly important in the case of very complex signal shapes like those resulting from interference and because the local significance of a small signal can change drastically under changes of a large background, due to the mismodelling systematic uncertainties. Further details are given in the following subsections.

6.2.2. Terminology

The terminology on searches and exclusions is taken from [214, 215].

Hypotheses The tested hypotheses are H_μ, where one *alternative hypothesis* is tested against a better known and already established *null hypothesis*. The *background only hypothesis* is denoted as H_0 and corresponds to $\mu = 0$. The H_1, where $\mu = 1$, represents the signal on top of the background, $S+B$, in short *signal hypothesis*, where the deviation of data from the fit background would fully agree with the modelled signal. H_0 and H_1 can represent either the null, or the alternative hypotheses, depending if the analysis refers to a search or to an exclusion.

[1] Some of the probability distributions most employed in this thesis are: the continuous **normal Gaussian** distribution $f(x) = \frac{1}{\sigma\sqrt{2\pi}} e^{-((x-\mu)/\sigma)^2/2}$, where μ is the mean value and σ the standard deviation (σ^2 the variance), and the **discreet Poisson counting** distribution $f(k,\lambda) = (\lambda^k e^{-\lambda})/k!$ to observe k events in an interval, where λ is the event rate.

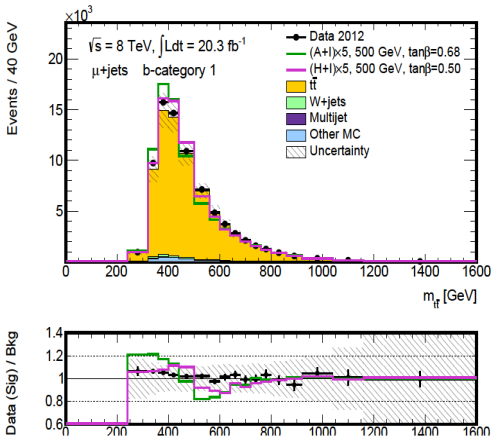

(a) *b*-tagging category 1

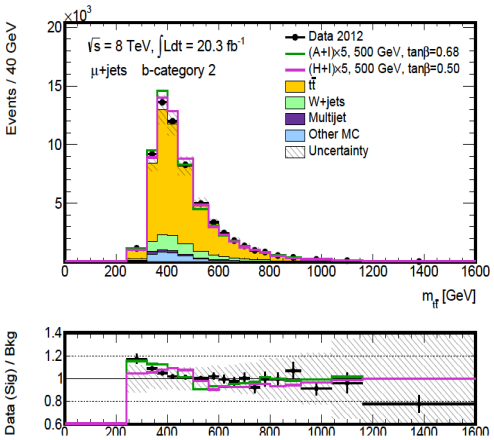

(b) *b*-tagging category 2

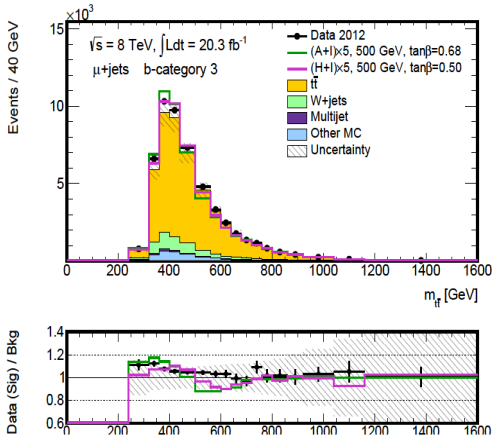

(c) *b*-tagging category 3

Figure 6.1.: Distribution of the reconstructed invariant $m_{t\bar{t}}$ in the μ+jets channel before the profile likelihood fit (**pre-fit**). The green and magenta lines represent the hypothetical $A + I$ and $H + I$ distributions at masses of 500 GeV, scaled by a factor of five. The *hashed area* represents the total uncertainty on the background. The *bottom pads* show the ratio of data over background and signal+background over background, respectively.

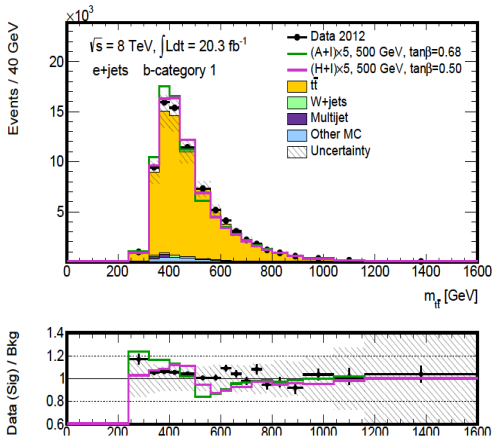

(a) *b*-tagging category 1

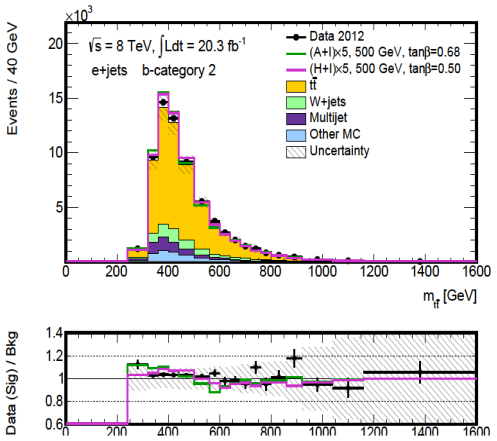

(b) *b*-tagging category 2

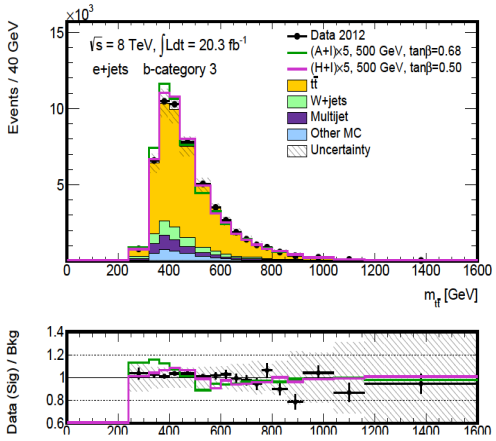

(c) *b*-tagging category 3

Figure 6.2.: Distribution of the reconstructed invariant $m_{t\bar{t}}$ in the e+jets channel before the profile likelihood fit (**pre-fit**). The green and magenta lines represent the hypothetical $A + I$ and $H + I$ distributions at masses of 500 GeV, with their invariant $m_{t\bar{t}}$ distributions scaled by a factor of five. The *hashed area* represents the total uncertainty on the background. The *bottom pads* show the ratio of data over background and signal+background over background, respectively.

Signal strength The data yield D in a given $m_{t\bar{t}}$ bin is formulated as a function of the yields of the expected signal S and background B in the same bin:

$$D = \mu \cdot S + B, \tag{6.1}$$

where μ is the signal strength, a free parameter that scales the signal yield of the specific hypothesis that is to be tested and adjusts it to best match the yields in data. A value of $\mu > 1$ ($\mu < 1$) indicates that the signal model underestimates (overestimates) the real value.

Likelihood functions and test statistics The profile fit employs a binned likelihood function $\mathcal{L}(\mu, \theta)$ constructed as the product of Poisson[1] probabilities of event numbers for all bins. The background and signal processes are characterized, besides parameters of primary interest such as event rate, by *nuisance parameters* (NPs) θ as well, representing the statistical and systematic uncertainties on $m_{t\bar{t}}$. The NPs corresponding to the systematic uncertainties are parametrized with Gaussian[1] distributions $\hat{\theta}$ as following: the background nominal yield is taken as the mean value θ_0; the relative change in background yield for an up/down variation of a given uncertainty is taken as the standard deviation σ_θ. The statistical uncertainty is represented with a Poisson distribution.

A test statistic q_μ is constructed as the following likelihood ratio [214]:

$$q_\mu = -2 \ln \lambda(\mu) = -2 \ln \frac{\mathcal{L}(\mu, \hat{\hat{\theta}}_\mu)}{\mathcal{L}(\hat{\mu}, \hat{\theta})}, \tag{6.2}$$

where the parameters with hat $\hat{\mu}$ and $\hat{\theta}$ maximize together globally the likelihood as Maximum Likelihood Estimators (MLE), while the double hat $\hat{\hat{\theta}}_\mu$ maximizes the likelihood for a given μ. The definition implies $0 \leq \lambda \leq 1$, where λ =1 represents good agreement between data and H_μ, and hence higher q_μ represents higher disagreement or incompatibility.

***P*-values** To quantify the total disagreement, in the following the *p-values* are defined [214], illustrated as well in Figure 6.3:

$$p_\mu = \int_{q_\mu,\ \text{data}}^{\infty} f(q_\mu|\mu) dq_\mu, \tag{6.3}$$

where $f(q_\mu|\mu)$ represents the probability density function (pdf) of q_μ assuming hypothesis H_μ. The p-value can be converted into the upper tail of a Gaussian distribution (Figure 6.3) with a Z-score:

$$Z = \Phi^{-1}(1 - p_\mu), \tag{6.4}$$

indicating that the p-value starts at Z number of standard deviations above the mean, with Φ^{-1} the inverse of the cumulative Gaussian distribution.

Intuitively, the p-value describes the following. It could be that the current LHC dataset is "untypical" and that re-runs of the experiment under the same conditions could provide data with

even less compatibility with the tested hypothesis, as the current dataset. An important question is how often would the observed data ("measurement") be less compatible. As multiple experimental re-runs are not technically possible, the p-value is calculated by throwing "toy experiments" to derive the pdf of q_μ. This is however computing extensive and the pdf are derived instead using the following approximate asymptotic formulae.

Results from Wald [216] and Wilks [217] show that for one parameter of interest μ the test statistics can be approximated as:

$$-2\ln\lambda(\mu) = \frac{(\hat{\mu}-\mu)^2}{\sigma'^2} + \mathcal{O}(1/\sqrt{N}), \tag{6.5}$$

where $\hat{\mu}$ represents a Gaussian distribution with mean $\mu\prime$ and standard deviation σ'. The standard deviation σ' is derived as covariance matrix [18] $V_{ij} = \mathrm{cov}[\hat{\theta}_i, \hat{\theta}_j]$ of the estimators $\hat{\theta}_i$ of all NP θ_i. The approximation holds if the last term, that depends on the sample size N, can be neglected. In that regard the data and background yields must be large enough in all bins, usually minimum $\mathcal{O}(10)$ events in a bin, condition already fulfilled in all six channels from Figure 6.1 and 6.2.

Ref [214] shows in Eq. [19] and [55] that with the above formula $f(q_\mu|\mu)$ is expressed asymptotically as a non-central χ^2 distribution, which for the simple case $\mu = \mu'$ is a central half-χ^2 distribution:

$$f(q_\mu|\mu) = \frac{1}{2}\delta(q_\mu) + \frac{1}{2}\frac{1}{\sqrt{2\pi}}\frac{1}{\sqrt{q_\mu}}e^{-q_\mu/2} \tag{6.6}$$

Eq. 6.4 receives hence an asymptotic approximation:

$$Z = \Phi^{-1}(1-p_\mu) = \sqrt{q_\mu} \tag{6.7}$$

Exclusion *p*-values When no discovery is made, various regions in signal parameter space (signal hypotheses) are excluded by calculating the p-value on H_1, which is tested against H_0. The p-value here represents the probability that the observed dataset is actually compatible with the given signal hypothesis H_1, compared to other LHC datasets that could be taken. If that probability is too low, the respective H_1 is safe to be rejected, in practice at $p < 0.05$, equivalent to $Z = 1.64$ standard deviations away from the mean, also called at $1 - 0.05 = 95\%$ confidence level (CL). The regions not excluded can be re-investigated in follow-up measurements with higher sensitivity.

Modified *p*-values In experiments with low signal sensitivity, $H_0 \sim H_1$, which would mean that rejecting the $S + B$ could accidentally reject B as well. A modified p-value is employed to correct such a situation [215]:

$$CL_s = \frac{p_1}{1-p_0}, \tag{6.8}$$

which ensures that when H_1 is rejected, H_0 is accepted.

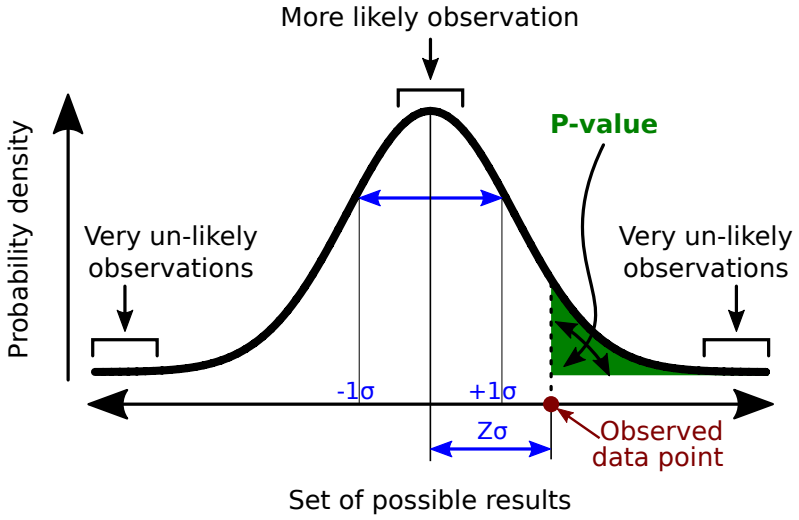

Figure 6.3.: A p-value (shaded green area) is the probability of an alternative (or more extreme) result, under the assumption of the null hypothesis. Only the right tail is investigated, also called a *one-sided p-value*. The intuitive meaning of the exclusion p-value is described in the text. [218]

6.2.3. Hypothesis Testing in the Presence of Interference Effects

The formula $\mu \cdot S + B$ from Eq. 6.1 must be modified to include the interference effect as well. Considering that in Eq. 4.14 and 4.15 S has an amplitude at the power of two, while I is at the power one, the shape of the binned reconstructed $m_{t\bar{t}}$ for each signal point listed in Section 5.2.3 can be parametrized linearly as:

$$\mu \cdot S + \sqrt{\mu} \cdot I + B = \sqrt{\mu} \cdot (S + I) + (\mu - \sqrt{\mu}) \cdot S + B, \tag{6.9}$$

where, as usual, S represents the pure resonant signal, I the interference term and B the total background dominated by SM $t\bar{t}$. Given that pure S cannot be separated from B, the physical manifestation of the resonance cannot be described with S only, but as the inclusive $S + B + I$, from which $S + I$ is a technical trick. The right-hand side of the equation is preferred in the limit setting because $S + I$ can be straightforwardly added to the expected background distribution and because it ensures a positive parameter of interest (PoI) $\sqrt{\mu}$. Its second term shows that S is however needed for setting the limits. The case $\mu = 1$ corresponds to the type-II 2HDM defined in Section 4.1.2.

The test statistics q_μ is scanned and the largest μ that satisfies $p_\mu \leq 0.05$ is chosen as upper limit μ_{up} at 95% CL. μ_{up} is hence at $Z\sigma$ distance from $\hat{\mu}$ [214]:

$$\mu_{up} = \hat{\mu} + \sigma \cdot Z = \hat{\mu} + \sigma \cdot \Phi^{-1}(1 - \alpha), \qquad \text{where} \quad \alpha = 0.05 \tag{6.10}$$

The signal strength is scanned in this analysis with the constraint $0 \leq \hat{\mu} \leq \mu$. The constraint $\hat{\mu} \leq \mu$ is due to the fact that a one-sided p-value is employed. Data with $\mu < \hat{\mu}$ does not necessarily show less compatibility, thus q_μ is set in those regions to 0. Moreover, $0 \leq \mu$ because μ is employed with square root.

The above μ_{up} is called *observed* and measured by scanning the test statistics on the full dataset. To derive the so-called *expected* μ_{up}, the test statistics is scanned on an artificial dataset called *Asimov*. In the Asimov dataset the bin-by-bin yields are consistent with the expected background yields. Hence now $\hat{\mu}$, the best estimate for μ, is set to zero.

The expected upper limits are derived with Eq. 6.7 and 6.10. The expected median upper value is derived by solving the Asimov test statistics for α =0.05:

$$q_{\mu_{up}^{med},\ Asimov} = 1.64^2, \tag{6.11}$$

which allows then the calculation of σ as:

$$\sigma^2 = \frac{(\mu_{up}^{med})^2}{q_{\mu_{up}^{med},\ Asimov}}, \tag{6.12}$$

and the 1–2 σ error bands as:

$$\mu_{up+n} = \sigma \cdot (\Phi^{-1}(1-\alpha) + n), \qquad \text{where} \quad n = 1, 2 \tag{6.13}$$

6.2.4. Profile Likelihood Fit under the Background-only Hypothesis

The above formalism is implemented in a framework based on the tools RooStats [219], RooFit [220] and HistFactory [221].

The data has abundant statistics, which increases the possibility of having a full fluctuation. Exploiting this fact, the NPs are allowed to vary from their original central value to their best fit MLE, in a background-only ($\mu = 0$) fit to the dataset. The phenomenon is called *NP pull*. When real data is used (Figure 6.5), the NP central values will be pulled away from the expected θ_0 to the MLE $\hat{\theta}$, in order to minimise the difference between data and background expectation within the known uncertainties. When Asimov data is used (Figure 6.4), the NPs remain centred at the nominal θ_0, since the nominal background prediction is not changed and only the sizes of the systematic uncertainties are constraint. The non-centrality of a NP θ can be described as:

$$\text{pull}_\theta = \frac{\hat{\theta} - \theta_0}{\sigma_\theta}, \tag{6.14}$$

with the parameters as defined for Eq. 6.2. The systematic effects are considered uncorrelated before the fit, but because all NPs are constrained by the same dataset, some of them become correlated or anti-correlated through the fit. NPs of similar shape are for example anti-correlated: when one is scaled with one variation up to correct for a mismodelling, the other must be scaled down to not over-correct. The treatment of the NP correlations is considered as well, as a covariance matrix [18] of the NP estimators, similarly to Ref. [22], to which the correlation matrix can be seen in Figure [55] of its ATLAS internal documentation [153].

Figure 6.4 and Figure 6.5 illustrate the constraints of the NPs after a profile likelihood fit under the background-only hypothesis, respectively to the Asimov data and to the full 8 TeV dataset.

Both types of profiling fit constrain similarly the uncertainty sizes, most notable being the ones with high impact on the background yield[2], corresponding to the SM $t\bar{t}$ (cross-section, top quark mass, MC generator) and PDF, whose effects are now considerably constraint (reduced).

These large constraints on the modelling uncertainties are due to the fact that they are estimated in a coarse way, by simply comparing two generators. This likely overestimates the uncertainties, while the data-background agreement is usually much better, hence the heavy constraints. This is a generally accepted phenomenon, for lack of a better alternative at the moment.

The pulls in Figure 6.5 are useful in quantifying the agreement between data and background pulls and the relative size of the uncertainties constraints. The strongest pulls are found at the SM $t\bar{t}$ cross-section uncertainty, of 1 σ pre-fit standard deviation upwards, and of more than 1 σ downwards at the data-driven multijet estimation in the electron channel. The former is due to mismodelling in the lowest $m_{t\bar{t}}$ bins, close to the turn-on region. The latter is due to insufficient statistics in the multijets estimation.

The post-fit $m_{t\bar{t}}$ spectra using real data have been used as well as input for BumpHunter in [22]. The observed (data) mass has a very high compatibility with the post-fit background spectrum, as can be seen in Figure 6.6 for the muon channel and Figure 6.7 for the electron channel, separately for each b-tagging category. The uncertainty bands have been much reduced as well, in comparison to the pre-fit bands in Figure 6.1 and Figure 6.2.

6.2.5. Upper Limits Interpretation in 2HDM

As a last step in the signal exclusion procedure, the upper limits on μ are derived from fitting under the $S+I+B$ hypothesis given by Eq. 6.9, by varying the PoI $\sqrt{\mu}$ and the NPs. The scan on the test statistics of μ assumes that the shape templates of $m_{t\bar{t}}$ for S and especially $S+I$ remain constant. A change in μ corresponds to a change in cross-section and hence in couplings of the Higgs states to the top and bottom quarks, which would modify the width and hence the shape of the interference pattern. However, for a very first public result on interference effects [1], this simplifying assumption was a good approximation, that was explicitly stated.

Tables 6.2 to 6.5 list the expected upper limits (median and margins of the 1σ and 2σ bands) and observed upper limits on μ, at 95% CL, separately for each signal parameter point.

It should be noted that the cross-section of $S+I$ is not well defined theoretically, therefore no cross-section limits can be derived. Moreover, at the time of this analysis, an interpolation between mass points in order to exclude masses was not yet possible. This was due to concerns regarding a full cancellation between peak and dip ("nothingness") in some points of the signal parameter space, for example at $m_H = 550$ GeV [222]. Hence no exclusions in the two-dimensional mass-tan β plane are derived, but only one-dimensional in the tan β parameter space (considering $\sin(\beta-\alpha)=1$), separately for the mass points 500 and 750 GeV and separately for A and H, as shown in Figure 6.8. The line $\mu = 1$ represents the investigated type-II 2HDM model and the region below its crossing with the observed line becomes excluded in the model, at 95% CL. The

[2] There are as well NPs with impact on μ, which show how the limits will change when one NP is varied or eliminated and depends on the tested signal hypothesis. These impacts are left for follow-up analyses.

observed upper limits points are connected linearly rather than interpolated, because one cannot assume a baseline function for the interpolation, that would correctly describe the limit points. The observed line is within $\pm 2\,\sigma$ from the expected line, another sign that there is no significant deviation from the background-only hypothesis.

For the neutral pseudoscalar A (scalar H) with a mass of 500 GeV, the region excluded is $\tan\beta < 0.85$ ($\tan\beta < 0.45$). At masses of 750 GeV the respective lines would cross at $\tan\beta < 0.3$ (if crossing at all), which is a region excluded already by the perturbativity conditions (end of Section 4.1.2). Hence no $\tan\beta$ values are excluded in this model at 750 GeV.

Appendix D.2 describes an alternative signal region exclusion approach, based on the CLs technique, that avoids the assumption of constant $m_{t\bar{t}}$ shape template. The exclusion regions are however identical and the μ-scan method is preferred because it provides more information for re-interpretation in other models.

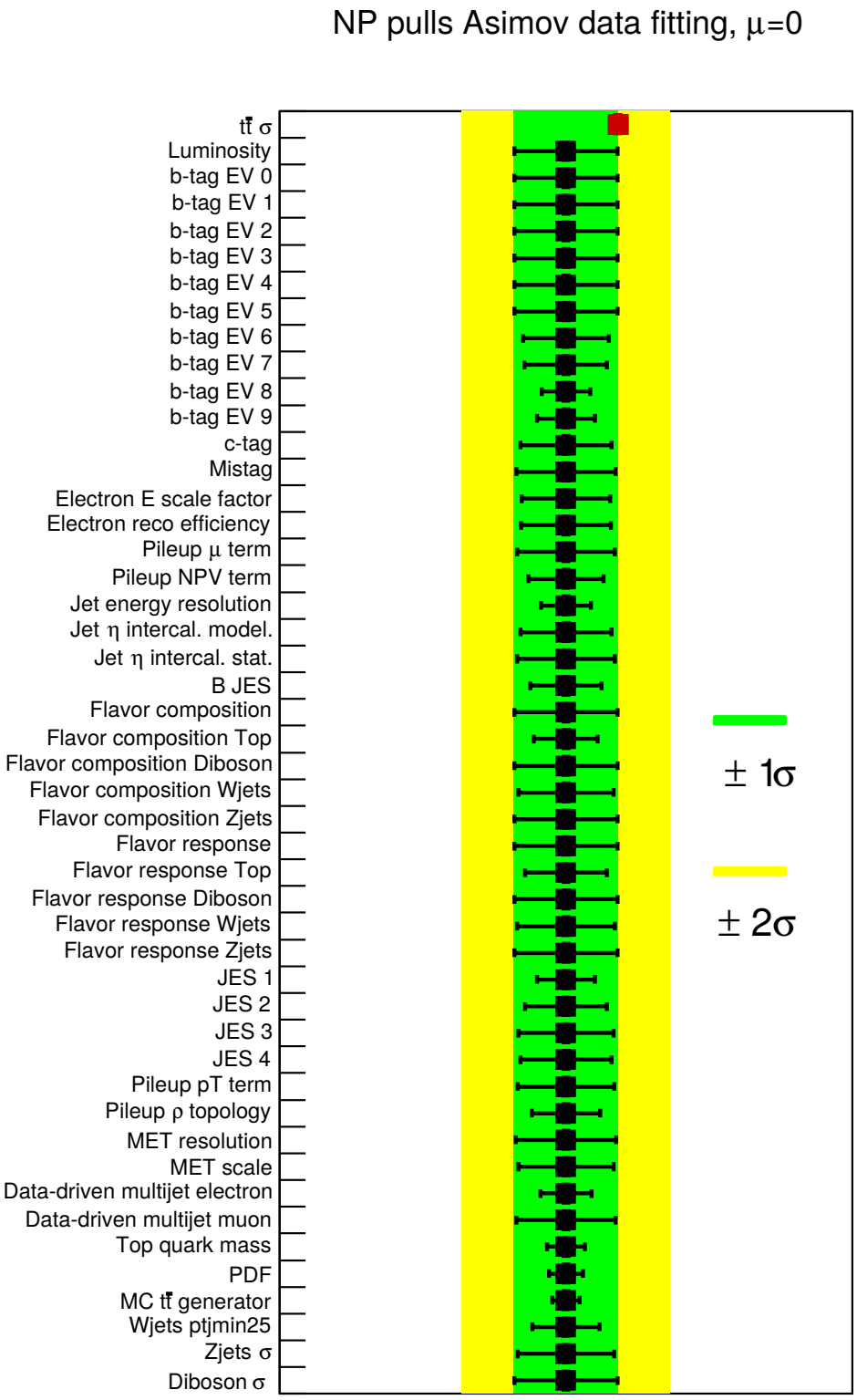

Figure 6.4.: Constraints of the nuisance parameters after a profile likelihood fit, under the background-only hypothesis, to the **Asimov data** (expected nominal background). The green (yellow) bands represent the 1 (2) σ pre-fit standard deviation of the NPs. The error bars represent the constraints, or post-fit 1 σ standard deviation. All six channels are fit concurrently.

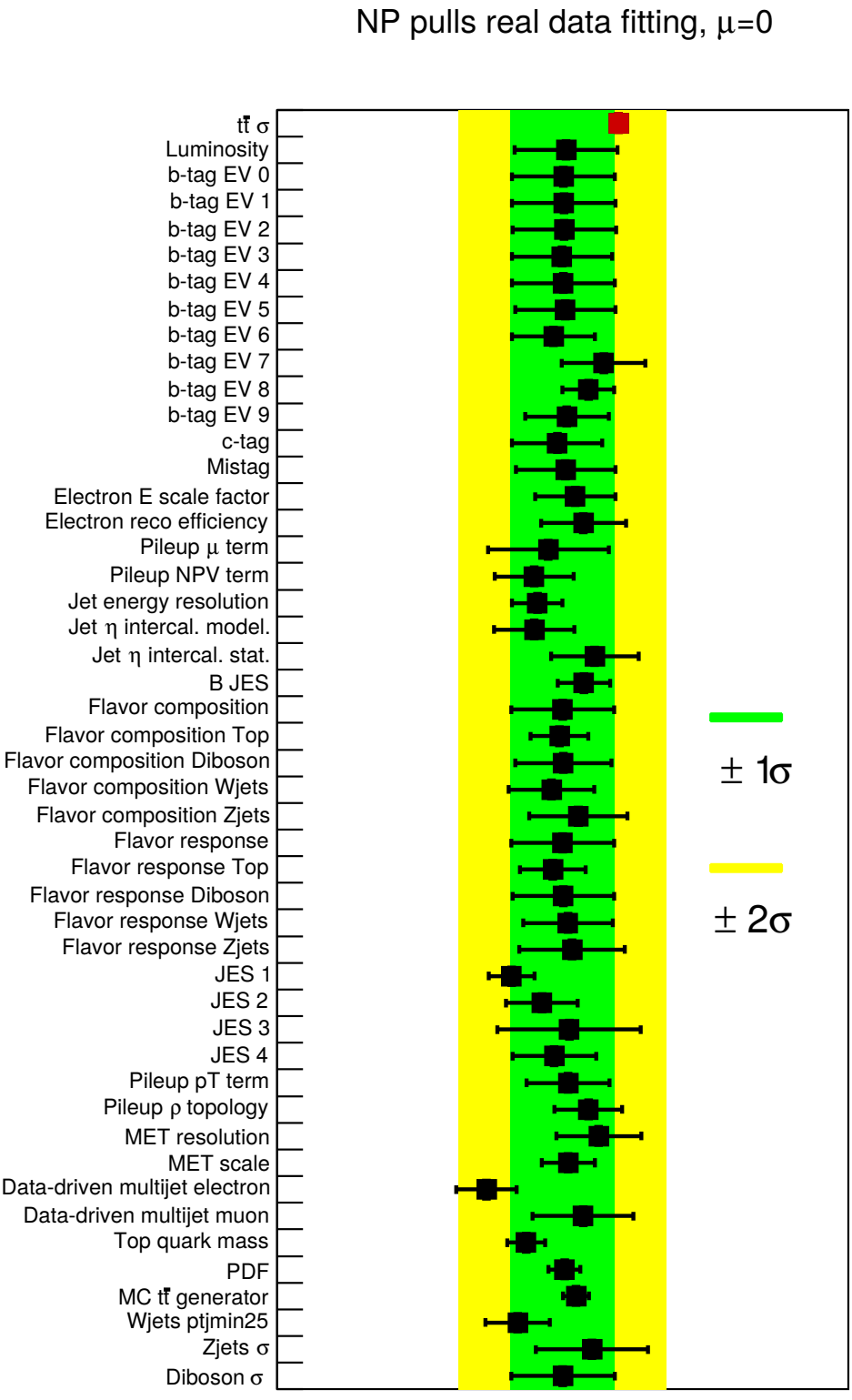

Figure 6.5.: Pulls and constraints of the nuisance parameters after a profile likelihood fit, under the background-only hypothesis, to the **full 8 TeV dataset**. The green (yellow) bands represent the 1 (2) σ pre-fit standard deviation of the NPs. The pulls correspond to the deviation of the central markers from the middle of the green band. The error bars represent the constraints, or post-fit 1 σ standard deviation. All six channels are fit concurrently.

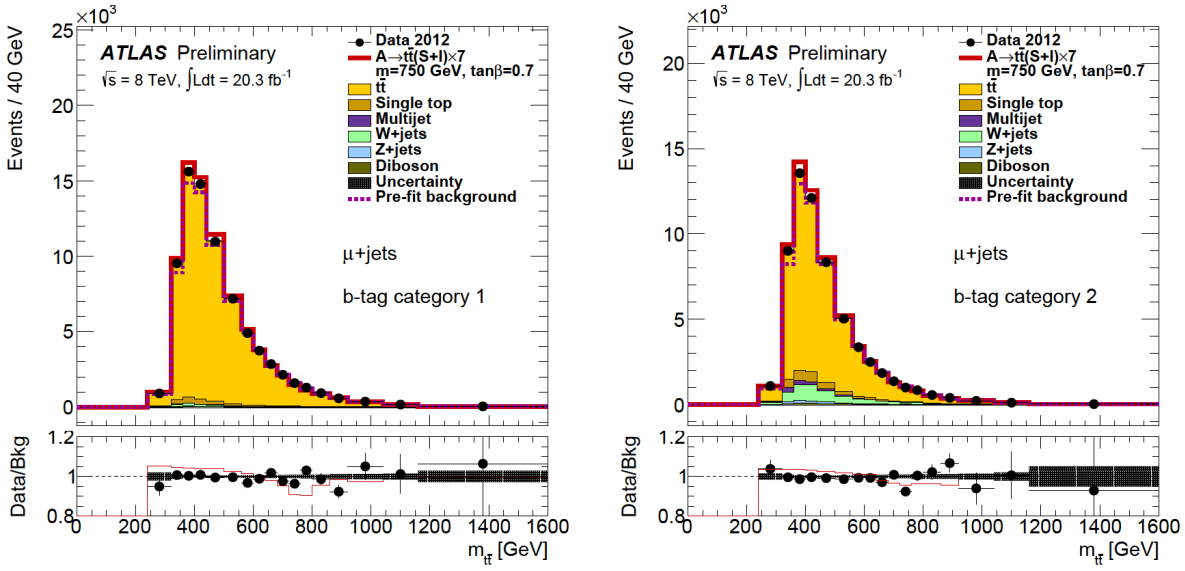

(a) *b*-tagging category 1 **(b)** *b*-tagging category 2

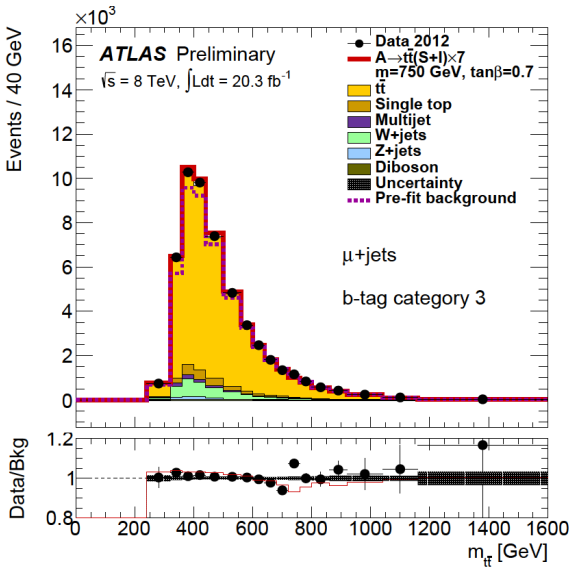

(c) *b*-tagging category 3

Figure 6.6.: Distribution of the reconstructed invariant $m_{t\bar{t}}$ in the μ+jets channel after the profile-likelihood fit (**post-fit**). The post-fit total background shows improvement in the agreement to data, in comparison to the total pre-fit background (dashed line). The *red line* represents the distribution of the hypothetical pseudoscalar A with $m_{\mathrm{A}} = 750$ GeV, displayed scaled by a factor of seven. The *shaded area* represents the total constrained uncertainty on the background. The *bottom pads* show the ratio of data over background and signal+background over background, respectively.

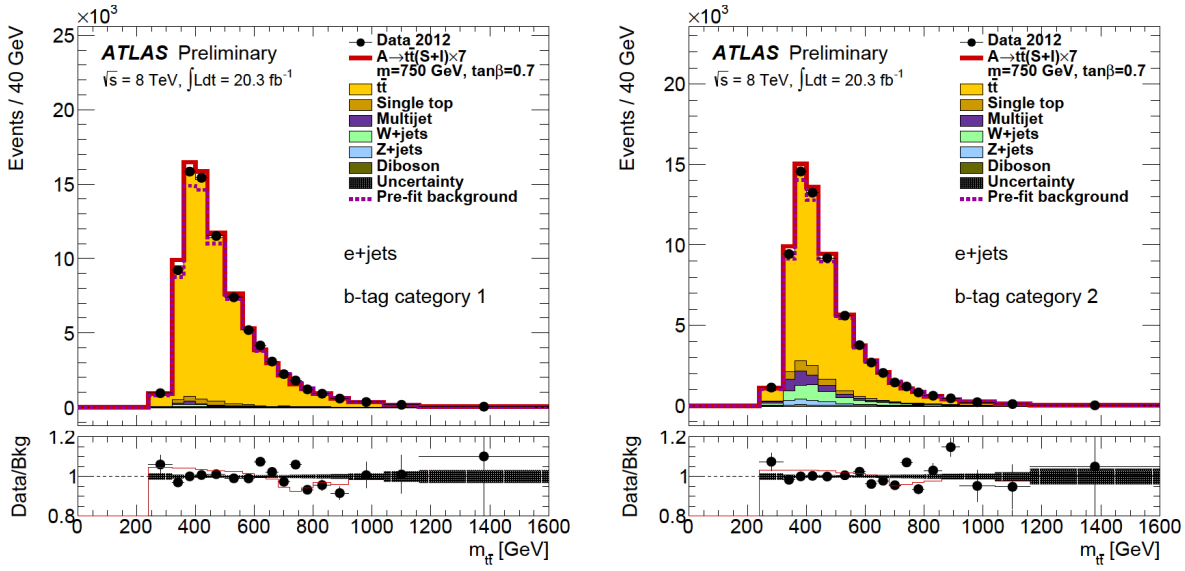

(a) *b*-tagging category 1

(b) *b*-tagging category 2

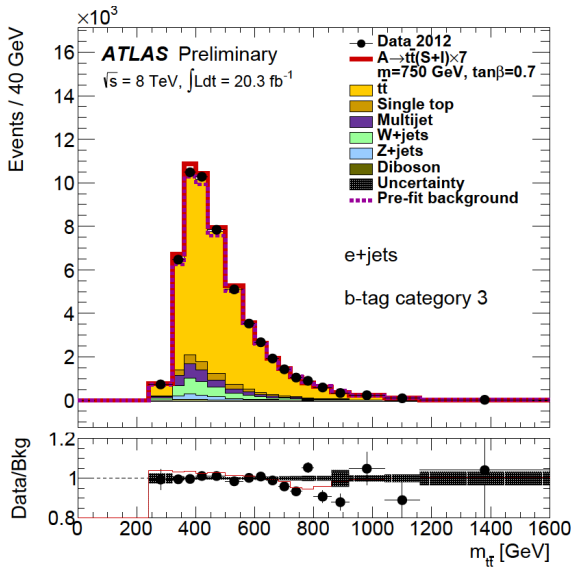

(c) *b*-tagging category 3

Figure 6.7.: Distribution of the reconstructed invariant $m_{t\bar{t}}$ in the e+jets channel after the profile-likelihood fit (**post-fit**). The post-fit total background shows improvement in the agreement to data, in comparison to the total pre-fit background (dashed line). The *red line* represents the distribution of the hypothetical pseudoscalar A with $m_{\mathrm{A}} = 750$ GeV, displayed scaled by a factor of seven. The *shaded area* represents the total constrained uncertainty on the background. The *bottom pads* show the ratio of data over background and signal+background over background, respectively.

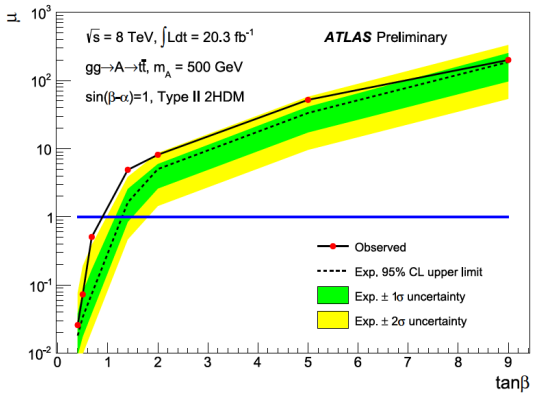

(a) neutral pseudoscalar A, $m_A = 500$ GeV exclude $\tan\beta < 0.85$

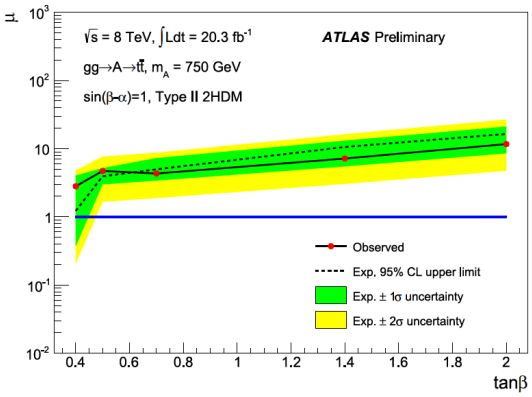

(b) neutral pseudoscalar A, $m_A = 750$ GeV

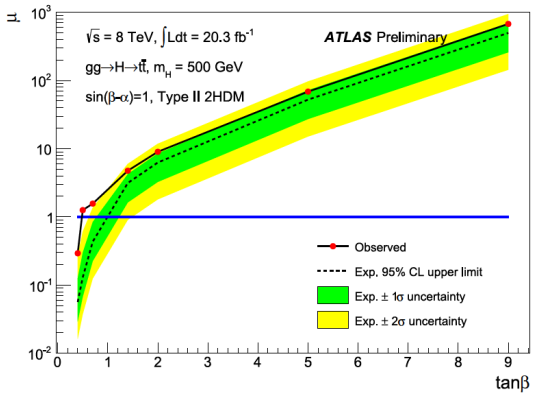

(c) neutral scalar H, $m_H = 500$ GeV exclude $\tan\beta < 0.45$

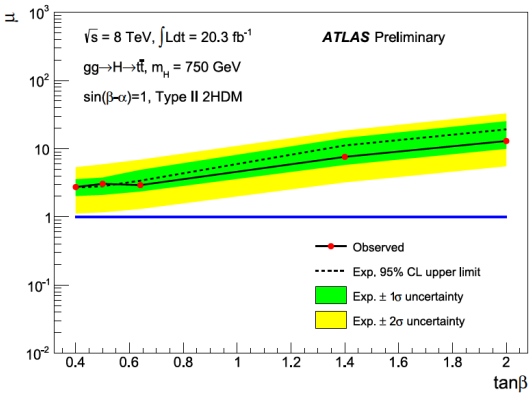

(d) neutral scalar H, $m_H = 750$ GeV

Figure 6.8.: Observed and expected upper limits on the signal strength parameter μ, as a function of the parameter $\tan\beta$, based on the μ scan technique. The blue line at $\mu = 1$ represents the type-II 2HDM defined in Section 4.1.2, and its crossing with the observed line sets the exclusion regions.

$\tan\beta$	Γ [GeV]	Exp. Median	Exp. [-1 σ, +1 σ]	Exp. [-2 σ, +2 σ]	Observed
0.40	142.95	0.018	[0.009, 0.038]	[0.005, 0.077]	0.025
0.50	91.48	0.034	[0.017, 0.078]	[0.009, 0.190]	0.073
0.68	49.46	0.074	[0.038, 0.168]	[0.021, 0.386]	0.508
1.40	11.68	1.63	[0.84, 2.56]	[0.47, 3.85]	4.89
2.00	5.75	5.02	[2.60, 5.95]	[1.44, 8.65]	8.13
5.00	1.14	33.36	[17.32, 41.10]	[9.60, 57.64]	51.93
9.00	1.02	186.37	[96.76, 252.05]	[53.68, 330.80]	199.57

Table 6.2.: The observed and expected upper limits on μ at 95% CL, for the pseudoscalar A with $m_A = 500$ GeV.

$\tan\beta$	Γ [GeV]	Exp. Median	Exp. [-1 σ, +1 σ]	Exp. [-2 σ, +2 σ]	Observed
0.40	230.23	1.22	[0.37, 4.04]	[0.20, 4.79]	2.81
0.50	147.35	3.93	[2.99, 5.17]	[1.66, 7.67]	4.71
0.70	75.18	4.98	[3.40, 7.28]	[1.89, 8.73]	4.32
1.40	18.82	10.58	[5.49, 13.12]	[3.04, 16.30]	7.16
2.00	9.26	16.46	[8.54, 21.12]	[4.74, 26.71]	11.68

Table 6.3.: The observed and expected upper limits on μ at 95% CL, for the pseudoscalar A with $m_A = 750$ GeV.

$\tan\beta$	Γ [GeV]	Exp. Median	Exp. [-1 σ, +1 σ]	Exp. [-2 σ, +2 σ]	Observed
0.40	80.55	0.056	[0.029, 0.125]	[0.016, 0.273]	0.292
0.50	51.55	0.129	[0.067, 0.298]	[0.037, 0.610]	1.257
0.70	26.30	0.433	[0.225, 0.842]	[0.124, 1.370]	1.565
1.40	6.59	3.13	[1.62, 4.23]	[0.90, 6.00]	4.75
2.00	3.25	6.27	[3.25, 8.51]	[1.80, 11.82]	9.00
5.00	0.90	52.30	[27.15, 71.96]	[15.06, 96.81]	68.58
9.00	0.74	497.32	[258.21, 691.85]	[143.26, 941.02]	673.77

Table 6.4.: The observed and expected upper limits on μ at 95% CL, for the scalar H with $m_H = 500$ GeV.

$\tan\beta$	Γ [GeV]	Exp. Median	Exp. [-1 σ, +1 σ]	Exp. [-2 σ, +2 σ]	Observed
0.40	189.64	2.68	[2.02, 3.56]	[1.12, 5.34]	2.73
0.50	121.37	2.81	[2.10, 3.76]	[1.16, 5.89]	3.05
0.64	74.08	3.39	[2.35, 4.88]	[1.30, 6.88]	2.92
1.40	15.50	11.15	[5.78, 14.31]	[3.21, 18.43]	7.58
2.00	7.63	19.19	[9.96, 25.24]	[5.52, 32.79]	12.94

Table 6.5.: The observed and expected upper limits on μ at 95% CL, for the scalar H with $m_H = 500$ GeV.

Chapter 7.

Summary and Outlook

Summary

This analysis is the first one at the LHC that considers and treats statistically the interference (I) between signal (S) and background (B), in this case in the $t\bar{t}$ final state. Constraints are derived in the parameter region of large Higgs boson masses and low $\tan\beta < 10$ for a generic type-II 2HDM in the alignment limit, a region not well covered by searches in any other final state [19].

The resonances investigated are the neutral heavy spin-0 Higgs bosons, the CP-odd A and CP-even H, produced via gg-fusion and decaying to $t\bar{t}$, $gg \to A/H \to t\bar{t}$, since the low $\tan\beta$ enhances the coupling of A/H to t. The intermediate t/b loop in the gg-fusion yields a strong interference of the scalar with the dominant SM continuum background $gg \to t\bar{t}$, that distorts the Breit-Wigner resonance peak of the scalar into a peak-dip structure. The analysis required a dedicated and challenging generation of $S + I$, that removed the B contribution from the inclusive $S + B + I$.

The search is conducted on the full pp collisions dataset recorded by ATLAS at $\sqrt{s} = 8$ TeV, corresponding to an integrated luminosity of 20.3 fb^{-1}. The $t\bar{t}$ invariant mass is reconstructed in signal candidate events with a high-transverse momentum electron or muon, large missing transverse energy and at least four jets. No significant deviation from the expected SM background is observed in data in the $m_{t\bar{t}}$ spectrum.

Exclusion limits are derived in the context of type-II 2HDM model [6]. The lighter of the two CP-even spin-0 states, of the model, h, is assumed to have the couplings of the discovered SM Higgs boson, which sets the alignment limit $\sin(\beta - \alpha) = 1$. Upper limits on the signal strength μ are derived at 95% CL for each A and H state separately, for the 500 and 750 GeV mass points, in the low $\tan\beta$ parameter space. It is assumed that the complex phase of the I term and hence the shape of $m_{t\bar{t}}^{S+I}$ does not change with μ. The observed $\tan\beta$ exclusion limits are reported at 95% CL for $\mu = 1$, which represents the type-II 2HDM model. At 500 GeV, the region excluded for the pseudoscalar A is $\tan\beta < 0.85$, while for the scalar H it is $\tan\beta < 0.45$. At 750 GeV no meaningful upper limits can be set, hence the exclusion of $\tan\beta \leq 0.3$, required already to ensure that the Yukawa coupling of the top quark is perturbative (end of Section 4.1.2), is further adopted.

Recognition

The analysis is published in Ref. [1], together with its ATLAS internal documentation in Ref. [4], and was presented at the 38th International Conference on High Energy Physics [223]. Furthermore, the limits provided by this analysis have been recast by phenomenologists to set bounds on spin-0

pseudoscalar mediators that interact directly with the dark matter [224]. This analysis set as well grounds for the interference treatment in vector-like quarks $T/Y \to Wb$ [225].

Outlook

This analysis has been continued and improved upon with a follow-up analysis at $\sqrt{s} = 8$ TeV from Ref. [21]. The one-dimensional $\tan\beta$ exclusion has been extended to the $m_{A/H} - \tan\beta$ plane by increasing substantially the signal parameter points through an event-by-event reweighting procedure, based on ratios of amplitude contributions. Reweighting avoids the detector simulation, reducing hence substantially the computing time. The "nothingness" phenomenon mentioned in Section 6.2.5 is also investigated and it is proved that no cancellation occurs, hence the interpolation in mass is safe.

In this follow-up analysis, the correction factor k_I on the normalisation of the interference term $I = (S + I) - S$ is taken as $\sqrt{k_S \times k_B}$, where k_S and k_B correct the signal and background MadGraph5 cross-sections to the ones computed at NNLO. This approach is recommended in Ref. [226] to improve the $k_I = k_S$ approach used in this thesis.

The search treats the states A and H as simultaneously contributing to the $m_{t\bar{t}}$ spectrum, an approach recommended by the LHC Dark Matter Working Group for the pseudoscalar mediator benchmark, where A and H are assumed degenerate [227].

CMS performed a similar analysis at $\sqrt{s} = 13$ TeV and integrated luminosity of $\int L(t)\ \mathrm{d}t = 36\ \mathrm{fb}^{-1}$ [228], extending the interpretation from the generic 2HDM to hMSSM [17, 18], where A and H are not degenerate any more, but have a small mass splitting between them. Limits as a function of a generalised coupling are included as well. These improvements are planned likewise for the ATLAS search at $\sqrt{s} = 13$ TeV.

The modelling of the interference has been in the meantime improved as well to approximate NLO accuracy in QCD [132]. A better sensitivity at higher $\tan\beta$ (narrower interference patterns) can be also achieved by improving the $m_{t\bar{t}}$ resolution with the new particle flow algorithm [229] and dedicated calibrations [230]. All these results will improve the accuracy of future searches.

Appendix A.

Particle Detection Principles

The following sections describe the interaction of particles through matter in a general purpose detector such as ATLAS.

A.1. Interactions of Particles in Matter

Interactions of Charged Particles (Figure A.1)

At intermediate energies $0.1 \leq \beta\gamma \leq 1000$, a charged particle leaves an ionisation trail. Its mean ionisation loss $\langle -dE/dx \rangle$ follows the Bethe-Bloch formula, for simplicity without corrections [51]:

$$\left\langle -\frac{dE}{dx} \right\rangle \propto \frac{z^2 Z}{A\beta^2} \left(\frac{1}{2} \ln \frac{2m_e c^2 \gamma^2 \beta^2 T_{\max}}{I^2} - \beta^2 \right), \tag{A.1}$$

where z is the particle's charge, $Z(A)$ the matter's atomic number (mass), $\beta = v/c$, $\gamma = 1/\sqrt{1-\beta^2}$, $T_{\max}$ the maximum energy transfer to an electron in matter, I the matter's excitation energy. The ionisation is proved to decrease with increasing Z. Hence trackers should be low in Z, considering that a high-Z material gives as well high scattering.

The particle slows down in matter and the ionisation $\langle -dE/dx \rangle$ increases with the decreasing momentum. At $\beta\gamma = 3 - 4$, or momentum 1 MeV for electrons, 300–400 MeV for muons and pions, 3 GeV for protons, the $\langle -dE/dx \rangle$ is minimum, called a *minimum ionising particle mip*.

After a threshold E_c called *critical energy*, the linear radiative loss dominates the logarithmic ionisation loss. Fast charged particles radiate now photons, due to being deviated in the atomic nuclear and electric field, phenomenon called *bremsstrahlung* ("deceleration radiation") [51]:

$$\left\langle -\frac{dE}{dx} \right\rangle = z^2 \left(\frac{m_e}{M} \right)^2 \frac{E}{X_0} \qquad \text{where} \qquad X_0 \propto \frac{A}{Z(Z+1)\ln Z^{-1/3}}, \tag{A.2}$$

where X_0 is the *radiation length* specific to the matter, for example 1.75 cm in iron. Bremsstrahlung is negligible for particles heavier than electrons. Integrating for electrons leads to $E = E_0 e^{-x/X_0}$, with E_0 the initial energy, showing that in one X_0 an electron loses $\approx 65\%$ of its energy.

Interactions of Hadrons

At low energies, hadrons interact with matter nuclei via elastic scatterings. At higher energies the interactions become inelastic and the incoming particle splits a target nucleus in nucleons. At even

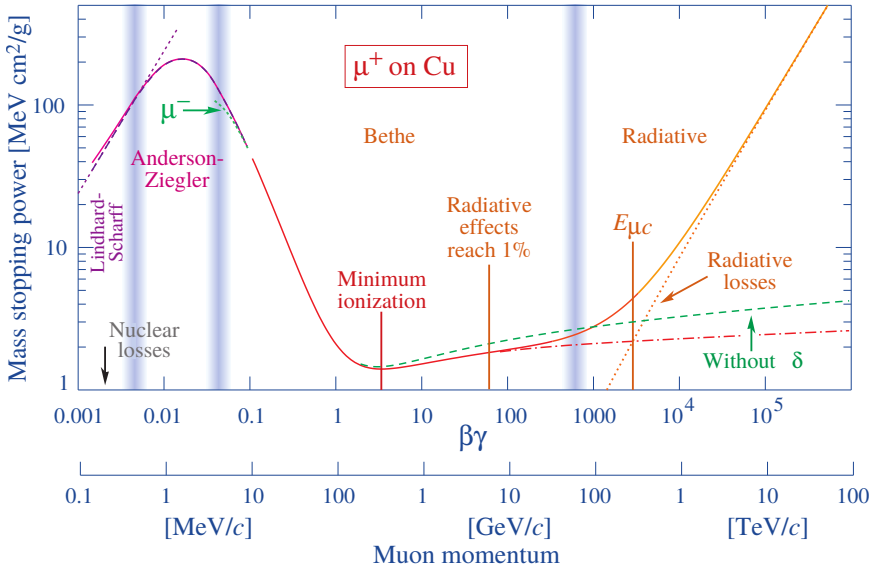

Figure A.1.: Mass stopping power $-dE/dx$ (the solid curve) for positive muons in copper, function of $\beta\gamma = p/(Mc)$, as explained in the text. Ionisation losses are at $0.1 \leq \beta\gamma \leq 1000$, while radiative losses are at higher energies. [51, 231]

higher energies, the interactions are governed by the strong force and create new hadrons, mostly pions. The path $\lambda_{\mathrm{I}} \approx 35 \times A^{1/3}/\rho$ [g/cm^2], called *hadronic interaction length*, with ρ the material density, represents the mean distance travelled by the hadron before an inelastic interaction [231].

Interactions of Muons

Muons are minimum ionising at $p = 300$–400 MeV. Since $m_\mu = 200 \times m_e$, their bremsstrahlung loss is suppressed and their E_{c} is at hundreds of GeV (347 GeV in iron), in comparison to tens of MeV at electrons. Their lifetime is $\tau = 2.2$ µs, thus they decay via the weak force (to electrons and neutrinos) after ≈ 700 m. Muons are moreover not affected by the strong force. Thus muons produced in ATLAS are *mip* over a large energy range and do not usually radiate or decay, having an ionisation of $a \approx 2$ MeV g^{-1}cm^2. A 1 TeV muon passing 3 m through iron loses 23 GeV. [51]

Interactions of Neutrinos

Neutrinos are neutral, have negligible mass and are sensitive only to the weak interaction, with a scattering cross-section $\sigma \approx 10$ [fb] $\times E$ [GeV] (Figure 28 in [232]). Hence for a 10 GeV neutrino produced in ATLAS, the average distance travelled between two interactions in matters is $\lambda = A/(\rho\sigma N_A) > 10^6$ km [51]. Therefore, detectors such as ATLAS cannot detect neutrinos directly, they can only reconstruct neutrinos via the missing transverse energy (Section 5.3.9).

A.2. Silicon Detectors

The silicon detectors operate as p-n junctions: at the interface of two heavily doped p and n semiconductors (p^+ and n^+), the electrons diffuse into the p-type, the holes into the n-type, and the

two form an electric field preventing free carriers to pass (*depletion layer*). To operate as a detector, a *reverse bias* is applied, that increases the depletion layer even more. Charged particles crossing the depletion layer release electron-hole pairs, that drift and get collected by the p/n readout as signals. In time however, strongly ionising particles deposit permanent charge, which issues leakage currents and decreases the collected charge efficiency. This is called radiation damage, and requires temporary solutions such as increasing the cooling, the reverse bias or the oxygenation, until the detector is replaced. [233]

A.3. General Calorimetry

Electromagnetic versus Hadronic Calorimeters

In **EM calorimeters**, at energies above E_c, electrons and photons transform into one another in a cascade of bremsstrahlung and e^+e^- conversions. With X_0 as unit (Eq. A.2), the number of particles at depth $t = x/X_0$ is $N(t) = 2^t$ and their energy $E(t) = E_0 \cdot 2^{-t}$. The maximum particle count is reached when the particles reach E_c, thus $t_{max} \propto \ln(E_0/E_c)$, i.e. the calorimeter should be built in length logarithmically with the initial energies. The lateral shower is determined by multiple scatterings. [233, 234]

In **HAD calorimeters**, if the incoming hadron's energy is high enough, the hadron will trigger a similar exponential cascade of inelastic nuclear interactions in a *hadronic shower*, in unit length λ_I. Since $\lambda_I \gg X_0$, the HAD showers are longer than EM showers. The HAD showers are also wider, since their width is caused by large p_T transfers.

The two calorimeter types allow actually both EM and HAD showers. The electrons and photons lose their energy the fastest and must be stopped in the first calorimeter, called EM, before reaching the next one, HAD, which is thus also allowed a less granularity. EM calorimeters must reach low X_0 via a high Z, while HAD high A and low λ_I.

Hadronic jets have EM content as well, as most jet particles are pions, among which one third are $\pi^0 \to \gamma\gamma$. Thus it is important that the calorimeters respond[1] identically to EM and HAD energies, called **compensation**, via adjusting the absorber vs. sensor thickness, the A and Z, or via offline algorithms.

Calorimeter Energy Resolution

The energy resolution for single particles (since for jets it is more complex) is expressed as:

$$\frac{\sigma_E}{E} = \frac{a}{\sqrt{E}} \oplus \frac{b}{E} \oplus c \tag{A.3}$$

The factor a represents the statistics term and originates from the sampling nature and shower development fluctuations. Homogeneous calorimeters have the best energy resolution. Sampling

[1] The calorimeter response is the average signal per unit of deposited energy.

calorimeters receive in addition a component s/f_{sampling}, with s the sensor thickness and f_{sampling} the ratio of ionisation losses in the sensor layer versus the absorber and sensor together.

The factor b is due to electronic noise, affecting low energy measurements, while the constant term c is due to calibration uncertainties, affecting performance at high energies.

The resolution improves with E, as opposed to the p_{T} resolution, which deteriorates with p_{T}. The HAD calorimeter resolution is much worse than the EM one, since 30–40% of shower remains undetected, due to the energy used to break up nuclear bindings, nuclear fragments stopped early in the absorber or escaping long-lived neutral particles. [51, 233]

Particle Identification

Electrons and photons are discriminated against hadrons based on the position, length and width of their showers, procedure which decides if the shower is EM or HAD. Electrons are discriminated against photons based on the fact that electrons have inner detector tracks associated. Electrons are discriminated against other charged particles with the requirement $E/p = 1$. Combined calorimeter and inner detector measurements allow to calculate the particle mass $m = \sqrt{E^2 - p^2}$, which is used as well to tag the particles.

Appendix B.

Simulation Setup and Validation - NOVELTY

B.1. Setup in MadGraph5_aMC@NLO: Code Excerpts

The following is a code example that generates in MadGraph5_aMC@NLO the signal $gg \to A \to t\bar{t}$ (S), the SM-QCD background $gg \to t\bar{t}$ (B) and their interference (I), for a CP-odd A of mass 500 GeV and for a $\tan\beta$ choice of 0.4. The parameter $\sin(\beta - \alpha)$ is set to 1, to align to SM.

To generate $S + B + I$, generate B with allowing all intermediate processes implemented in the model (QED and QCD couplings parameters set to maximum of 99). Hence A, H and interferences are included as well, while the CP-even H is removed with the flag "/h". The top quarks are explicitly further decayed to the semileptonic and dileptonic channels. The "lhapdf" parton distribution functions library is employed, with PDF set to CT10 (code number 10800). There is no kinematic cut on the decay products ("cut_decays" false), as not to affect the final cross-section. The top mass MT is set to 172.5 GeV, the pseudoscalar mass MP to 500 GeV. Each proton beam has 4 TeV, for a total of $\sqrt{s} = 8$ TeV. The total width of A is WH1, provided by 2HDM calculators (Section 4.1.2) for the given choice of $\tan\beta$ and $\sin(\beta - \alpha)$. The couplings to t and b are calculated based on their Yukawa coefficients from Table 4.1, as $m_{t,b} \cdot c_{t,b}$.

To generate $S + I$, this code remains unchanged, while a separate code removes the B amplitudes. $S + I$ must be however generated in one single run of the maximum allowed 1 million events, to allow the generator to converge.

```
import model Higgs_Effective_Couplings_FormFact
define l+ = e+ mu+ ta+
define l- = e- mu- ta-
define j = g u c d s u~ c~ d~ s~ b b~

generate g g > t t~ / h QED=99 QCD=99, (t > b w+, w+ > l+ vl),
(t~ > b~ w-, w- > j j) @1
add process g g > t t~ / h QED=99 QCD=99, (t > b w+, w+ > j j),
(t~ > b~ w-, w- > l- vl~) @2
add process g g > t t~ / h QED=99 QCD=99,  (t > b w+, w+ > l+ vl),
(t~ > b~ w-, w- > l- vl~) @3

output <directory>
```

```
launch
set pdflabel 'lhapdf'
set lhaid 10800
set cut_decays F
set MT  172.5
set MP  500
set WH1  142.950490
set YMT 431.250000
set YMB 1.880000
set nevents 1000000
set ebeam1 4000
set ebeam2 4000
```

To generate only signal, the processes are replaced with:

```
generate g g > h1,( h1 > t t~,(t > b w+,w+ > l+ vl),(t~ > b~ w-,w- > j j))@1
add process g g > h1,( h1 > t t~,(t > b w+,w+ > j j),(t~ > b~ w-,w- > l- vl~))@2
add process g g > h1,( h1 > t t~,(t > b w+,w+ > l+ vl),(t~ > b~ w-,w- > l- vl~))@3
```

, where $h1$ is the symbol for A. All processes are generated with the normalisation and factorisation dynamical scales set to $\sqrt{\sum_{\text{decay products}}(p_{\text{T}}^2 + m^2)}$.

B.2. Validation of the $S + I$ Generation

Figures B.1 to B.3 illustrate the "direct" approach to generate $S + I$ in MadGraph5, cross-validated with the "indirect" approach as in Section 4.3.1. In the "indirect" approach the $S + B + I$ and B samples have 600 million events. All distributions are at parton level, with no ISR or FSR. The top quarks are decayed as well in MadGraph5. The two approaches show good agreement.

B.3. Validation of the $S + I$ Showering

Figures B.4 to B.5 illustrate truth jets level comparison between various shower test configurations, as in Section 4.4.2.

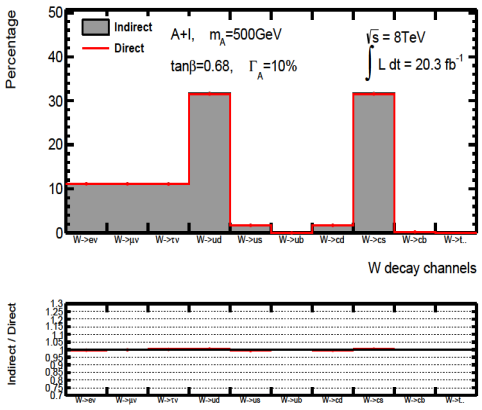

(a) $A + I$, W decay BR

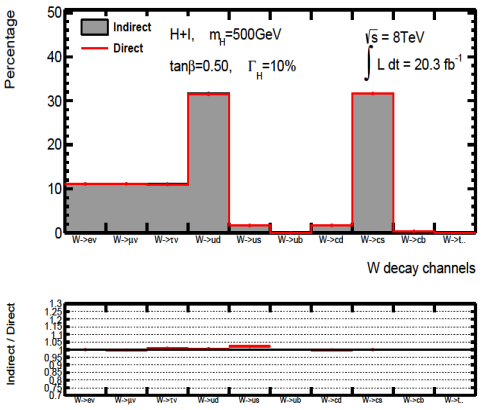

(b) $H + I$, W decay BR

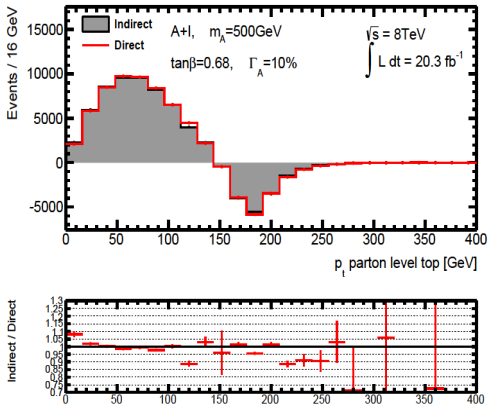

(c) $A + I$, top quark p_{T}

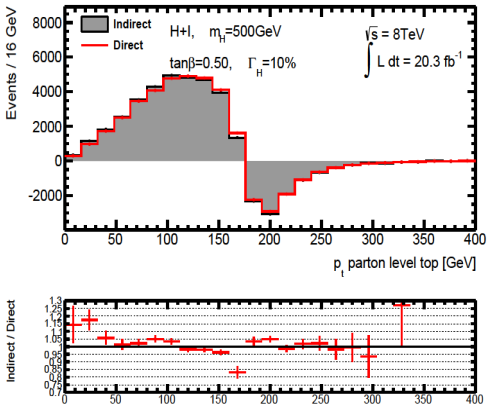

(d) $H + I$, top quark p_{T}

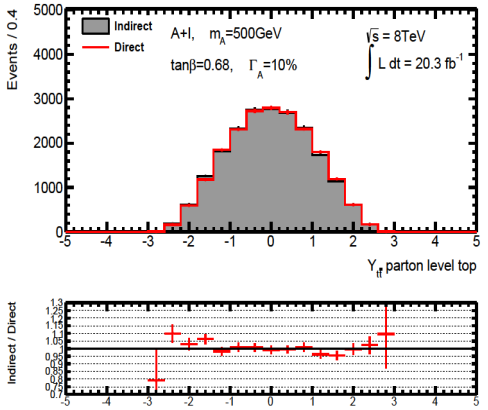

(e) $A + I$, $Y_{t\bar{t}}$

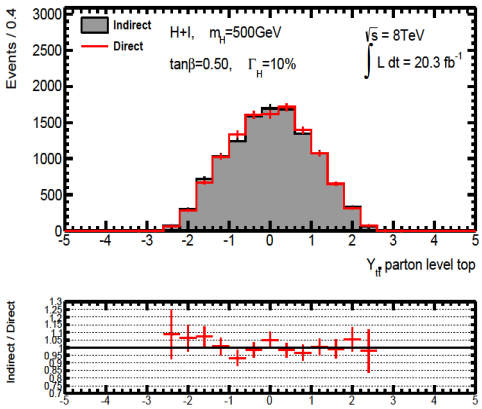

(f) $H + I$, $Y_{t\bar{t}}$

Figure B.1.: Comparison between "indirect" and "direct" approach to generate $S + I$ for A (left) and H (right), at scalar mass points 500 GeV and total decay widths of 10% from the mass point: W decay channels, showing the correct theoretical BR (first row), top quarks transverse momentum (second row) and $t\bar{t}$ pseudorapidity (third row).

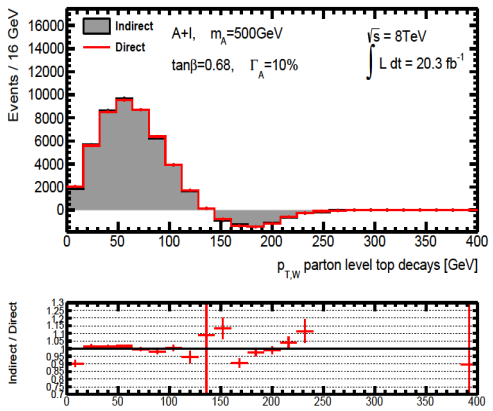

(a) $A + I$, W p_{T}

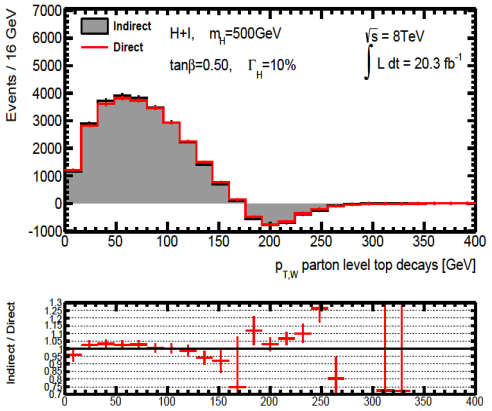

(b) $H + I$, W p_{T}

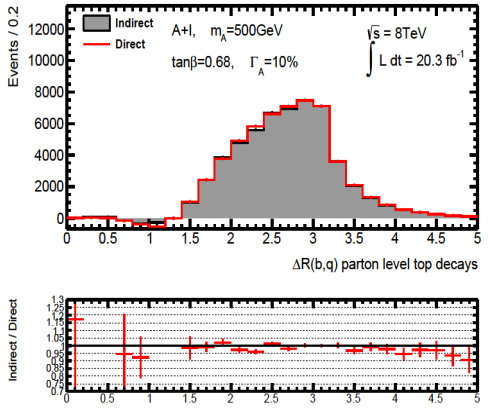

(c) $A + I$, $\Delta R(b, q)$

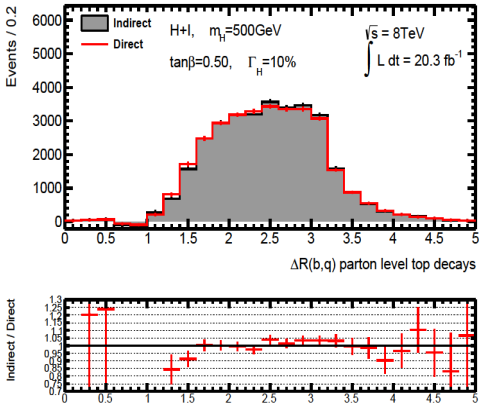

(d) $H + I$, $\Delta R(b, q)$

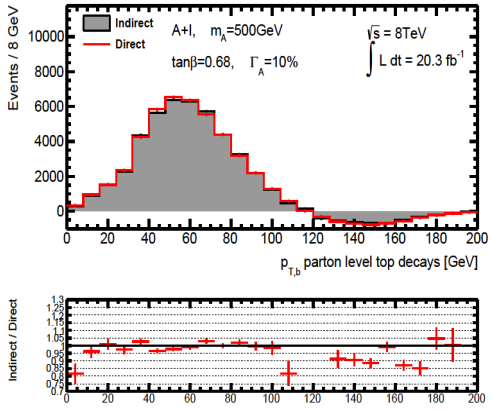

(e) $A + I$, b quark p_{T}

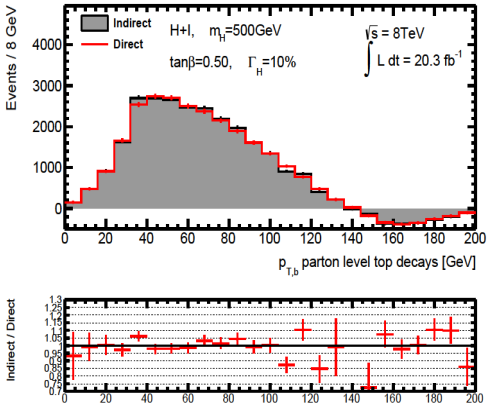

(f) $H + I$, b quark p_{T}

Figure B.2.: Comparison between "indirect" and "direct" approach to generate $S + I$ for A (left) and H (right), at scalar mass points 500 GeV and total decay widths of 10% from the mass point: transverse momentum of W as sum of its two quarks or lepton+neutrino (first row), the ΔR angle between the b-quark and the two quarks from the W decay (second row), the transverse momentum of the b quark.

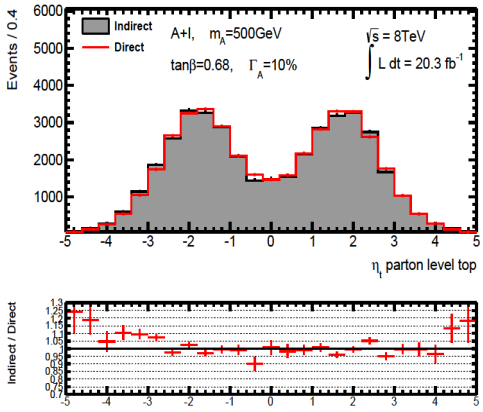

(a) $A + I$, top quark η

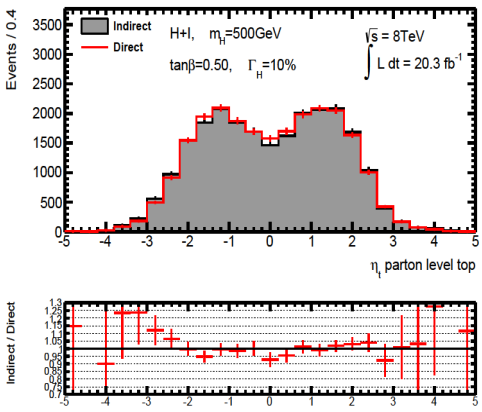

(b) $H + I$, top quark η

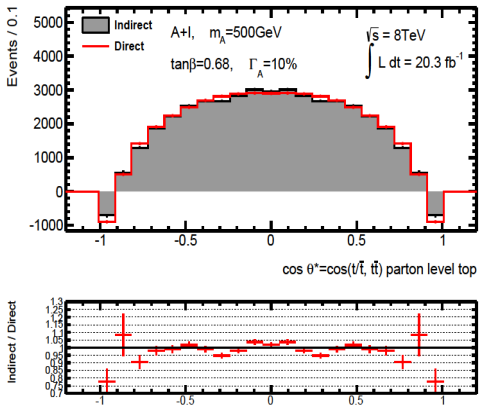

(c) $A + I$, $\cos(\theta^*)$

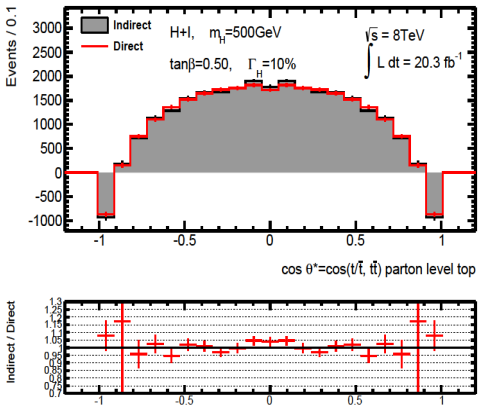

(d) $H + I$, $\cos(\theta^*)$

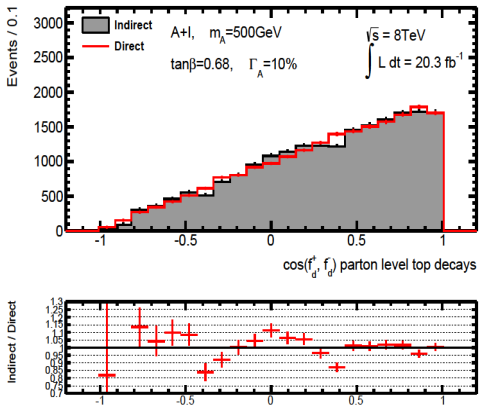

(e) $A + I$, $\cos(f_d^+, f_d^-)$

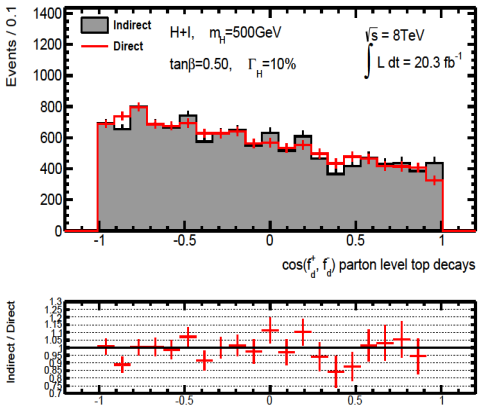

(f) $H + I$, $\cos(f_d^+, f_d^-)$

Figure B.3.: Comparison between "indirect" and "direct" approach to generate $S + I$ for A (left) and H (right), at scalar mass points 500 GeV and total decay widths of 10% from the mass point: top quark η (first row); the Collins-Soper angle θ^* and the angle between the two down-type fermions in the $t\bar{t}$ rest frame, as explained in Section 4.4.1 (second and third rows).

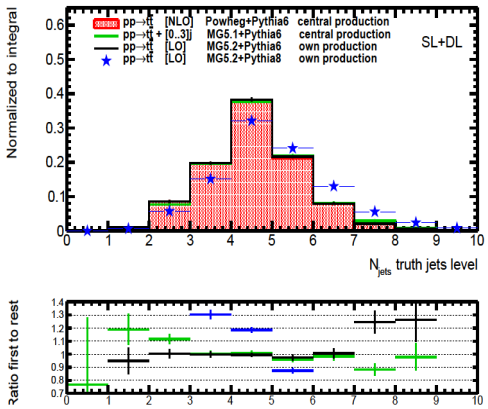

(a) number of jets

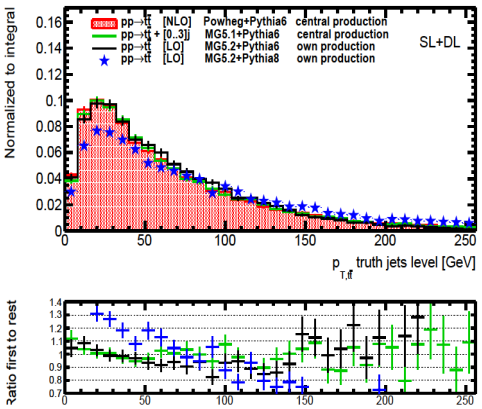

(b) $p_{\mathrm{T},t\bar{t}}$

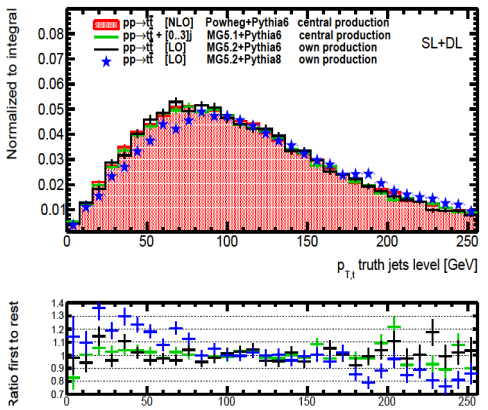

(c) $p_{\mathrm{T},t}$

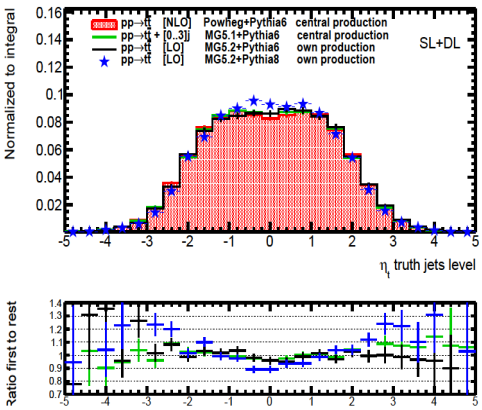

(d) η_t

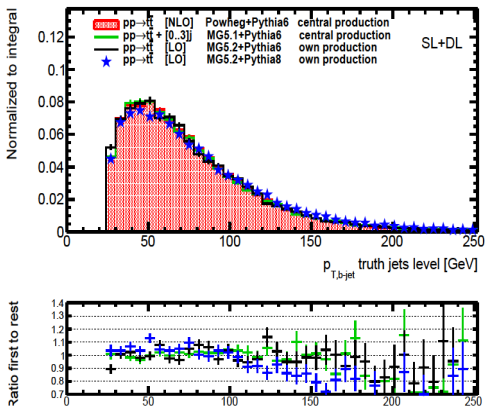

(e) $p_{\mathrm{T},b-\mathrm{jet}}$

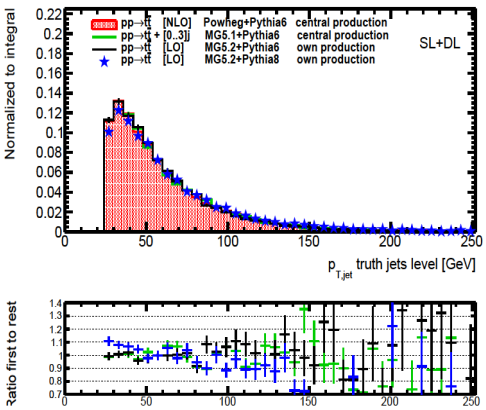

(f) $p_{\mathrm{T,jet}}$

Figure B.4.: Comparison between various $pp \to t\bar{t}$ showering configurations in the semileptonic+dileptonic $t\bar{t}$ decay channels, in order to validate a configuration for the showering of $S + I$.

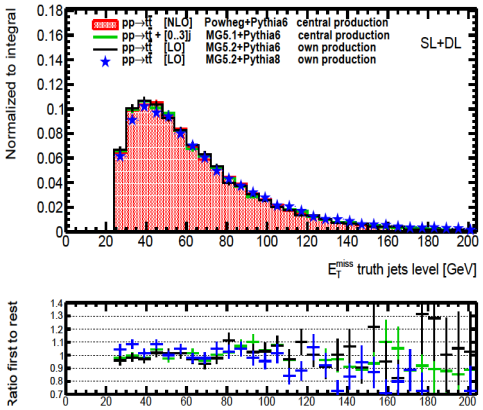

(a) $E_{\mathrm{T}}^{\mathrm{miss}}$

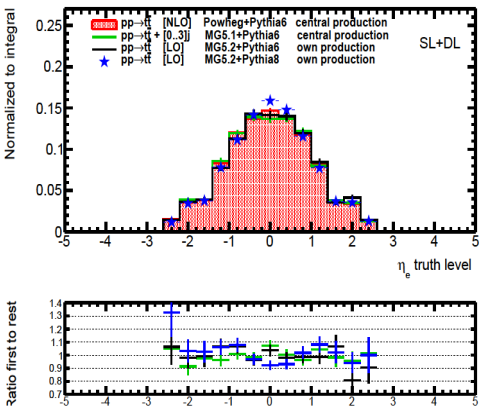

(b) η_e

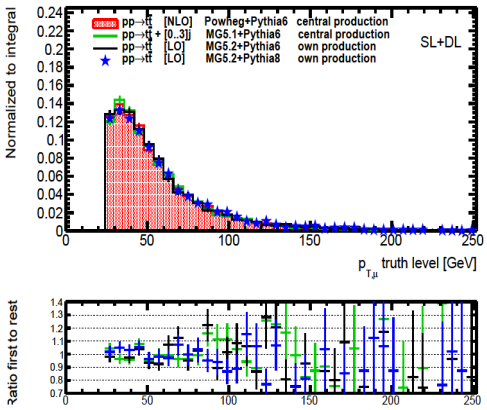

(c) $p_{\mathrm{T},\mu}$

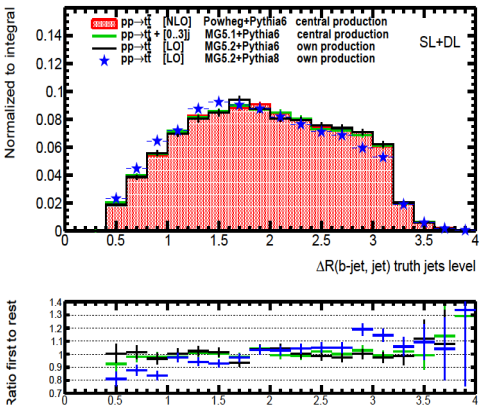

(d) $\Delta R(b-\mathrm{jet},\mathrm{jet})$

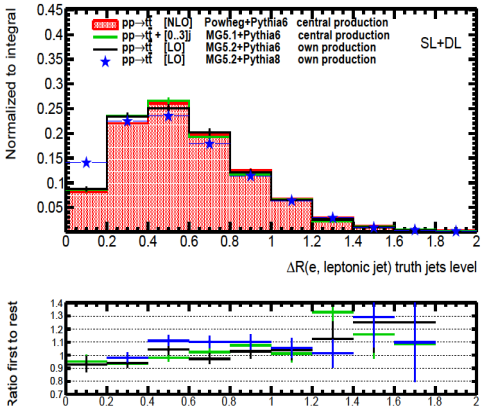

(e) $\Delta R(e,\mathrm{largeleptonjet})$

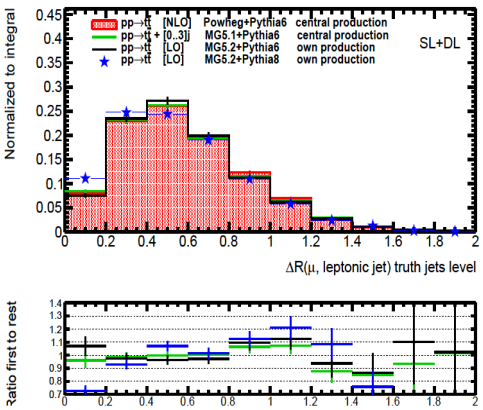

(f) $\Delta R(\mu,\mathrm{leptonjet})$

Figure B.5.: Comparison between various $pp \to t\bar{t}$ showering configurations in the semileptonic+dileptonic $t\bar{t}$ decay channels, in order to validate a configuration for the showering of $S + I$. In (e) and (f) a lepton jet is defined as the sum between the corresponding lepton and the closest jet (which must be a b-jet).

Appendix C.

Distributions of Systematic Shifts

This appendix shows the effect of the systematic variations described in Section 5.7 on the reconstructed $m_{t\bar{t}}$ distribution, separately in the e+jets and μ+jets channels. In each figure the nominal mass spectrum is drawn in black and the up and down variations in green and red respectively. The shaded grey band represents the statistical uncertainty on the total background. Only the systematics that have a visible effect are displayed, in the inclusive b-tagging category.

Section C.1 displays the experimental and modelling effects on the total background, namely the total MC modelled background sources introduced in Sections 5.2, together with the QCD source, data-driven as described in Section 5.5.

Section C.2 displays the experimental effects on a chosen $A + I$ signal parameter point with $m_A = 500$ GeV and $\tan\beta = 0.68$. Since the up/down variations have a strong oscillation around the nominal value, the maximum between the two has been displayed in the bottom ratio pad, only for illustration purposes of this section. A smoothed version of the up-/down-variation histograms is used in the statistical analysis, using the statistical smoothing algorithm implemented in TRexFitter. In Section 5.7.5 two additional systematic variations specific only to the modelling of S and $S + I$ are presented, shown in Figure 5.8.

C.1. Systematics of Total Background

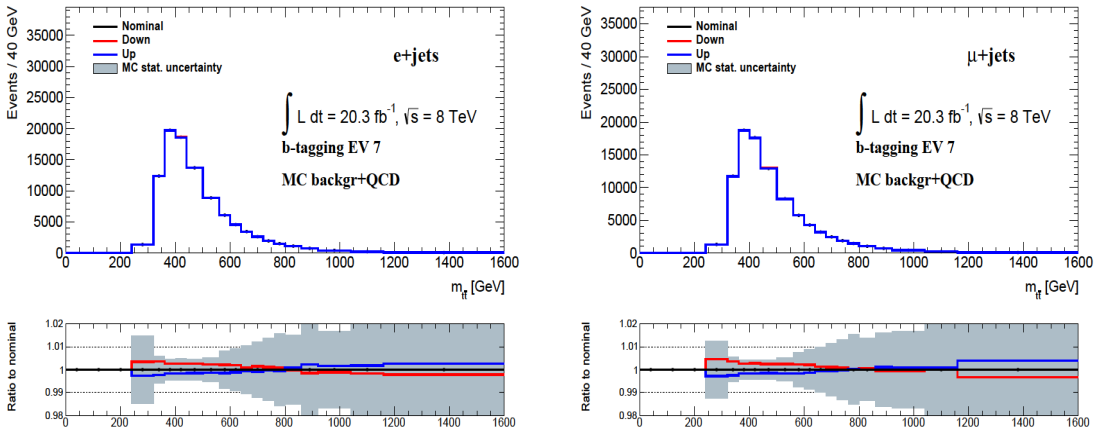

(a) b-tagging, component 7, e+jets

(b) b-tagging, component 7, μ+jets

Figure C.1.: Distributions of **total background** uncertainties and their relative ratio to the nominal distribution, as described in the text.

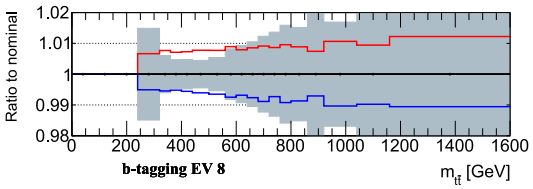

(1) b-tagging, component 8, e+jets

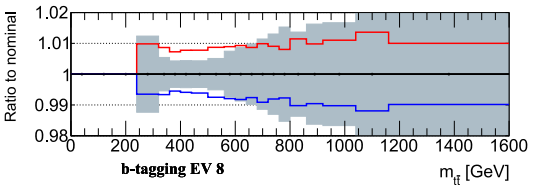

(2) b-tagging, component 8, μ+jets

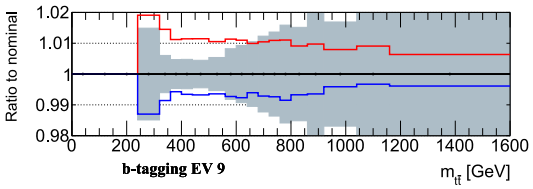

(3) b-tagging, component 9, e+jets

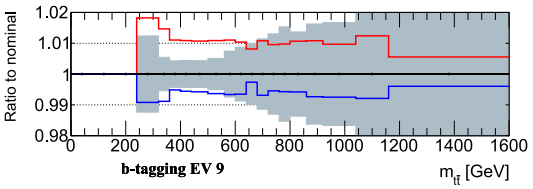

(4) b-tagging, component 9, μ+jets

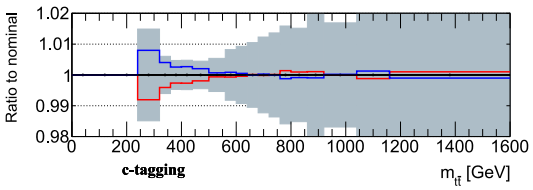

(5) c-tagging, e+jets

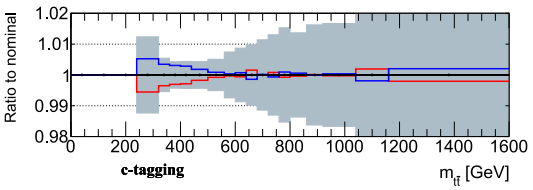

(6) c-tagging, μ+jets

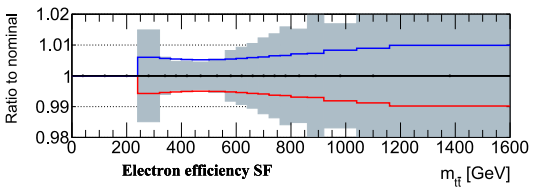

(7) e efficiency SF, e+jets

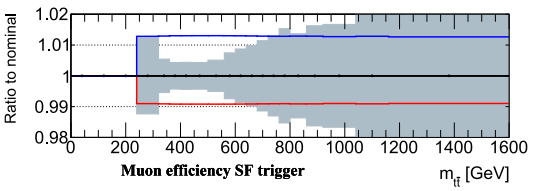

(8) μ efficiency SF, μ+jets

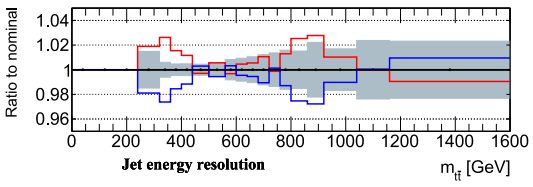

(9) Jet energy resolution, e+jets

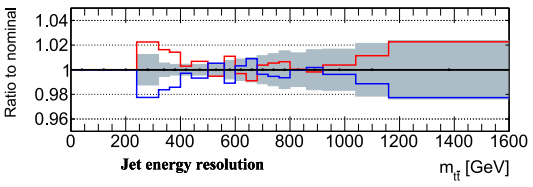

(10) Jet energy resolution, μ+jets

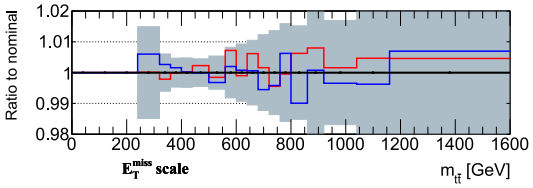

(11) $E_{\mathrm{T}}^{\mathrm{miss}}$ scale, e+jets

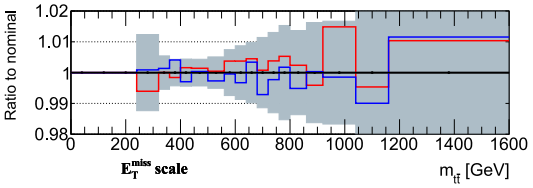

(12) $E_{\mathrm{T}}^{\mathrm{miss}}$ scale, μ+jets

Figure C.2.: Ratios of the up and down systematic distributions to the nominal distribution for the **total background**, as described in the text.

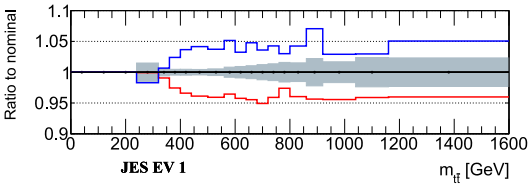

(13) JES in-situ 1, e+jets

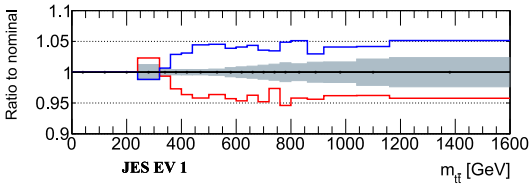

(14) JES in-situ 1, μ+jets

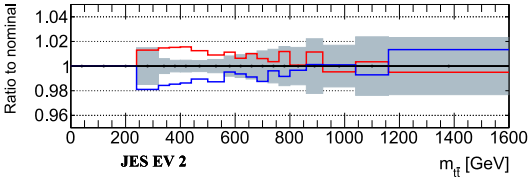

(15) JES in-situ 2, e+jets

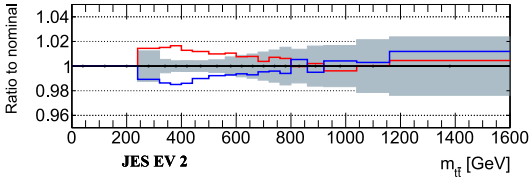

(16) JES in-situ 2, μ+jets

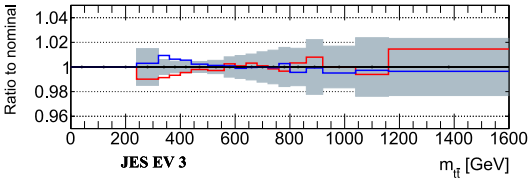

(17) JES in-situ 3, e+jets

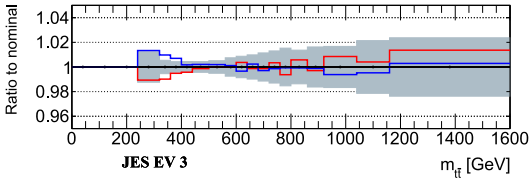

(18) JES in-situ 3, μ+jets

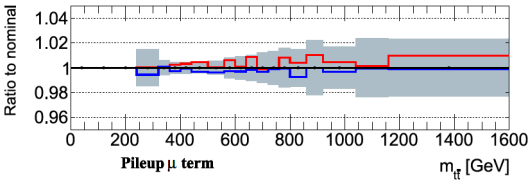

(19) Pileup μ term, e+jets

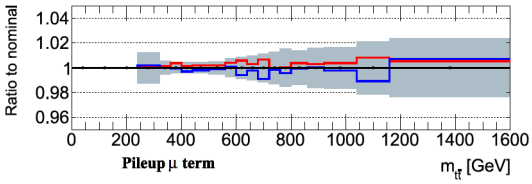

(20) Pileup μ term, μ+jets

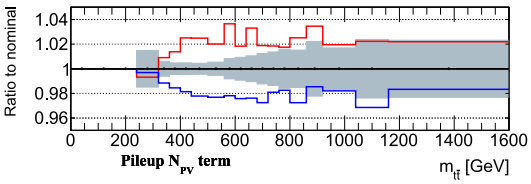

(21) Pileup N_{PV} term, e+jets

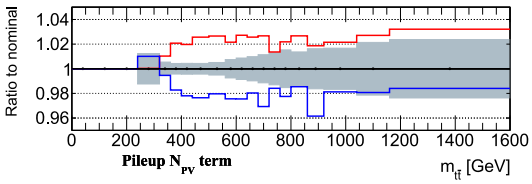

(22) Pileup N_{PV} term, μ+jets

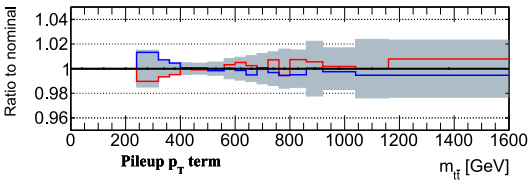

(23) Pileup p_{T} term, e+jets

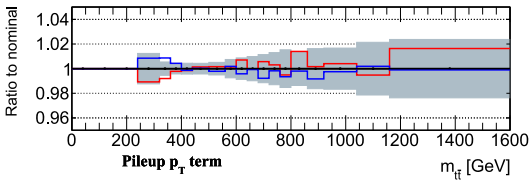

(24) Pileup p_{T} term, μ+jets

Figure C.2.: Ratios of the up and down systematic distributions to the nominal distribution for the **total background**, as described in the text (continued).

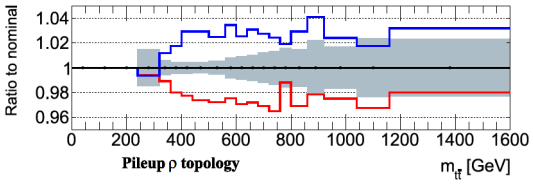

(25) Pileup ρ, e+jets

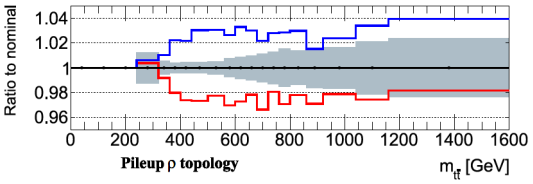

(26) Pileup ρ, μ+jets

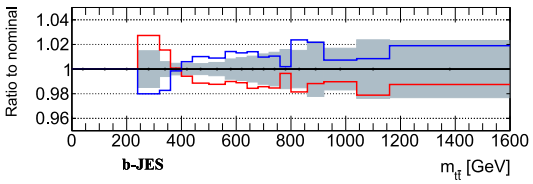

(27) b-JES, e+jets

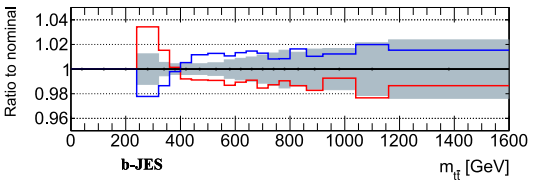

(28) b-JES, μ+jets

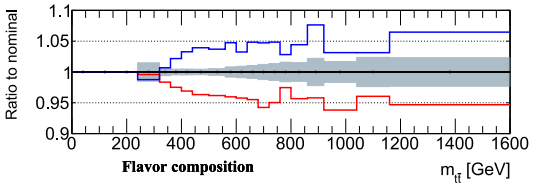

(29) Flavor composition, e+jets

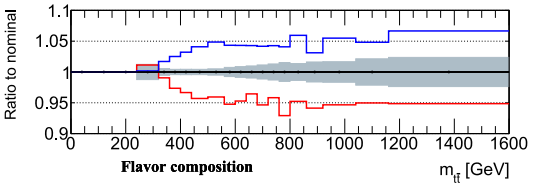

(30) Flavor composition, μ+jets

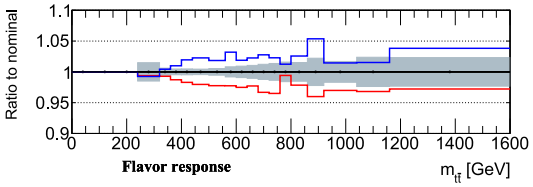

(31) Flavor response, e+jets

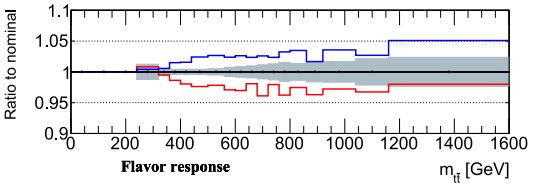

(32) Flavor response, μ+jets

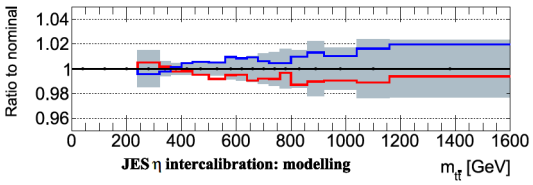

(33) η intercalib. modelling, e+jets

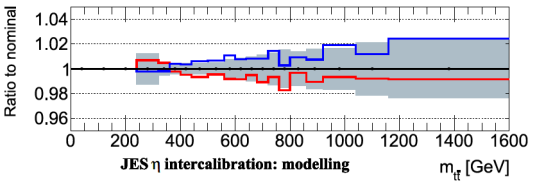

(34) η intercalib. modelling, μ+jets

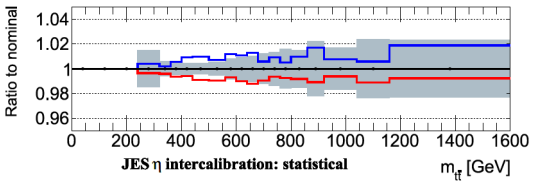

(35) η intercalib. stat., e+jets

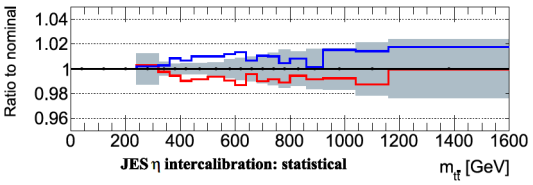

(36) η intercalib. stat., μ+jets

Figure C.2.: Ratios of the up and down systematic distributions to the nominal distribution for the **total background**, as described in the text (continued).

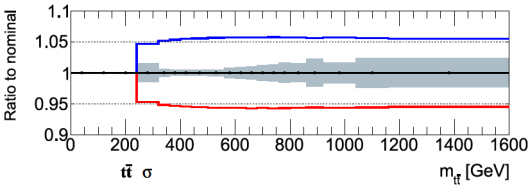

(37) $t\bar{t}$ cross-section, e+jets

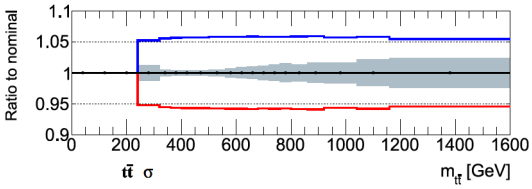

(38) $t\bar{t}$ cross-section, μ+jets

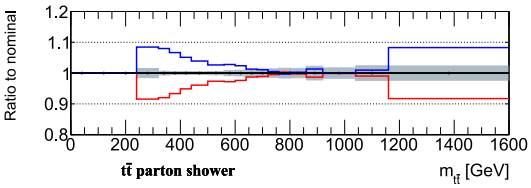

(39) $t\bar{t}$ parton shower, e+jets

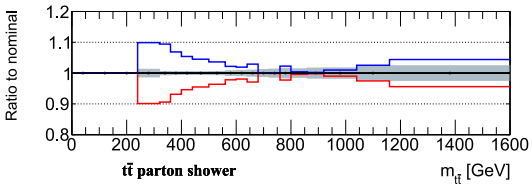

(40) $t\bar{t}$ parton shower, μ+jets

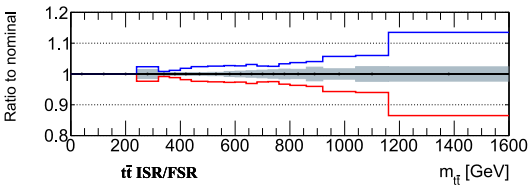

(41) $t\bar{t}$ ISR/FSR, e+jets

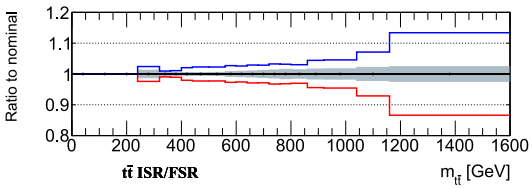

(42) $t\bar{t}$ ISR/FSR, μ+jets

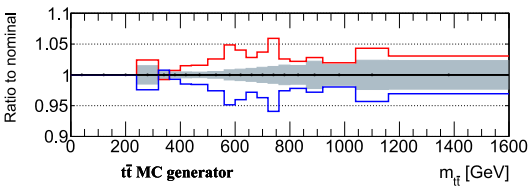

(43) $t\bar{t}$ MC generator, e+jets

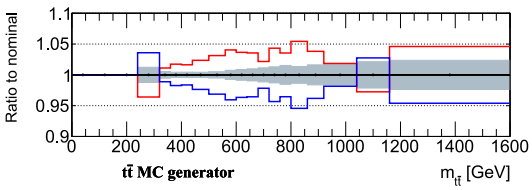

(44) $t\bar{t}$ MC generator, μ+jets

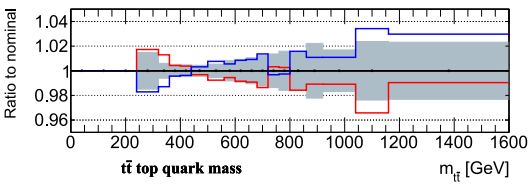

(45) $t\bar{t}$ top quark mass, e+jets

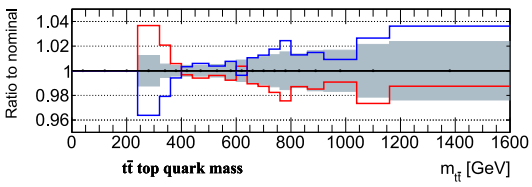

(46) $t\bar{t}$ top quark mass, μ+jets

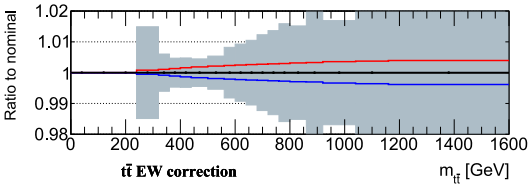

(47) $t\bar{t}$ EW correction, e+jets

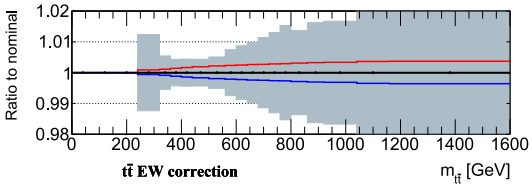

(48) $t\bar{t}$ EW correction, μ+jets

Figure C.2.: Ratios of the up and down systematic distributions to the nominal distribution for the **total background**, as described in the text (continued).

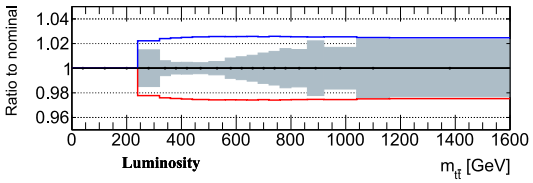

(49) Luminosity, e+jets

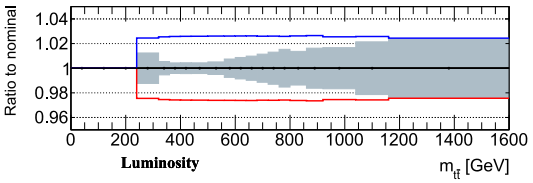

(50) Luminosity, μ+jets

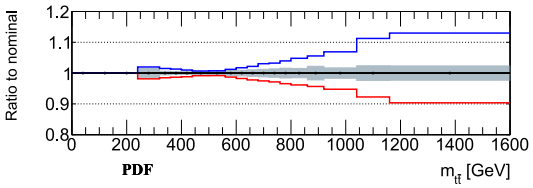

(51) PDF, e+jets

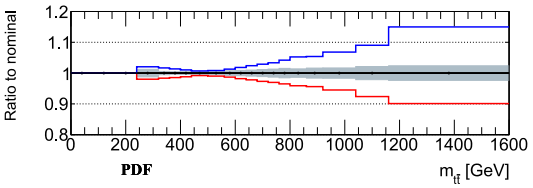

(52) PDF, μ+jets

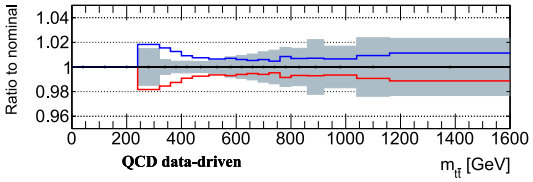

(53) QCD, e+jets

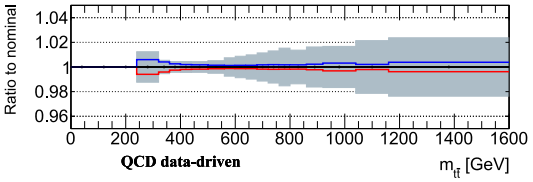

(54) QCD, μ+jets

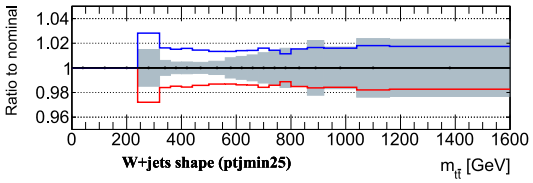

(55) W+jets ptjmin25, e+jets

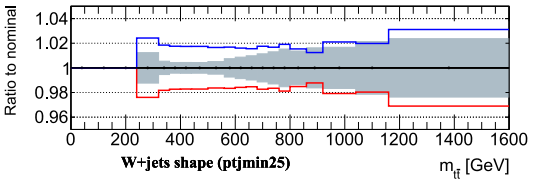

(56) W+jets ptjmin25, μ+jets

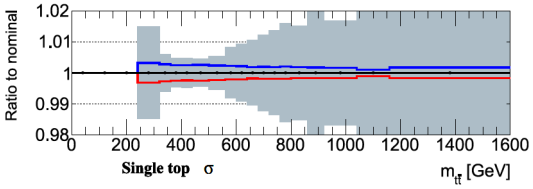

(57) single top, e+jets

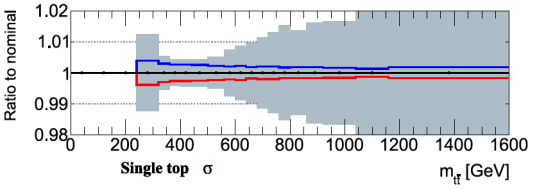

(58) single top, μ+jets

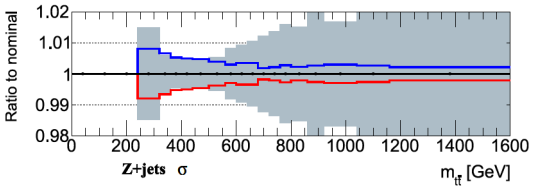

(59) Z+jets, e+jets

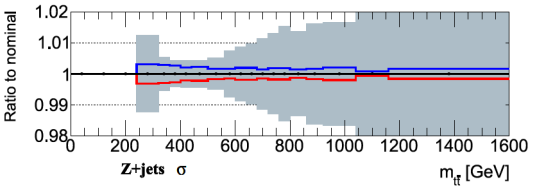

(60) Z+jets, μ+jets

Figure C.2.: Ratios of the up and down systematic distributions to the nominal distribution for the **total background**, as described in the text (continued).

C.2. Systematics of Signal with Interference - NOVELTY

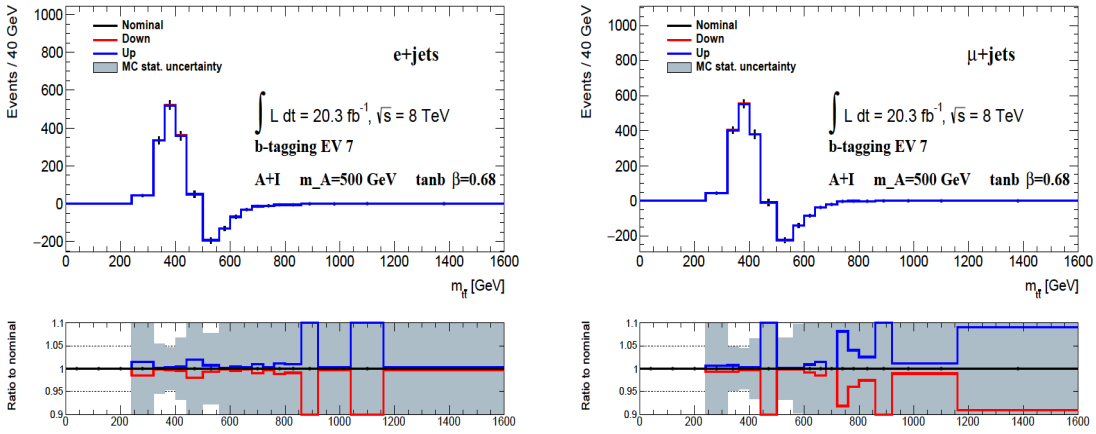

(a) b-tagging, component 7, e+jets

(b) b-tagging, component 7, μ+jets

Figure C.3.: Distributions of **signal with interference** uncertainties and their relative ratio to the nominal distribution, as described in the text.

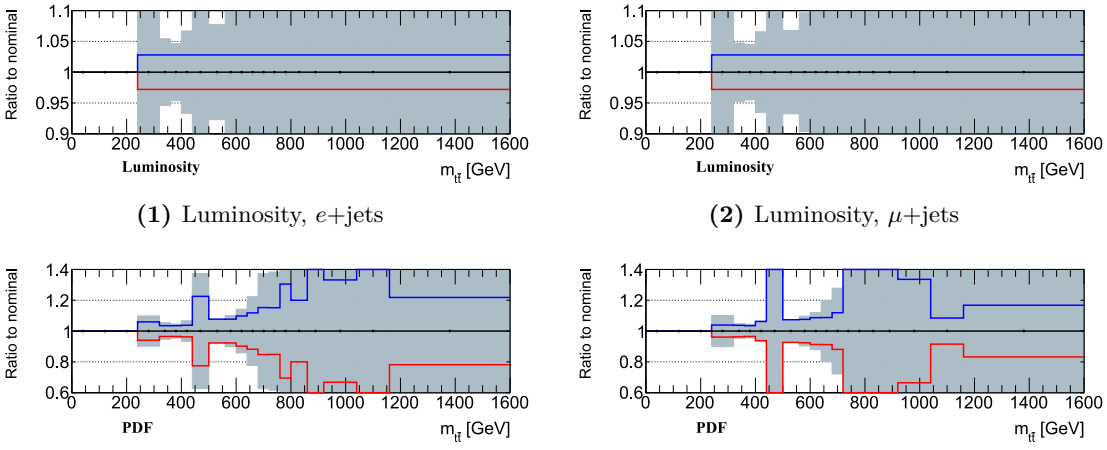

(1) Luminosity, e+jets

(2) Luminosity, μ+jets

(3) PDF, e+jets

(4) PDF, μ+jets

Figure C.4.: Ratios of the up and down systematic distributions to the nominal distribution for the **signal with interference**, as described in the text.

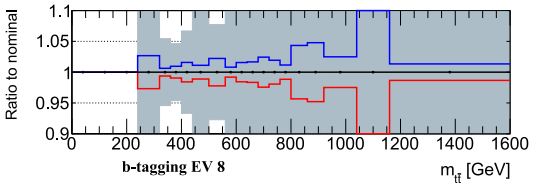

(5) b-tagging, component 8, e+jets

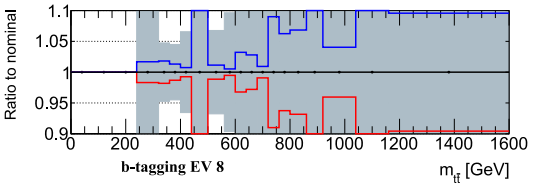

(6) b-tagging, component 8, μ+jets

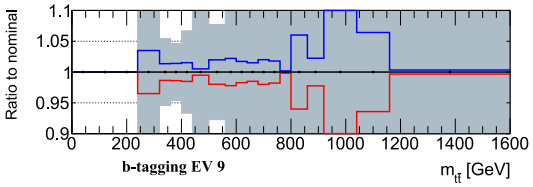

(7) b-tagging, component 9, e+jets

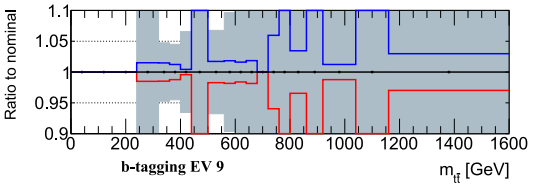

(8) b-tagging, component 9, μ+jets

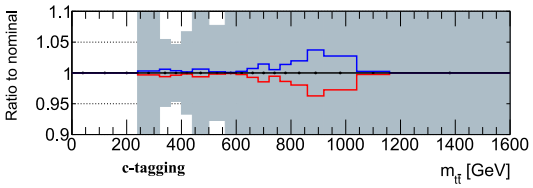

(9) c-tagging, e+jets

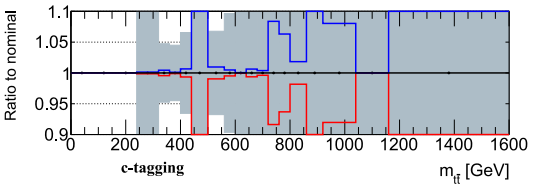

(10) c-tagging, μ+jets

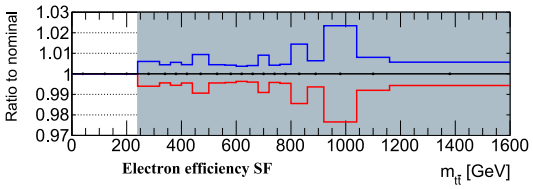

(11) e efficiency SF, e+jets

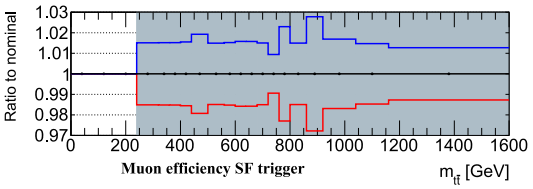

(12) μ efficiency SF, μ+jets

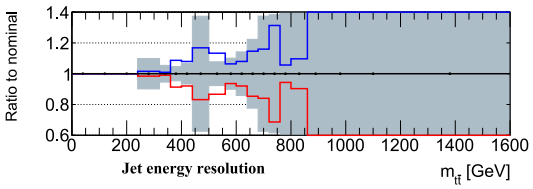

(13) Jet energy resolution, e+jets

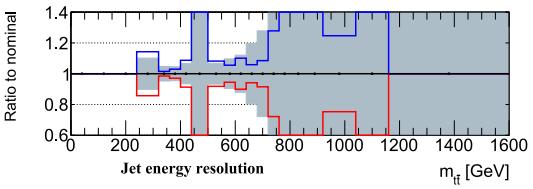

(14) Jet energy resolution, μ+jets

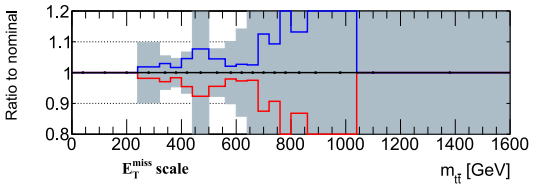

(15) $E_{\mathrm{T}}^{\mathrm{miss}}$ scale, e+jets

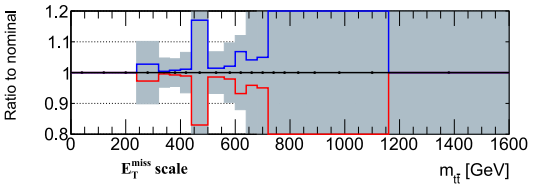

(16) $E_{\mathrm{T}}^{\mathrm{miss}}$ scale, μ+jets

Figure C.4.: Ratios of the up and down systematic distributions to the nominal distribution for the **signal with interference**, as described in the text (continued).

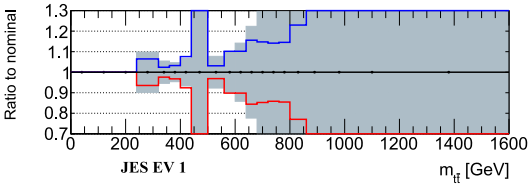

(17) JES in-situ 1, e+jets

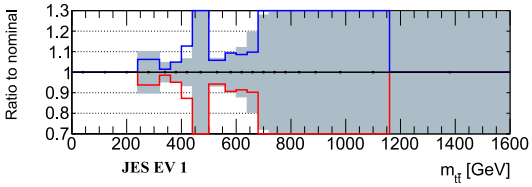

(18) JES in-situ 1, μ+jets

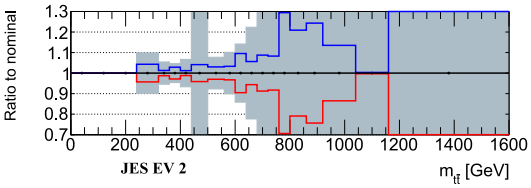

(19) JES in-situ 2, e+jets

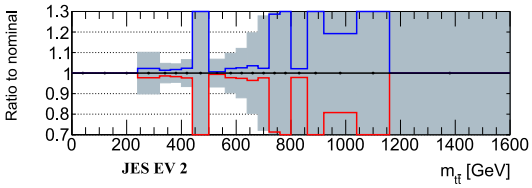

(20) JES in-situ 2, μ+jets

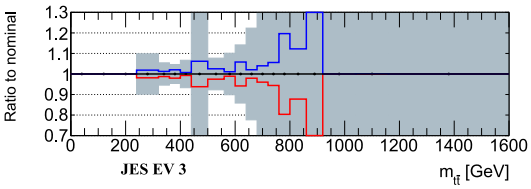

(21) JES in-situ 3, e+jets

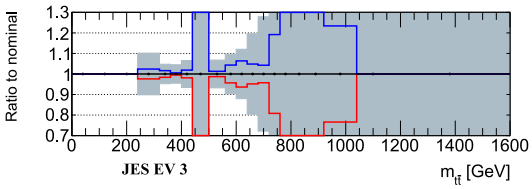

(22) JES in-situ 3, μ+jets

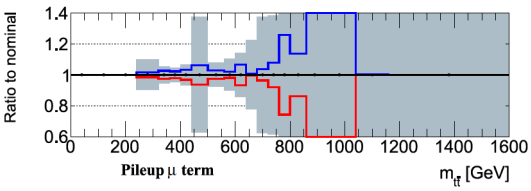

(23) Pileup μ term, e+jets

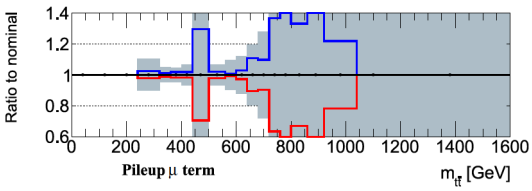

(24) Pileup μ term, μ+jets

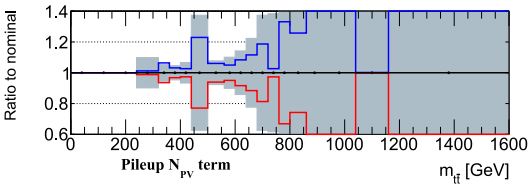

(25) Pileup N_{PV} term, e+jets

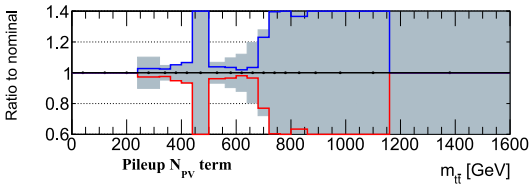

(26) Pileup N_{PV} term, μ+jets

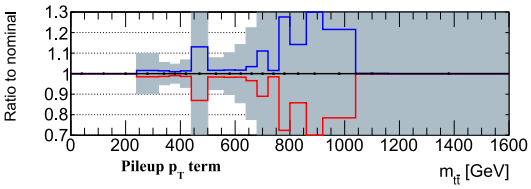

(27) Pileup p_{T} term, e+jets

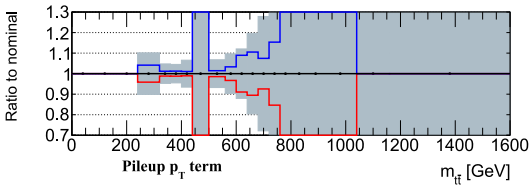

(28) Pileup p_{T} term, μ+jets

Figure C.4.: Ratios of the up and down systematic distributions to the nominal distribution for the **signal with interference**, as described in the text (continued).

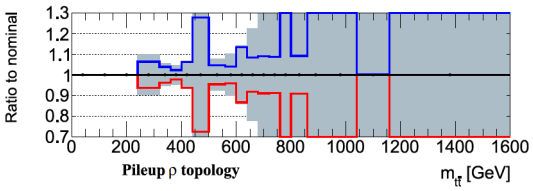

(29) Pileup ρ, e+jets

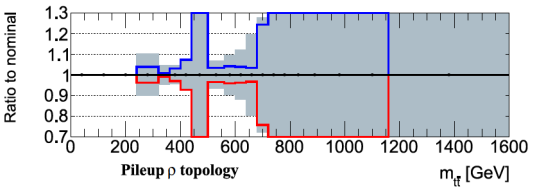

(30) Pileup ρ, μ+jets

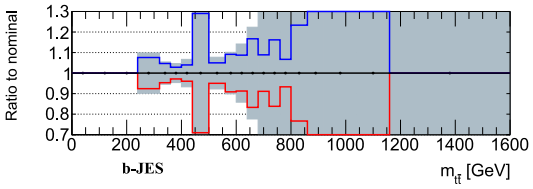

(31) b-JES, e+jets

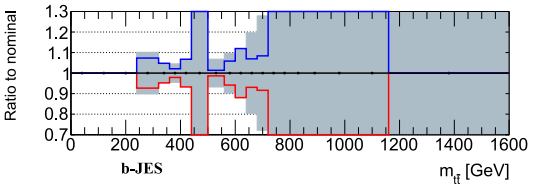

(32) b-JES, μ+jets

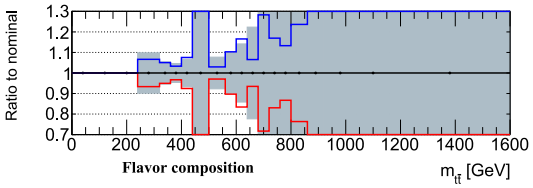

(33) Flavor composition, e+jets

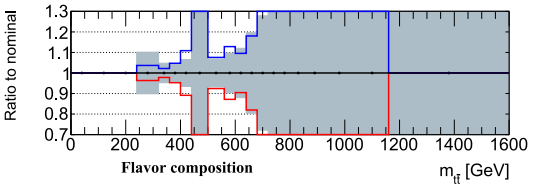

(34) Flavor composition, μ+jets

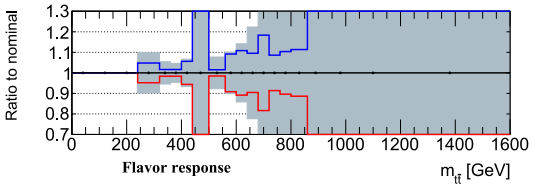

(35) Flavor response, e+jets

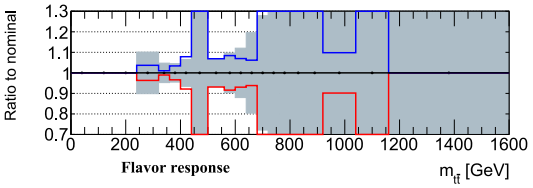

(36) Flavor response, μ+jets

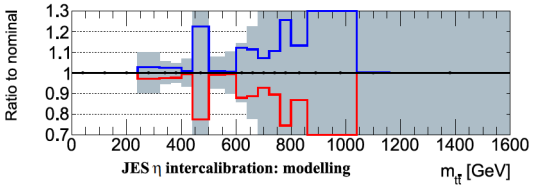

(37) η intercalib. modelling, e+jets

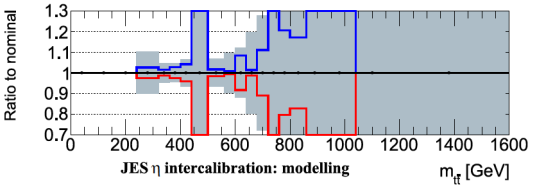

(38) η intercalib. modelling, μ+jets

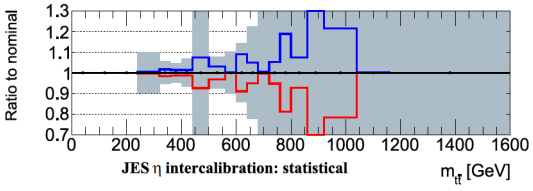

(39) η intercalib. stat., e+jets

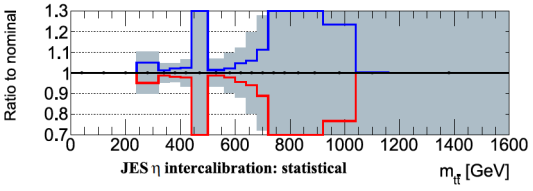

(40) η intercalib. stat., μ+jets

Figure C.4.: Ratios of the up and down systematic distributions to the nominal distribution for the **signal with interference**, as described in the text (continued).

Appendix D.

Additional Data Results

D.1. Comparison of Data and Background Expectations

This section compares various reconstructed kinematic distributions after event selection, between the data and the total background prediction, which is a stacked sum of all background contributions. The main comparisons between the invariant $m_{t\bar{t}}$ spectrum can be seen in Figure 6.1 and Figure 6.2. The background sources are, in order of their contribution to the total event yield after event selection: SM $t\bar{t}$, W+jets, multijets and further smaller background components (single top quark, Z+jets, dibosons, $t\bar{t}V$). The bottom pads show the ratio of data to the total background. The hashed area represents the total uncertainty on the background, summed in quadrature from all systematic and statistical contributions.

The events are divided into three b-tagging categories in each lepton channel, where the top quark candidates are matched to a b-jet by the χ^2 reconstruction algorithm. (Sections 5.3.10 and 5.4):

- *Category 1*: Both the hadronic and leptonic top quark candidates have b-jets associated.
- *Category 2*: Only the hadronic top quark candidate has a b-jet associated.
- *Category 3*: Only the leptonic top quark candidate has a b-jet associated.

The breakdown leads to six different categories of events: (e+jets, μ+jets) $\times$ (cat. 1, cat. 2, cat. 3). The data agrees with the background within the background uncertainties.

D.1.1. *b*-tagging Category 1

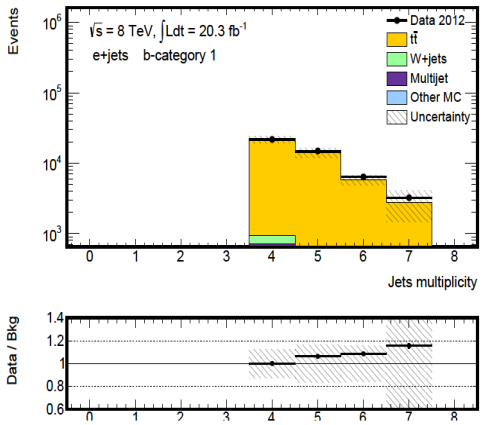

(a) jet multiplicity, e+jets

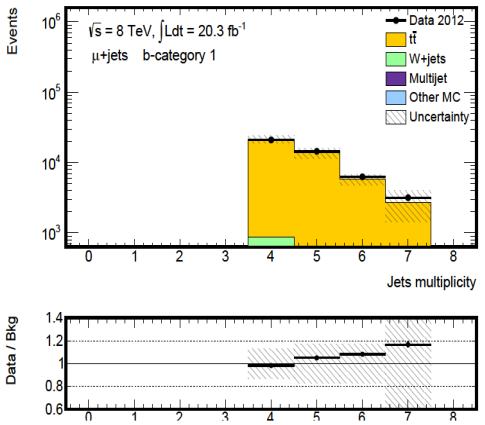

(b) jet multiplicity, μ+jets

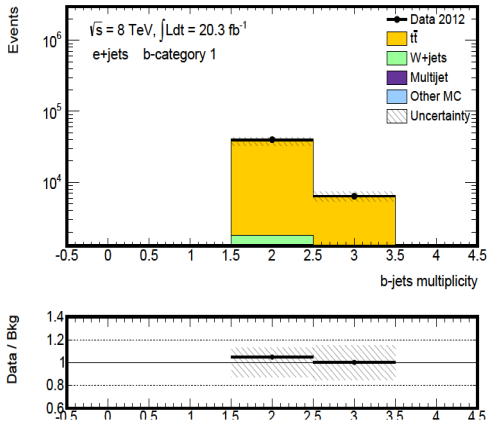

(c) b-jet multiplicity, e+jets

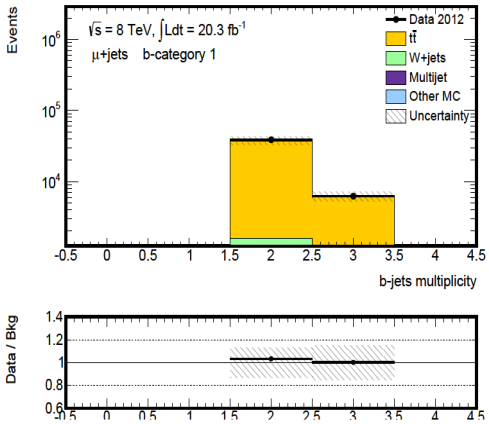

(d) b-jet multiplicity, μ+jets

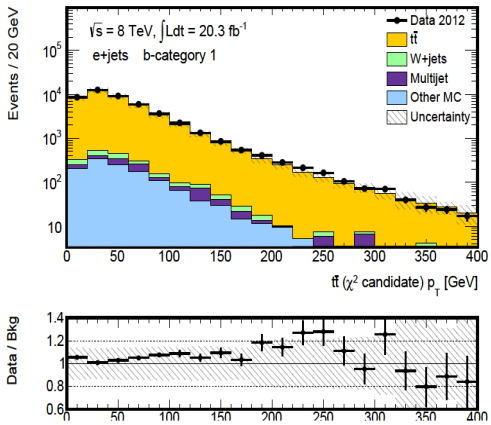

(e) $t\bar{t}$ p_{T}, e+jets

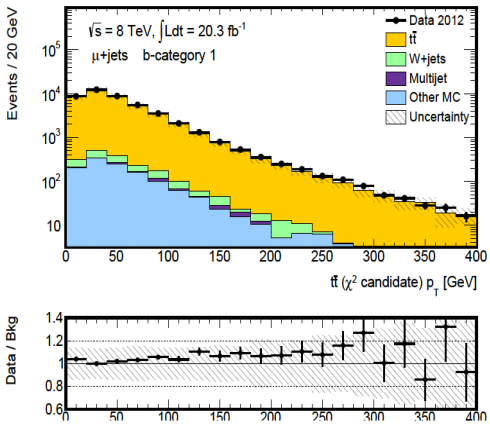

(f) $t\bar{t}$ p_{T}, μ+jets

Figure D.1.: Comparison between data and expected background of various kinematic distributions, in the ***b*-tagging category 1**, e+jets channel (left), respectively μ+jets channel (right).

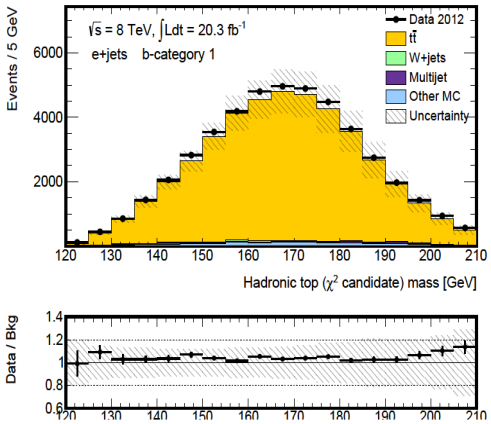

(a) hadronic top quark mass, e+jets

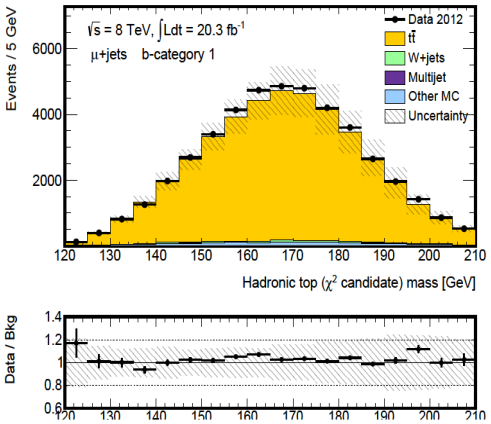

(b) hadronic top quark mass, μ+jets

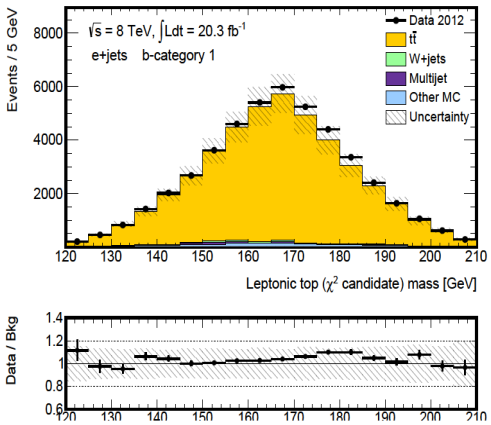

(c) leptonic top quark mass, e+jets

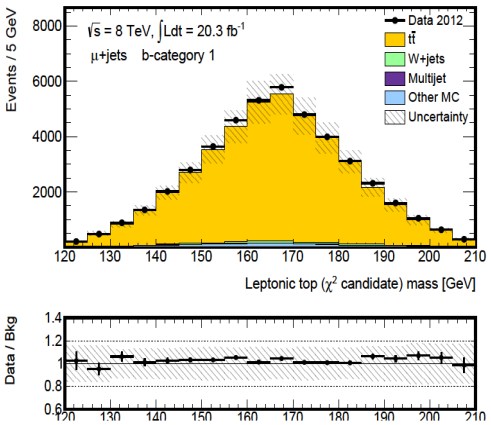

(d) leptonic top quark mass, μ+jets

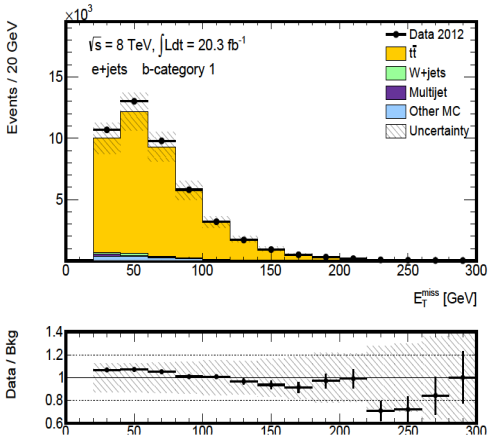

(e) $E_{\mathrm{T}}^{\mathrm{miss}}$, e+jets

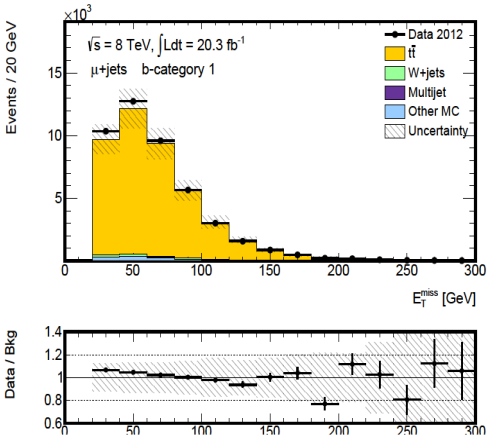

(f) $E_{\mathrm{T}}^{\mathrm{miss}}$, μ+jets

Figure D.2.: Comparison between data and expected background of various kinematic distributions, in the ***b*-tagging category 1**, e+jets channel (left), respectively μ+jets channel (right).

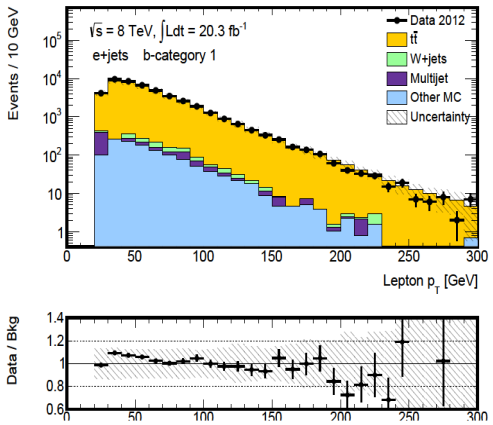

(a) lepton p_{T}, e+jets

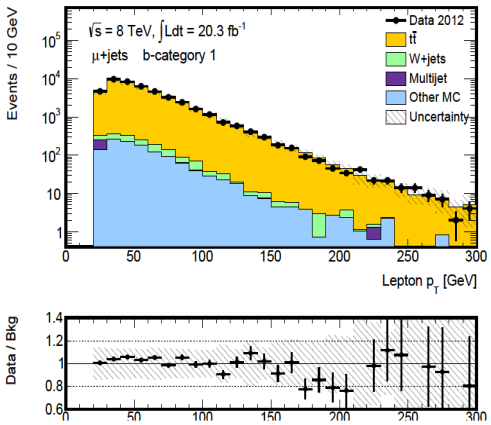

(b) lepton p_{T}, μ+jets

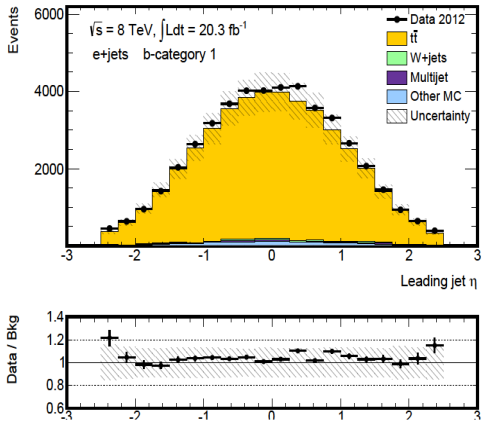

(c) leading jet η, e+jets

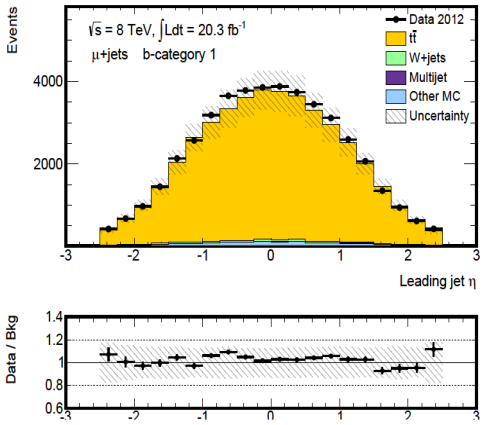

(d) leading jet η, μ+jets

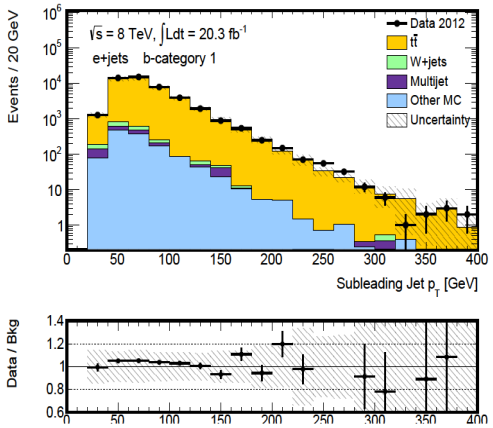

(e) subleading jet p_{T}, e+jets

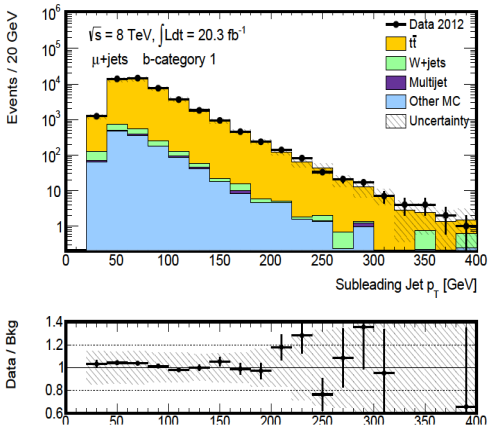

(f) subleading jet p_{T}, μ+jets

Figure D.3.: Comparison between data and expected background of various kinematic distributions, in the ***b*-tagging category 1**, e+jets channel (left), respectively μ+jets channel (right).

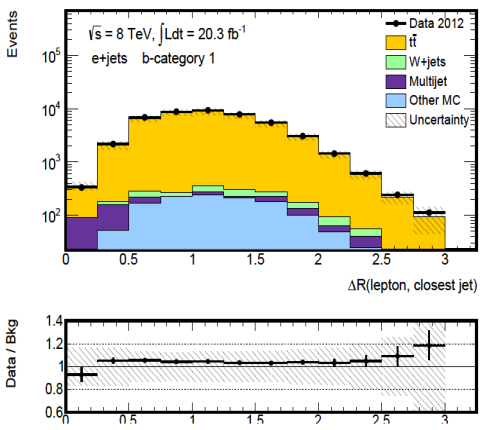

(a) ΔR(lepton, closest jet), e+jets

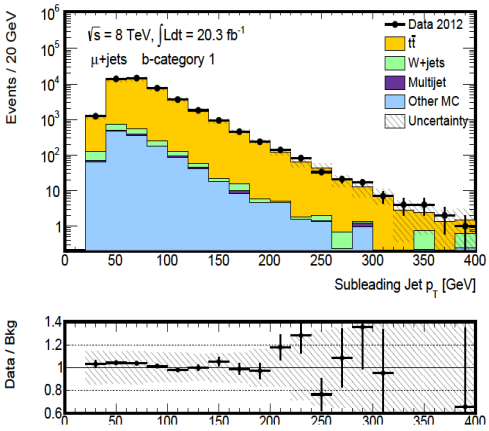

(b) ΔR(lepton, closest jet), μ+jets

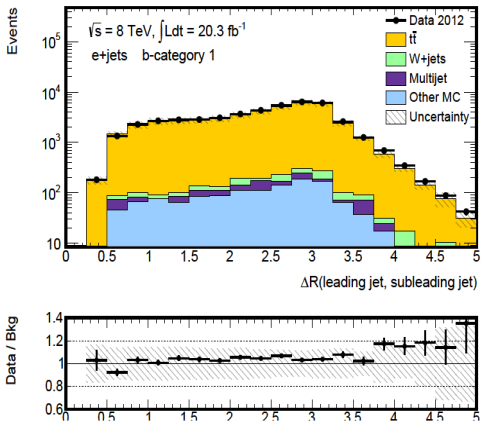

(c) ΔR(leading jet, subleading jet), e+jets

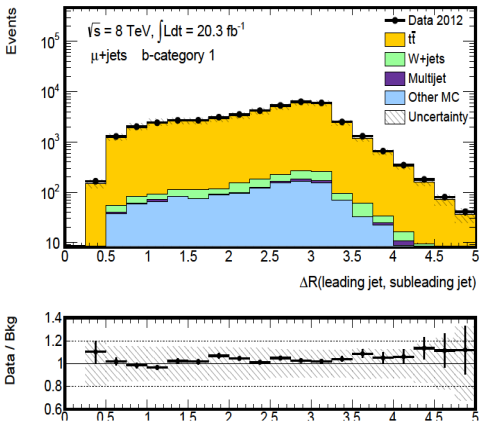

(d) ΔR(leading jet, subleading jet), μ+jets

Figure D.4.: Comparison between data and expected background of various kinematic distributions, in the ***b*-tagging category 1**, e+jets channel (left), respectively μ+jets channel (right).

D.1.2. *b*-tagging Category 2

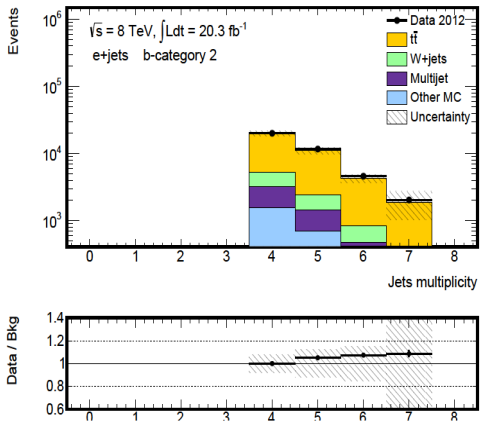

(a) jet multiplicity, e+jets

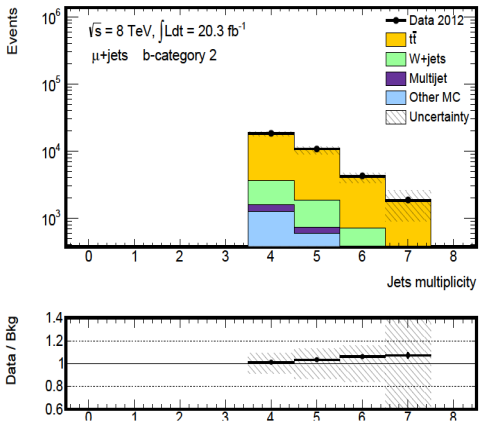

(b) jet multiplicity, μ+jets

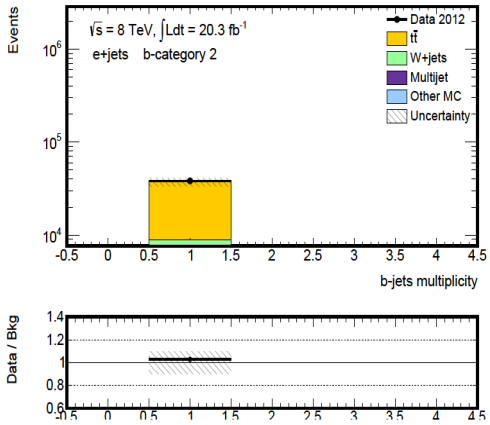

(c) b-jet multiplicity, e+jets

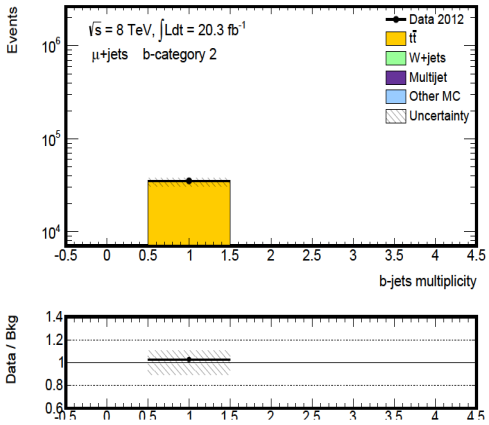

(d) b-jet multiplicity, μ+jets

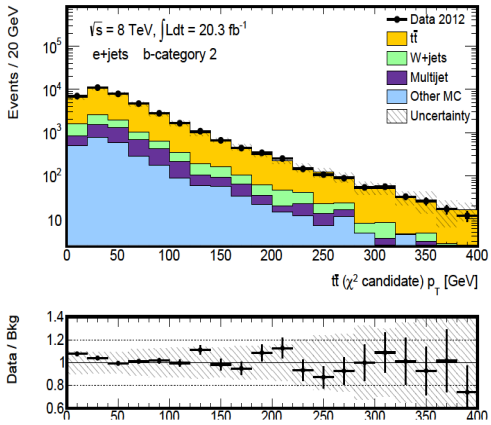

(e) $t\bar{t}$ p_{T}, e+jets

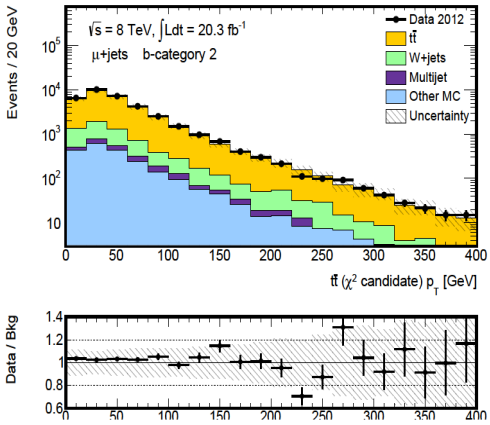

(f) $t\bar{t}$ p_{T}, μ+jets

Figure D.5.: Comparison between data and expected background of various kinematic distributions, in the ***b*-tagging category 2**, e+jets channel (left), respectively μ+jets channel (right).

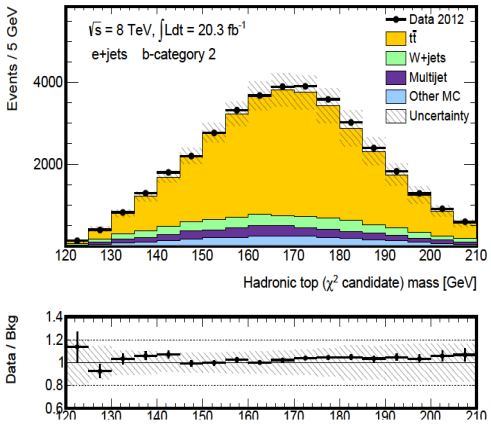

(a) hadronic top quark mass, e+jets

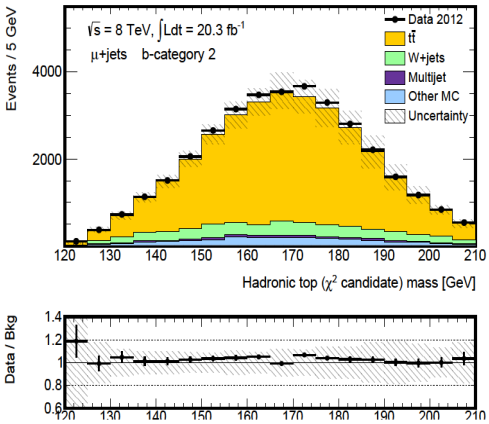

(b) hadronic top quark mass, μ+jets

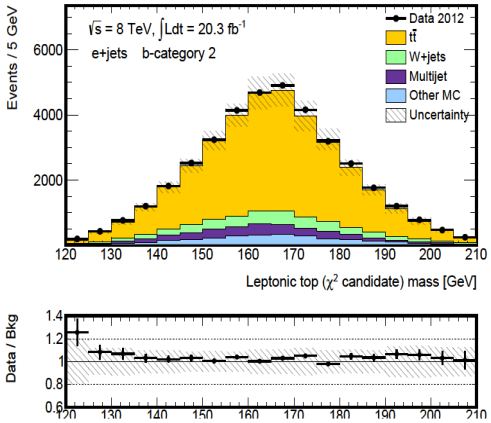

(c) leptonic top quark mass, e+jets

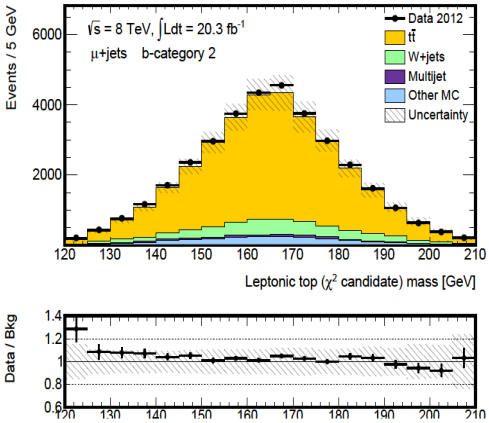

(d) leptonic top quark mass, μ+jets

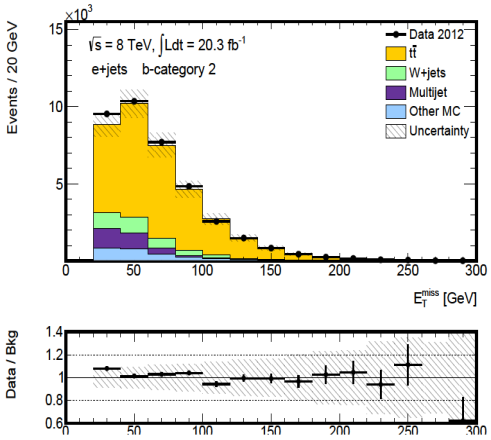

(e) $E_{\mathrm{T}}^{\mathrm{miss}}$, e+jets

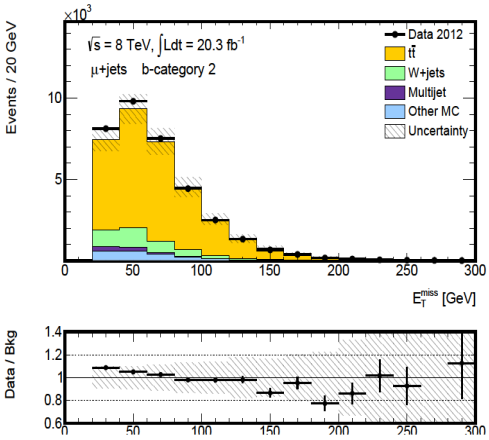

(f) $E_{\mathrm{T}}^{\mathrm{miss}}$, μ+jets

Figure D.6.: Comparison between data and expected background of various kinematic distributions, in the ***b*-tagging category 2**, e+jets channel (left), respectively μ+jets channel (right).

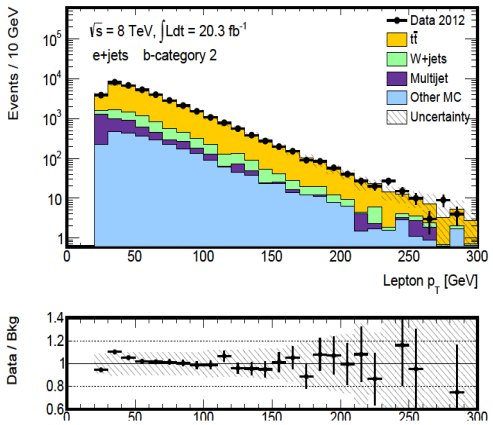

(a) lepton p_{T}, e+jets

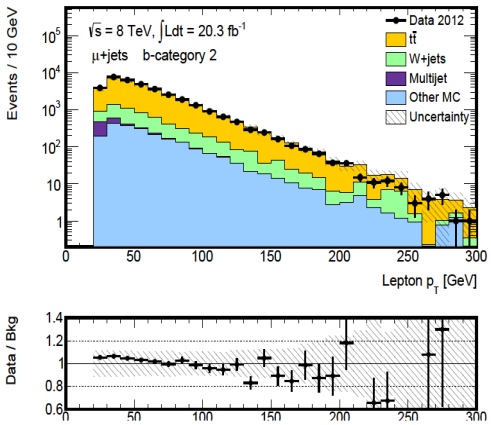

(b) lepton p_{T}, μ+jets

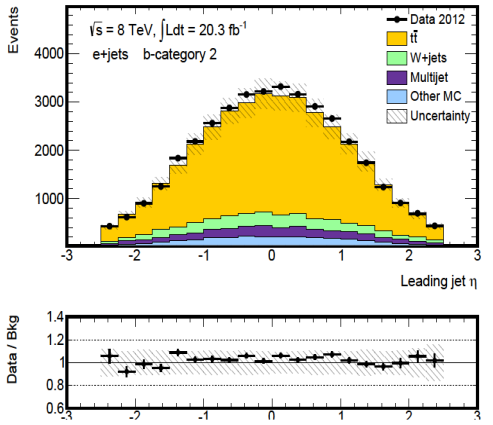

(c) leading jet η, e+jets

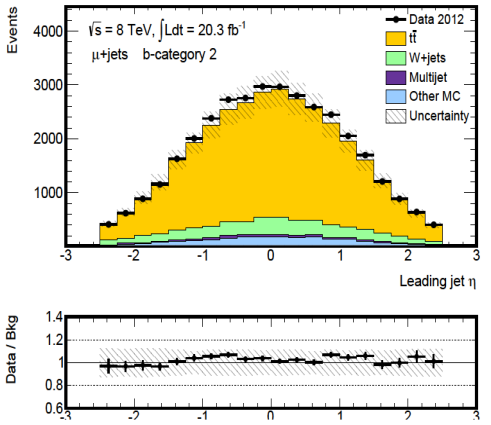

(d) leading jet η, μ+jets

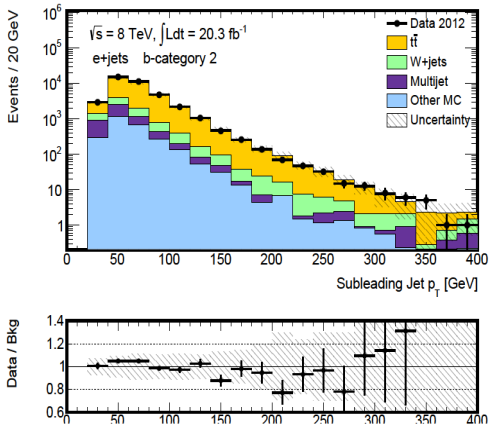

(e) subleading jet p_{T}, e+jets

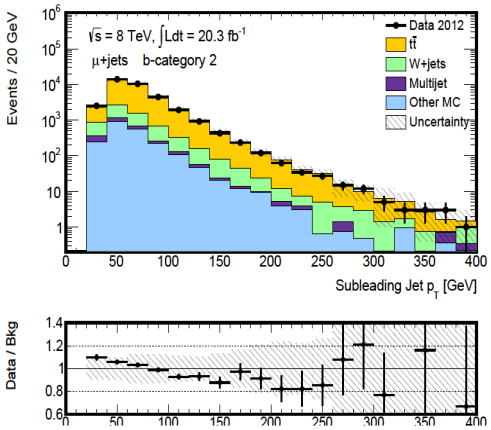

(f) subleading jet p_{T}, μ+jets

Figure D.7.: Comparison between data and expected background of various kinematic distributions, in the ***b*-tagging category 2**, e+jets channel (left), respectively μ+jets channel (right).

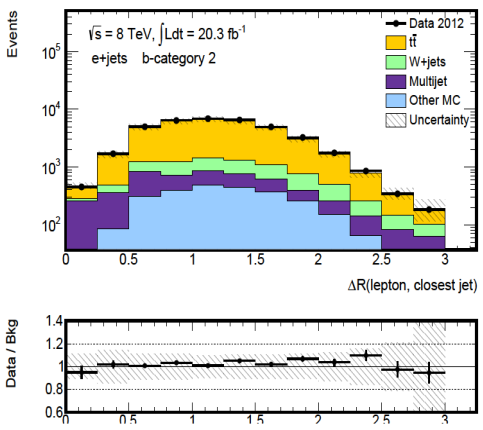

(a) ΔR(lepton, closest jet), e+jets

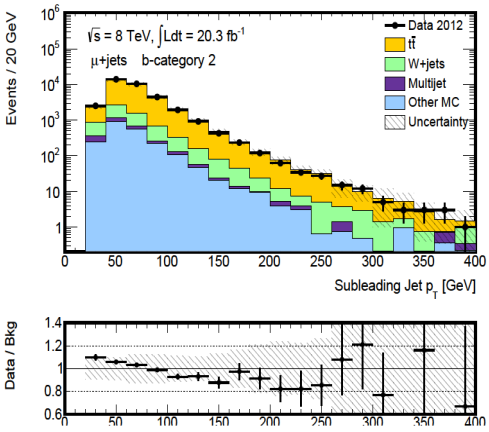

(b) ΔR(lepton, closest jet), μ+jets

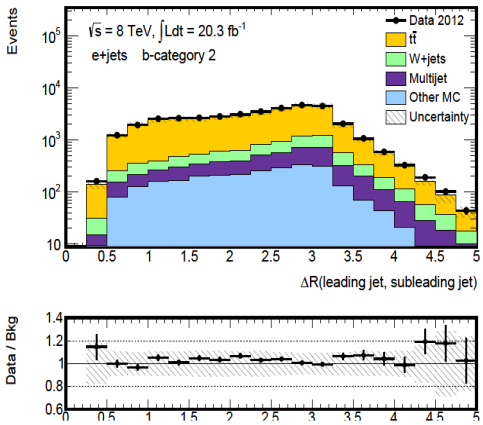

(c) ΔR(leading jet, subleading jet), e+jets

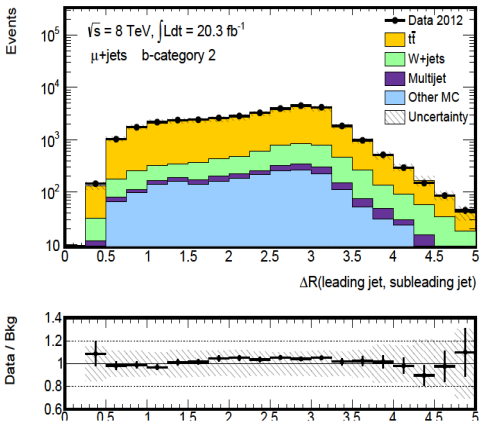

(d) ΔR(leading jet, subleading jet), μ+jets

Figure D.8.: Comparison between data and expected background of various kinematic distributions, in the ***b*-tagging category 2**, e+jets channel (left), respectively μ+jets channel (right).

D.1.3. *b*-tagging Category 3

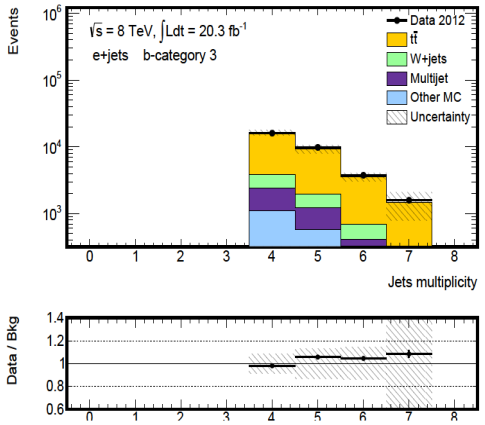

(a) jet multiplicity, e+jets

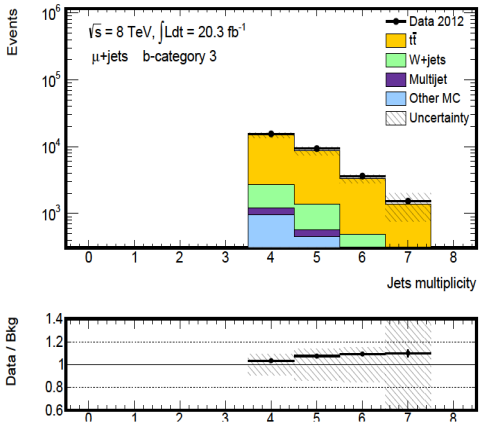

(b) jet multiplicity, μ+jets

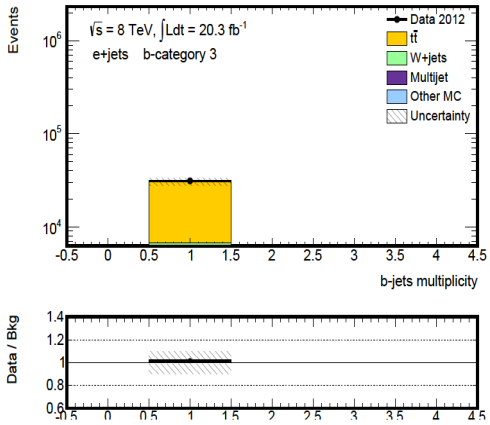

(c) b-jet multiplicity, e+jets

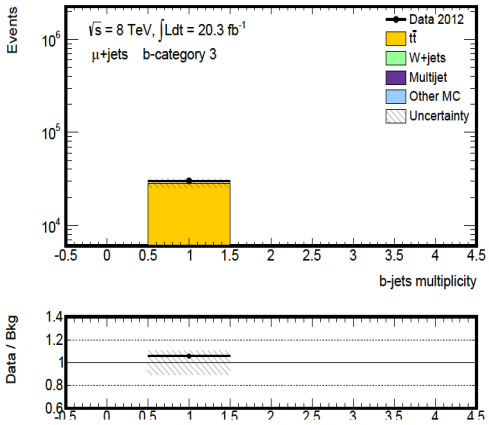

(d) b-jet multiplicity, μ+jets

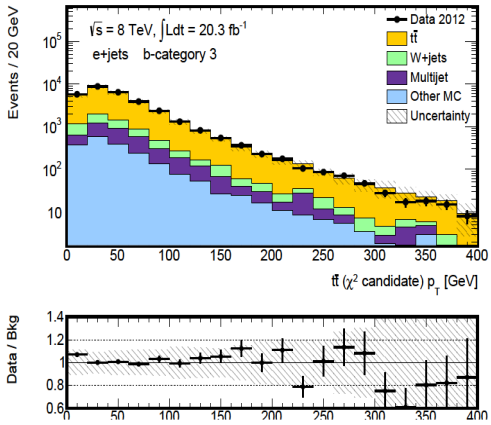

(e) $t\bar{t}$ p_{T}, e+jets

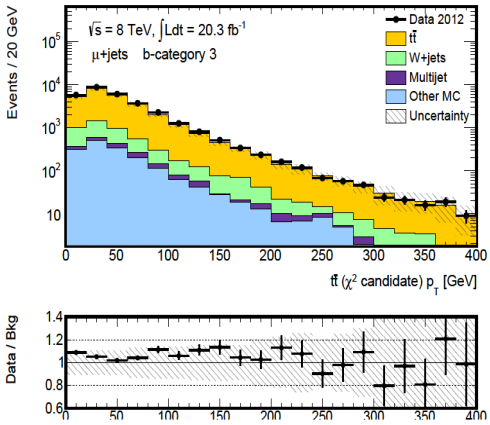

(f) $t\bar{t}$ p_{T}, μ+jets

Figure D.9.: Comparison between data and expected background of various kinematic distributions, in the ***b*-tagging category 3**, e+jets channel (left), respectively μ+jets channel (right).

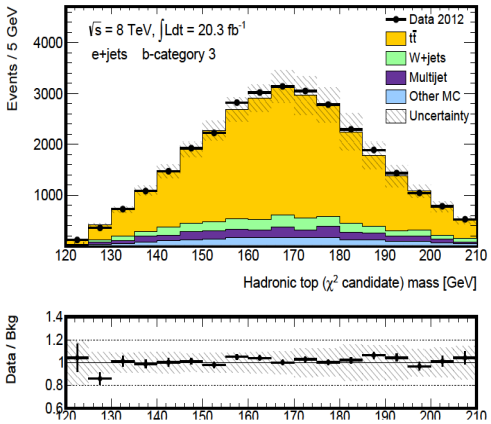

(a) hadronic top quark mass, e+jets

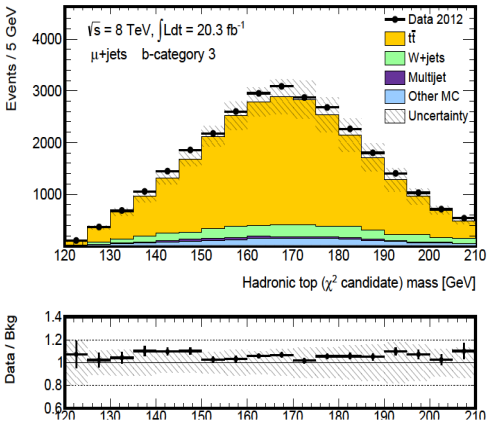

(b) hadronic top quark mass, μ+jets

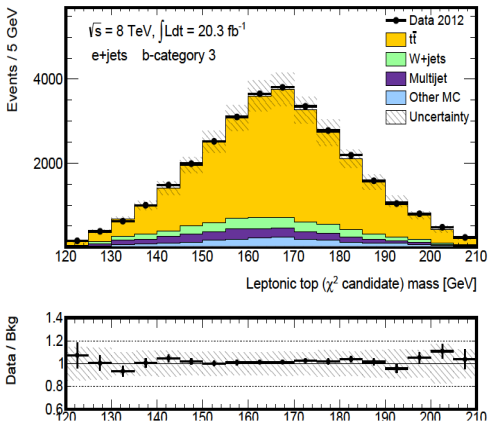

(c) leptonic top quark mass, e+jets

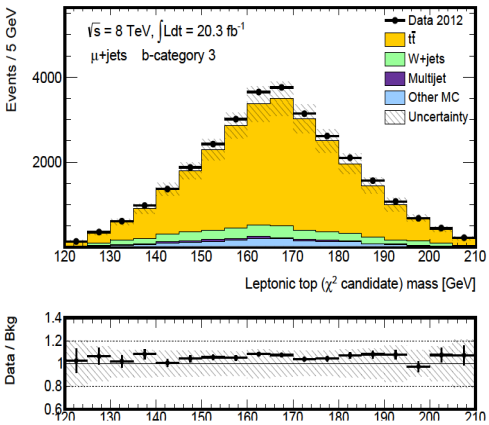

(d) leptonic top quark mass, μ+jets

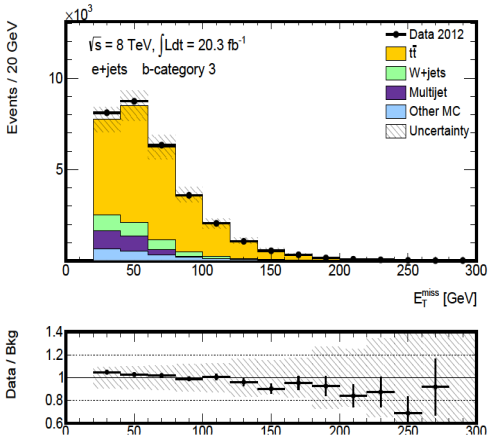

(e) $E_{\mathrm{T}}^{\mathrm{miss}}$, e+jets

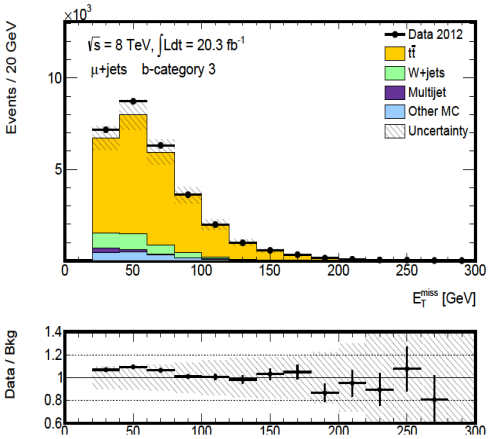

(f) $E_{\mathrm{T}}^{\mathrm{miss}}$, μ+jets

Figure D.10.: Comparison between data and expected background of various kinematic distributions, in the ***b*-tagging category 3**, e+jets channel (left), respectively μ+jets channel (right).

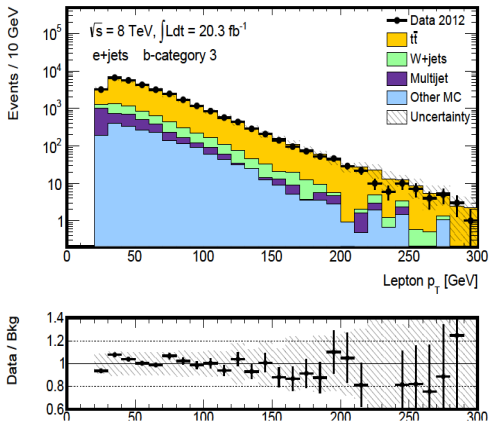

(a) lepton p_{T}, e+jets

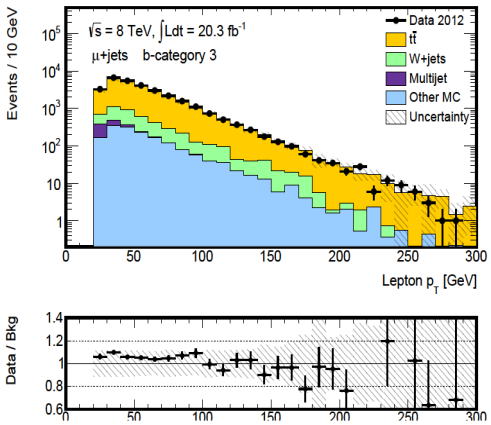

(b) lepton p_{T}, μ+jets

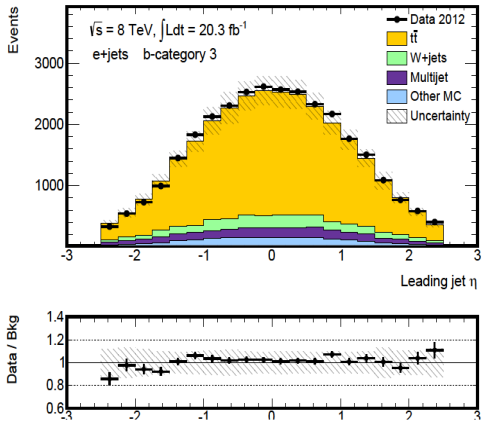

(c) leading jet η, e+jets

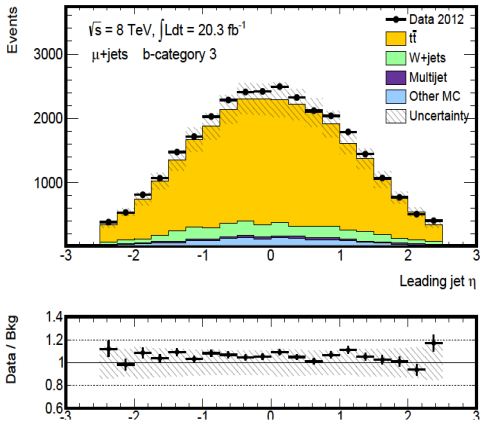

(d) leading jet η, μ+jets

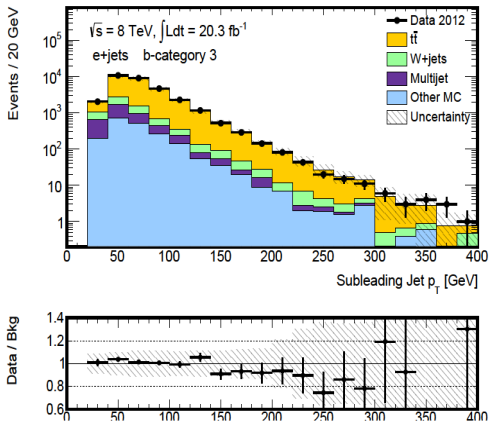

(e) subleading jet p_{T}, e+jets

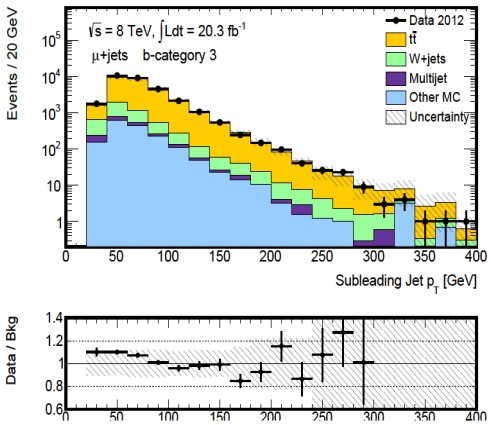

(f) subleading jet p_{T}, μ+jets

Figure D.11.: Comparison between data and expected background of various kinematic distributions, in the ***b*-tagging category 3**, e+jets channel (left), respectively μ+jets channel (right).

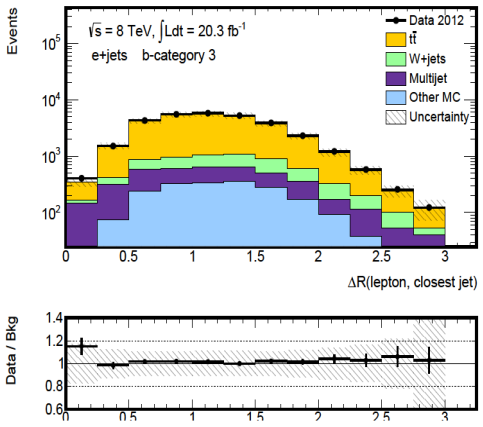

(a) ΔR(lepton, closest jet), e+jets

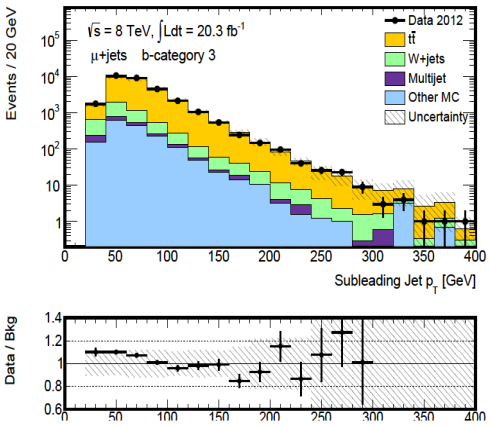

(b) ΔR(lepton, closest jet), μ+jets

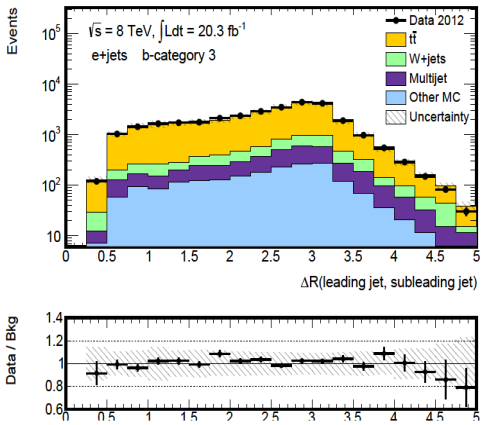

(c) ΔR(leading jet, subleading jet), e+jets

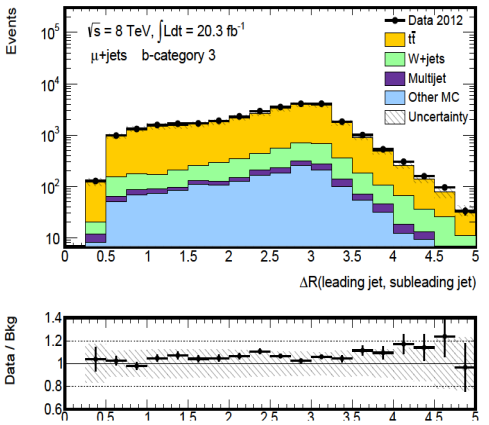

(d) ΔR(leading jet, subleading jet), μ+jets

Figure D.12.: Comparison between data and expected background of various kinematic distributions, in the ***b*-tagging category 3**, e+jets channel (left), respectively μ+jets channel (right).

D.2. Upper Limits Interpretation with the CLs Technique - NOVELTY

An alternative approach to quoting exclusion limits sets $\mu = 1$ and scans the modified p-values as defined in Eq. 6.8. It avoids hence the assumption of constant $m_{t\bar{t}}$ shape template for S and $S+I$, that is employed in the μ scan technique in Section 6.2. The shape is indeed constant for S, but for $S+I$ the shape would scale with $\sqrt{\mu}$. The scanned CLs values are listed in Tables D.1 to D.4. Figure D.13 shows that at high $\tan\beta$ the p-values tend to 1. This phenomenon is explained as a sensitivity decrease: at high $\tan\beta$ (narrower interference patterns), $m_{t\bar{t}}$ is more affected by the detector resolution and is more smeared away, as shown as well in Figures 5.6 and 5.7.

The observed regions below $p = CLs = 0.05$ are excluded: $\tan\beta < 0.85$ for $m_A = 500$ GeV and $\tan\beta < 0.45$ for $m_H = 500$ GeV. The exclusion regions are identical to the ones from the μ scan technique.

$\tan\beta$	Γ [GeV]	Exp. Median	Exp. [-1 σ, +1 σ]	Exp. [-2 σ, +2 σ]	Observed
0.40	142.95	5.2×10^{-12}	[8.8×10^{-15}, 2.1×10^{-9}]	[1.2×10^{-17}, 4.9×10^{-7}]	2.3×10^{-9}
0.50	91.48	7.2×10^{-7}	[8.2×10^{-9}, 4.5×10^{-5}]	[7.8×10^{-11}, 1.6×10^{-3}]	2.2×10^{-4}
0.68	49.46	4.8×10^{-6}	[7.9×10^{-8}, 2.1×10^{-4}]	[1.0×10^{-9}, 5.1×10^{-3}]	2.0×10^{-2}
1.40	11.68	0.097	[0.024, 0.303]	[0.005, 0.648]	0.525
2.00	5.75	0.401	[0.208, 0.670]	[0.099, 0.897]	0.625
5.00	1.14	0.711	[0.538, 0.874]	[0.391, 0.970]	0.776
9.00	1.02	0.982	[0.967, 0.993]	[0.949, 0.998]	0.975

Table D.1.: The observed and expected CLs (modified p-values) for the pseudoscalar A with $m_A = 500$ GeV. The signal strength μ is set to 1.

$\tan\beta$	Γ [GeV]	Exp. Median	Exp. [-1 σ, +1 σ]	Exp. [-2 σ, +2 σ]	Observed
0.40	230.23	0.038	[0.006, 0.169]	[0.001, 0.483]	0.301
0.50	147.35	0.103	[0.027, 0.315]	[0.006, 0.660]	0.527
0.70	75.18	0.282	[0.120, 0.559]	[0.046, 0.842]	0.485
1.40	18.82	0.733	[0.567, 0.885]	[0.422, 0.973]	0.755
2.00	9.26	0.865	[0.763, 0.947]	[0.659, 0.988]	0.880

Table D.2.: The observed and expected CLs (modified p-values) for the pseudoscalar A with $m_A = 750$ GeV. The signal strength μ is set to 1.

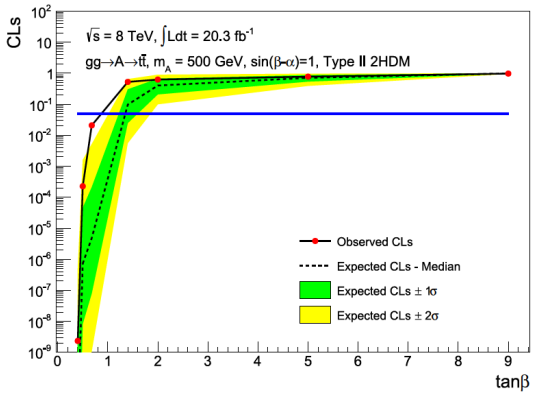

(a) neutral pseudoscalar A, $m_A = 500$ GeV exclude $\tan\beta < 0.85$

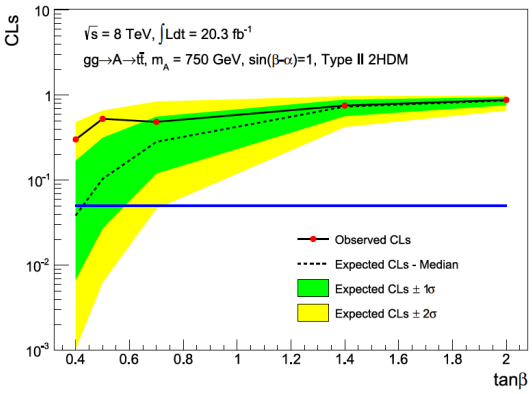

(b) neutral pseudoscalar A, $m_A = 750$ GeV

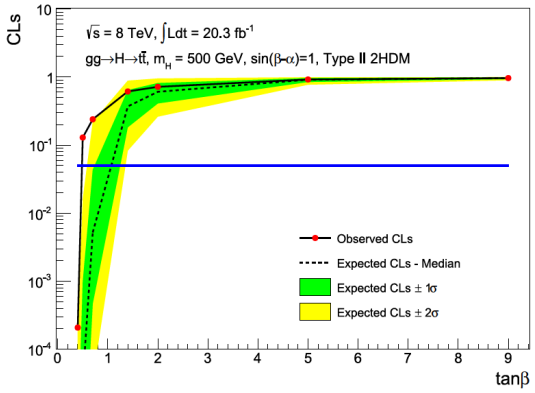

(c) neutral scalar H, $m_H = 500$ GeV exclude $\tan\beta < 0.45$

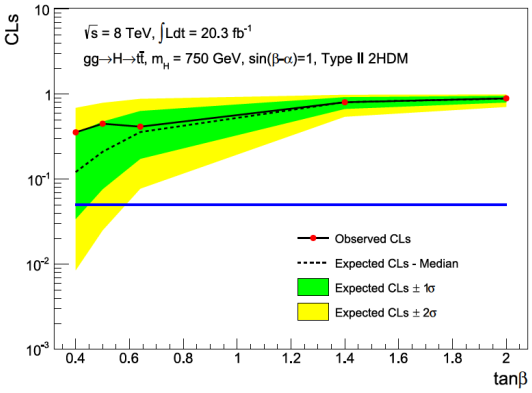

(d) neutral scalar H, $m_H = 750$ GeV

Figure D.13.: Scan of the observed and expected CLs (modified p-values) in the context of the type-II 2HDM defined in Section 4.1.2, as a function of the parameter $\tan\beta$. The crossing of the $p = 0.05$ blue line with the observed line sets the excluded regions.

$\tan\beta$	Γ [GeV]	Exp. Median	Exp. [-1 σ, +1 σ]	Exp. [-2 σ, +2 σ]	Observed
0.40	80.55	3.8×10^{-8}	[2.5×10^{-10}, 4.0×10^{-6}]	[1.4×10^{-12}, 2.3×10^{-4}]	2.0×10^{-4}
0.50	51.55	3.3×10^{-5}	[8.3×10^{-7}, 9.7×10^{-4}]	[1.7×10^{-8}, 1.6×10^{-2}]	1.3×10^{-1}
0.70	26.30	5.2×10^{-3}	[4.6×10^{-4}, 4.3×10^{-2}]	[3.6×10^{-5}, 2.1×10^{-1}]	2.3×10^{-1}
1.40	6.59	0.370	[0.182, 0.643]	[0.083, 0.885]	0.613
2.00	3.25	0.606	[0.409, 0.815]	[0.262, 0.952]	0.717
5.00	0.90	0.914	[0.845, 0.967]	[0.771, 0.993]	0.921
9.00	0.74	0.963	[0.931, 0.986]	[0.896, 0.997]	0.964

Table D.3.: The observed and expected CLs (modified p-values) for the scalar H with $m_H = 500$ GeV. The signal strength μ is set to 1.

$\tan\beta$	Γ [GeV]	Exp. Median	Exp. [-1 σ, +1 σ]	Exp. [-2 σ, +2 σ]	Observed
0.40	189.64	0.121	[0.034, 0.346]	[0.008, 0.690]	0.356
0.50	121.37	0.210	[0.076, 0.475]	[0.025, 0.790]	0.449
0.64	74.08	0.358	[0.173, 0.633]	[0.077, 0.880]	0.415
1.40	15.50	0.806	[0.671, 0.920]	[0.543, 0.982]	0.804
2.00	7.63	0.887	[0.799, 0.956]	[0.708, 0.991]	0.893

Table D.4.: The observed and expected CLs (modified p-values) for the scalar H with $m_H = 750$ GeV. The signal strength μ is set to 1.

Bibliography

[1] ATLAS Collaboration, *Search for heavy Higgs bosons A/H decaying to a top-quark pair in pp collisions at $\sqrt{s} = 8$ TeV with the ATLAS detector*, ATLAS-CONF-2016-073, (2016), https://cds.cern.ch/record/2206229.

[2] D. Dicus, A. Stange and S. Willenbrock, *Higgs decay to top quarks at hadron colliders*, Phys. Lett. **B333** (1994) 126–131, arXiv:hep-ph/9404359 [hep-ph].

[3] R. Frederix and F. Maltoni, *Top pair invariant mass distribution: A Window on new physics*, JHEP **01** (2009) 047, arXiv:0712.2355 [hep-ph].

[4] M. Stanescu-Bellu, K. Mönig, J. Wang, T. Kuhl, J. K. Behr and S. Calvet, *Search for a heavy pseudo-scalar/scalar particle decaying to a top quark pair in pp collisions at $\sqrt{s} = 8$ TeV with the ATLAS detector*, ATL-COM-PHYS-2016-105, (2016), https://cds.cern.ch/record/2129368.

[5] LHC/LC Study Group , *Physics interplay of the LHC and the ILC*, Phys. Rept. **426** (2006) 47–358, arXiv:hep-ph/0410364 [hep-ph].

[6] G. C. Branco, P. M. Ferreira, L. Lavoura, M. N. Rebelo, M. Sher and J. P. Silva, *Theory and phenomenology of two-Higgs-doublet models*, Phys. Rept. **516** (2012) 1–102, arXiv:1106.0034 [hep-ph].

[7] H. E. Haber and G. L. Kane, *The Search for Supersymmetry: Probing Physics Beyond the Standard Model*, Phys. Rept. **117** (1985) 75–263.

[8] J. E. Kim, *Light Pseudoscalars, Particle Physics and Cosmology*, Phys. Rept. **150** (1987) 1–177.

[9] M. Bauer, U. Haisch and F. Kahlhoefer, *Simplified dark matter models with two Higgs doublets: I. Pseudoscalar mediators*, JHEP **05** (2017) 138, arXiv:1701.07427 [hep-ph].

[10] J. Abdallah et al., *Simplified Models for Dark Matter and Missing Energy Searches at the LHC*, arXiv:1409.2893 [hep-ph].

[11] M. Kobayashi and T. Maskawa, *CP Violation in the Renormalizable Theory of Weak Interaction*, Prog. Theor. Phys. **49** (1973) 652–657.

[12] BaBar Collaboration, *Observation of direct CP violation in $B^0 \to K^+\pi^-$ decays*, Phys. Rev. Lett. **93** (2004) 131801, arXiv:hep-ex/0407057 [hep-ex].

[13] A. D. Sakharov, *Violation of CP Invariance, C asymmetry, and baryon asymmetry of the universe*, Pisma Zh. Eksp. Teor. Fiz. **5** (1967) 32–35, [JETP Lett.5,24(1967); Sov. Phys. Usp.34,no.5,392(1991); Usp. Fiz. Nauk161,no.5,61(1991)].

[14] A. Djouadi, *The Anatomy of electro-weak symmetry breaking. II. The Higgs bosons in the minimal supersymmetric model*, Phys. Rept. **459** (2008) 1–241, arXiv:hep-ph/0503173 [hep-ph].

[15] ATLAS Collaboration, *Observation of a new particle in the search for the Standard Model Higgs boson with the ATLAS detector at the LHC*, Phys. Lett. **B716** (2012) 1–29, arXiv:1207.7214 [hep-ex].

[16] CMS Collaboration, *Observation of a New Boson at a Mass of 125 GeV with the CMS Experiment at the LHC*, Phys. Lett. **B716** (2012) 30–61, arXiv:1207.7235 [hep-ex].

[17] A. Djouadi, L. Maiani, A. Polosa, J. Quevillon and V. Riquer, *Fully covering the MSSM Higgs sector at the LHC*, JHEP **06** (2015) 168, arXiv:1502.05653 [hep-ph].

[18] A. Djouadi, L. Maiani, G. Moreau, A. Polosa, J. Quevillon and V. Riquer, *The post-Higgs MSSM scenario: Habemus MSSM?*, Eur. Phys. J. **C73** (2013) 2650, arXiv:1307.5205 [hep-ph].

[19] ATLAS Collaboration, *Constraints on new phenomena via Higgs boson couplings and invisible decays with the ATLAS detector*, JHEP **11** (2015) 206, arXiv:1509.00672 [hep-ex].

[20] ATLAS Collaboration, *BSM Higgs exclusion in the hMSSM, September 2019*, https://atlas.web.cern.ch/Atlas/GROUPS/PHYSICS/CombinedSummaryPlots/HIGGS/ATLAS_HIGGS5100_BSM_hMSSM_tanb_vs_mA_Summary/ATLAS_HIGGS5100_BSM_hMSSM_tanb_vs_mA_Summary.png.

[21] ATLAS Collaboration, *Search for Heavy Higgs Bosons A/H Decaying to a Top Quark Pair in pp Collisions at $\sqrt{s} = 8$ TeV with the ATLAS Detector*, Phys. Rev. Lett. **119** no. 19, (2017) 191803, arXiv:1707.06025 [hep-ex].

[22] ATLAS Collaboration, *A search for $t\bar{t}$ resonances using lepton-plus-jets events in proton-proton collisions at $\sqrt{s} = 8$ TeV with the ATLAS detector*, JHEP **08** (2015) 148, arXiv:1505.07018 [hep-ex].

[23] R. M. Harris, C. T. Hill and S. J. Parke, *Cross-section for topcolor Z-prime(t) decaying to t anti-t: Version 2.6*, arXiv:hep-ph/9911288 [hep-ph].

[24] R. M. Harris and S. Jain, *Cross Sections for Leptophobic Topcolor Z' Decaying to Top-Antitop*, Eur.Phys.J. **C72** (2012) 2072, arXiv:1112.4928 [hep-ph].

[25] D. Abercrombie et al., *Dark Matter Benchmark Models for Early LHC Run-2 Searches: Report of the ATLAS/CMS Dark Matter Forum*, Phys. Dark Univ. **26** (2019) 100371, arXiv:1507.00966 [hep-ex].

[26] B. Lillie, L. Randall and L.-T. Wang, *The Bulk RS KK-gluon at the LHC*, JHEP **0709** (2007) 074, arXiv:hep-ph/0701166 [hep-ph].

[27] K. Agashe, H. Davoudiasl, G. Perez and A. Soni, *Warped Gravitons at the LHC and Beyond*, Phys.Rev. **D76** (2007) 036006, arXiv:hep-ph/0701186 [hep-ph].

[28] A. L. Fitzpatrick, J. Kaplan, L. Randall and L.-T. Wang, *Searching for the Kaluza-Klein Graviton in Bulk RS Models*, JHEP **0709** (2007) 013, arXiv:hep-ph/0701150 [hep-ph].

[29] E. Rutherford, *The scattering of alpha and beta particles by matter and the structure of the atom*, Phil. Mag. Ser.6 **21** (1911) 669–688.

[30] J. Chadwick, *The Existence of a Neutron*, Proc. Roy. Soc. Lond. **A136** no. 830, (1932) 692–708.

[31] J. C. Maxwell, *A dynamical theory of the electromagnetic field*, Phil. Trans. Roy. Soc. Lond. **155** (1865) 459–512.

[32] M. Planck, *Ueber eine Verbesserung der Wiens'chen Spektralgleichung*, j-VERH-DTSCH-PHYS-GES **2** no. 13, (1900) 202–204.

[33] M. Planck, *Zur Theorie des Gesetzes der Energieverteilung im Normalspektrum.*, j-VERH-DTSCH-PHYS-GES **2** no. 17, (1900) 237–245.

[34] A. Einstein, *Concerning an heuristic point of view toward the emission and transformation of light*, Annalen Phys. **17** (1905) 132–148.

[35] E. Fermi, *An attempt of a theory of beta radiation. 1.*, Z. Phys. **88** (1934) 161–177.

[36] TASSO Collaboration, *Evidence for Planar Events in e+ e- Annihilation at High-Energies*, Phys. Lett. **86B** (1979) 243–249.

[37] PETRA Collaboration, *Discovery of Three Jet Events and a Test of Quantum Chromodynamics at PETRA Energies*, Phys. Rev. Lett. **43** (1979) 830.

[38] UA1 Collaboration, *Experimental Observation of Isolated Large Transverse Energy Electrons with Associated Missing Energy at s**(1/2) = 540-GeV*, Phys. Lett. **122B** (1983) 103–116.

[39] UA1 Collaboration, *Experimental Observation of Lepton Pairs of Invariant Mass Around 95-GeV/c**2 at the CERN SPS Collider*, Phys. Lett. **126B** (1983) 398–410.

[40] UA2 Collaboration, *Observation of Single Isolated Electrons of High Transverse Momentum in Events with Missing Transverse Energy at the CERN anti-p p Collider*, Phys. Lett. **122B** (1983) 476–485.

[41] UA2 Collaboration, *Evidence for Z0 —> e+ e- at the CERN anti-p p Collider*, Phys. Lett. **129B** (1983) 130–140.

[42] S. L. Glashow, *Partial Symmetries of Weak Interactions*, Nucl. Phys. **22** (1961) 579–588.

[43] A. Salam and J. C. Ward, *Electromagnetic and weak interactions*, Phys. Lett. **13** (1964) 168–171.

[44] S. Weinberg, *A Model of Leptons*, Phys. Rev. Lett. **19** (1967) 1264–1266.

[45] S. L. Glashow, J. Iliopoulos and L. Maiani, *Weak Interactions with Lepton-Hadron Symmetry*, Phys. Rev. **D2** (1970) 1285–1292.

[46] G. 't Hooft and M. J. G. Veltman, *Regularization and Renormalization of Gauge Fields*, Nucl. Phys. **B44** (1972) 189–213.

[47] F. Halzen and A. Martin, *Quarks and Leptons: An introductory course in modern particle physics*, John Wiley and Sons, (1984).

[48] M. E. Peskin and D. V. Schroeder, *An Introduction to quantum field theory*, Addison-Wesley, (1995).

[49] B. R. Martin and G. Shaw, *Particle physics*, John Wiley, third edition ed., (2008).

[50] F. Mandl and G. Shaw, *Quantum field theory*, John Wiley and Sons, rev. ed. ed., (1993).

[51] Particle Data Group , *Review of Particle Physics*, Phys. Rev. D **98** no. 10, (2018) 030001.

[52] Super-Kamiokande Collaboration, *Evidence for oscillation of atmospheric neutrinos*, Phys. Rev. Lett. **81** (1998) 1562–1567, arXiv:hep-ex/9807003 [hep-ex].

[53] ATLAS, CDF, CMS, D0 Collaboration, *First combination of Tevatron and LHC measurements of the top-quark mass*, arXiv:1403.4427 [hep-ex].

[54] P. A. M. Dirac, *The quantum theory of the electron*, Proc. Roy. Soc. Lond. **A117** (1928) 610–624.

[55] E. Majorana, *Theory Of The Symmetry Of Electrons And Positrons*, Nuovo Cim. **14** (1937) 171–184.

[56] ATLAS Collaboration, *Search for heavy Majorana or Dirac neutrinos and right-handed W gauge bosons in final states with two charged leptons and two jets at* $\sqrt{s} = 13$ *TeV with the ATLAS detector*, JHEP **01** (2019) 016, arXiv:1809.11105 [hep-ex].

[57] K. G. Wilson, *Confinement of Quarks*, Phys. Rev. **D10** (1974) 2445–2459, [,319(1974)].

[58] CREMA Collaboration, *Laser Spectroscopy of Muonic Hydrogen and the Puzzling Proton*, J. Phys. Soc. Jap. **85** no. 9, (2016) 091003.

[59] S. Bethke, G. Dissertori and G. P. Salam, *World Summary of* α_s *(2015)*, EPJ Web Conf. **120** (2016) 07005.

[60] L3 Collaboration, *Measurement of the running of the electromagnetic coupling at large momentum-transfer at LEP*, Physics Letters B **623** no. 1, (2005) 26 – 36.

[61] E. Noether, *Invariant Variation Problems*, Gott. Nachr. **1918** (1918) 235–257, arXiv:physics/0503066 [physics], [Transp. Theory Statist. Phys.1,186(1971)].

[62] A. J. MacFarlane, A. Sudbery and P. H. Weisz, *On Gell-Mann's lambda-matrices, d- and f-tensors, octets, and parametrizations of SU(3)*, Commun. Math. Phys. **11** (1968) 77–90.

[63] F. Englert and R. Brout, *Broken Symmetry and the Mass of Gauge Vector Mesons*, Phys. Rev. Lett. **13** (1964) 321–323, [,157(1964)].

[64] P. W. Higgs, *Broken Symmetries and the Masses of Gauge Bosons*, Phys. Rev. Lett. **13** (1964) 508–509, [,160(1964)].

[65] T. van Ritbergen and R. G. Stuart, *Complete 2-Loop Quantum Electrodynamic Contributions to the Muon Lifetime in the Fermi Model*, Phys. Rev. Lett. **82** (1999) 488–491.

[66] J. E. Kim, P. Langacker, M. Levine and H. H. Williams, *A Theoretical and Experimental Review of the Weak Neutral Current: A Determination of Its Structure and Limits on Deviations from the Minimal SU(2)-L x U(1) Electroweak Theory*, Rev. Mod. Phys. **53** (1981) 211.

[67] *LHC Higgs Cross Section Working Group*, https://twiki.cern.ch/twiki/bin/view/LHCPhysics/LHCHXSWG.

[68] M. Czakon and A. Mitov, *Top++: A Program for the Calculation of the Top-Pair Cross-Section at Hadron Colliders*, Comput. Phys. Commun. **185** (2014) 2930, arXiv:1112.5675 [hep-ph].

[69] M. Beneke, P. Falgari, S. Klein and C. Schwinn, *Hadronic top-quark pair production with NNLL threshold resummation*, Nucl. Phys. **B855** (2012) 695–741, arXiv:1109.1536 [hep-ph].

[70] M. Cacciari, M. Czakon, M. Mangano, A. Mitov and P. Nason, *Top-pair production at hadron colliders with next-to-next-to-leading logarithmic soft-gluon resummation*, Phys. Lett. **B710** (2012) 612–622, arXiv:1111.5869 [hep-ph].

[71] P. Bärnreuther, M. Czakon and A. Mitov, *Percent Level Precision Physics at the Tevatron: First Genuine NNLO QCD Corrections to $q\bar{q} \to t\bar{t} + X$*, Phys. Rev. Lett. **109** (2012) 132001, arXiv:1204.5201 [hep-ph].

[72] M. Czakon and A. Mitov, *NNLO corrections to top-pair production at hadron colliders: the all-fermionic scattering channels*, JHEP **12** (2012) 054, arXiv:1207.0236 [hep-ph].

[73] M. Czakon and A. Mitov, *NNLO corrections to top pair production at hadron colliders: the quark-gluon reaction*, JHEP **1301** (2013) 080, arXiv:1210.6832 [hep-ph].

[74] M. Czakon, P. Fiedler and A. Mitov, *Total Top-Quark Pair-Production Cross Section at Hadron Colliders Through $O(\alpha_S^4)$*, Phys.Rev.Lett. **110** (2013) 252004, arXiv:1303.6254 [hep-ph].

[75] N. Kidonakis, *Next-to-next-to-leading-order collinear and soft gluon corrections for t-channel single top quark production*, Phys. Rev. **D83** (2011) 091503, arXiv:1103.2792 [hep-ph].

[76] N. Kidonakis, *NNLL resummation for s-channel single top quark production*, Phys. Rev. **D81** (2010) 054028, arXiv:1001.5034 [hep-ph].

[77] N. Kidonakis, *Two-loop soft anomalous dimensions for single top quark associated production with a W^- or H^-*, Phys.Rev. **D82** (2010) 054018, arXiv:1005.4451 [hep-ph].

[78] B. Andersson, G. Gustafson, G. Ingelman and T. Sjostrand, *Parton Fragmentation and String Dynamics*, Phys. Rept. **97** (1983) 31–145.

[79] B. R. Webber, *A QCD Model for Jet Fragmentation Including Soft Gluon Interference*, Nucl. Phys. **B238** (1984) 492–528.

[80] D. E. Soper, *Basics of QCD Perturbation Theory*, arXiv:hep-ph/9702203 [hep-ph].

[81] G. Altarelli and G. Parisi, *Asymptotic Freedom in Parton Language*, Nucl. Phys. **B126** (1977) 298–318.

[82] S. Dulat, T.-J. Hou, J. Gao, M. Guzzi, J. Huston, P. Nadolsky, J. Pumplin, C. Schmidt, D. Stump and C. P. Yuan, *New parton distribution functions from a global analysis of quantum chromodynamics*, Phys. Rev. **D93** no. 3, (2016) 033006, arXiv:1506.07443 [hep-ph].

[83] A. D. Martin, W. J. Stirling, R. S. Thorne and G. Watt, *Parton distributions for the LHC*, Eur. Phys. J. **C63** (2009) 189–285, arXiv:0901.0002 [hep-ph].

[84] C. Lefèvre, *The CERN accelerator complex. Complexe des accélérateurs du CERN*, CERN-DI-0812015, (2008), http://cds.cern.ch/record/1260465.

[85] L. Evans and P. Bryant, *LHC Machine*, Journal of Instrumentation **3** no. 08, (2008) S08001.

[86] O. S. Brüning, P. Collier, P. Lebrun, S. Myers, R. Ostojic, J. Poole and P. Proudlock, *LHC Design Report*, CERN-2004-003-V-1, (2004), http://cds.cern.ch/record/782076.

[87] ALICE Collaboration, *The ALICE experiment at the CERN LHC*, Journal of Instrumentation **3** no. 08, (2008) S08002.

[88] ATLAS Collaboration, *The ATLAS Experiment at the CERN Large Hadron Collider*, Journal of Instrumentation **3** no. 08, (2008) S08003.

[89] CMS Collaboration, *The CMS experiment at the CERN LHC*, Journal of Instrumentation **3** no. 08, (2008) S08004.

[90] LHCb Collaboration, *The LHCb Detector at the LHC*, Journal of Instrumentation **3** no. 08, (2008) S08005.

[91] LHCf Collaboration, *The LHCf detector at the CERN Large Hadron Collider*, Journal of Instrumentation **3** no. 08, (2008) S08006.

[92] MoEDAL Collaboration, *Technical Design Report of the MoEDAL Experiment*, CERN-LHCC-2009-006, MoEDAL-TDR-001, (2009), http://cds.cern.ch/record/1181486.

[93] TOTEM Collaboration, *The TOTEM Experiment at the CERN Large Hadron Collider*, Journal of Instrumentation **3** no. 08, (2008) S08007.

[94] *LHC sets new world record with 1.18 TeV per beam*, http://press.cern/press-releases/2009/11/lhc-sets-new-world-record.

[95] C. Gemme, *The ATLAS upgrade program*, in *Proceedings, 2nd Conference on Large Hadron Collider Physics Conference (LHCP 2014): New York, USA, June 2-7*, (2014), arXiv:1409.5002 [physics.ins-det].

[96] *The Large Hadron Collider timeline*, http://timeline.web.cern.ch/timelines/The-Large-Hadron-Collider.

[97] *The Large Electron-Positron Collider timeline*, http://timeline.web.cern.ch/timelines/The-Large-Electron-Positron-Collider.

[98] *Large Hadron Collider Commissioning with beam*, http://lhc-commissioning.web.cern.ch/lhc-commissioning.

[99] *ATLAS Luminosity Public Results*, http://twiki.cern.ch/twiki/bin/view/AtlasPublic/LuminosityPublicResults.

[100] G. Apollinari, I. Béjar Alonso, O. Brüning, P. Fessia, M. Lamont, L. Rossi and L. Tavian, *High-Luminosity Large Hadron Collider (HL-LHC): Technical Design Report V. 0.1*, CERN-2017-007-M, (2017), http://cds.cern.ch/record/2284929.

[101] CLICdp and CLIC Collaboration, *Updated baseline for a staged Compact Linear Collider*, arXiv:1608.07537 [physics.acc-ph].

[102] T. Behnke, J. E. Brau, B. Foster, J. Fuster, M. Harrison, J. M. Paterson, M. Peskin, M. Stanitzki, N. Walker and H. Yamamoto, *The International Linear Collider Technical Design Report - Volume 1: Executive Summary*, arXiv:1306.6327 [physics.acc-ph].

[103] C. Lippmann, *Particle identification*, Nucl. Instrum. Meth. **A666** (2012) 148–172, arXiv:1101.3276 [hep-ex].

[104] ATLAS Collaboration, *Measurements of the charged-particle distributions at* $\sqrt{s} = 8$ *and 13 TeV with the ATLAS detector*, PoS **DIS2016** (2016) 199.

[105] J. J. Goodson, *Search for Supersymmetry in States with Large Missing Transverse Momentum and Three Leptons including a Z-Boson*. PhD thesis, May, 2012. http://cds.cern.ch/record/1449722. Presented 17 Apr 2012.

[106] ATLAS Collaboration, *ATLAS inner detector: Technical design report. Vol. 1*, CERN-LHCC-97-16, ATLAS-TDR-4, (1997), http://cds.cern.ch/record/331063.

[107] ATLAS Collaboration, *ATLAS Insertable B-Layer Technical Design Report*, CERN-LHCC-2010-013. ATLAS-TDR-19, (2010), https://cds.cern.ch/record/1291633.

[108] ATLAS Collaboration, *Expected Performance of the ATLAS Experiment - Detector, Trigger and Physics*, arXiv:0901.0512 [hep-ex].

[109] ATLAS Collaboration, *ATLAS liquid argon calorimeter: Technical design report*, CERN-LHCC-96-41, (1996), http://cds.cern.ch/record/331061.

[110] ATLAS Collaboration, *ATLAS tile calorimeter: Technical design report*, CERN-LHCC-96-42, (1996), http://cds.cern.ch/record/331062.

[111] ATLAS Collaboration, *ATLAS muon spectrometer: Technical design report*, CERN-LHCC-97-22, ATLAS-TDR-10, (1997), http://cds.cern.ch/record/331068.

[112] ATLAS Collaboration, *ATLAS magnet system: Technical design report*, CERN-LHCC-97-18, (1997), http://cds.cern.ch/record/338080.

[113] ATLAS Collaboration, *ATLAS high-level trigger, data acquisition and controls: Technical design report*, CERN-LHCC-2003-022, ATLAS-TRD-016, (2003), http://cds.cern.ch/record/616089.

[114] A. Djouadi, *The Anatomy of electro-weak symmetry breaking. I: The Higgs boson in the standard model*, Phys. Rept. **457** (2008) 1–216, arXiv:hep-ph/0503172 [hep-ph].

[115] ATLAS Collaboration, *Search for bottom-squark pair production with the ATLAS detector in final states containing Higgs bosons, b-jets and missing transverse momentum*, JHEP **12** (2019) 060, arXiv:1908.03122 [hep-ex].

[116] ATLAS Collaboration, *Search for electroweak production of charginos and sleptons decaying into final states with two leptons and missing transverse momentum in* $\sqrt{s} = 13$ *TeV pp collisions using the ATLAS detector*, Eur. Phys. J. **C80** no. 2, (2020) 123, arXiv:1908.08215 [hep-ex].

[117] L. Alvarez-Gaume and E. Witten, *Gravitational Anomalies*, Nucl. Phys. **B234** (1984) 269.

[118] P. Fayet, *Supergauge Invariant Extension of the Higgs Mechanism and a Model for the electron and Its Neutrino*, Nucl. Phys. **B90** (1975) 104–124.

[119] ATLAS Collaboration, *Beyond Standard Model Higgs boson searches at a High-Luminosity LHC with ATLAS*, ATL-PHYS-PUB-2013-016, (2013), http://cds.cern.ch/record/1611190.

[120] T. D. Lee, *A Theory of Spontaneous T Violation*, Phys. Rev. D **8** (1973) 1226–1239.

[121] O. U. Shanker, *Flavor Violation, Scalar Particles and Leptoquarks*, Nucl. Phys. **B206** (1982) 253–272.

[122] J. F. Gunion and H. E. Haber, *The CP conserving two Higgs doublet model: The Approach to the decoupling limit*, Phys. Rev. **D67** (2003) 075019, arXiv:hep-ph/0207010 [hep-ph].

[123] J. Bernon, J. F. Gunion, H. E. Haber, Y. Jiang and S. Kraml, *Scrutinizing the alignment limit in two-Higgs-doublet models: m_h=125 GeV*, Phys. Rev. **D92** no. 7, (2015) 075004, arXiv:1507.00933 [hep-ph].

[124] LHC Higgs Cross Section Working Group , *Handbook of LHC Higgs Cross Sections: 4. Deciphering the Nature of the Higgs Sector*, arXiv:1610.07922 [hep-ph].

[125] R. V. Harlander, S. Liebler and H. Mantler, *SusHi: A program for the calculation of Higgs production in gluon fusion and bottom-quark annihilation in the Standard Model and the MSSM*, Comput. Phys. Commun. **184** (2013) 1605–1617, arXiv:1212.3249 [hep-ph].

[126] R. V. Harlander, S. Liebler and H. Mantler, *SusHi Bento: Beyond NNLO and the heavy-top limit*, Comput. Phys. Commun. **212** (2017) 239–257, arXiv:1605.03190 [hep-ph].

[127] D. Eriksson, J. Rathsman and O. Stal, *2HDMC: Two-Higgs-Doublet Model Calculator Physics and Manual*, Comput. Phys. Commun. **181** (2010) 189–205, arXiv:0902.0851 [hep-ph].

[128] C. N. Yang, *Selection Rules for the Dematerialization of a Particle into Two Photons*, Phys. Rev. **77** (1950) 242–245.

[129] D. Buarque Franzosi and C. Zhang, *MG bottom and top loop structure in ggH/ggA*, http://cp3.irmp.ucl.ac.be/projects/madgraph/wiki/Models/ggHFullLoop.

[130] K. J. F. Gaemers and F. Hoogeveen, *Higgs Production and Decay Into Heavy Flavors With the Gluon Fusion Mechanism*, Phys. Lett. **B146** (1984) 347.

[131] D. Buarque Franzosi and M. T. Frandsen, *Symmetries and composite dynamics for the 750 GeV diphoton excess*, arXiv:1601.05357 [hep-ph].

[132] D. Buarque Franzosi, E. Vryonidou and C. Zhang, *Scalar production and decay to top quarks including interference effects at NLO in QCD in an EFT approach*, JHEP **10** (2017) 096, arXiv:1707.06760 [hep-ph].

[133] J. Alwall, M. Herquet, F. Maltoni, O. Mattelaer and T. Stelzer, *MadGraph 5 : Going Beyond*, JHEP **06** (2011) 128, arXiv:1106.0522 [hep-ph].

[134] J. Alwall, R. Frederix, S. Frixione, V. Hirschi, F. Maltoni, O. Mattelaer, H. S. Shao, T. Stelzer, P. Torrielli and M. Zaro, *The automated computation of tree-level and next-to-leading order differential cross sections, and their matching to parton shower simulations*, JHEP **07** (2014) 079, arXiv:1405.0301 [hep-ph].

[135] *Discussions with the MadGraph authors*, http://answers.launchpad.net/mg5amcnlo/+question/238699.

[136] D. Berdine, N. Kauer and D. Rainwater, *Breakdown of the Narrow Width Approximation for New Physics*, Phys. Rev. Lett. **99** (2007) 111601, arXiv:hep-ph/0703058 [hep-ph].

[137] ATLAS Collaboration, *Measurement of the correlations between the polar angles of leptons from top quark decays in the helicity basis at* $\sqrt{s} = 7\,TeV$ *using the ATLAS detector*, Phys. Rev. **D93** no. 1, (2016) 012002, arXiv:1510.07478 [hep-ex].

[138] J. C. Collins and D. E. Soper, *Angular Distribution of Dileptons in High-Energy Hadron Collisions*, Phys. Rev. **D16** (1977) 2219.

[139] M. Jezabek and J. H. Kuhn, *V-A tests through leptons from polarized top quarks*, Phys. Lett. **B329** (1994) 317–324, arXiv:hep-ph/9403366 [hep-ph].

[140] A. Czarnecki, M. Jeżabek and J. H. Kühn, *Lepton spectra from decays of polarized top quarks*, Nuclear Physics B **351** no. 1, (1991) 70 – 80.

[141] W. Bernreuther, A. Brandenburg, Z. G. Si and P. Uwer, *Top quark pair production and decay including spin effects at hadron colliders: Predictions at NLO QCD*, Int. J. Mod. Phys. **A18** (2003) 1357–1364, arXiv:hep-ph/0111346 [hep-ph].

[142] W. Bernreuther, M. Flesch and P. Haberl, *Signatures of Higgs bosons in the top quark decay channel at hadron colliders*, Phys. Rev. **D58** (1998) 114031, arXiv:hep-ph/9709284 [hep-ph].

[143] S. Frixione, P. Nason and G. Ridolfi, *A Positive-weight next-to-leading-order Monte Carlo for heavy flavour hadroproduction*, JHEP **09** (2007) 126, arXiv:0707.3088 [hep-ph].

[144] P. Nason, *A New method for combining NLO QCD with shower Monte Carlo algorithms*, JHEP **0411** (2004) 040, arXiv:hep-ph/0409146 [hep-ph].

[145] S. Frixione, P. Nason and C. Oleari, *Matching NLO QCD computations with Parton Shower simulations: the POWHEG method*, JHEP **0711** (2007) 070, arXiv:0709.2092 [hep-ph].

[146] S. Alioli, P. Nason, C. Oleari and E. Re, *A general framework for implementing NLO calculations in shower Monte Carlo programs: the POWHEG BOX*, JHEP **1006** (2010) 043, arXiv:1002.2581 [hep-ph].

[147] T. Sjostrand, S. Mrenna and P. Z. Skands, *PYTHIA 6.4 Physics and Manual*, JHEP **05** (2006) 026, arXiv:hep-ph/0603175 [hep-ph].

[148] P. Z. Skands, *Tuning Monte Carlo Generators: The Perugia Tunes*, Phys. Rev. **D82** (2010) 074018, arXiv:1005.3457 [hep-ph].

[149] J. Alwall, S. Höche, F. Krauss, N. Lavesson, L. Lönnblad, F. Maltoni, M. Mangano, M. Moretti, C. Papadopoulos, F. Piccinini et al., *Comparative study of various algorithms*

for the merging of parton showers and matrix elements in hadronic collisions, The European Physical Journal C **53** no. 3, (2007) 473–500.

[150] T. Sjöstrand, S. Mrenna and P. Skands, *A brief introduction to PYTHIA 8.1*, Computer Physics Communications **178** no. 11, (2008) 852–867.

[151] H.-L. Lai, M. Guzzi, J. Huston, Z. Li, P. M. Nadolsky, J. Pumplin and C.-P. Yuan, *New parton distributions for collider physics*, Physical Review D **82** no. 7, (2010).

[152] ATLAS Collaboration, *Summer 2013 top-antitop resonance search*, http://twiki.cern.ch/twiki/bin/viewauth/AtlasProtected/Summer2013TopResonances.

[153] A. Altheimer et al., *A search for $t\bar{t}$ resonances in the lepton plus jets final state using 20 fb^{-1} of pp collisions at $\sqrt{s} = 8$ TeV*, ATL-COM-PHYS-2014-003, (2014), http://cds.cern.ch/record/1640960.

[154] B. Acharya et al., *Object selection and calibration, background estimations and MC samples for top quark analyses using the full 2012 data set*, ATL-COM-PHYS-2013-1016, (2013), http://cds.cern.ch/record/1563201.

[155] ATLAS Collaboration, *Search for resonances decaying into top-quark pairs using fully hadronic decays in pp collisions with ATLAS at $\sqrt{s} = 7$ TeV*, JHEP **01** (2013) 116, arXiv:1211.2202 [hep-ex].

[156] M. Beneke, I. Efthymiopoulos, M. L. Mangano, J. Womersley et al., *Top Quark Physics*, https://cds.cern.ch/record/429963.

[157] ATLAS Collaboration, *Measurement of the top quark pair production cross section in pp collisions at $\sqrt{s} = 7$ TeV in dilepton final states with ATLAS*, Phys. Lett. **B707** (2012) 459–477, arXiv:1108.3699 [hep-ex].

[158] ATLAS Collaboration, *The ATLAS Simulation Infrastructure*, Eur. Phys. J. **C70** (2010) 823–874, arXiv:1005.4568 [physics.ins-det].

[159] GEANT4 Collaboration, *GEANT4: A Simulation toolkit*, Nucl. Instrum. Meth. **A506** (2003) 250–303.

[160] ATLAS Collaboration, *The simulation principle and performance of the ATLAS fast calorimeter simulation FastCaloSim*,.

[161] M. Czakon and A. Mitov, *Top++: A Program for the Calculation of the Top-Pair Cross-Section at Hadron Colliders*, Comput. Phys. Commun. **185** (2014) 2930, arXiv:1112.5675 [hep-ph].

[162] J. Kühn, A. Scharf and P. Uwer, *Weak Interactions in Top-Quark Pair Production at Hadron Colliders: An Update*, Phys.Rev. **D91** no. 1, (2015) 014020, arXiv:1305.5773 [hep-ph].

[163] S. Frixione, E. Laenen, P. Motylinski, B. R. Webber and C. D. White, *Single-top hadroproduction in association with a W boson*, JHEP **07** (2008) 029, arXiv:0805.3067 [hep-ph].

[164] M. Garzelli, A. Kardos, C. Papadopoulos and Z. Trocsanyi, *$t\bar{t}W^{\pm}$ and $t\bar{t}Z$ Hadroproduction at NLO accuracy in QCD with Parton Shower and Hadronization effects*, JHEP **1211** (2012) 056, arXiv:1208.2665 [hep-ph].

[165] J. Pumplin, D. R. Stump, J. Huston, H. L. Lai, P. M. Nadolsky and W. K. Tung, *New generation of parton distributions with uncertainties from global QCD analysis*, JHEP **0207** (2002) 012, arXiv:hep-ph/0201195 [hep-ph].

[166] M. L. Mangano, M. Moretti, F. Piccinini, R. Pittau and A. D. Polosa, *ALPGEN, a generator for hard multiparton processes in hadronic collisions*, JHEP **0307** (2003) 001, arXiv:hep-ph/0206293 [hep-ph].

[167] R. Gavin, Y. Li, F. Petriello and S. Quackenbush, *W Physics at the LHC with FEWZ 2.1*, Comput.Phys.Commun. **184** (2013) 208–214, arXiv:1201.5896 [hep-ph].

[168] S. Schumann and F. Krauss, *A Parton shower algorithm based on Catani-Seymour dipole factorisation*, JHEP **03** (2008) 038, arXiv:0709.1027 [hep-ph].

[169] T. Gleisberg, S. Hoeche, F. Krauss, M. Schonherr, S. Schumann, F. Siegert and J. Winter, *Event generation with SHERPA 1.1*, JHEP **0902** (2009) 007, arXiv:0811.4622 [hep-ph].

[170] S. Hoeche, F. Krauss, S. Schumann and F. Siegert, *QCD matrix elements and truncated showers*, JHEP **05** (2009) 053, arXiv:0903.1219 [hep-ph].

[171] T. Gleisberg and S. Hoeche, *Comix, a new matrix element generator*, JHEP **12** (2008) 039, arXiv:0808.3674 [hep-ph].

[172] J. M. Campbell and R. Ellis, *MCFM for the Tevatron and the LHC*, Nucl.Phys.Proc.Suppl. **205-206** (2010) 10–15, arXiv:1007.3492 [hep-ph].

[173] M. Shochet, L. Tompkins, V. Cavaliere, P. Giannetti, A. Annovi and G. Volpi, *Fast TracKer (FTK) Technical Design Report*, CERN-LHCC-2013-007. ATLAS-TDR-021, (2013), http://cds.cern.ch/record/1552953. ATLAS Fast Tracker Technical Design Report.

[174] T. Cornelissen, M. Elsing, S. Fleischmann, W. Liebig, E. Moyse and A. Salzburger, *Concepts, Design and Implementation of the ATLAS New Tracking (NEWT)*, ATL-SOFT-PUB-2007-007. ATL-COM-SOFT-2007-002, (2007), https://cds.cern.ch/record/1020106.

[175] ATLAS Collaboration, *Performance of primary vertex reconstruction in proton-proton collisions at $\sqrt{s} = 7$ TeV in the ATLAS experiment*, ATLAS-CONF-2010-069, (2010), https://cds.cern.ch/record/1281344.

[176] ATLAS Collaboration, *Performance of pile-up mitigation techniques for jets in pp collisions at $\sqrt{s} = 8$ TeV using the ATLAS detector*, Eur. Phys. J. **C76** no. 11, (2016) 581, arXiv:1510.03823 [hep-ex].

[177] ATLAS Collaboration, *Luminosity Determination in pp Collisions at $\sqrt{s} = 7$ TeV Using the ATLAS Detector at the LHC*, Eur. Phys. J. **C71** (2011) 1630, arXiv:1101.2185 [hep-ex].

[178] ATLAS Collaboration, *Electron performance measurements with the ATLAS detector using the 2010 LHC proton-proton collision data*, Eur. Phys. J. **C72** (2012) 1909, arXiv:1110.3174 [hep-ex].

[179] ATLAS Collaboration, *Electron reconstruction and identification efficiency measurements with the ATLAS detector using the 2011 LHC proton-proton collision data*, Eur. Phys. J. **C74** no. 7, (2014) 2941, arXiv:1404.2240 [hep-ex].

[180] ATLAS Collaboration, *Measurement of the muon reconstruction performance of the ATLAS detector using 2011 and 2012 LHC proton–proton collision data*, Eur. Phys. J. **C74** no. 11, (2014) 3130, arXiv:1407.3935 [hep-ex].

[181] K. Rehermann and B. Tweedie, *Efficient Identification of Boosted Semileptonic Top Quarks at the LHC*, JHEP **03** (2011) 059, arXiv:1007.2221 [hep-ph].

[182] ATLAS Collaboration, *Topological cell clustering in the ATLAS calorimeters and its performance in LHC Run 1*, Eur. Phys. J. **C77** (2017) 490, arXiv:1603.02934 [hep-ex].

[183] M. Cacciari, G. P. Salam and G. Soyez, *The anti-k_t jet clustering algorithm*, JHEP **04** (2008) 063, arXiv:0802.1189 [hep-ph].

[184] M. Cacciari, G. P. Salam and G. Soyez, *FastJet User Manual*, Eur. Phys. J. **C72** (2012) 1896, arXiv:1111.6097 [hep-ph].

[185] ATLAS Collaboration, *Jet energy measurement and its systematic uncertainty in proton-proton collisions at $\sqrt{s} = 7$ TeV with the ATLAS detector*, Eur. Phys. J. **C75** (2015) 17, arXiv:1406.0076 [hep-ex].

[186] ATLAS Collaboration, *Jet energy measurement with the ATLAS detector in proton-proton collisions at $\sqrt{s} = 7$ TeV*, Eur. Phys. J. **C73** no. 3, (2013) 2304, arXiv:1112.6426 [hep-ex].

[187] ATLAS Collaboration, *Pile-up subtraction and suppression for jets in ATLAS*, ATLAS-CONF-2013-083, (2013), https://cds.cern.ch/record/1570994.

[188] ATLAS Collaboration, *Jet energy resolution in proton-proton collisions at $\sqrt{s} = 7$ TeV recorded in 2010 with the ATLAS detector*, Eur. Phys. J. **C73** no. 3, (2013) 2306, arXiv:1210.6210 [hep-ex].

[189] ATLAS Collaboration, *Commissioning of the ATLAS high-performance b-tagging algorithms in the 7 TeV collision data*, ATLAS-CONF-2011-102, (2011), https://cds.cern.ch/record/1369219.

[190] ATLAS Collaboration, *Performance of Missing Transverse Momentum Reconstruction in Proton-Proton Collisions at 7 TeV with ATLAS*, Eur. Phys. J. **C72** (2012) 1844, arXiv:1108.5602 [hep-ex].

[191] ATLAS Collaboration, *ATLAS High-Level Trigger performance for calorimeter-based algorithms in LHC Run-I*, Journal of Physics: Conference Series **513** no. 1, (2014) 012022.

[192] ATLAS Collaboration, *Performance of the ATLAS muon trigger in pp collisions at $\sqrt{s} = 8$ TeV*, Eur. Phys. J. **C75** (2015) 120, arXiv:1408.3179 [hep-ex].

[193] ATLAS Collaboration, *Muon reconstruction efficiency and momentum resolution of the ATLAS experiment in proton-proton collisions at $\sqrt{s} = 7$ TeV in 2010*, Eur. Phys. J. **C74** no. 9, (2014) 3034, arXiv:1404.4562 [hep-ex].

[194] T. Chwalek, *Messung der W-Boson-Helizitätsanteile in Top-Quark-Zerfällen mit dem CDF II Experiment und Studien zu einer frühen Messung des ttbar-Wirkungsquerschnitts mit dem CMS Experiment*. PhD thesis, 2010. https://cds.cern.ch/record/1416031. Presented 12 Feb 2010.

[195] ATLAS Collaboration, *Measurement of the charge asymmetry in top quark pair production in pp collisions at $\sqrt{s} = 7$ TeV using the ATLAS detector*, Eur. Phys. J. **C72** (2012) 2039, arXiv:1203.4211 [hep-ex].

[196] ATLAS Collaboration, *Measurements of top quark pair relative differential cross-sections with ATLAS in pp collisions at $\sqrt{s} = 7$ TeV*, Eur. Phys. J. **C73** no. 1, (2013) 2261, arXiv:1207.5644 [hep-ex].

[197] ATLAS Collaboration, *Estimation of non-prompt and fake lepton backgrounds in final states with top quarks produced in proton-proton collisions at $\sqrt{s} = 8$ TeV with the ATLAS detector*, ATLAS-CONF-2014-058, (2014), https://cds.cern.ch/record/1951336.

[198] ATLAS Collaboration, *Measurement of the top quark pair production cross-section with ATLAS in the single lepton channel*, Phys. Lett. **B711** (2012) 244–263, arXiv:1201.1889 [hep-ex].

[199] ATLAS Collaboration, *Jet energy resolution and selection efficiency relative to track jets from in-situ techniques with the ATLAS Detector Using Proton-Proton Collisions at a Center of Mass Energy sqrts = 7 TeV*, ATLAS-CONF-2010-054, (2010), https://cds.cern.ch/record/1281311.

[200] D0 Collaboration, *b-Jet Identification in the D0 Experiment*, Nucl. Instrum. Meth. **A620** (2010) 490–517, arXiv:1002.4224 [hep-ex].

[201] ATLAS Collaboration, *Calibration of b-tagging using dileptonic top pair events in a combinatorial likelihood approach with the ATLAS experiment*, ATLAS-CONF-2014-004, (2014), https://cds.cern.ch/record/1664335.

[202] ATLAS Collaboration, *Calibration of the performance of b-tagging for c and light-flavour jets in the 2012 ATLAS data*, ATLAS-CONF-2014-046, (2014), https://cds.cern.ch/record/1741020.

[203] ATLAS Collaboration, *Improved luminosity determination in pp collisions at sqrt(s) = 7 TeV using the ATLAS detector at the LHC*, Eur. Phys. J. **C73** no. 8, (2013) 2518, arXiv:1302.4393 [hep-ex].

[204] ATLAS Collaboration, *Jet energy measurement and systematic uncertainties using tracks for jets and for b-quark jets produced in proton-proton collisions at $\sqrt{s} = 7$ TeV in the ATLAS detector*, ATLAS-CONF-2013-002, (2013), https://cds.cern.ch/record/1504739.

[205] ATLAS Collaboration, *Light-quark and Gluon Jets: Calorimeter Response, Jet Energy Scale Systematics and Properties*, ATLAS-CONF-2012-138, (2012), https://cds.cern.ch/record/1480629.

[206] R. D. Ball et al., *Parton distributions with LHC data*, Nucl. Phys. **B867** (2013) 244–289, arXiv:1207.1303 [hep-ph].

[207] S. Alekhin et al., *The PDF4LHC Working Group Interim Report*, arXiv:1101.0536 [hep-ph].

[208] S. Frixione and B. R. Webber, *Matching NLO QCD computations and parton shower simulations*, JHEP **06** (2002) 029, arXiv:hep-ph/0204244 [hep-ph].

[209] S. Frixione, F. Stoeckli, P. Torrielli, B. R. Webber and C. D. White, *The MCaNLO 4.0 Event Generator*, arXiv:1010.0819 [hep-ph].

[210] G. Corcella, I. G. Knowles, G. Marchesini, S. Moretti, K. Odagiri, P. Richardson, M. H. Seymour and B. R. Webber, *HERWIG 6: An Event generator for hadron emission reactions with interfering gluons (including supersymmetric processes)*, JHEP **01** (2001) 010, arXiv:hep-ph/0011363 [hep-ph].

[211] G. Corcella, I. G. Knowles, G. Marchesini, S. Moretti, K. Odagiri, P. Richardson, M. H. Seymour and B. R. Webber, *HERWIG 6.5 release note*, arXiv:hep-ph/0210213 [hep-ph].

[212] ATLAS Collaboration, *Measurement of the top quark-pair production cross section with ATLAS in pp collisions at* $\sqrt{s} = 7$ *TeV*, Eur. Phys. J. **C71** (2011) 1577, arXiv:1012.1792 [hep-ex].

[213] G. Choudalakis, *On hypothesis testing, trials factor, hypertests and the BumpHunter*, in *Proceedings, PHYSTAT 2011 Workshop on Statistical Issues Related to Discovery Claims in Search Experiments and Unfolding, CERN,Geneva, Switzerland 17-20 January 2011*, (2011), arXiv:1101.0390 [physics.data-an].

[214] G. Cowan, K. Cranmer, E. Gross and O. Vitells, *Asymptotic formulae for likelihood-based tests of new physics*, Eur. Phys. J. **C71** (2011) 1554, arXiv:1007.1727 [physics.data-an], [Erratum: Eur. Phys. J.C73,2501(2013)].

[215] A. L. Read, *Presentation of search results: The CL(s) technique*, J. Phys. **G28** (2002) 2693–2704, [11(2002)].

[216] A. Wald, *Tests of Statistical Hypotheses Concerning Several Parameters When the Number of Observations is Large*, Transactions of the American Mathematical Society **54** no. 3, (1943) 426–482, http://www.jstor.org/stable/1990256.

[217] S. S. Wilks, *The Large-Sample Distribution of the Likelihood Ratio for Testing Composite Hypotheses*, Annals Math. Statist. **9** no. 1, (1938) 60–62.

[218] *P-value*, http://en.wikipedia.org/wiki/P-value.

[219] L. Moneta, K. Belasco, K. S. Cranmer, S. Kreiss, A. Lazzaro, D. Piparo, G. Schott, W. Verkerke and M. Wolf, *The RooStats Project*, PoS **ACAT2010** (2010) 057, arXiv:1009.1003 [physics.data-an].

[220] W. Verkerke and D. P. Kirkby, *The RooFit toolkit for data modeling*, eConf **C0303241** (2003) MOLT007, arXiv:physics/0306116 [physics].

[221] ROOT Collaboration, *HistFactory: A tool for creating statistical models for use with RooFit and RooStats*, CERN-OPEN-2012-016, (2012), https://cds.cern.ch/record/1456844.

[222] S. Jung, J. Song and Y. W. Yoon, *Dip or nothingness of a Higgs resonance from the interference with a complex phase*, Phys. Rev. **D92** no. 5, (2015) 055009, arXiv:1505.00291 [hep-ph].

[223] D. Ferreira de Lima, *Search for new resonances coupling to third generationquarks in pp collisions at 13 TeV at ATLAS*, on behalf of the ATLAS Collaboration, 38th International

Conference on High Energy Physics, Chicago, 2016, https://indico.cern.ch/event/432527/contributions/2208689/attachments/1321196/1981357/ichep-2016-tt-tb.pdf.

[224] M. Bauer, U. Haisch and F. Kahlhoefer, *Simplified dark matter models with two Higgs doublets: I. Pseudoscalar mediators*, JHEP **05** (2017) 138, arXiv:1701.07427 [hep-ph].

[225] M. Aaboud, G. Aad, B. Abbott, O. Abdinov, B. Abeloos, D. K. Abhayasinghe, S. H. Abidi, O. S. AbouZeid, N. L. Abraham and et al., *Search for single production of vector-like quarks decaying into Wb in pp collisions at $\sqrt{s}$ = 13 TeV with the ATLAS detector*, Journal of High Energy Physics **2019** no. 5, (2019), http://dx.doi.org/10.1007/JHEP05(2019)164.

[226] B. Hespel, F. Maltoni and E. Vryonidou, *Signal background interference effects in heavy scalar production and decay to a top-anti-top pair*, JHEP **10** (2016) 016, arXiv:1606.04149 [hep-ph].

[227] LHC Dark Matter Working Group , *LHC Dark Matter Working Group: Next-generation spin-0 dark matter models*, Phys. Dark Univ. **27** (2020) 100351, arXiv:1810.09420 [hep-ex].

[228] CMS Collaboration, *Search for heavy Higgs bosons decaying to a top quark pair in proton-proton collisions at $\sqrt{s}$ = 13 TeV*, arXiv:1908.01115 [hep-ex].

[229] ATLAS Collaboration, *Jet reconstruction and performance using particle flow with the ATLAS Detector*, Eur. Phys. J. **C77** no. 7, (2017) 466, arXiv:1703.10485 [hep-ex].

[230] ATLAS Collaboration, *LHC-ATLAS Phase-I upgrade: calibration and simulation of a new trigger readout system for the Liquid Argon calorimeter*, ATL-LARG-PROC-2020-003, (2020), https://cds.cern.ch/record/2709549.

[231] S. Tavernier, *Experimental Techniques in Nuclear and Particle Physics*, Springer, (2010).

[232] J. A. Formaggio and G. P. Zeller, *From eV to EeV: Neutrino Cross Sections Across Energy Scales*, Rev. Mod. Phys. **84** (2012) 1307–1341, arXiv:1305.7513 [hep-ex].

[233] C. Grupen and B. Shwartz, *Particle Detectors*, Cambridge Monographs on Particle Physics, Nuclear Physics and Cosmology, Cambridge University Press, 2 ed., (2008).

[234] R. Wigmans, *Calorimetry: Energy measurement in particle physics*, Int. Ser. Monogr. Phys. **107** (2000) 1–726.